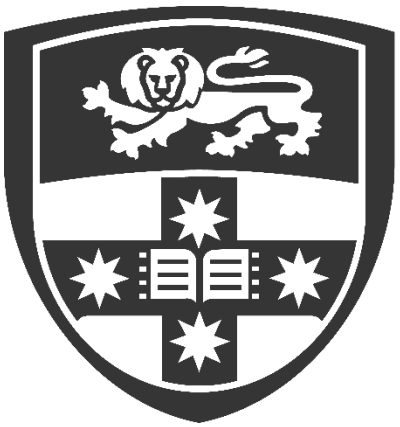

THE UNIVERSITY OF SYDNEY

Developing 3D Models of Paediatric Solid Tumours

Samuel David Peter Bax

BSc (Hons), MRes

A thesis submitted in fulfilment of the requirements for the degree of Doctor of Philosophy,

The University of Sydney, Faculty of Medicine and Health. 2025

Statement of Originality

This is to certify that, to the best of my knowledge, the intellectual content of this thesis is the product of my own work, and that all the assistance receiving in preparing this submission, including all sources used, have been acknowledged within the text. This thesis has not been submitted for any other degree or purposes.

Samuel Bax – 23rd April 2025

Abstract

High-grade gliomas (HGGs) are aggressive brain tumours with no curative therapies, and survival rates have remained unchanged for decades. Although treatments often appear promising in preclinical studies using conventional 2D assays and animal models, they frequently fail at clinical trials due to a lack of efficacy or unacceptable toxicity. More representative 3D *in vitro* models of the tumour and healthy brain microenvironment are urgently required to address these discrepancies and to improve patient outcomes. Research presented in this thesis aimed to establish and explore applications for 3D stem cell-derived cortical organoids, tumour spheroids, assembloid co-cultures, and patient-derived organoids (PDOs) in the context of HGGs. Initially, we developed a functional assay for assessing neurotoxicity using dorsal cortical organoids mimicking the structure and cellular populations of the developing human neocortex. Spontaneous electrical activity in organoids, measured by micro-electrode array (MEA), was significantly altered upon chronic exposure to kinase inhibitors, and changes to signalling pathways associated with neuronal development were also observed. Next, we evaluated the potency of a novel EphA2-targeted chimeric antigen receptor (CAR)-T cell therapy against 3D HGG models. Treatment sensitivity decreased from 2D to 3D spheroid models, necessitating increased dosage and duration. When treatment was administered to assembloid co-culture models comprising both tumour and organoid components, CAR-T cells were trafficked though organoid tissue to target tumour cells; however, sensitivity was further diminished, more closely reflecting *in vivo* responses. Lastly, PDOs were established from paediatric glioblastoma multiforme (pGBM) patient tumour samples, and circulating tumour DNA (ctDNA) was isolated from culture medium. ctDNA exhibited hotspot mutations consistent with clinical reports from the primary tumour, offering

an alternative resource for diagnosis, preclinical therapeutic screening, and personalised treatment selection. Collectively, this research underscores the importance of 3D *in vitro* models in drug development and clinical workflows, demonstrating their utility in predicting neurotoxicity, assessing treatment efficacy, and enhancing diagnostic characterisation.

Acknowledgments

As I finally reach the end of a challenging three and a half years, there are so many people to thank who have supported this research, and without whom none of this would have been possible.

First and foremost, I have nothing but the utmost gratitude to Geraldine, who has been the most supportive supervisor anyone could ask for. Since I joined the department five years ago, not only have you given countless amounts of feedback on experiments and to get this thesis into decent shape, but you've also been the advocate behind-the-scenes building connections, finding new resources, and securing funding to keep our research going. I'll always appreciate your perspective and occasional reminders to not undervalue myself or my accomplishments, which I'll admit I have a tendency to do sometimes.

My thanks also go out to my co-supervisor Anai and her team at the Stem Cell & Organoid Facility, particularly Milan and Scott. When I started this project, there were many gaps in my knowledge which your expertise helped to fill, and progress would have been much slower and more frustrating without those insights.

Like many students before me, I have to profusely thank Yuyan, whose dedication and knowledge in the lab is unrivalled. You've been an enduring support throughout the highs and lows of the past few years, maintained a keen interest in FAB group's experiments, and helped to make sure that all potential crises are averted.

In the FAB group, I've worked daily alongside some of the most hardworking and talented researchers, both past and present. Vic, Amy, and Louise - you did so much to teach me and get me back up to scratch after being away from the lab for years. You all set such a high standard that I've done my best to emulate. Teah and Sam – your enthusiasm for

research has at times managed to infect even this chronic pessimist. You've made the long TC days far more tolerable and you're both great additions to the team.

All of the CCRU has contributed in some form or another to this research. Both Natalie and Smadar were pivotal in the latter chapter of this thesis, clearing time in their schedules to get patient samples consented and to help with all things PCR-related, for which I'm incredibly appreciative. The same goes to Safaa and Sayali for their assistance with Westerns and flow experiments. I wish you both all the best with your own PhD struggles, and have no doubt that your own research careers will be amazing. Just as important, the moral support and camaraderie of the department make it a great environment to work in, so my heartfelt thanks go to Amanda, Josh, Janett, Dan, Kavi, Robyn, Li, Aysen, Dianne, Oscar, Melissa, Bryce, Jody, Ken, and the other students during my time with the unit.

Importantly, I must also acknowledge the patients and their families who contributed tissue and granted consent for its use in this research. I was incredibly fortunate and privileged to be able to work in a hospital research lab, and to have the opportunity to work on such a meaningful area of research. Similarly, my thanks to the sources of funding for my degree, which included the Balance Foundation, Dooley's Lidcombe Catholic Club, and the Sydney Children's Hospitals Foundation.

Finally, I have to thank my family for all their sacrifices and support in pursuing this degree. Emma – when this opportunity came up, you agreed I should pursue it as the best decision for our long-term future. As difficult as we've both found it, you've been by my side through the tough times and I couldn't have done any of this without you. To my mum, Tessa – you instilled in me a hard-work ethic, the value of an education, and to aim as high as possible. I wouldn't have turned out to be half the person I am today without your influence. To my in-laws, Elayne and Richard – thank you for taking me in and treating me as one of

your own. I greatly appreciate your support, and hope I've been able to repay some of the faith you've had in me. Lastly, a mention to the menagerie at home – Ollie, Lola, Ted, and Scout – whose antics and unending enthusiasm always brighten my day.

Abbreviations

2D	Two-dimensional
3D	Three-dimensional
5-FU	Fluorouracil
ABCG1, ABCG2	ATP-binding cassette super-family G member 1,2
ACCR	Australian Childhood Cancer Registry
ACK	Ammonium-chloride-potassium
ACVR1	Activin A receptor type I
AD	Alzheimer's disease
ADHD	Attention-deficit/hyperactivity disorder
AIHW	Australian Institute of Health and Welfare
Akt	Alpha serine-threonine kinase/Protein kinase B
ALK	Anaplastic lymphoma kinase
ALL	Acute lymphoblastic leukaemia
ALT	Alternative lengthening of telomeres
AMPA	α-Amino-3-hydroxy-5-methyl-4-isoxazolepropionic acid
ANZCHOG	Australian and New Zealand Children's Haematology/Oncology Group
APC	Antigen-presenting cell
ARF	Alternate reading frame
ASCs	Adult stem cells
ASD	Autism spectrum disorder
ATP	Adenosine triphosphate
ATRX	Alpha-thalassemia/mental retardation, X-linked
B7-H3	B7 homolog 3
BBB	Blood-brain barrier
BCMA	B-cell maturation antigen
BCNU	Bis-chloroethylnitrosourea

BDNF	Brain-derived neurotrophic factor
BF	Bright-field
BLAST	Basic Local Alignment Search Tool
BMP	Bone morphogenetic protein
BRAF	Rapidly accelerated fibrosarcoma - B
BSA	Bovine serum albumin
CAR	Chimeric antigen receptor
CCG	Children's Cancer Group
CCL2	Chemokine ligand 2
CCNU	1-(2-chloroethyl)-3-cyclohexyl-1-nitrosourea/Lomustine
CDK-4, CDK-6	Cyclin-dependent kinase 4, 6
CDKN2A/B	Cyclin-dependent kinase inhibitor 2A/B
cfDNA	Cell-free DNA
CHW	Children's Hospital at Westmead
ClpP	Caseinolytic peptidase P
CMMRD	Constitutional mismatch repair deficiency
CNQX	Cyanquixaline
CNS	Central nervous system
COG	Children's Oncology Group
CRISPR	Clustered regularly interspaced short palindromic repeats
CRS	Cytokine release syndrome
ctDNA	Circulating tumour DNA
CTIP2	Chicken ovalbumin upstream promoter transcription factor (COUP-TF)-interacting protein 2
CTL	Cytotoxic T lymphocyte
CTLA-4	Cytotoxic T-lymphocyte associated protein 4
DALYs	Disability-adjusted life-years
D-AP5	D(-)-2-amino-5-phosphonopentanoate
DAPI	4′,6-diamidino-2-phenylindole
ddPCR	Droplet digital polymerase chain reaction
DIPG	Diffuse intrinsic pontine glioma

DMEM	Dulbecco’s modified eagle medium
DMG	Diffuse midline glioma
DMSO	Dimethyl sulfoxide
DNA	Deoxyribonucleic acid
DPBS	Dulbecco’s phosphate buffered solution
DRD2	Dopamine receptor D2
DTI	Diffuse tension imaging
DTT	Dithiothreitol
dUTP	Deoxyuridine phosphate
ECM	Extracellular matrix
EDTA	Ethylenediaminetetraacetic acid
EGF	Epidermal growth factor
EGFR	Epidermal growth factor receptor
eGFP	Enhanced green fluorescent protein
EGFR	Epidermal growth factor receptor
EphA2	Ephrin type-A receptor 2
eRMS	Embryonal rhabdomyosarcoma
E:T	Effector:Target
ETSV2	ETS variant transcription factor 2
EZH2	Enhancer of zeste homolog 2
EZHIP	Enhance of zeste homolog inhibitor protein
FACS	Fluorescence-activated cell sorting
FAM	Fluorescein amidite
FASD	Fetal alcohol syndrome disorder
FBS	Fetal bovine serum
FDA	US Food and Drug Administration
FGF	Fibroblast growth factor
FITC	Fluorescein isothiocyanate
FOP	Fibrodysplasia ossificans progressiva
FOXG1	Forkhead box protein G1

FOXO	Forkhead box O
FSC-A	Forward scatter – area
FSC-H	Forward scatter - height
G328V	Valine substitution at glycine 328
G34R/V	Arginine/valine substitution at glycine 34
GABA	Gamma-aminobutyric acid
$GABA_A$	GABA Type A receptor
GAPDH	Glyceraldehyde 3-phosphate dehydrogenase
GBD	Global Burden of Disease Study
GBM	Glioblastoma multiforme
GD2	Ganglioside G2
gDNA	Genomic DNA
GDNF	Glial cell line-derived neurotrophic factor
GFAP	Glial fibrillary acidic protein
GLICO	Glioma-cortical organoid
GM-CSF	Granulocyte macrophage colony stimulating factor
GNS	Glioma neural stem
GOF	Gain-of-function
GTP	Guanosine triphosphate
H3	Histone 3
H3K27me3	Trimethylation of histone 3 lysine 27
HBSS	Hanks' Balanced Salt Solution
HDAC	Histone deacetylase
HD-CMOS	High-density complementary metal-oxide semiconductor
HEPES	4-(2-hydroxyethyl)-1-piperazineethanesulfonic Acid
HER2	Human epidermal growth factor receptor 2
hESC	Human embryonic stem cell
HEX	Hexachlorofluorescein
HGG	High-grade glioma
HIF1α	Hypoxia inducible factor 1 alpha

hiPSC	Human induced pluripotent stem cell
HLA	Human leukocyte antigen
HMOX1	Heme oxygenase 1
hNPC	Human neural progenitor cell
hPSC	Human pluripotent stem cell
HSV	Herpes simplex virus
IBI	Inter-burst interval
ID1, ID2	Inhibitor of differentiation 1, 2
IDH	Isocitrate dehydrogenase
IDO	Indoleamine 2,3-dioxygenase
IFL	Inner fibre layer
IgG	Immunoglobulin G
IL13Rα2	Interleukin-13 receptor subunit alpha-2
INK4A	Inhibitor of cyclin-dependent kinase 4
IQ	Intelligence quotient
ISI	Inter-spike interval
ISVZ	Inner sub-ventricular zone
ITS	Insulin-transferrin-selenium sodium pyruvate solution
K27M	Methionine substitution at lysine 27
K3326*	Polymorphic stop codon at lysine 3326
LDEV	Lactate dehydrogenase elevating virus
LDH	Lactate dehydrogenase
LGG	Low-grade glioma
LOF	Loss-of-function
LVV	Lentiviral vector
MAP2	Microtubule-associated protein 2
MAPK	Mitogen-activated protein kinase
MATCH	Molecular Analysis for Therapy Choice trial
MCTS	Multicellular tumour spheroid
MDM2, MDM4	Mouse double minute 2, 4

MDSC	Myeloid-derived suppressor cell
MEA	Micro-electrode array
MEM-NEAA	Minimum essential medium, non-essential amino acids
METH	Methamphetamine
MGMT	Methylated-DNA--protein-cysteine methyltransferase/ O^6-alkylguanine DNA alkyltransferase AGT
MHC	Major histocompatibility complex
MICBO-TF	Microglia-containing brain organoid tumour fusion
MISCO	Midbrain, striatal, and cortical organoid (assembloid)
MMP10	Matrix metalloproteinase 10
MOI	Multiplicity of infection
MPH	Methylphenidate hydrochloride
MRI	Magnetic resonance imaging
mTOR	Mammalian target of rapamycin
MTX	Methotrexate
NCI	National Cancer Institute
NCS-1	Neuronal calcium sensor 1
NESTIN	Neuroepithelial stem cell protein
NF1	Neurofibromatosis 1
NMDA	N-methyl-D-aspartate
NSCs	Neural stem cells
NSCLC	Non-small cell lung cancer
NT-3	Neurotrophin-3
NTC	Non-template control
NOE/NEC	Not otherwise specified/not elsewhere classified
O6BG	O^6-benzylguanine
OCT	Optimal cutting temperature
OPCs	Oligodendrocyte precursor cells
oRGs	Outer radial glia
OSVZ	Outer sub-ventricular zone
P53/TP53	Tumour protein 53

PAGE	Polyacrylamide gel electrophoresis
PARP	Poly (ADP-ribose) polymerase
PAX2, 6	Paired box protein-2/6
PBMCs	Peripheral blood mononuclear cells
PBS	Phosphate-buffered saline
PBTC	Paediatric Brain Tumour Consortium
PCR	Polymerase chain reaction
pCV	Prednisone, CCNU/lomustine, vincristine
PDE	Patient-derived explant
PDGFR	Platelet-derived growth factor receptor
PD-1	Programmed cell death 1
PD-L1	Programmed cell death ligand 1
PDMS	Polydimethylsiloxane
PDO	Patient-derived organoid
PDX	Patient-derived xenograft
PE	Phycoerythrin
PEDOT	Poly(3,4-ethylenedioxythiophene)
PEG	Poly(ethylene) glycol
PEGDA	Poly(ethylene) glycol diacrylate
PFA	Paraformaldehyde
PFS	Progression-free survival/Posterior fossa syndrome
pGBM	Paediatric glioblastoma
P-gp	P-glycoprotein
pHGG	Paediatric high-grade glioma
PI3K	Phosphatidylinositol 3'-kinase
PI3KCA	Phosphatidylinositol-4,5-bisphosphate 3-kinase catalytic subunit alpha
PLO	Poly-L-Ornithine
PMSF	Phenylmethylsulphonyl fluoride
POLD	DNA polymerase delta
POLE	DNA polymerase epsilon

PRC2	Polycomb repressive complex 2
PSD-95	Post-synaptic density protein 95
PTEN	Phosphatase and tensin homolog
PTPN11	Protein tyrosine phosphatase non-receptor type 11
R206H	Histidine substitution at arginine 206
RAS	Rat sarcoma gene
Rb	Retinoblastoma
RETM	Renaissance Essential Tumour Medium
RLU	Relative Light Units
RNA	Ribonucleic acid
ROCK	Rho-associated protein kinase
ROUT	Removal of outliers test
RTK	Receptor tyrosine kinase
S100ß	S100 calcium-binding protein ß
SATB1, SATB2	Special AT-rich sequence-binding protein 1 & 2
SCHN	Sydney Children's Hospital Network
SDS	Sodium dodecyl sulphate
SEGA	Subependymal giant cell astrocytoma
SHH	Sonic hedgehog homolog
siRNA	Short interfering RNA
SMAD	Suppressor of mothers against decapentaplegic
SmGM	Smooth muscle growth medium
SOX1, SOX2	(Sex-determining region Y)-box 1 & 2
SRS	Stereotactic radiosurgery
SSC-A	Side scatter - area
STR	Short tandem repeat
SVZ	Sub-ventricular zone
TAE	Tris-acetate-EDTA
TAM	Tumour-associated macrophage
TBR2	T-box brain protein 2/Eomesdermin

TBS	Tris-buffered saline
TCGA	The Cancer Genome Atlas
TE	Tris-EDTA
TERT	Telomerase reverse transcriptase
TGF-β	Transforming growth factor beta
TKI	Tyrosine kinase inhibitor
TIMP3	Tissue inhibitor of metalloproteinases 3
TMZ	Temozolomide
TNFα	Tumour necrosis factor alpha
TREM2	Triggering receptor expressed on myeloid cells 2
TSC	Tuberous sclerosis complex
TSM	Tumour stem medium
ULA	Ultra-low attachment
VAF	Variant allele frequency
VBM	Voxel-based morphometry
VEGF	Vascular endothelial growth factor
VEGFR	Vascular endothelial growth factor receptor
WHO	World Health Organisation
Wnt	Wingless-related integration site
YKL-40	Chitinase-3-like protein 1
YLDs	Years lived with disability

List of Tables

List of Figures

Table of Contents

Introduction 1

1.1 - Overview of Brain Cancer in Australia

In 2023, the Australian Institute of Health and Welfare (AIHW) estimated there were 165,000 cancer diagnoses and 51,000 cancer-related deaths in Australia in adults. Between 2000 and 2023, incidence of adult cancer diagnoses increased by 88%, attributed to an increasing population size and a longer-lived population. In contrast, the 5-year survival rate for cancer overall has improved from 53% in 1990-1994 to 71% survival by 2015-2019, due to advances in cancer screening and available treatment options [AIHW 2023].

Paediatric cancer statistics have followed broadly comparable trends, as reported by the Australian Childhood Cancer Registry (ACCR), which collects data from all Australian states and territories. Between 2000 and 2020, cancer diagnoses in children 0-14 years old increased from 595 to 840 cases per annum (41% increase), with prevalence highest in children between 0-4 years old. Similarly to adult cancers, 5-year survival rates of paediatric cancers overall have improved from 72.5% in 1983-1994 to 86.4% survival in 2007-2018 [ACCR]. Improvements to the outcomes for paediatric cancer patients have been driven by a number of factors, such as a better understanding of the differences between childhood and adult disease, wider identification of oncogenic mutations and biomarkers, greater consideration of the long-term impacts of treatment on childhood development, and the emergence and incorporation of immunotherapies. Substantial survival increases have been

observed in some of the most prevalent cancers, with the notable exception of paediatric brain cancer.

Cancers of the central nervous system (CNS) are the second-most frequently diagnosed in children aged 0-14, representing 189 of 840 cases in 2020 (22.5%) [ACCR]. Outcomes vary widely, with lower-grade tumours exhibiting 5-year survival rates exceeding 90%, while patients with high-grade gliomas (HGGs) have limited therapeutic recourse and 5-year survival rates as low as 1-2%. The poor prognosis of patients with HGGs is a significant contributor to brain tumours being the leading cause of cancer-related deaths in children, accounting for approximately 40% of total paediatric cancer deaths. Furthermore, brain tumours rank as the third-leading cause of overall childhood mortality in most economically developed countries [AIHW 2023].

In addition to poor mortality rates, brain cancer possesses a high disease burden, described as the impact of disease on patients and the requirements of the healthcare system for effective diagnosis and management. The Global Burden of Disease (GBD) Study quantifies burden by the number of disability-adjusted life-years (DALYs); a summation of the years of life lost (YLLs) and years lived with disability (YLDs) [Force 2019]. Analysis of global data collected by the GBD Study in 2017 estimated that cancer resulted in 11.5 million DALYs in children aged 0-19, of which 2.08 million DALYs (18.1%) were due to brain cancers, second only to leukaemias (34.1%) [Force 2019]. Specialist diagnostic equipment, multidisciplinary teams and multimodal treatments are all implemented when managing brain cancer patient care, requiring a robust and advanced healthcare system [Patel 2019].

1.1.1 - Glioblastoma Multiforme

Gliomas are brain tumours arising from glial cells – a group of cells consisting of astrocytes, oligodendrocytes, microglia, and their progenitors, and which comprise around

half of the total brain mass [Jakel & Dimou 2017]. As such, gliomas present across the entire CNS and exhibit symptoms dependent upon location, including chronic headaches, nausea, vomiting, impaired motor function, and seizures**.** Gliomas are the most prevalent category of primary brain tumour, accounting for 45% of all paediatric solid tumours, and can be divided into low-grade glioma (LGG; WHO grades I and II) and HGGs (WHO grades III and IV) based upon their histological features [Ostrom 2022].

The more-common LGGs constitute 30-40% of all primary paediatric brain tumours and have 5-year and 10-year overall survival rates in excess of 90%. LGGs are typically slow-growing, well-circumscribed tumours, and gross surgical resection of superficial lesions is a favourable indicator of patient survival [Wisoff 2011]. Complete resection of LGG tumours may not be possible in more deep-seated or delicate regions, and residual disease is treated with adjuvant chemotherapy. Radiotherapy may also be used in older patients where risk of cognitive impairment is considered minimal. Routine radiological surveillance is recommended, with disease progression or recurrence detected in almost half of cases and requiring further treatment [Udaka 2013, Blionas 2018, Ajithkumar 2024].

In contrast, HGGs represent an estimated 8-12% of all CNS tumours in children, and are responsible for the majority of cancer-related deaths. They are characterised by high intratumoural heterogeneity and rapid infiltration throughout the CNS, considerably restricting available treatment options.

Throughout this thesis, there will be a focus on models of two paediatric HGGs (pHGGs); paediatric glioblastoma multiforme (pGBM) and diffuse intrinsic pontine glioma (DIPG). Therefore, the following sections will provide some background information on these tumours and the obstacles encountered by clinicians and researchers.

GBM is a WHO grade IV astrocytic tumour most frequently presenting in the parietal and frontal lobes of the brain, and invading to nearby regions of the CNS [Bohn 2018]. GBM occurs as either primary or secondary disease, with the former arising from *de novo* mutations, and the latter progressing from WHO grade II and III astrocytoma [Ohgaki & Kleihues 2013]. Primary GBM accounts for approximately 90% of cases, and is typically diagnosed in older patients, with a median age at diagnosis of 64 years. In comparison, secondary GBM is more often found in younger patients (median age 40 years) and has longer survival duration than primary GBM [Wilson T 2014]. Stupp et al. established the current clinical management protocol, consisting of maximal resection of the tumour site, post-operative radiotherapy, and treatment with the alkylating agent temozolomide (TMZ) [Stupp 2005].

GBM pathogenesis is a complex multi-stage process, involving the accumulation of numerous mutations to cell signalling pathways responsible for cell cycle regulation. The Cancer Genome Atlas (TCGA) project specifically identified three main pathways present in the majority of GBM diagnoses; RTK/AKT/PI3K (88% cases), p53 (87% cases), and retinoblastoma (78% cases) [Cancer Genome Atlas Research Network 2008].

Several receptor tyrosine kinases (RTKs) and their ligands are associated with GBM, including epidermal growth factor receptor (EGFR), platelet-derived growth factor receptor (PDGFR), and vascular endothelial growth factor receptor (VEGFR). Alterations to EGFR are observed in approximately 50% of GBM cases, with amplification most frequently occurring, followed by a mutation involving intragenic in-frame deletion of exons 2-7, known as EGFRvIII variant [An Z 2018]. Aberrant EGFR signalling causes hyperactivation of phosphoinositide 3-kinase (PI3K), phosphorylating and inducing AKT activity, and leading to the dysregulation of downstream targets such as mTOR and FOXO. Dysregulation of these targets is pivotal for cellular differentiation, survival, and apoptosis in several cancers,

including GBM [Hashemi 2023]. Mutations and loss-of-function of associated tumour suppressors PTEN and NF-1 have similar implications, activating PI3K pathway effectors AKT and RAS, respectively. [Luo 2022, Hashemi 2023] EGFRvIII mutation, PTEN knockout, and inactivation of $p16^{INK4A}$ and p19/ARF in combination are also implicated in gliomagenesis via AKT/mTOR activation [Bachoo 2002, Zhu H 2009, An Z 2018].

Under normal conditions, PDGFR-α regulates the development of glial progenitor cells and oligodendrocyte differentiation. Alterations to PDGFRs have been linked with several neurological disorders, and the development of low-grade and high-grade astrocytoma [Sil 2018]. PDGFR-α alterations are present in approximately 10% of adult GBMs, with amplifications, point mutations and truncation all reported in human clinical samples [Alentorn 2012, Peng 2021]. PDGFR-α mutations lead to aberrant activation of PI3K and its effectors leading to tumorigenic processes, as previously described. In GBM, activation of PDGFR-α also recruits SHP-2/PTPN11, in turn upregulating effectors in the EGFR/PI3K/AKT and RAS/MAPK pathways [Liu 2011].

VEGF and its receptors are closely associated with angiogenesis – which is aberrantly active in cancers, supporting the development of vasculature networks to support tumour growth. As a diffusely infiltrative tumour, the majority of GBM express VEGF at high levels [Loureiro 2020]**.** The hypoxic tumour microenvironment inactivates prolyl hydroxylases, leading to stabilisation of hypoxia-inducible factor HIF-1α, which in turn recruits co-activator CBP/p300 to activate transcription of hypoxic responsive genes, including *VEGF* [Kaur 2005]. Hypoxia-independent induction of angiogenesis may also occur, with epidermal growth factor (EGF) stimulating PI3K and MAPK pathways under normoxic conditions, leading to VEGF activation [Nicolas 2019].

The p53/ARF/MDM2 pathway is the second-most frequently altered in GBM, with mutations present in 87% of cases [Cancer Genome Atlas Research Network 2008]. Under normal conditions, low expression of the tumour suppressor p53 is maintained through MDM2- and MDM4-mediated ubiquitination and degradation. In response to DNA damage, $p14^{ARF}$ binds to MDM2, removing it to the nucleolus to prevent p53 inactivation [Weber 1999]. Subsequent induction of p53 then leads to activation of downstream apoptosis, senescence, or DNA repair effector pathways [Kung & Weber 2022]. ARF has also been observed to upregulate TIMP3 in order to inhibit endothelial cell migration and angiogenic vessel formation in GBM [Zerrouqi 2012]. The most common alteration to the p53 pathway is a homozygous deletion of the *CDKN2A/ARF* locus in approximately 60% of GBM, preventing the inactivation of MDM2 [Zhang Y 2018]. Amplification of *MDM2* and *MDM4* is reported in 14% and 7% of GBM cases respectively, leading to a similar suppression of p53 activity, though MDM2 amplification only occurs in instances of wild-type p53 [Reifenberger 1993]. Directly, missense mutations to *TP53* gene confer loss- or gain-of-function (LOF/GOF), impacting the tumour suppressive capacity of p53 and promoting tumour progression. Oncogenic properties of p53 GOF have been reported across numerous cancers, with links to increased proliferation, angiogenesis, invasion, and resistance to treatment [Muller & Vousden 2014]. Mutant p53 upregulates CCL2 and TNFα expression in GBM cells, leading to increased immune cell infiltration and inflammation associated with poorer patient outcomes [Ham 2019]**.** p53 GOF also plays a role in chemoresistance to TMZ treatment by upregulating *MGMT*, which repairs drug-induced DNA damage in GBM cells [Wang X 2013].

Lastly, TCGA identified disruption to the $p16^{INK4A}$/CDK-4/retinoblastoma pathway as the third-most frequent series of alterations in GBM [Cancer Genome Atlas Research Network 2008]. In normal cells, tumour suppressor gene *RB1* controls cellular proliferation

by regulating progression from G1 to S-phase. RB protein is phosphorylated by cyclin-dependent kinases CDK-4 and CDK-6, which are in turn regulated by CDK inhibitors $p16^{INK4A}$ and $p18^{CDKN2C}$. RB activation prompts the release of E2F transcription factors which then progress the cell cycle [Du & Searle 2009, Malumbres & Barbacid 2009]. In GBM, mutations which directly inactivate *RB1 or* $p16^{INK4A}$, or CDK-4 amplification, lead to aberrant expression of E2F1, uncontrolled cell cycling, and increased expression of anti-apoptotic genes [Kanu 2009]. Furthermore, homozygous deletion of the *INK4A/ARF* locus at chromosome 9p21 occurs in approximately half of all malignant glioma, and more frequently in primary rather than secondary GBM. This deletion affects the production of both $p16^{INK4A}$ and $p14^{ARF}$, dysregulating both the retinoblastoma and p53 pathways, respectively [Labuhn 2001]. Contrary to its normal function in regulating cell cycle progression, RB has also been demonstrated to inhibit apoptosis in GBM, increasing tumour resistance to treatment by positively regulating autophagy of cells upon stress [Biasoli 2013].

The complex signalling across multiple pathways presents a challenge in understanding and treating GBM. Therefore, attempts have been made to elucidate tumoural subtypes to better guide clinical management. Bulk tumour transcriptome analysis from TCGA data established four molecular subtypes; classical, neural, proneural and mesenchymal [Verhaak 2010]. Neural was later dropped from the Verhaak classification following identification of normal neural lineage contamination. Subsequent proteomic analysis found that classical GBM exhibited decreased expression of pro-apoptotic genes and downregulation of MAPK signalling. Mesenchymal disease had comparably higher activation of MAPK, as well as increased expression of endothelial markers such as VEGFR-2, extensive inflammation, and tumoural necrosis. Proneural GBM demonstrated increased PI3K pathway activity compared with mesenchymal, and both subtypes activated mTOR by different mechanisms [Brennan 2013, Zhang P 2020]. Evaluation of clinical data of molecular

subtypes found mesenchymal GBM to have the poorest outcome, with a median survival of 11.5 months post-diagnosis, compared to 14.7 months in classical and 17 months in proneural GBM [Wang Q 2017].

In 2016, the World Health Organisation (WHO) released the *Classification of Tumours of the CNS*, categorising GBM into four distinct histopathological subtypes; isocitrate dehydrogenase (IDH) wild-type, IDH-mutated, glioblastoma not otherwise specified (NOS), and glioblastoma not-elsewhere classified (NEC) [Louis 2016]. IDH enzymes contribute to major metabolic processes including the Krebs cycle, and are pivotal in maintaining cellular homeostasis. *IDH* mutations promote astrocyte transformation, and are detected in >80% of WHO grade II and III glioma, 73% of secondary GBM tumours, and only 3.7% of primary GBM tumours [Nobusawa 2009]. *IDH*-mutated secondary GBM has a more favourable survival duration than wild-type (31 months compared with 15 months) and is indicative of chemosensitivity to TMZ [Yan 2009, SongTao 2011]. Patient survival extends further still in tumours with *IDH* mutations in the absence of *MGMT* promoter methylation [Hertler 2023]. Lower levels of HIF-1α suppress angiogenesis pathways in IDH-mutated GBM, and transcriptomic analysis reported dramatically increased vasculature formation processes in wild-type disease, leading to the more aggressive phenotype [Kickingereder 2015, Álvarez-Torres 2023].

1.1.2 - Paediatric Glioblastoma & Diffuse Intrinsic Pontine Glioma

While adult and paediatric glioblastoma share similar histological features, the 2016 WHO report acknowledged distinct molecular signatures present in pGBM separating the two entities. Due to its rarity, and literature frequently grouping all pHGGs together, incidence varies between cohorts, but occurs in approximately 0.85 per 100,000 children and affects males slightly more often [Ostrom 2022]. The majority of cases arise in the supratentorial

brain, particularly the cerebral hemispheres where 35-50% tumours are detected and patients have a median age of 9 years old upon diagnosis. Infratentorial cases most frequently emerge in the brain stem (<20%) or cerebellum (1-2%). Non-brain stem infratentorial GBM more commonly affects younger children, rather than adolescents or young adults [Fangusaro 2012]. Overall survival duration for pGBM is generally longer than adult GBM, ranging from 10-73 months post-diagnosis, and reported 5-year survival rates vary between 15% and 40%. Negative prognostic factors include older age upon diagnosis, and tumours arising in the midline regions of the brain where critical function occurs and therapeutic intervention is limited [Singla 2021]. Tumourigenesis remains poorly understood, however contributing factors include prior exposure to ionising radiation and cancer predisposition conditions such as Li-Fraumeni syndrome (p53 inactivation), Turcot syndrome (constitutional mismatch repair deficiency; CMMRD), and neurofibromatosis-1 (NF1) [Das K & Kumar 2017].

Although IDH mutations allow for categorisation of subtypes of adult glioma, the majority of pHGGs are IDH wild-type. IDH mutations are typically only seen in pGBM patients >14 years old, and confer similar survival benefits as in adult GBM when compared to wild-type [Pollack 2011a]. pHGGs are further distinguished by mutations to genes encoding for histone H3 variants, occurring in approximately 50% of pHGGs compared to 1% of adult HGGs. K27M mutation is a substitution of methionine in place of lysine 27, most frequently on H3.3 variant encoded by *H3F3A*, but also occurring on *HIST1H3B* and *HISTH3C* for H3.1, and rarely on *HIST2H3C* for H3.2 variants. These tumours are generally restricted to the midline regions such as the thalamus and pons, and are defined as H3K27M-mutant diffuse midline gliomas (DMGs). G34R/V mutations exchange glycine 34 for arginine or valine on H3.3, and present in 16% of cortical pHGGs. G34R/V-mutant tumours arise in older patients with a median age of 15 years old, and longer survival time than H3.1- or H3.3K27M tumours [Kasper & Baker 2020].

Korshunov and colleagues categorised pGBM into three H3-/IDH- wild-type molecular subtypes with distinct clinical outcomes [Korshunov 2017]. The largest subtype, pedGBM_MYCN, was characterised by *MYCN* amplification (50% cases), *TP53* mutations (67%), and amplification of *CDK4/6* (22%). These tumours had the youngest median age upon diagnosis at 8 years old, and the poorest clinical prognosis with median overall survival just 14 months. Although more commonly associated with other cancers, such as neuroblastoma, *MYCN* has been implicated in initiating tumourigenesis in H3 wild-type and mutant pHGGs [Bjerke 2013]. The second largest group was pedGBM_RTK1, in which a third of tumours displayed *PDGFRA* amplification. Median age was the highest at 11 years old, and median overall survival of 21 months. Amplified *PDGFRA* in non-brain stem pHGGs confers a poorer prognosis than in the absence of *PDGFRA* amplification [Koschmannn 2016a]. Finally, pedGBM_RTK2 tumours exhibited *EGFR* amplification in 50% of cases, along with *TERT* promoter mutations (64%), *CDKN2A/B* homozygous deletions (72%). ped_RTK2 tumours had the longest overall survival at 44 months post-diagnosis, likely in part due to the absence of *MGMT* promoter methylation in this subtype reducing chemoresistance [Korshunov 2017]. A similar study of H3-/IDH-wild-type HGGs by Mackay et al., which incorporated other tumours into their classification system, also noted a prognostically favourable subtype with BRAF V600E, NF1, or RTK fusions similar to LGGs [Mackay 2017].

Additional markers related to the p53, Rb and RTK pathways continue to be investigated for prognostic significance. Among the most prominent for pGBM are *ATRX* alterations, observed in around 30% of cases of mutated p53 in older children. Mutations or loss of *ATRX* promotes alternative lengthening of telomeres (ALT), and is hypothesised to impair non-homologous end joining DNA repair pathways in GBM. *ATRX*-mutated tumours are therefore more responsive to treatment and associated with better prognosis [Koschmann

2016b, Uppar 2019]. As research progresses, it is likely that further changes to classification of pGBM will occur to better guide clinical intervention and management.

Alongside pGBM, this thesis examines another fatal paediatric brain tumour, DIPG, which is a diffuse midline glioma (DMG) situated in the pons. As with GBM, epidemiology of DIPG varies depending upon definition and cohort, but affects approximately 1 per 100,000 children, equivalent to 20-30 diagnoses in Australia and New Zealand each year [Valvi 2024]. Due to tumoural infiltration and disruption of critical midline structures, therapeutic options are significantly restricted. Pontine biopsy has historically been avoided due to potential risk of neurological damage, restricting diagnosis to MRI imaging, and limiting the availability of tumour tissue for research. Diagnostic attitudes are changing regarding biopsies of suspected DIPG, allowing for further understanding of the molecular alterations driving disease progression, however targeted chemotherapy and immunotherapy currently remain ineffective and only administered under clinical trial. Radiotherapy is the only course of treatment to improve symptoms and slow disease progression, with re-irradiation considered if progression occurs after six months or more. As a result, prognosis of DIPG is uniformly dismal, with median survival of less than a year post-diagnosis, and a 5-year survival rate of just 1-2% [Valvi 2024, Hoffman 2018].

DIPGs are a subset of tumours termed ‘DMG, H3K27-altered’ [Louis 2016]. K27M substitutions on histone variants 3.1 and 3.3 comprise more than 80% of DIPG cases, driving tumorigenesis through inactivation of PRC2, which serves to regulate gene expression and maintain cell identity. H3K27M binds to the methyltransferase EZH2 sub-unit of PRC2, inhibiting its activity and leading to global loss of trimethylated H3K27 (H3K27me3), broad epigenetic dysregulation, induction of tumourigenesis pathways, and promotion of a self-renewing stem-like state in cancer cells [Jiao & Liu X 2015, Liu I 2022]. H3.1 K27M tumours typically arise in younger patients, conferring longer survival compared to H3.3

K27M. Histological distinctions can be made between the two entities, with H3.1 K27M resembling anaplastic astrocytoma, while H3.3 K27M appears more like GBM [Castel 2015]. The remaining 20% of DIPG cases are H3 wild-type, and characterised by the absence of K27M substitutions and overexpression of *EZHIP.* Loss of H3K27me3 is likewise observed in this subgroup, with *EZHIP* binding to the EZH2 sub-unit of PRC2 independently from K27M [Castel 2020].

Many of the pathways characterising GBM tumourigenesis are also altered in DIPG, including mutations to *TP53*, *PDGFRA* and *PTEN*. Exclusive to DIPG are mutations to *ACVR1*, encoding the BMP receptor ALK2. *ACVR1* mutations have been detected in a quarter of DIPG cases, with a tendency toward H3.1 K27M tumours, and the role of ACVR1 in disease initiation and progression continues to be explored. *ACVR1* mutations were previously reported in fibrodysplasia ossificans progressiva (FOP); a musculoskeletal disease whereby the connective tissues are transformed to bone. Upregulation of phosphorylated SMAD1/5/8 and downstream *ID1* and *ID2* confirms aberrant BMP signalling also present in *ACVR1*-mutant DIPG [Buczkowicz 2014]. In patient-derived DIPG cell lines, *ACVR1* R206H mutation in combination with H3.1K27M and loss of *TP53* initiates glioma formation, however requires amplification of *PDGFRA* signalling to further tumour development [Hoeman 2019]. In murine models, *ACVR1* G328V mutation suppresses oligodendrocyte differentiation, and collaborates with *PIK3CA* to initiate tumour formation [Fortin 2020]. Hyperactivation of PI3K signalling, including *PI3KCA* and *PIK3R1*, occurs in 55% of *ACVR1*-mutated DIPG. As with GBM, mutations and amplification of *PDGFRA* activate the PI3K/AKT/mTOR pathway in DIPG, leading to tumour cell proliferation and angiogenesis [Mackay 2017, Duchatel 2024].

1.1.3 - Clinical Trials for Paediatric High-Grade Glioma

Alterations to key signalling pathways give rise to tumour formation, unrestricted proliferation, differentiation, angiogenesis, and invasion. As multiple pathways are often engaged simultaneously, and HGGs are highly heterogeneous tumours, standard single-target agents demonstrate limited efficacy in patients. In response, clinical trials have sought to employ novel approaches, including combination therapies, kinase inhibition, and immunotherapies, together with conventional surgery and radiotherapy to improve participant outcomes. As of October 2024, 41 clinical trials are open to enrolment for paediatric patients with CNS tumours in Australia and New Zealand, per the Australia & New Zealand Children's Haematology/Oncology Group (ANZCHOG).

Early trials conducted by the Children's Cancer Group (CCG), later known as the Children's Oncology Group (COG), compared the inclusion of chemotherapy in treatment versus radiotherapy alone in patients with high-grade astrocytic tumours. Between 1976 and 1981, the CCG-943 phase III trial demonstrated the pCV regimen (adjuvant prednisone, CCNU/lomustine and vincristine) improved 5-year progression-free survival (PFS) to 46%, versus 18% in participants only treated with radiotherapy [Sposto 1989]. In an attempt to address progression and chemoresistance, the subsequent CCG-945 trial compared the pCV regimen with an 8-in-1 combination of alkylating agents, including lomustine, vincristine, prednisone, hydroxyurea, procarbazine, cisplatin, cytosine arabinoside, and dacarbazine/DITC. CCG-945 included 172 participants diagnosed with pHGG, and infants were not subjected to radiotherapy [Finlay 1995]. Long-term analyses of the trial observed no improvements in pGBM survival rates from the chemotherapy panel, determining the extent of surgical resection to be the most important prognostic factor [Wisoff 1998, Batra 2013]. Furthermore, cohorts from both CCG-943 and 945 were later found to have included brain

tumours with more favourable outcomes, such as LGGs, explaining the apparent initial improvements to survival rates [Das K & Kumar 2017].

Following the establishment of the Stupp protocol in treating adult GBM with maximal resection, radiotherapy, and adjuvant TMZ, the ACNS0126 phase II trial evaluated its efficacy across 107 pGBM, anaplastic astrocytoma, and gliosarcoma patients, and 63 DIPG patients [Cohen 2011a, Cohen 2011b]. As with adult GBM, poorer outcomes were noted in paediatric patients with *MGMT* overexpression restricting TMZ-induced DNA damage. While event-free survival and overall survival rates in ACNS0126 were not higher than the historical controls, more rigorous histological examination was applied to the cohort, and therapeutic side effects considered more tolerable. Consequently, TMZ was adopted as the main chemotherapeutic agent for treatment of pHGG, and clinical trials have sought to increase efficacy through combination with other chemotherapies. A Paediatric Brain Tumour Consortium (PBTC) phase II study targeted TMZ resistance by adding O^6-benzylguanine (O6BG), which binds to and inactivates *MGMT*, however no significant survival increases were noted across 41 participants [Warren 2012]. A similar approach was tested in the ACNS0423 study, whereby lomustine and TMZ was administered to 108 pGBM and anaplastic astrocytoma patients in an attempt to overcome *MGMT*-related chemoresistance, with slight improvements observed over ACNS0126 outcomes [Jakacki 2016].

Many studies have focused on kinase inhibitors targeting key signalling pathways dysregulated in HGGs. EGFR presents an appealing target, with alterations in around half of adult GBM cases, and anti-EGFR therapies are routinely administered in treatment of non-small cell lung carcinoma (NSCLC) and colorectal adenocarcinoma. Anti-EGFR monoclonal antibodies (cetuximab, panitumumab) target the extracellular ligand-binding domain of EGFR, regardless of mutational profile. RTK inhibitors (erlotinib, gefitinib, osimertinib, afatinib), which bind to the adenosine triphosphate (ATP) receptor site, target specific *EGFR*

alterations. For example, gefitinib is effective against mutations in exons 19 and 21 [Rahban 2024]. Both therapeutic mechanisms lead to inhibition of downstream signalling, reducing tumour proliferation, differentiation, and metastatic processes. Based upon nine clinical trials, a 2020 Cochrane review determined that EGFR inhibitors were ineffective in adult GBM, offering no benefit to overall or progression-free survival [Lee A 2020]. Similar findings have been reported in pHGGs, including from a PBTC phase II study of gefitinib in brainstem glioma, however further trials into other EGFR inhibitors are ongoing [Pollack 2011b]. Limiting factors for these treatments include clearance from the CNS by efflux via P-glycoprotein (P-gp/ABCB1) and breast cancer resistance protein (ABCG2) [Agarwal 2010]. It has also been reported that the altered extracellular domain of mutant EGFRvIII, present in approximately 50% of EGFR-amplified GBM cases and resulting from deletions in exons 2-7 of *EGFR*, reduces inhibitor binding and therefore sensitivity to treatment [Vivanco 2012].

The characteristic infiltrative nature of HGGs has made targeting angiogenesis via kinase inhibitors a potential avenue for controlling disease progression. Early studies focused on anti-VEGF inhibitor imatinib, which was well-tolerated in refractory pHGGs but showed no effect on disease progression at phase II trials [Pollack 2007, Baruchel 2009]. Anti-PDGFR crenolanib has also been assessed at phase I trials in newly diagnosed DIPG and recurrent pHGGs, with efficacy evaluation ongoing [Tinkle 2021]. Another prominent anti-VEGF agent is monoclonal antibody bevacizumab, which may delay progression in some cases of recurrent adult GBM. The HERBY phase II trial (NCT01390948) found addition of bevacizumab to TMZ and radiotherapy had no effect on survival rates [Grill 2018]. Bevacizumab in combination with DNA topoisomerase I inhibitor irinotecan (NCT0038179), or with histone deacetylase (HDAC) inhibitor vorinostat (NCT01236560) likewise saw no effective response in pHGGs [Gururangan 2010, Lulla 2024]. In light of these findings, studies have sought to overcome efflux mechanisms and target multiple angiogenic pathways

simultaneously. Dasatinib, originally designed to target *BCR-ABL1* fusion gene in leukaemia, has potent anti-PDGFR effects and has been trialled in pHGGs. Although ineffective as a monotherapy, a phase II trial (NCT03352427) combined dasatinib with mTOR inhibitor everolimus. Everolimus was shown to block P-gp activity in preclinical models, allowing prolonged activity of other kinase inhibitors within the CNS. Clinical results indicated improved survival rates against *PDGFR*-altered DIPG and other pHGGs [Miklja 2020]. Small-molecule inhibitor sunitinib targets a broad range of cancer-associated RTKs, including both pro-angiogenic VEGFRs and PDGFRs, and is approved for use in renal cell carcinoma and gastrointestinal stromal tumours. Phase II ACNS1021 trial (NCT01462695) tested sunitinib against ependymoma and pHGGs, however this was also unsuccessful [Wetmore 2016].

The role of PI3K/AKT/mTOR has been extensively characterised across the majority of cancer types, with dozens of PI3K and mTOR inhibitors developed for potential anti-cancer effects, however only a handful demonstrate lasting activity in the CNS. mTOR inhibitors sirolimus/rapamycin and temsirolimus were trialled in various paediatric malignancies, demonstrating acceptable toxicity but mostly limited efficacy in pHGGs [Geoerger 2012, Becher 2017, Qayed 2020]. Among the candidates is everolimus, an immunosuppressant approved for the treatment of subependymal giant cell astrocytoma (SEGA). These tumours arise from tuberous sclerosis complex (TSC), a condition whereby the loss of *TSC2* gene leads to over-activation of mTOR, driving the formation of benign tumours. Everolimus has been trialled across various LGGs and ependymomas in an attempt to slow tumoural growth via mTOR inhibition, as well as reduce P-gp-mediated efflux to enhance other chemotherapies. In addition to the dasatinib trial mentioned above, everolimus has been tested in combination with CDK-4/CDK-6 inhibitor ribociclib at phase I/II trial (NCT2813135) in progressive paediatric malignancies, including 2 patients with pHGGs in

the cohort [Bautista 2021]. In DIPG preclinical models, everolimus was used to increase the brain penetration of multi-RTK inhibitor vandetanib, which also targets *ACVR1* mutations. Following work in mouse models, researchers tested the safety and toxicity profile of the vandetanib and everolimus combination in 4 DIPG patients [Carvalho 2022]. A small study from the Bambino Gesù Children's Hospital in Italy demonstrated slight improvements in survival duration when DIPG patients with elevated mTOR/p-mTOR were treated with everolimus, highlighting the importance of obtaining biopsied tissue to inform personalised treatment approaches [Del Baldo 2022]. A case report of a 14-year-old patient with *TSC2*-mutant pGBM also observed at least 33 months progression-free survival by incorporating everolimus into treatment [Zureick 2019].

Clinical trials for PI3K inhibitors have mostly focused on treatment of adult cancers, as *PI3KCA* mutations are only present in around 1% of paediatric malignancies. DMGs are the exception, with *PIK3CA* alterations detected in 17.5% of cases and offering a potential therapeutic target. Early PI3K inhibitors had unacceptable toxicities, however newer drugs are more well-tolerated and can be considered for use in childhood cancers [Pearson 2024]. PI3K/mTOR inhibitor samotolisib was evaluated in an arm of the NCI-COG Paediatric MATCH trial, comprising 17 participants with PI3K/mTOR mutations and the absence of MAPK pathway alterations. No therapeutic benefit was observed across the cohort, which included 5 pHGG patients, with follow-up trials planning to combine samotolisib with other agents [Laetsch 2024]. Paxalisib is a brain-penetrant pan-PI3K/AKT/mTOR inhibitor tailored to treat adult GBM, and which demonstrated extended overall and progression-free survival in unmethylated *MGMT* cases [Wen 2020]. In DIPG patients, a phase II trial (NCT05009992) is ongoing combining paxalisib with ONC201 (dordaviprone). ONC201 targets dopamine receptor DRD2, which is downregulated in DIPG, and hyperactivates mitochondrial protease ClpP to initiate apoptosis and reverse effects of global loss of H3K27me3. Analysis of 5 trials

of ONC201 monotherapy concluded clinical benefit in H3K27M-altered DMGs, with median overall survival extending to 20 months, and a phase III clinical trial (NCT05580562) is currently enrolling participants [Arrillaga-Romany 2024]. Despite this breakthrough, PI3K/AKT signalling pathways are activated in response to ONC201, leading to metabolic adaptation, reduced sensitivity, and inevitable disease progression. Combination treatment of ONC201 with paxalisib may overcome PI3K/AKT-mediated treatment resistance in DIPG, further extending the rare benefit gained [Jackson E 2023, Duchatel 2024].

1.1.4 – CAR-T Cell Therapy and EphA2

An alternative approach is immunotherapy, in which the immune system is recruited to recognise and target cancer cells. Over the past two decades, immunotherapies have improved the outcomes of refractory and relapsed haematological malignancies, and researchers have sought to translate these results to solid tumours. Immunotherapies have significant potential to enhance responses to HGGs, which are considered 'cold' tumours due to an immunosuppressive microenvironment limiting infiltration of immune cells to the tumour site. Clinical trials have tested several immune checkpoint inhibitors and vaccinations to target HGGs [Federico 2021, Arrieta 2023], but chimeric antigen receptor T (CAR-T) cell therapies are the focus of this thesis and are briefly reviewed here.

In CAR-T cell therapy, T lymphocytes are isolated from the patient and genetically modified via viral or transposon vectors, or through CRISPR-Cas9 genome editing. The transduced T cells express chimeric antigen receptors (CARs) on the cell surface, specifically recognising tumour-associated antigens (TAAs). Following expansion, CAR-T cells are then infused back into the patient at the tumour site or intravenously, with direct cytotoxicity against cancer cells expressing the target antigen, and the release of cytokines to promote a prolonged endogenous response [Feins 2019]. Currently, there are 6 CAR-T cell therapies

approved by the US Food and Drug Administration (FDA) which target either CD19 or B-cell maturation antigen (BCMA) in B-cell lymphomas, leukaemia, and multiple myeloma [Goyco Vera 2024].

CAR-T cell therapies have proven less efficacious against solid tumours, lacking durable treatment responses. Trafficking of CAR-T cells to specific tissue sites remains a challenge. particularly to CNS tumours where T cells must cross the blood-brain barrier [del Baldo 2023]. EGFRvIII and IL13Rα2 CAR-T trials in adult GBM also attributed diminished efficacy to tumoural heterogeneity preventing complete coverage by single-target CARs, leading to clonal expansion of tumour cell populations lacking the target antigen. Analysis of tissue samples reported infiltration of immunosuppressive T_{reg} and myeloid cells, and upregulation of cytokines IL-10, TGF-ß, and PD-L1 to the tumour following EGFRvIII-directed CAR-T therapy. This influx of immune cells also reduced glucose levels accessible to CAR-T cells, further diminishing their cytotoxicity [O'Rourke 2017]. Second and third-generation CAR-T therapies have been designed with additional costimulatory domains to address these concerns, and to target multiple antigens simultaneously [Antonucci 2022].

Differences between the immune components of the tumour microenvironment of paediatric and adult HGGs have been reported, suggesting that pHGGs might benefit from immunotherapies [Lin G 2018, Lieberman 2019, Njonkou 2022, Messiaen 2023]. For example, Lieberman et al. observed that the DIPG microenvironment did not have increased T lymphocyte or macrophage infiltration compared to normal brain tissue, and they did not overexpress PD-L1 or TGF-ß [Lieberman 2019]. Early clinical trial reports showed that repeated infusions of CARs were generally well-tolerated in paediatric patients, though cytokine release syndrome (CRS) has been observed in some cases, in which immune cells release inflammatory cytokines, further activating additional immune cells in a systemic positive feedback loop [Lee DW 2019, Majzner 2022]. Molecular analysis has identified

several TAAs which are abundantly expressed in pHGGs, and are either absent or expressed at low levels in normal healthy brain tissue. Phase I and II clinical trials are currently underway evaluating CARs targeting IL13Rα2 (NCT02208362), GD2 (NCT04196413), HER2 (NCT03500991, NCT02442297), EGFRvIII (NCT02209376), and B7-H3 (NCT04185038) [Brown 2024, Majzner 2022, Ahmed N 2017, Vitanza 2021, O'Rourke 2017, Vitanza 2023].

Among the prospective therapeutic targets is the RTK ephrin type-A receptor 2 (EphA2), which has been implicated in several cancer types, including brain tumours [Binda 2012]. Under normal conditions, EphA2 is involved in the regulation of embryogenesis, epithelial tissue development, and tissue repair. EphA2 canonically interacts with ephrin ligands, particularly ephrin A1, causing receptor dimerization, autophosphorylation of tyrosine residue sites, and subsequent kinase activation. Canonical activation of EphA2 has tumour suppressive effects, with decreased proliferation, cell motility, and induction of apoptosis through inhibition of RAS/MAPK and PI3K/AKT pathways. In cancers, ephrin ligand expression is suppressed, prioritising non-canonical activation, whereby EphA2 is phosphorylated by ligand-independent interactions at serine 897. Non-canonical activation of EphA2 regulates self-renewal, decreased cell-ECM interactions, increased motility, and invasion in glioma stem-like cells [Wilson K 2021]. EphA2 overexpression is observed in pHGGs, including pGBM and DIPG, with an inverse relationship reported between malignant tissue expression levels and patient prognosis [Okada 2008, Arnone 2021]. Studies have demonstrated that EphA2 expression is restricted to tumoural regions, with little to no presence in normal brain tissue, highlighting the antigen as a prospective therapeutic target with minimal toxicities [Coffman 2003, Wykosky 2008].

Anti-EphA2 therapeutic options may promote antigen internalisation and degradation, inhibit ephrin ligand binding and EphA2 activation, or directly deliver cytotoxic effects to

over-expressing target cells. Soluble ephrins, short interfering RNAs (siRNAs), monoclonal antibodies, dendritic cell-based vaccinations, and RTK inhibitors, have all been evaluated in preclinical models of breast, ovarian, lung, and brain cancers [Xiao T 2020]. Several EphA2-directed CAR-T cell therapies have also been developed, demonstrating efficacy across various preclinical models. Phase I trials have been performed for one such CAR construct, testing the safety profile in a small cohort of three adult GBM participants [Lin 2021]. In our department at the Children's Hospital at Westmead (CHW), we have developed second-generation EphA2 CAR-T cells which have received approval to progress to clinical trial for osteosarcoma and Ewing sarcoma [Hsu 2021]. Research is now underway to investigate their applications in other paediatric cancers, and this thesis evaluated the efficacy of EphA2 CAR-T cells against 3D *in vitro* models of pGBM and DIPG.

1.2 - Cognitive Side Effects of Paediatric Brain Cancer Treatment

Numerous signalling pathways are intertwined in driving progression in pHGGs, limiting the initial treatment response and eventually leading to resistance and recurrence. While seeking to implement aggressive strategies against these cancers, researchers and clinicians must also weigh the potential benefits against the risks of off-target effects, particularly in the context of the developing brain. Lasting cognitive impairments can result from any treatment modality, and many of the mechanisms by which this can occur remain poorly understood and difficult to predict. The overlap between neurotoxicity and symptoms arising from disease further complicate neurological assessment. Side effects resulting from paediatric neurosurgery and cranial radiotherapy are well-known and extensively reviewed elsewhere [Lonjaret 2017, Foster 2021, Padovani 2012], however are outside of the scope of this research. Instead, this section will summarise information concerning long-term neurological side effects associated with chemotherapy.

Chemotherapy is acknowledged to have wide-ranging side effects on the CNS, both resulting from treatment of systemic disease and brain tumours specifically. Collectively termed chemotherapy-induced cognitive impairment, or 'chemofog/chemobrain', symptoms have been reported in approximately 75% of patients during treatment, and persisting in 35% of patients post-treatment [Janelsins 2011]. Nausea, disorientation, and fatigue are often observed in the initial hours or days from chemotherapy administration and may be partially alleviated by altering dosage, administration method, or chemotherapeutic agent where possible. As with radiotherapy, neurological morbidities can arise in the subsequent months and years, and may progress in severity. Long-term side effects include difficulties with memory, concentration, multitasking, impaired executive function, personality changes, endocrine dysfunction, and sleep disorders. These effects have a severe impact on patient quality-of-life, making work and socialisation a challenge for cancer survivors. In very rare cases, chemotherapeutic toxicity can lead to encephalopathy, coma, and death [Mounier 2020, Dietrich 2020].

Determining the specific pathophysiological mechanisms of chemotherapy-associated cognitive impairment is challenging due to multimodal treatment approaches. Furthermore, scans of the brain and cognitive assessments are conducted retrospectively, once neurotoxicity has already occurred [Ikonomidou 2018]. Commonly-administered drugs such as ifosfamide, cisplatin, cytarabine, fludarabine, asparagine, and methotrexate are all known to have neurotoxic effects, though incidence varies considerably [Alessi 2022]. Methotrexate (MTX) is arguably the most closely associated with detrimental effects on cognition, inhibiting folate-dependent DNA synthesis of tumour cells. Off-target folate inhibition leads to the accumulation of homocysteine, producing oxygen radicals that cause oxidative damage to endothelial and neuronal tissue [Williams & Cole 2021]. MTX induces apoptosis and causes long-term dysregulation to the proliferation of neural progenitor cells such as

oligodendrocyte precursor cells (OPCs), impacting attention, memory, and executive function [Wigmore 2010, Jarmolowicz 2019, Gibson 2019]. MTX also reportedly increases microglial activation, decreasing brain-derived neurotrophic factor (BDNF) expression, and disrupting axonal myelination [Geraghty 2019].

Ifosfamide is closely associated with neurotoxicity and leukoencephalopathy, occurring in 10-30% of patients receiving the treatment intravenously, and as many as 50% receiving oral administration. Ifosfamide metabolite chloroacetaldehyde crosses the blood-brain barrier, and is proposed to have direct neurotoxic effects, deplete glutathione in the CNS, and impair fatty acid metabolism [Ajithkumar 2007].

Platinum-based agents cause impairments to hearing and balance in as many as 50% of paediatric cancer survivors, in combination with or in the absence of radiotherapy [Knight 2005]. Cisplatin has specifically been observed to induce neuronal mitochondrial dysfunction and neuronal apoptosis, and decrease synaptic integrity in the hippocampus and prefrontal cortex of animals, causing attention and memory deficits. Cisplatin also led to increased reactive oxygen species (ROS) in rat models, whereas the less toxic alternative carboplatin did not have the same effect [Kelley 2014, Andres 2014, Lomeli 2017].

Research into the long-term neurocognitive impact of chemotherapy on children initially focused on acute lymphoblastic leukaemia (ALL) patients. As the most-common paediatric malignancy, ALL offers a large cohort of patients treated mainly by chemotherapy and subsequently exhibiting neurocognitive deficits. In contrast, determining chemotherapeutic neurotoxicity in CNS tumour patients has proven difficult due to neurological impacts from disease and the inclusion of other treatment modalities. Anderson et al. estimated in their review of a decade of literature that between a quarter and a third of ALL patients experience long-term neurocognitive decline, with deficits most often observed

in visual processing, visual-motor functioning, and executive function [Anderson 2009]. The extent of these deficits is dependent on a number of factors relating to the patient and chemotherapeutic protocols. As with radiotherapy, younger children are more susceptible to chemotherapy-associated neurotoxicity, particularly at the age of 5 years and under [Hill 1997]. Interestingly, multiple studies have reported a sex-based difference in response to chemotherapy, with females suffering greater impairment to visual-motor functioning than males [Brown RT 1998, Buizer 2005]. Chemotherapy administration method has also been noted to influence patient outcomes, with intrathecal administration of MTX (injection via spinal canal) associated with higher morbidities than intravenous or oral administration [Buizer 2009]. As previously mentioned, oral administration has potentially worse outcomes than intravenous treatment with ifosfamide [Ajithkumar 2007].

Chemotherapy-induced cognitive impairment is supported by numerous neuroimaging studies using MRI techniques, such as voxel-based morphometry (VBM) and diffusion tension imaging (DTI), to analyse structural changes and differences in fractional anisotropy and diffusivity of the brains of childhood ALL survivors compared to healthy controls [Zhou 2020]. For example, Genschaft et al. reported decreased neocortical and subcortical grey matter and smaller hippocampal volume, as well as associated memory deficits, from 27 survivors who had been treated with chemotherapy alone for ALL before the age of 11 [Genschaft 2013]. Edelmann et al. evaluated ALL survivors who had been treated with either chemotherapy alone, or chemotherapy with cranial radiotherapy, at least 15 years prior to imaging. The authors found lower volumes of grey and white matter, and a lower ratio of white matter to intracranial volume in the frontal and temporal lobes of treatment groups. Processing speed, verbal memory, and academic performance were all lower compared to controls, with deficits unsurprisingly aggravated in survivors who had been treated with both chemotherapy and radiotherapy [Edelmann 2014]. van der Plas and colleagues found a 6%

decrease in white matter volume and 5% decreased grey matter volume in a cohort of 67 ALL survivors on average 8 years post-diagnosis. Mean IQ score was measured at 95 points within this group, compared to 110 points in the control group [van der Plas 2020].

As neuroimaging and cognitive performance assessments are only able to detect abnormalities once significant neurological damage has already occurred, biomarkers detectable by blood or cerebrospinal fluid (CSF) are being investigated with the intention of identifying at-risk patients. It is hoped that in doing so, intervention therapies can be undertaken to mitigate the cognitive impacts [Williams & Cole 2021]. Most prominent are cytokines involved in promoting inflammation and oedema, activation of the immune response, and regulation of neuronal functioning, including IL-1ß, IL-6, IL-8, TNF-α, and c-reactive protein (CRP). One study suggested an increase in serum concentration of IL-1ß, IL-6, and CRP was correlated with significant decreases in executive functioning and processing speed in female ALL survivors, and TNF-α with inattention in males [Cheung 2017]. Previous research from the same authors had linked pro-inflammatory uric acid with cognitive impairment in adolescent ALL survivors [Cheung 2016]. In paediatric brain tumour patients, identifying biomarkers specifically resulting from treatment rather than disease has proven more challenging. In a small long-term study of medulloblastoma patients, GFAP and YKL-40 concentration increases were suggested as potential markers of astrocyte injury and neuroinflammation [Fernström 2024].

Management of treatment-associated cognitive impairment primarily involves non-pharmacological approaches that aim to improve affected functions. Cognitive rehabilitation involves education and skills training to provide patients with strategies for adapting to daily life and work that may become difficult. Cognitive behavioural therapy may also be prescribed for similar effects, and to provide stress reduction and emotional support. ‘Brain training’ tasks such as computer-assisted cognitive training and puzzles may also be

implemented to target and reinforce processing speed, attention, and problem-solving skills. Activities which promote mindfulness, including meditation, exercise, and yoga, have been reported to offset some of the deficits to attention, behavioural regulation, and emotional well-being. Meta-analysis suggests that there is some benefit to these non-pharmacological interventions, however research bias has been criticised and studies have mainly focused on select adult populations only [Treanor 2016, Karschnia 2019, Zeng 2020].

Pharmacological interventions comprise CNS stimulants and drugs which may improve cognition in other neurological conditions. Methylphenidate hydrochloride (MPH) is a dopaminergic and noradrenergic agonist used in the management of attention-deficit/hyperactivity disorder (ADHD), and which targets the fronto-striatal network involved in attention, memory, decision-making, and behavioural regulation. St Jude Children's Research Hospital conducted multiple studies into the efficacy of MPH in paediatric ALL and malignant brain tumour survivors who had been previously treated with chemotherapy and/or cranial radiotherapy. Results showed acute improvements to attention, behaviour, and social skills in participants that received MPH compared with the placebo, and which persisted with long-term use (>12 months), but the effect was found to not be dose-dependent [Thompson 2001, Mulhern 2004, Conklin 2010]. MPH and modafinil, a stimulant used to treat narcolepsy, have been trialled in adult primary brain tumour patients. Daily administration of either drug appeared to improve cognition and fatigue, however as patients were receiving active treatment of chemotherapy and radiotherapy at the same time, these observations may have been due to reduced tumoural burden [Gehring 2012]. Anti-dementia drugs memantine and donepezil have been repurposed for cognitive recovery following brain tumour treatment in adults, with results indicating potential benefits to processing speed, language, executive function, and visuospatial, verbal and figural memory [Karschnia 2019]. A phase II study tested efficacy and safety of donepezil in 11 paediatric brain tumour patients, reporting

improved executive function and memory after 24 weeks [Castellino 2012]. Even so, the benefits of pharmacological intervention for treatment-associated cognitive impairment are disputed and remain in clinical trial.

To summarise, all therapeutic approaches for paediatric cancer carry an inherent risk of side effects, particularly neurotoxicity from treatments targeting CNS tumours. The developing brains of children and adolescents are susceptible to neurotoxicity, but our understanding of the mechanisms and predictions for when it will occur remain limited. These concerns are further compounded by the extended use of certain treatments, such as kinase inhibitors, which may inadvertently disrupt other crucial pathways. For example, BRAF/MEK combination therapy (dabrafenib and trametinib) has demonstrated increased progression-free survival in paediatric LGGs in the clinic [Bouffet 2023]. However, as BRAF is a component of the ERK/MAPK signalling pathway involved in neural development, long-term inhibition may cause cognitive deficits yet to be elucidated [Iroegbu 2021]. Given these uncertainties, there is an urgent requirement for preclinical models which can investigate the neurocognitive impacts of these treatments before they reach the clinic.

1.3 - Preclinical Models of Cancer

Effective therapies with acceptable toxicity profiles are required to address the dismal outcomes of pHGG. As discussed, many treatments have been evaluated in early-stage clinical trials, but fail to demonstrate sufficient improvement over existing options to justify their progression to late-stage trials or eventual regulatory approval. This problem is not strictly limited to brain tumours, with an MIT study estimating a success rate of 3.4% across all oncology drugs over 15 years of clinical trial data, compared to 20.9% for other therapeutic groups [Wong 2019]. Separate analysis of the clinical development of 640 novel therapies in phase II and III trials determined lack of efficacy to be the leading cause of

failure, accounting for 56.7% of unsuccessful cases, increasing to 71.2% and 63.7% in neurological and anti-cancer agents, respectively [Hwang 2016]. The disparity between preclinical and clinical results has led to the increasing acknowledgement that conventional preclinical models are not adequately representative of human biological systems or disease, and therefore cannot reliably predict treatment response. As such, significant changes to *in vitro* cell cultures and *in vivo* animal models are necessary to improve drug development success rates and ensure that treatments are made available to vulnerable patients [Hingorani 2019].

1.3.1 - Conventional Two-Dimensional Culture

Two-dimensional (2D) cell culture has been a valuable research tool since its introduction more than a century ago. Cells are seeded and adhere directly to the cultureware surface (plastic or glass), forming a monolayer of cells which are relatively easy and inexpensive to maintain. Despite significant volumes of research derived from experiments with 2D cultures, these models are considered unrepresentative of the physiological environment *in vivo*. The difference in dimensionality leads to altered cell-cell and cell-substrate interactions and cell morphology, in turn impacting proliferation rates, surface receptor expression and configuration, and gene and protein expression [Kapałczyńska 2018]. Furthermore, unlike the *in vivo* tumour microenvironment, all cells within the monolayer are exposed to equal concentrations of oxygen, nutrients, growth factors, and drugs. Equal exposure across the monolayer to administered drugs provides an unrepresentative response, and unexpected resistance may then arise at a later stage in the development pipeline [Fontoura 2020]. These conditions can also cause selective pressure on particular populations of cultured cells, such as tumour cells requiring hypoxia, decreasing heterogeneity of the culture and reducing research focus to a single clonal population which is not fully characteristic of the primary tumour. Cells which are cultured for extended durations and

undergo serial passage experience gradual genetic drift, changing the cell phenotype from the primary sample. For example, one of the most-frequently used 'immortalised' GBM cell lines, U87-MG, is known to genetically differ from the tumour it was derived from more than 50 years ago [Allen 2016].

Adaptations to the standard 2D culture protocol can address some of these shortcomings. Primary cell lines derived from patient surgical samples are an alternative to continually-cultured cell lines. Short-term culture under defined serum-free medium conditions maintains heterogeneity, and frequent short tandem repeat (STR) profiling monitors genetic drift to ensure cells continue to resemble the primary tissue sample. Primary cell lines are challenging to establish and culture for long periods of time however, and selection of some populations remains unavoidable following sample processing [da Hora 2019].

Prior to cell seeding, cultureware may be coated with a range of commercial basement membrane matrices (Matrigel, Geltrex) or individual component proteins (collagen, laminin, vitronectin, fibronectin). Cells cultured on these surfaces are supported by a scaffold resembling the extracellular matrix (ECM) and demonstrate cell-extracellular matrix interactions similar to those observed *in vivo*. Similarly, cancer cells sense and respond to external mechanical properties of the substrate, such as rigidity, which can be controlled through the use of tuneable hydrogels (polyacrylamide, poly(ethylene glycol)). Glioma cells display differential proliferation, migration and cell signalling when cultured on substrate rigidities corresponding to brain tissue at different stages of disease progression [Grundy 2016].

1.3.2 - Three-Dimensional Tumour Models

Three-dimensional (3D) cell culture is the process by which cells are grown in non-adherent conditions allowing for organisation and interaction across all three dimensions. Consequently, cell-cell interactions, cell-ECM interactions, cellular differentiation, proliferation, and apoptosis observed *in vivo* are more accurately represented by 3D cultures *in vitro* compared with conventional 2D monolayer culture. Oxygen, growth factors, nutrients, and waste are distributed along a concentration gradient, resulting in an outer proliferative layer, followed by an inner quiescent region, and a hypoxic necrotic core [Chaicharoenaudomrung 2019]. This gradient is particularly beneficial for tumour models, with avascularity, diminished blood flow, and hypoxia crucial features of the solid tumour microenvironment and contributing to disease progression [Leek 2016]. Cells within the culture are also exposed to administered drugs across this concentration gradient, rather than homogeneously, as is the case for monolayers. This leads to increased treatment resistance more in line with expected patient response [Fontoura 2020].

3D culture can be broadly categorised based upon the technique employed - matrix-free or matrix-supported. Matrix-free culture methods can be undertaken by forcing spheroid formation in suspension. Adhesion to the cultureware surface may be prevented through the use of hanging drop plates, whereby cells are seeded into droplets of growth medium hanging from the plate lid, or ultra-low attachment plates coated with a hydrophobic hydrogel layer preventing cellular adhesion [Foty 2011, Nath 2016]. These static culture methods are simple to setup in a high-throughput manner, generate reproducible spheroids across plate wells, and do not require expensive equipment. Alternatively, spheroids can be established in bioreactors, which include spinning flasks and orbital shakers, compelling cells to aggregate by centrifugal forces. Increased diffusion of oxygen and nutrients across the cultures in

bioreactors allows for greater growth and limits the formation of hypoxic cores [Ahmed S 2019].

In matrix-supported culture, cells are embedded into a natural, synthetic, or composite scaffold resembling the ECM. In addition to structural support, the encompassing matrix provides cytokines and growth factors to the 3D culture. Matrices are selected for their mechanical properties, including rigidity, pore size, and the presence of cross-linking compounds, to promote physiological cell morphology, proliferation, differentiation, and signalling. In tumour models, the matrix also provides an extracellular environment into which invasive cell populations can migrate through. Matrix compounds such as Matrigel and collagen must be handled at low temperatures and quickly to avoid premature polymerisation, restricting the extended use of automated pipetting systems and reducing culture throughput. Once embedded in the polymerised scaffold, manipulation and physical access to the 3D culture is restricted and requires matrix-dissolving enzymes which can compromise culture integrity [Langhans 2018].

3D *in vitro* culture methods have been established for most solid tumour types, though generation protocols vary significantly across the literature, including definitions and nomenclature for ostensibly similar models. For example, the basic model whereby cells are dissociated from a 2D monolayer environment and cultured as a 3D aggregate has been referred to by multiple names, including tumourospheres, oncospheres, and multicellular tumour spheroids (MCTS). Prefixes denoting the cell type have also been used, such as gliospheres (glioma), sarcospheres (sarcoma), and mammospheres (breast cancer) [Weiswald 2015]. In this thesis, the following models will be referred to – tumour spheroids, patient-derived organoids, cortical organoids, and assembloid co-cultures.

Tumour spheroids are the most primitive of 3D cancer models and can be derived from continually-cultured cell lines, primary patient-derived cell lines, or single-cell suspensions of dissociated tumour tissue samples. Spheroids can aggregate in both matrix-supported or matrix-free culture methods, and are maintained in serum-free stem cell medium. Basic cell-cell interactions and concentration gradients form, with a proliferative outer region and inner hypoxic core. Tumour spheroids are the most-widely used 3D culture model for brain cancer, and are generally used for measuring increased drug resistance compared to monolayers or for modelling tumour invasion into surrounding matrix. Some heterogeneity may be present within spheroids, depending upon the source cell line used.

Patient-derived organoids (PDOs), also known as tumour organoids or tumouroids, are more complex models directly established from processed patient surgical specimens without prior adherent culture. In early generation protocols, resected tumour tissue is mechanically dissociated into smaller fragments while visible regions of normal tissue, necrosis, and haemorrhage are removed. Remaining tissue undergoes enzymatic dissociation using collagenase type I and dispase, alongside erythrocyte lysis buffer to remove contaminating red blood cells. The resulting heterogeneous single-cell suspension is seeded into non-adherent culture conditions, self-organising into PDOs within a couple of weeks. Propagation and passage of these cultures can be performed through enzymatic dissociation and re-seeding of cells. PDOs resemble the primary tumour architecture while maintaining intratumoural heterogeneity and gene expression profiles, however enzymatic dissociation may lead to clonal selection and removal of certain cellular populations. This methodology was used by Sundar et al. to generate 10 adult and 3 paediatric GBM PDOs, as well a PDO from a single DIPG sample. In line with clinical expectations, GBM organoids had limited sensitivity to TMZ and radiotherapy treatment compared to the more simplistic tumour spheroid models [Sundar 2022].

More recent explant-based protocols address potential selection by forgoing enzyme steps, instead directly placing *ex vivo* tissue fragments into serum-free medium in the absence of growth factors such as EGF and FGF. Propagation is performed by bisecting PDOs with dissection scissors or scalpels to further limit selective pressure. Jacob et al. used the explant-based protocol to generate PDOs from 53 adult GBM tumour samples with a 91.4% success rate. An independent neuropathologist confirmed histological similarity to the corresponding parental tumours based upon haematoxylin and eosin (H&E) staining. Further analysis showed expression of glial cell markers GFAP and S100β, glioma stem cell markers NESTIN, BLPB, HOPX, SOX2, and OLIG2, and intact CD31+ vasculature. Inter- and intra-tumoural heterogeneity was confirmed by bulk RNA-seq, with gene expression signatures exhibiting high similarity to parental tumours, including *EGFR*. Notable exceptions were blood and immune-related genes, owing to the removal of blood during sample processing and reported lack of immune cell expansion in PDOs. The research also explored the applications of PDOs, including the establishment of a biobank of samples, *in vitro* screening of trametinib, everolimus, CAR-T cells, and radiotherapy, and *in vivo* patient-derived xenografts (PDX) in mice [Jacob 2020]. Adapting this protocol, PDOs have been established modelling various other brain tumours, including ependymomas, medulloblastomas, and LGGs [Abdullah 2022, Lago 2023].

PDOs offer a promising platform for tumour characterisation and guiding precision medicine, however inherent limitations exist with this model. Establishment success rate is dependent upon external factors, such as restricted biopsy sample size from paediatric patients, variable cell viability, prior clinical treatment, and areas of calcification and necrosis. Furthermore, clinical applicability may be hindered by months of culture required to expand PDO numbers and perform comprehensive drug screening [Driehuis 2020]. To overcome some of these limitations, Dantes et al. proposed an additional application for

PDOs, reminiscent of liquid biopsy techniques. The authors established pancreatic ductal adenocarcinoma PDOs from surgical specimens and fine needle aspirates, then isolated the cell-free DNA (cfDNA) shed into the growth medium as early as 72 hours following culture commencement. Unlike circulating tumour DNA (ctDNA) detected in the blood and CSF by conventional liquid biopsy, ctDNA from the supernatant of PDOs had higher purity and concentration. Digital droplet PCR (ddPCR) analysis showed concordance in *KRAS* mutations and mutant allele frequency between ctDNA, PDOs, and the primary tumour samples. This allowed for information concerning potential therapeutic targets to be more quickly relayed to clinicians without compromising ongoing culture efforts [Dantes 2020]. The protocol has since been applied to the characterisation of pancreatic cancer, gastric cancer, and normal lung, gastric, and cardiac organoids [Hennig 2022, Kim 2023, Silver 2023]. Recently, cfDNA was collected from cerebral organoids and suggested as a potential diagnostic tool for neurodegenerative and neurodevelopmental disorders, however this has not yet been investigated in the context of brain tumour PDOs [Silver 2024].

1.3.3 - Cerebral and Cortical Organoids

The development of representative models of the human brain have long been sought in a bid to better understand neural development and the mechanisms by which dysregulation leads to neurological disorders and disease. Initially, neuronal monolayers were established through the differentiation of human embryonic stem cells (hESCs) and induced pluripotent stem cells (iPS/iPSCs) using dual SMAD inhibitors (Noggin and SB431542) to prevent mesodermal and endodermal formation and induce cells towards an anterior neuroectodermal lineage [Chambers 2009]. This method was further refined by Shi et al. to allow for the generation of a range of cortical projection neurons, which showed similarities to cortical development *in utero*. Different neuronal types were produced with increasing duration in culture, with deep-layer, early-born neurons observed two weeks following induction, and

last-born, layer 2 neurons produced after three months. Likewise, while individual functioning synapses were reported after 45 days, functional cortical networks demonstrating communication across the culture took up to three months to develop [Shi 2012a]. However, these monolayers remained limited by their dimensionality and the inability to account for the influences of the local microenvironment and other cell types.

Early 3D models of the developing human brain were derived from neural stem cells (NSCs) as neurospheres [Reynolds 1992]. Neurospheres are cultured in serum-free growth medium containing EGF and FGF, which allow for maintenance of NSCs and differentiation into neurons, astrocytes and oligodendrocytes. However, neurospheres do not recapitulate human brain structures, and culture conditions cause changes to cell fate [Machon 2005]. Neurosphere models have since been replaced with the development of cerebral organoid models which address these shortcomings.

In the context of normal tissue, the term 'organoid' refers to 3D cultures derived from hESCs, iPSCs, or adult stem cells (ASCs) isolated from primary tissue samples. Through aforementioned matrix-supported or matrix-free methods, stem cells aggregate into an embryoid body, differentiate, and self-organise into multicellular organotypic cultures resembling complex tissue structures [Corrò 2020]. Intestinal organoids were the first such model to be established when Sato and colleagues isolated $Lgr5^{+}$ stem cells from crypts of the mouse small intestine. These stem cells were embedded into Matrigel and cultured in growth medium containing EGF, R-spondin 1 and Noggin growth factors previously described as promoting intestinal epithelial and crypt proliferation. Organoids recapitulated the *in vivo* crypt structure and expression profiles, and were successfully passaged enzymatically twice-weekly [Sato 2009]. Alterations to this methodology have subsequently led to the establishment of organoids modelling a range of tissues, including breast, liver, lung, kidney, and pancreas. In the process, organoids have offered insight into key

developmental processes and provided researchers with a powerful platform for testing novel therapeutic agents.

The first human cerebral organoid model was reported by Lancaster et al. embedding neuroectoderm derived from embryoid bodies into Matrigel droplets, then culturing in a spinning bioreactor. Consistent with normal human brain development, neuroepithelium formed early in culture, followed by heterogeneous outer areas resembling discrete brain regions, including cerebral cortex, choroid plexus, immature retina, and meninges. Characterisation of organoids revealed localised expression of forebrain markers PAX6 and FOXG1, midbrain marker Otx1/2, and hindbrain markers Gbx2, Krox20, and PAX2. Dorsal cortical regions demonstrated clear progenitor organisation, including formation of ventricular zone (VZ), and a subventricular zone (SVZ) separated by an inner fibre layer into inner and outer subventricular zones (ISVZ/OSVZ). These sub-ventricular structures contained intermediate progenitors and outer radial glia (oRG) stem cell populations not present in mouse models. Cerebral organoids reached maximal size in two months, limited by the diffusion of nutrients to the core, but could be maintained in culture for at least ten months [Lancaster 2013]. Further studies of cerebral organoids, also termed whole-brain organoids, have observed the presence of various glial populations, excitatory and inhibitory neurons, and photosensitive retinal cells [Quadrato 2017].

The unguided differentiation protocol is restricted by significant inter-organoid variability and intra-organoid heterogeneity, presenting obstacles for targeted research. Thus, guided methodologies have been implemented with defined growth factors and small molecules inducing differentiation toward desired lineages, giving rise to region-specific organoids [Qian 2019]. Initially, guided differentiation protocols were developed to establish dorsal- and ventral-specific cortical organoids which exhibited neuronal layering (subplate, cortical plate, and Cajal-Retzius zones), approximating foetal brain in the early-second

trimester. As with the cortical regions of whole-brain organoids, these cortical organoids displayed sub-ventricular organisation and contained oRG populations not observed in foetal mouse brain models [Kadoshima 2013]. Region-specific organoids have been observed to contain an increase in cell type diversity with increasing culture times, as well as an enrichment of genes associated with neuronal and glial cell maturation previously noted in foetal brain development [Camp 2015]. In addition to cortical organoids, further models have been established corresponding to the hippocampus, choroid plexus, cerebellum, pituitary gland, and hypothalamus [Sakaguchi 2015, Muguruma 2015, Ozone 2016, Huang WK 2021].

At present, cerebral and cortical organoids lack the maturity or complexity to model late-stage foetal or postnatal brain architecture. This is attributed to the absence or under-representation of crucial cell types such as OPCs, microglia, and endothelial cells in many organoid models [Di Lullo 2017]. For example, dorsal cortical organoids have diminished numbers of inhibitory interneurons (or association neurons) compared to *in vivo* neocortex, as they mostly originate from the ganglionic eminences of the ventral telencephalon during corticogenesis [Delgado 2022]. This was overcome by the fusion of dorsal and ventral cortical organoid models to form a dorsal-ventral axis, across which interneurons were then observed to migrate [Bagley 2017]. Formation of vasculature is also considered particularly important, as lack of vasculature restricts organoid nutrient access and growth, and prevents modelling of the blood-brain barrier. Vascular-like networks in cerebral organoids have been produced by embedding organoids with iPSC-derived endothelial cells, and through co-culture of organoids with human ETS variant 2 (ETV2)-expressing hESCs [Pham 2018, Cakir 2019]. Recently, a vascularised model was created by fusing a cerebral organoid and a hESC-derived endothelial organoid, resulting in the presence of vascular progenitors, microglia, and endothelial cells, and the formation of vessels capable of sustaining liquid

flow [Sun 2022]. Modifications continue to be incorporated into cerebral and cortical organoid models to improve their representation of the human brain tissue.

1.3.4 – Pathophysiological Modelling with Cerebral Organoids

Alongside their role in modelling normal brain development, organoids have been applied to understand the pathogenesis of psychiatric, developmental, and neurodegenerative disorders. iPSCs derived from the somatic cells of patients retain the disease-related phenotype, and development of neural architecture is altered accordingly. Prior studies used stem cells to establish 2D cultures modelling the condition of interest. For example, Shi et al. derived iPSCs from patients with Down Syndrome – a population disproportionately affected by Alzheimer's Disease (AD), possibly due to encoding of amyloid precursor protein on chromosome 21. Cortical neurons differentiated from these iPSCs formed intracellular and extracellular AD-associated amyloid aggregates, and hyperphosphorylated tau protein in cell bodies and dendrites [Shi 2012b). The development of 3D organoid systems offers researchers a far more complex and representative model however, and was initially demonstrated using intestinal organoids for the study of cystic fibrosis [Dekkers 2013]. Cerebral organoids can similarly mimic neurological disorders through the use of iPSCs, genetic manipulation methods, or the exposure of organoids to environmental factors during culture.

Microcephaly was the first condition modelled by cerebral organoids, and is characterised *in vivo* by impaired cortex formation during foetal or early postnatal development, resulting in decreased brain and head size and accompanying cognitive disability. Lancaster et al. generated whole-brain organoids from iPSCs of a microcephaly patient with a *CDK5RAP2* mutation. Organoids maintained expression of this mutation and were smaller than healthy controls, with decreased regions of neuroepithelium, fewer radial

glial cells, and the presence of prematurely differentiated neurons at the expense of progenitor cells, leading to an overall decrease in neuron number [Lancaster 2013]. Similar observations were noted in region-specific organoids infected with Zika virus, known to cause abnormalities, including microcephaly, upon exposure during pregnancy [Qian 2016]. Likewise, organoids modelling Aicardi-Goutières syndrome, which is associated with microcephaly, also demonstrated decreased size over time as a result of increased neuronal cell death [Thomas 2017]. Numerous other neurodevelopmental and neurodegenerative conditions have been investigated using organoids, including schizophrenia, Rett syndrome, Prader-Willi syndrome, AD, and Parkinson's disease [Susaimanickam 2022].

Cerebral organoids can also facilitate the identification of potential targets for therapeutic intervention. Autism spectrum disorder (ASD) is a group of neurodevelopmental conditions with a broad range of presentations, including difficulties with social interaction and communication, repetition of behaviours, and fixation on objects and interests. Neuroimaging and gene expression studies of brain tissue post-mortem have linked *de novo* and inherited genetic mutations to approximately 15% of cases ("secondary" autism), while the factors responsible for the remainder are unknown (idiopathic autism) [Casanova 2020]. iPSC-derived cortical organoids were established from four patients and their families with severe idiopathic ASD, and the mutual phenotype of macrocephaly. No genetic mutations were detected, however transcriptome analysis noted upregulation of genes associated with proliferation, neuronal differentiation, and synaptic formation. Cell cycle was observed to be accelerated in organoids, and an overexpression of *FOXG1* led to an increase in GABAergic inhibitory neurons, presenting *FOXG1* as a potential therapeutic target [Mariani 2015]. Subsequent mouse models showed that dysregulation of *FOXG1* in the second postnatal week impacted excitatory and inhibitory neuronal circuit function and led to presentation of altered

social behaviours [Miyoshi 2021]. Interestingly, LOF for *FOXG1* has also been linked to diminished brain size in Rett syndrome patients [Kortüm 2011].

In cancer research, implementation of cerebral organoids in co-culture models allows for study of the interaction of tumour cells in a microenvironment resembling *in vivo* brain tissue. Linkous et al. published a cerebral organoid glioma (GLICO) model in which hESC-derived cerebral organoids were grown for approximately three weeks, then co-cultured with patient-derived GBM cell lines. Tumour cells infiltrated through the organoid in a cell line-dependent manner, with the formation of tumour microtubes promoting tumoural growth and cell-cell interactions. The co-culture could be maintained for at least two weeks, during which the abundance of tumour cells led to necrosis within the organoid, further resembling histopathological features of GBM *in vivo*. Tumour cells within the GLICO model displayed decreased sensitivity to TMZ, bis-chloroethylnitrosourea (BCNU), and radiotherapy compared to 2D monolayers [Linkous 2019]. Similar findings were reported from comparable co-culture models in which researchers xenografted human GBM cells to mouse cerebral organoids, and a separate study measuring metastatic NSCLC in human cerebral organoids [da Silva 2018, Choe 2020].

Our department has developed two separate protocols for co-culturing dorsal cortical organoids with patient-derived DIPG and GBM cell lines. The first co-culture model, known as ‘mosaic’, involved enzymatic dissociation of dorsal cortical organoids and re-seeding them in ultra-low attachment plates with tumour cells. The organoid reformed with multiple tumour sites arising throughout, mimicking the diffuse characteristics of pHGGs, and was enriched for tumour cell-neuronal cell interactions. The second co-culture model, termed ‘assembloid’, comprised an intact tumour spheroid engrafted to an organoid by culturing them intact within the same plate well. In assembloids, tumour cell-tumour cell interactions were enriched as they infiltrated through the organoid from the single primary site. Proteomic

analysis of the co-cultures suggested decreases to adhesion and interactions with the extracellular environment, supported by data showing decreased integrin expression at the periphery of DIPG cells within the organoid. This corresponds to tumour cells changing to a more representative invasive phenotype upon reaching the brain organoid. [Prior 2024]. Research presented in this thesis investigated the utility of co-culture models for therapeutic screening of CAR-T cells, comparing treatment responses in GBM and DIPG assembloids against conventional *in vitro* models.

1.3.5 – Evaluating Neurotoxicity with Cerebral Organoids

Healthy brain development may be influenced by numerous extrinsic factors, both environmental and therapeutic, however the precise cellular responses are challenging to predict. Animal models have historically been used to screen for neurotoxicity, though low throughput and species differences make this approach time-consuming and results may not translate well to humans [Chen H 2019]. As described, cerebral organoids allow for the analysis of human-specific cellular development, recapitulating early foetal development. Many studies have used organoids to evaluate neurotoxic effects of recreational drugs and environmental compounds that a foetus could be actively or passively exposed to during early pregnancy [Fan 2022]. However, these *in vitro* systems do not account for maternal protective mechanisms, such as inactivation of toxins by the liver, the placental barrier, and the foetal blood-brain barrier [Sarieva 2021].

Alcohol consumption during pregnancy is strongly associated with neurological deficits, collectively known as foetal alcohol spectrum disorders (FASD). Multiple studies have subjected cerebral organoids to physiologically-relevant concentrations of ethanol, noting impaired development and function. Arzua et al. utilised a two-month-old cerebral organoid model, testing acute exposure of ethanol at different concentrations. They reported

that organoids experienced metabolic stress and mitochondrial dysfunction, and that neurons were more susceptible to ethanol-induced apoptosis than astrocytes. Bioinformatic analyses found dysregulation to genes related to neurodevelopment, nervous system physiology, and neurodegeneration, and that affected pathways were linked to altered social behaviours and psychiatric disorders [Arzua 2020]. Other studies have looked at the effects of long-term exposure to ethanol in neural development. Zhu et al. focused on early stages of brain development, treating cerebral organoids from days 10 to 30. Ethanol-treated organoids had an imbalance of excitatory and inhibitory neurons, and enrichment of *GSX2*, *RPSO2*, and the Hippo signalling pathway. These pathways are associated with neurogenesis, brain size, and craniofacial morphology, corresponding to cognitive dysfunction, microcephaly, and distinctive facial structures in children with FASD [Zhu Y 2017]. Adams and colleagues used a lower concentration of ethanol than previous studies, but extended exposure duration in cortical organoids to two months. Ethanol altered post-translational histone modifications and chromatin accessibility, disrupting development of cytoskeleton, glial cells, and glutamatergic synapses [Adams 2023]. Lastly, a study in forebrain organoids observed ethanol exposure dysregulating multiple processes in oRGs. This included increased apoptosis, decreased migration and proliferation, altered morphology, and premature transformation of oRGs to astrocytes [Lü 2023].

Nicotine is another drug of clinical importance due to its widespread community consumption via smoking and vaping, and foetal exposure during pregnancy has been linked with cognitive deficits and ADHD [Pagani 2014]. Wang et al. cultured whole-brain organoids in a PDMS-based microfluidic system, continuously exposing early-stage organoids to levels of nicotine comparable to plasma concentrations in heavy smokers. After two weeks of exposure, researchers reported increased expression of immature neuronal marker TUJ1, indicating premature neuronal differentiation, as well as disrupted cortical development

across the forebrain, midbrain, and hindbrain structures of the organoids [Wang Y 2018]. Both nicotine and ethanol were included in a broad study of narcotics in dorsal cortical organoids, demonstrating enrichment in signalling pathways involved in cortical neurogenesis and axonal guidance. Significant alterations were also observed in expression of L-phenylalanine and regulators of GTP signalling, corresponding to impaired neurodevelopment [Notaras 2021].

Illicit drugs are a loosely-categorised group of compounds prohibited by law from recreational use due to their potential for adverse long-term effects. Extensive research has focused on their neurological impacts on adult and adolescent brains, however multi-drug use frequently complicates standard prenatal exposure studies. Organoids therefore present an opportunity for controlled screening. Lee et al. administered cocaine in six-week-old cortical organoids, when rapid neuroepithelial growth was occurring. Cocaine exposure generated ROS and led to inhibition of progenitor cell proliferation, premature neuronal differentiation, and disrupted development. The authors identified cytochrome P450 3A5 (CYP3A5) as responsible for metabolism of cocaine in humans and driving cocaine-associated deficits, with CYP3A5 knockdown reversing these alterations. Different CYP450 enzymes metabolised cocaine in rodents, highlighting the importance of species specificity for *in vitro* models [Lee CT 2017]. Reumann et al. developed an intricate model of the dopaminergic system, creating an assembloid comprising ventral midbrain, striatal, and cortical organoids (MISCO). MISCOs were treated with cocaine from day 40 to 130 in culture, with increased density of dopaminergic varicosities measured in striatal and cortical regions, as previously reported *in vivo*. Chronic cocaine exposure altered neuronal activity across the entire assembloid, and RNA-seq data showed a downregulation in genes associated with neuronal circuit formation, including dendritic and axonal development, and synaptic organisation. Importantly, the pathological effects from cocaine administration continued after drug

withdrawal from culture, indicating persistent long-term impacts on neuronal function [Reumann 2023]. Methamphetamine (METH) is another controlled substance known to possess neurodegenerative qualities, which were explored *in vitro* with whole-brain organoids. A single study treated organoids with METH for a week, noting transcriptional changes in astrocytes and neural progenitor cells, resulting in a neuroinflammatory response. Transcription factors FOS and JUN have previously been reported to regulate apoptosis in METH-treated animal models, and were singled-out as mediating METH-associated neurotoxicity in organoids [Dang 2021].

Besides recreational drug use, neurotoxicity can occur through incidental exposure to toxins in the environment. The feasibility of using cerebral organoids for evaluating chemical neurotoxicity was explored by Sandström and colleagues, who used methylmercury chloride, trimethyltin chloride, and paraquat dichloride – compounds with known neurotoxic effects. Neurotoxicity was confirmed by increases in extracellular lactate dehydrogenase (LDH), and heme oxygenase 1 (HMOX1) and GFAP mRNA as measures of cellular stress compared to ibuprofen-treated negative controls [Sandström 2017]. Another study looked at the risk of common food contaminant acrylamide, which was previously shown to transfer from mother to foetus during pregnancy and had exhibited neurotoxicity in animal models. Acrylamide-treated whole-brain organoids demonstrated increased apoptosis and decreased differentiation of neurons, with decreased expression of neuronal markers TUJ1, SOX9, SOX2, and GFAP. Furthermore, the authors reported an accumulation of hyperphosphorylated tau protein, which is closely linked to neurodegenerative conditions, cognitive impairment, and memory loss [Bu 2020]. Most recently, research by Renner et al. screened 84 compounds against midbrain organoids, including pesticides, therapeutic drugs, neurotoxicants, and flame retardants. The screen included methylmercury and acrylamide, as well as compounds that had evaluated in other *in vitro* brain models, such as the pesticide rotenone, which is strongly linked to

Parkinson's disease and had been tested on neural progenitor-derived neurospheres [Pamies 2018, Kobolak 2020]. The screen correctly identified the known neurotoxic compounds based on decreased organoid viability and decreased expression of TH^+ dopaminergic neurons and $MAP2^+$ neurons [Renner 2021].

Of particular relevance to this thesis, cerebral organoids have been used to further study the neurotoxic effects of anti-cancer agents. In their comprehensive compound screen, Renner et al. included the chemotherapeutic agents hydroxyurea and fluorouracil (5-FU). While organoid viability was only slightly reduced by both drugs, TH^+ dopaminergic neurons were significantly reduced by 5-FU treatment in one of the midbrain organoid lines, in accordance with previous animal studies [Renner 2021, Nishimura 2011]. Vincristine is a potent chemotherapeutic agent which targets the microtubules of tumour cells to induce apoptosis. Vincristine is used in the treatment of brain tumours, however significant side effects have been reported in patients, including impaired neurodevelopment [Cavaletti 2010]. This neurotoxicity was examined in brain organoids by Liu and colleagues, who demonstrated that vincristine inhibited microtubule-associated tubulin and fibronectin, subsequently inhibiting matrix metalloproteinase 10 (MMP10) and disrupting ECM signalling [Liu F 2019]. Scholz et al. tested paclitaxel on two-month-old cerebral organoids, performing a single 14-hour administration at different concentrations, before washing out the drug and measuring apoptosis and proliferation. Paclitaxel-induced apoptosis and reduced proliferation were observed in a dose-dependent manner, indicated by expression of neuronal calcium sensor 1 (NCS-1) and cleaved caspase 3. Neuronal and astrocyte progenitor cells and mature neurons were susceptible to apoptosis, while mature astrocytes were unaffected by paclitaxel [Scholz 2022]. Lastly, the EGFR inhibitor gefitinib was tested on whole-brain organoids and co-cultures of organoids with lung cancer cells. No significant difference in expression of apoptotic markers PARP-1, cleaved caspase 3, or the Bax/Bcl-2 ratio was

reported in treated organoids or organoid regions of co-cultures, suggesting little to no neurotoxicity at 10μM concentration [Choe 2020].

In these reviewed studies, measurement of impaired neurodevelopment and neurotoxicity is mostly based upon changes to baseline gene and protein expression, immunoassays for proliferative and apoptotic markers, or lytic ATP-based cell viability assays. How these cellular alterations translate functionally is increasingly being investigated through electrophysiological analyses. Cerebral organoids develop functional neurons, astrocytes, and synapses exhibiting spontaneous electrical activity [Paşca A 2015]. Complex synchronised neural networks form upon increased culture duration and following defined maturation protocols, including supplementation with small molecules and growth factors to induce a physiological phenotype resembling cortex *in utero* [Trujillo 2019].

Conventional techniques for evaluating *in vitro* electrical activity include patch clamping and calcium imaging. Patch clamping involves passing an electrical current through isolated neurons, measuring the potential of ion channels in the cellular membrane. Although this provides high temporal resolution of individual cells, assessment of cell-cell interactions or neural networks is not possible, greatly restricting their applications in organoids. Calcium imaging uses fluorescent indicators that bind to Ca^{2+} ions and allows for real-time measurement of neural activity based upon corresponding signal intensity. Temporal resolution is lower than patch clamping, but image acquisition can occur across small groups of neurons simultaneously, allowing for analysis of synaptic connections and small-scale networks. Calcium imaging is mostly limited to a single z-plane due to the challenges of orientating live samples, preventing high-throughput use across entire 3D structures [Passaro 2021].

In order to combine the temporal resolution of patch clamping with the network capacity of calcium imaging, researchers have turned to commercial and proprietary micro-electrode array (MEA) systems. In this methodology, electrodes are constructed from electrically-conductive materials such as gold, platinum, or poly(3,4-ethylenedioxythiophene) (PEDOT)-based polymers and arranged into the desired spatial configuration. Cell cultures are positioned on the electrodes and action potentials detected across the interface. Various parameters may be calculated from the frequency of events in order to determine the functionality of individual neurons and synapses, and across the entire neural network. Spatial resolution varies between systems and is dependent upon the number of electrodes within the array in direct contact with the cell culture. In planar MEA systems, grids of electrodes are arranged across a single horizontal plane upon which cells or organoids can be embedded and cultured. Spike, needle, or cantilever MEA accesses neuronal activity within the inner regions of organoids by piercing them on an electrode spike. Shell MEA systems manufacture bespoke arrays from flexible materials that can be wrapped or folded around the organoid, ensuring acquisition across all three dimensions [Choi 2021].

Literature concerning MEA applications with cerebral organoids has focused on proof-of-concept studies for novel organoid and MEA methodologies, evaluation of neural activity in iPSC-derived disease models, and comparisons of electrophysiological responses to acute or chronic drug exposure. Drug studies have mainly highlighted agonistic and antagonistic effects on ionotropic receptors. Inhibitory neurotransmitter γ-aminobutyric acid (GABA) binds to the GABA type A ($GABA_A$) receptor, allowing the influx of Cl^- ions into the neuron, hyperpolarising the membrane, and decreasing its capacity to generate action potentials. The benzodiazepine diazepam (Valium) enhances GABA affinity to the receptor, facilitating binding and impairing neuronal firing [Campo-Soria 2006]. In whole-brain organoid slices, Sharf et al. observed that the total number of firing events was unaffected by

diazepam, however treatment induced dose-dependent decreases to the regularity and complexity of neuronal firing [Sharf et al 2022]. In contrast, excitatory neurotransmitter glutamate binds to N-methyl-D-aspartate (NMDA) receptors, causing conformational changes to the ion channel to facilitate neurotransmission. Acute glutamate treatment, along with administration of co-agonist glycine, demonstrated amplified neuronal activity in two-month-old organoids [Huang Q 2022]. As expected, non-competitive antagonism of NMDA receptors by methadone has the opposite effect, inhibiting neuronal activity, as well as restricting cortical organoid growth [Yao 2020]. A follow-up study compared methadone with buprenorphine; another medication for management of opioid use disorder but with fewer side effects in patients. When organoids were treated with buprenorphine, inhibition of neural activity was lessened compared with methadone, and there was no significant growth arrest. As buprenorphine was shown to act via κ-opioid receptor binding, but not through NMDA antagonism, these results were used to hypothesise the pathophysiological mechanisms of methadone [Yao 2023].

Electrophysiological assessment by MEA shows cerebral and cortical organoids establish functional neural networks resembling *in vivo* brain regions and are capable of responding to pharmacological stimulation. The feasibility of this approach in cancer research has been tentatively tested with chemotherapy-associated neurotoxicity of vincristine in several *in vitro* models, in which altered axonal parameters corresponded to clinical reports [Suzuki 2023]. It remains a largely unexplored area of research however, and could provide valuable information to inform the drug development process. Prediction and understanding of neurotoxicity mechanisms at an early preclinical stage could prevent patients being exposed to long-term side effects from new and emerging treatments, or inform clinicians of potential management options to ameliorate these deficiencies. In this thesis, we investigated potential neurotoxicity resulting from chronic exposure to kinase inhibitors in cortical

organoids, measuring alterations to electrophysiology using a commercial planar MEA system.

1.4 - Project Overview and Aims

pHGGs are highly heterogeneous, infiltrative brain tumours with molecular and mutational profiles distinguishing them from adult disease. Patient outcomes are uniformly dismal, with no curative treatments and few palliative management options available. Despite promising preclinical studies, novel treatments have been unable to translate results to clinical trial, with neurotoxicity and lack of efficacy the main causes of failure. This discrepancy is attributed to conventional 2D *in vitro* preclinical models not sufficiently recapitulating the healthy brain or tumour microenvironment, and the significant species differences present in animal models. In recent years, 3D *in vitro* models have been posited which are more representative of normal human tissue and disease. In this thesis, stem cell-derived brain organoids, PDOs, tumour spheroids, and assembloid co-culture models were evaluated in the context of pHGG and potential treatment options.

In Chapter 3, an existing protocol for generating dorsal cortical organoids was advanced to produce a more mature phenotype. A planar MEA system evaluated electrophysiology of these organoids and alterations induced by chronic exposure to kinase inhibitors. Chapter 4 assessed the efficacy of a novel EphA2-directed CAR-T cell therapy against patient-derived pGBM and DIPG cell lines. Increasingly complex models incorporating dimensionality were utilised, including tumour spheroids and assembloid co-cultures. Lastly, Chapter 5 consisted of the establishment and characterisation of PDOs from patient tumour samples. Mutational profiles of PDOs and ctDNA were compared against clinical reports to confirm their feasibility in supplying additional information concerning the

primary tumour. Overall, this thesis aimed to demonstrate the importance of 3D *in vitro* cultures in drug development and precision medicine.

Materials & Methods 2

2.1 - Materials

Table 2.1 - Chemicals, Reagents, Commercial Kits, and Assays

Item	Catalogue Number	Manufacturer
Accutase® solution	#A6964	Sigma-Aldrich (subsidiary of Merck Group, Darmstadt, Germany)
Acrylamide (N, N'-Methylenebis), 99%	#146072	Sigma-Aldrich (subsidiary of Merck Group, Darmstadt, Germany)
Agarose I	#0710	Amresco (Ohio, USA)
AllPrep® DNA/RNA Mini Kit	#80204	QIAGEN N.V. (Hilden, Germany)
Amphotericin B solution	#A2942	Sigma-Aldrich (subsidiary of Merck Group, Darmstadt, Germany)
Antibiotic-Antimycotic, 100X	#15240062	Life Technologies (subsidiary of Thermo Fisher Scientific, Massachusetts, USA)
B27™ without vitamin A supplement, 50X	#12587	Life Technologies (subsidiary of Thermo Fisher Scientific, Massachusetts, USA)
Beta-mercaptoethanol	#M6250	Sigma-Aldrich (subsidiary of Merck Group, Darmstadt, Germany)

Bicuculline, ≥97.0%	#14340	Sigma-Aldrich (subsidiary of Merck Group, Darmstadt, Germany)
BIT 9500 serum substitute	#09500	StemCell Technologies (Vancouver, Canada)
Bovine serum albumin (BSA), Fraction V, IgG-free	#30063-572	Life Technologies (subsidiary of Thermo Fisher Scientific, Massachusetts, USA)
Brain-derived neurotrophic factor (BDNF), human	#78005	StemCell Technologies (Vancouver, Canada)
BrainPhys™ hPSC Neuron Kit	#05795	StemCell Technologies (Vancouver, Canada)
Bright-Glo™ luciferase assay system	#E2620	Promega (Wisconsin, USA)
Bromophenol blue	#97061	VWR International (subsidiary of Avantor, Pennsylvania, USA)
CellAdhere™ dilution buffer	#07183	StemCell Technologies (Vancouver, Canada)
CellTiter-Glo® 3D cell viability assay	#G9683	Promega (Wisconsin, USA)
CellTracker™ fluorescence probes DeepRed	#C34565	Invitrogen (subsidiary of Thermo Fisher Scientific, Massachusetts, USA)
Cholera toxin	#C8052	Sigma-Aldrich (subsidiary of Merck Group, Darmstadt, Germany)
CNQX disodium salt hydrate ≥98%	#C239	Sigma-Aldrich (subsidiary of Merck Group, Darmstadt, Germany)
Collagen I from rat tail	#354236	Corning (New York, USA)
cOmplete™, mini, EDTA-free protease inhibitor cocktail	#11836170001	Roche (Basel, Switzerland)
Coomassie Brilliant Blue R-250	#BIOCB0037	Astral Scientific (New South Wales, Australia)
CTS™ immune cell serum replacement	#A2596102	Life Technologies (subsidiary of Thermo Fisher Scientific, Massachusetts, USA)
CTS™ Optmizer™ T cell expansion serum-free media	#A1048501	Life Technologies (subsidiary of Thermo Fisher Scientific, Massachusetts, USA)

D(-)-2-Amino-5-phosphonopentanoic acid	#A8054	Sigma-Aldrich (subsidiary of Merck Group, Darmstadt, Germany)
DAPI (4′,6-diamidino-2-phenylindole)	#D9564	Sigma-Aldrich (subsidiary of Merck Group, Darmstadt, Germany)
ddPCR Supermix for Probes (No dUTP)	#186-3023	Bio-Rad Laboratories (California, USA)
Dibutyryl-cAMP	#100-0244	StemCell Technologies (Vancouver, Canada)
Dimethyl sulfoxide (DMSO)	#D2650	Sigma-Aldrich (subsidiary of Merck Group, Darmstadt, Germany)
DNase I	#10104159001	Sigma-Aldrich (subsidiary of Merck Group, Darmstadt, Germany)
dNTP Mix (10mM)	#72004	Sigma-Aldrich (subsidiary of Merck Group, Darmstadt, Germany)
Donkey serum	#D9663	Sigma-Aldrich (subsidiary of Merck Group, Darmstadt, Germany)
Dorsomorphin	#72102	StemCell Technologies (Vancouver, Canada)
Dulbecco's modified eagle medium (DMEM) high glucose, sodium pyruvate	#11995065	Life Technologies (subsidiary of Thermo Fisher Scientific, Massachusetts, USA)
Dulbecco's modified eagle medium/nutrient mixture F-12 (DMEM/F-12)	#11320033	Life Technologies (subsidiary of Thermo Fisher Scientific, Massachusetts, USA)
Dulbecco's phosphate buffered solution (DPBS) without calcium and magnesium	#14190250	Life Technologies (subsidiary of Thermo Fisher Scientific, Massachusetts, USA)
EasySep™ human T cell isolation kit	#17951	StemCell Technologies (Vancouver, Canada)
Epidermal growth factor (EGF), human, recombinant	#100-26 #PHG0311	Shenandoah BioTechnologies (Pennsylvania, USA) Life Technologies (subsidiary of Thermo Fisher Scientific, Massachusetts, USA)

Ethidium bromide	#15585-011	Invitrogen (subsidiary of Thermo Fisher Scientific, Massachusetts, USA)
Ethyl alcohol, pure, 200 proof, ≥99.5%	#459836	Sigma-Aldrich (subsidiary of Merck Group, Darmstadt, Germany)
Ethylenediaminetetraacetic acid (EDTA) 0.5 M pH 8.0 RNase-free	#AM9260G	Invitrogen (subsidiary of Thermo Fisher Scientific, Massachusetts, USA)
FavorPrep™ PCR Clean-Up Mini Kit	#FAGCK 001	FavorGen (Pingtung, Taiwan)
Fetal bovine serum (FBS), qualified	#26140079	Life Technologies (subsidiary of Thermo Fisher Scientific, Massachusetts, USA)
Fibroblast growth factor basic 154aa (FGF2), human, recombinant	#100-146 #PHG0026	Shenandoah BioTechnologies (Pennsylvania, USA) Life Technologies (subsidiary of Thermo Fisher Scientific, Massachusetts, USA)
Fluoromount™ aqueous mounting medium	#F4680	Sigma-Aldrich (subsidiary of Merck Group, Darmstadt, Germany)
Gefitinib (ZD1839)	#4765S	Cell Signaling Technology (Massachusetts, USA)
GelRed® nucleic acid stain	#SCT123	Millipore (subsidiary of Merck Group, Darmstadt, Germany)
Gentamicin	#15750060	Life Technologies (subsidiary of Thermo Fisher Scientific, Massachusetts, USA)
Glacial acetic acid	#10063	Millipore (subsidiary of Merck Group, Darmstadt, Germany)
Glucose solution	#A2490-01	Life Technologies (subsidiary of Thermo Fisher Scientific, Massachusetts, USA)
GlutaMax™ supplement	#35050061	Life Technologies (subsidiary of Thermo Fisher Scientific, Massachusetts, USA)
Glycine	#0167	VWR International (subsidiary of Avantor, Pennsylvania, USA)

HaeIII restriction enzyme	#R0108S	New England BioLabs (Massachusetts, USA)
Hanks' Balanced Salt Solution (HBSS), no calcium, no magnesium, no phenol red	#14175095	Life Technologies (subsidiary of Thermo Fisher Scientific, Massachusetts, USA)
Heparin 2mg/ml solution	#07980	StemCell Technologies (Vancouver, Canada)
HEPES (4-(2-hydroxyethyl)-1-piperazineethanesulfonic acid) 1M solution	#15630080	Life Technologies (subsidiary of Thermo Fisher Scientific, Massachusetts, USA)
Horse serum	#16050-122	Invitrogen (subsidiary of Thermo Fisher Scientific, Massachusetts, USA)
Ibuprofen	#I7905	Sigma-Aldrich (subsidiary of Merck Group, Darmstadt, Germany)
IL-15, human, recombinant	#130-095-762	Miltenyi Biotec (Bergisch Gladbach, Germany)
IL-7, human, recombinant	#130-0395-362	Miltenyi Biotec (Bergisch Gladbach, Germany)
Immobilon®-P PVDF Membrane, 0.45mm	#IPVH00010	Millipore (subsidiary of Merck Group, Darmstadt, Germany)
Insulin, human recombinant, zinc solution	#12585014	Life Technologies (subsidiary of Thermo Fisher Scientific, Massachusetts, USA)
Insulin-transferrin-selenium sodium pyruvate (ITS) without vitamin A 100X	#5130004	Life Technologies (subsidiary of Thermo Fisher Scientific, Massachusetts, USA)
JumpStart™ Taq DNA polymerase	#D9307	Sigma-Aldrich (subsidiary of Merck Group, Darmstadt, Germany)
KnockOut™ Dulbecco's modified eagle medium/nutrient mixture F-12 (DMEM/F-12)	#12660012	Life Technologies (subsidiary of Thermo Fisher Scientific, Massachusetts, USA)
Laminin mouse protein natural	#23017015	Life Technologies (subsidiary of Thermo Fisher Scientific, Massachusetts, USA)
L-Ascorbic Acid, ≥99%	#A4403	Thermo Scientific Chemicals (Massachusetts, USA)

L-Cysteine	#168149	Sigma-Aldrich (subsidiary of Merck Group, Darmstadt, Germany)
LDN193189 dihydrochloride	#72147	StemCell Technologies (Vancouver, Canada)
LEGENDplex™ Hu CD8/NK Panel V02 (13-plex) with Filter Plate	#741186	BioLegend (subsidiary of PerkinElmer, Massachusetts, USA)
L-Glutamine, 100X	#25030081	Life Technologies (subsidiary of Thermo Fisher Scientific, Massachusetts, USA)
LookOut® Mycoplasma PCR Detection Kit	#MP0035	Sigma-Aldrich (subsidiary of Merck Group, Darmstadt, Germany)
Lorlatinib (PF-6463922)	#S7536	Selleckchem (Houston, USA)
Matrigel growth factor reduced basement membrane matrix, lactate dehydrogenase elevating virus (LDEV)-free	#354230	Corning (New York, USA)
Minimal essential media non-essential amino acids (MEM-NEAA) 100X solution	#11140050	Life Technologies (subsidiary of Thermo Fisher Scientific, Massachusetts, USA)
MseI restriction enzyme	#R0525S	New England BioLabs (Massachusetts, USA)
N-2 supplement 100X solution	#17502001	Life Technologies (subsidiary of Thermo Fisher Scientific, Massachusetts, USA)
Neurobasal™ medium	#21103049	Life Technologies (subsidiary of Thermo Fisher Scientific, Massachusetts, USA)
Neurobasal™ medium without vitamin A	#10888022	Life Technologies (subsidiary of Thermo Fisher Scientific, Massachusetts, USA)
NeuroCult™ NS-A Proliferation Kit (Human)	#05751	StemCell Technologies (Vancouver, Canada)
Neurotrophin-3 (NT-3), human/mouse	#78074	StemCell Technologies (Vancouver, Canada)
Novex™ Sharp Pre-Stained Protein Standards	#LC5800	Invitrogen (subsidiary of Thermo Fisher Scientific, Massachusetts, USA)
NuPAGE™ Bis-Tris Mini Protein Gels, 4-12%, 1.0mm	#NP0321	Invitrogen (subsidiary of Thermo Fisher Scientific, Massachusetts, USA)

NuPAGE™ MES SDS Running Buffer, 20X	#NP0002	Invitrogen (subsidiary of Thermo Fisher Scientific, Massachusetts, USA)
Papain from papaya latex, buffered aqueous solution	#P3125	Sigma-Aldrich (subsidiary of Merck Group, Darmstadt, Germany)
Paraformaldehyde	#158127	Sigma-Aldrich (subsidiary of Merck Group, Darmstadt, Germany)
Penicillin-streptomycin, 5000U/ml	#15070063	Life Technologies (subsidiary of Thermo Fisher Scientific, Massachusetts, USA)
Phenylmethanesulfonyl fluoride (PMSF)	#P7626	Sigma-Aldrich (subsidiary of Merck Group, Darmstadt, Germany)
Pierce™ BCA Protein Assay Kit	#23275	Thermo Fisher Scientific (Massachusetts, USA)
Pierce™ Bovine Serum Albumin Standard Ampules, 2mg/ml	#23209	Thermo Fisher Scientific (Massachusetts, USA)
Platelet-derived growth factor (PDGF) AA	#100-16	Shenandoah BioTechnologies (Pennsylvania, USA)
Platelet-derived growth factor (PDGF) BB	#100-18	Shenandoah BioTechnologies (Pennsylvania, USA)
pLentipuro3/TO/V5-GW-EGFP-Firefly Luciferase plasmid	#119816	Addgene (Massachusetts, USA)
Polybrene infection/transfection reagent	#TR1003	Sigma-Aldrich (subsidiary of Merck Group, Darmstadt, Germany)
Poly-L-orthinine	#P4957	Sigma-Aldrich (subsidiary of Merck Group, Darmstadt, Germany)
Ponceau S	#141194	Sigma-Aldrich (subsidiary of Merck Group, Darmstadt, Germany)
QIAamp Circulating Nucleic Acid Kit	#55114	QIAGEN N.V. (Hilden, Germany)
QIAamp DNA Mini Kit	#51304	QIAGEN N.V. (Hilden, Germany)
Quick-Load® 100bp DNA Ladder	#N0467S	New England BioLabs (Massachusetts, USA)
QX200 Droplet Generation Oil	#1864005	Bio-Rad Laboratories (California, USA)

Renaissance Essential Tumor Medium™ (RETM)	#AMS.CM-0001	Cellaria Biosciences (Massachusetts, USA)
RPMI medium 1640	#11875093	Life Technologies (subsidiary of Thermo Fisher Scientific, Massachusetts, USA)
SB-431542 hydrate	#72234	StemCell Technologies (Vancouver, Canada)
SmGM™-2 Smooth Muscle Cell Growth Medium -2 BulletKit™	#185312	Lonza Bioscience (Basel, Switzerland)
Sodium chloride	#BIOSB0476	Astral Scientific (New South Wales, Australia)
Sodium dodecyl sulphate (SDS)	#AM0227	Astral Scientific (New South Wales, Australia)
Sodium orthovanadate	#S6508	Sigma-Aldrich (subsidiary of Merck Group, Darmstadt, Germany)
Sodium pyruvate	#11360070	Life Technologies (subsidiary of Thermo Fisher Scientific, Massachusetts, USA)
Staurosporine	#9953S	Cell Signaling Technology (Massachusetts, USA)
STEMdiff™ Neural Progenitor Freezing Medium	#05838	StemCell Technologies (Vancouver, Canada)
STEMdiff™ Neural Progenitor Medium	#05833	StemCell Technologies (Vancouver, Canada)
STEMdiff™ SMADi Neural Induction Kit	#08581	StemCell Technologies (Vancouver, Canada)
StemPro™ neural supplement	#A1050801	Life Technologies (subsidiary of Thermo Fisher Scientific, Massachusetts, USA)
Sucrose	#S7903	Sigma-Aldrich (subsidiary of Merck Group, Darmstadt, Germany)
SuperSignal™ West Pico PLUS Chemiluminescent Substrate	#34580	Thermo Fisher Scientific (Massachusetts, USA)
T Cell TransAct™, human	#130-111-160	Miltenyi Biotec (Bergisch Gladbach, Germany)
Taurine, 99%	#T0625	Thermo Scientific Chemicals (Massachusetts, USA)
TeSR™-E6™ kit	#05946	StemCell Technologies (Vancouver, Canada)

TeSR™-E8™ kit	#05990	StemCell Technologies (Vancouver, Canada)
Tissue-Tek Optimal Cutting Temperature (OCT) compound	#4583	Sakura Finetek (California, USA)
Tris	#BIO3094T	Amresco (Ohio, USA)
Triton X-100	#T8787	Sigma-Aldrich (subsidiary of Merck Group, Darmstadt, Germany)
Trypan blue stain 0.4%	#15250061	Life Technologies (subsidiary of Thermo Fisher Scientific, Massachusetts, USA)
Trypsin inhibitor from glycine max (soybean)	#T9003	Sigma-Aldrich (subsidiary of Merck Group, Darmstadt, Germany)
Trypsin-EDTA 0.05% (v/v) with phenol red	#2530054	Life Technologies (subsidiary of Thermo Fisher Scientific, Massachusetts, USA)
Tween-20 Biotech Grade	#BIO0777	Astral Scientific (New South Wales, Australia)
Ultrapure™ 0.5M EDTA, pH 8.0	#15575020	Invitrogen (subsidiary of Thermo Fisher Scientific, Massachusetts, USA)
Ultrapure™ RNase/DNase-free distilled water	#10977015	Invitrogen (subsidiary of Thermo Fisher Scientific, Massachusetts, USA)
Urea	#U5378	Sigma-Aldrich (subsidiary of Merck Group, Darmstadt, Germany)
Vitronectin XF™ (xeno-free)	#07180	StemCell Technologies (Vancouver, Canada)
Y27632	#72304	StemCell Technologies (Vancouver, Canada)

Table 2.2 - Primary Antibodies

Antibody (Clone)	Host Species	Concentration; Methodology	Catalogue Number	Manufacturer
Akt (Polyclonal)	Rabbit	1:1000; Western blot	#9272	Cell Signaling Technology (Massachusetts, USA)
ALK (D5F3)	Rabbit	1:2000; Western blot	#3633	Cell Signaling Technology (Massachusetts, USA)
Beta-Tubulin III (D71G9)	Rabbit	1:200; Immunofluorescence organoid cryosection	#5568	Cell Signaling Technology (Massachusetts, USA)
Cleaved-Caspase 3 (Asp175)	Rabbit	1:200; Immunofluorescence organoid cryosection	#9661	Cell Signaling Technology (Massachusetts, USA)
Ctip2 (25B6)	Rat	1:300; Immunofluorescence organoid cryosection	#ab18465	Abcam (Cambridge, UK)
Ctip2/BCL11B (Polyclonal)	Rabbit	1:100; Immunofluorescence organoid cryosection 1:1000; Western blot	#HPA049117	Atlas Antibodies (Stockholm, Sweden)
EGFR (D38B1)	Rabbit	1:1000; Western blot	#4267	Cell Signaling Technology (Massachusetts, USA)
EphA2 PE-conjugated Mouse IgG2b, κ, (SHM16)	Mouse	5µl/million cells; Flow cytometry	#356804	BioLegend (subsidiary of PerkinElmer, Massachusetts, USA)
GAD67/GAD1 (EPR20578]	Rabbit	1:1000 Western blot	#ab213508	Abcam (Cambridge, UK)
GAPDH (6C5)	Mouse	1:5000 Western blot	#AM4300	Invitrogen (subsidiary of Thermo Fisher Scientific, Massachusetts, USA)

GFAP (D1F4Q)	Rabbit	1:500; Immunofluorescence organoid cryosection 1:1000; Western blot	#12389	Cell Signaling Technology (Massachusetts, USA)
Ki67 AlexaFluor® Conjugated (B56)	Mouse	1:50; Immunofluorescence organoid cryosection	#558615	BD Biosciences (New Jersey, USA)
MAP2 (HM-2)	Mouse	1:200; Immunofluorescence organoid cryosection 1:1000; Western blot	#M4403	Sigma-Aldrich (subsidiary of Merck Group, Darmstadt, Germany)
NESTIN (10C2)	Mouse	1:100; Immunofluorescence PDO cryosection	#ab22035	Abcam (Cambridge, UK)
NeuN (D4G40)	Rabbit	1:50; Immunofluorescence adherent cell line	#24307	Cell Signaling Technology (Massachusetts, USA)
p44/42 MAPK (Erk1/2) (Polyclonal)	Rabbit	1:1000; Western blot	#9102	Cell Signaling Technology (Massachusetts, USA)
p-Akt (Ser473)	Rabbit	1:1000; Western blot	#4060	Cell Signaling Technology (Massachusetts, USA)
p-ALK (Tyr1604)	Rabbit	1:1000; Western blot	#3341	Cell Signaling Technology (Massachusetts, USA)
PAX6 (EPR15858)	Rabbit	1:350; Immunofluorescence organoid cryosection	#ab195045	Abcam (Cambridge, UK)
PE-conjugated Mouse IgG2b, κ isotype control (27-35)	Mouse	5µl/million cells; Flow cytometry	#555058	BD Biosciences (New Jersey, USA)
p-EGFR (Tyr1068) (D7A5)	Rabbit	1:1000; Western blot	#3777	Cell Signaling Technology (Massachusetts, USA)
p-EGFR (Tyr1173) (21A9)	Rabbit	1:1000; Western blot	#4757	Cell Signaling Technology (Massachusetts, USA)

p-p44/42 MAPK (Erk1/2) (Thr202/Tyr204) (197G2)	Rabbit	1:1000; Western blot	#4377	Cell Signaling Technology (Massachusetts, USA)
S100ß (SH-B1)	Mouse	1:200; Immunofluorescence organoid cryosection 1:1000; Western blot	#S2532	Sigma-Aldrich (subsidiary of Merck Group, Darmstadt, Germany)
SATB1+SATB2 (SATBA4B10)	Mouse	1:200; Immunofluorescence organoid cryosection	#ab51502	Abcam (Cambridge, UK)
SATB2 (Polyclonal)	Rabbit	1:200; Immunofluorescence organoid cryosection 1:1000; Western blot	#HPA029543	Atlas Antibodies (Stockholm, Sweden)
SOX2 (D6D9)	Rabbit	1:200; Immunofluorescence organoid cryosection 1:1000; Western blot	#3579	Cell Signaling Technology (Massachusetts, USA)
TBR2/EOMES (Polyclonal)	Rabbit	1:50; Immunofluorescence organoid cryosection	#NBP1-80699	Novus Biologicals (Colorado, USA)
VGLUT1 (E8L5B)	Rabbit	1:1000; Western blot	#47181	Cell Signaling Technology (Massachusetts, USA)
Vimentin (D21H3)	Rabbit	1:50; Immunofluorescence organoid cryosection	#5741	Cell Signaling Technology (Massachusetts, USA)

Table 2.3 - Secondary Antibodies

Antibody	Concentration; Methodology	Catalogue Number	Manufacturer
AlexaFluor® 488-conjugated Donkey anti-mouse IgG (H+L) ReadyProbes secondary antibody	1:500; Immunofluorescence organoid cryosection	#R37114	Invitrogen (subsidiary of Thermo Fisher Scientific, Massachusetts, USA)
AlexaFluor® 488-conjugated Donkey anti-rabbit IgG (H+L) ReadyProbes secondary antibody	1:500; Immunofluorescence organoid cryosection	#R37118	Invitrogen (subsidiary of Thermo Fisher Scientific, Massachusetts, USA)
Cy3-conjugated Donkey anti-mouse IgG secondary antibody species adsorbed	1:500; Immunofluorescence organoid cryosection	#AP192C	Sigma-Aldrich (subsidiary of Merck Group, Darmstadt, Germany)
Cy5-conjugated Cy™5 AffiniPure™ Donkey Anti-Rabbit IgG (H+L)	1:500; Immunofluorescence organoid cryosection	#711-175-152	Jackson ImmunoResearch Laboratories (Pennsylvania, USA)
AlexaFluor® 488-conjugated Donkey anti-Rat IgG (H+L) Highly Cross-Adsorbed secondary antibody	1:500; Immunofluorescence organoid cryosection	#A21208	Invitrogen (subsidiary of Thermo Fisher Scientific, Massachusetts, USA)
Horseradish peroxidase-conjugated Donkey anti-mouse IgG (H+L) secondary antibody	1:1000; Western blot	#SA1-100	Invitrogen (subsidiary of Thermo Fisher Scientific, Massachusetts, USA)
Horseradish peroxidase-conjugated	1:1000; Western blot	#SA1-200	Invitrogen (subsidiary of Thermo Fisher

Donkey anti-rabbit IgG (H+L) secondary antibody	Scientific, Massachusetts, USA)

Table 2.4 - Equipment

Model	Manufacturer
Allegra X-12R Centrifuge	Beckman Coulter (California, USA)
Applied Biosystems Sanger Sequencing Instruments (via Australian Genome Research Facility)	Applied Biosystems (subsidiary of Thermo Fisher Scientific, Massachusetts, USA)
Branson Ultrasonics™ S-250A Sonifier™	Branson Ultrasonics (Connecticut, USA)
C1000 Touch™ Thermal Cycler	Bio-Rad Laboratories (California, USA)
ChemiDoc imaging system	Bio-Rad Laboratories (California, USA)
Cryostar™ NX70 Cryostat	Epredia (Michigan, USA)
CKX41 inverted phase-contrast microscope	Olympus LifeScience (Tokyo, Japan)
DMi8 inverted epifluorescence system	Leica Biosystems (Nußloch, Germany)
FACS Canto II flow cytometry system	BD Biosciences (New Jersey, USA)
Forma™ Steri-Cycle™ CO_2 incubator	Thermo Fisher Scientific (Massachusetts, USA)
IVIS® Lumina™ X5 imaging system	PerkinElmer (Massachusetts, USA)
Maestro Pro™ MEA system	Axion BioSystems (Georgia, USA)
Milli-Q® direct water purification system	Millipore (subsidiary of Merck Group, Darmstadt, Germany)
MiniAmp™ Thermal Cycler	Applied Biosystems (subsidiary of Thermo Fisher Scientific, Massachusetts, USA)

Mini Gel Tank	Invitrogen (subsidiary of Thermo Fisher Scientific, Massachusetts, USA)
New Brunswick™ s41i orbital shaking incubator	Eppendorf (Hamburg, Germany)
Odyssey® Fc imaging system	Li-Cor Biosciences (Nebraska, USA)
PowerPac 200 power supply	Bio-Rad Laboratories (California, USA)
PX1 PCR plate sealer	Bio-Rad Laboratories (California, USA)
Qubit 2.0 fluorometer	Invitrogen (subsidiary of Thermo Fisher Scientific, Massachusetts, USA)
QX200™ droplet generator	Bio-Rad Laboratories (California, USA)
QX200™ droplet reader	Bio-Rad Laboratories (California, USA)
TissueLyser II	QIAGEN N.V. (Hilden, Germany)
SpectraMax® iD3 plate reader	Molecular Devices (California, USA)
Stellaris 5 confocal microscope system	Leica Biosystems (Nußloch, Germany)
Ultra-Safe Class II biological safety cabinet	Clyde-APAC Air Filtration (New South Wales, Australia)
xCELLigence® real-time cell analyser	Agilent Technologies (California, USA)

Table 2.5 - Microscope systems

Microscope System	Objectives	Accessories	Software	Manufacturer
CKX41 Inverted Phase-Contrast Microscope	• UPLANFLN 4x/0.13 Dry	• DP12 camera	-	Olympus LifeScience (Tokyo, Japan)
DMi8 Inverted Epifluorescence System	• PL FLUOTAR 2.5x/0.07 Dry • PL FLUOTAR 10x Dry • PL FLUOTAR 20x Oil	• Cameras: DFC3000 monochrome and DFC700T colour • DAPI/FITC/TXR/Y5-T filters • LMT200 automated stage	LAS X v3.7.1.21655	Leica Biosystems (Nußloch, Germany)
Stellaris 5 Digital Light Sheet and Confocal Laser Scanning Microscope	• Obj. HC PL FLUOTAR 2.5x/0.07 • Obj. HC PL FlUOTAR 4x/0.13 • Obj. HC PL APO 20x/0.75 CS2 • Obj. HC PL APO 63x/1.40 OIL CS2	• Hamamatsu Orca-Flash 4.0 V3 Digital CMOS Camera (#13440-20CU) • 3 x HyD detectors and PMT for brightfield channel • Triple cube DAPI/FITC/TRITC fluorescent filters	LAS X v4.5.0.2531	Leica Biosystems (Nußloch, Germany)

Table 2.6 - Software packages

Software Name	Latest Version Used	Publisher
AxIS Navigator	3.7.3.2	Axion BioSystems (Georgia, USA)
AxIS Metric Plot Tool	2.5.0	Axion BioSystems (Georgia, USA)
FlowJo™	10.10	FlowJo LLC (subsidiary of BD Biosciences, New Jersey, USA)
GraphPad Prism	10.2.3 (403)	GraphPad Software (California, USA)
ImageJ (FIJI distribution)	1.54h	National Institutes of Health (NIH), USA
Image Studio	6.0	Li-Cor Biosciences (Nebraska, USA)
Leica Application Suite X	4.5.0.25531	Leica Biosystems (Nußloch, Germany)
Living Image®	4.8.0.21779	PerkinElmer (Massachusetts, USA)
QX Manager Software SE	2.2	Bio-Rad Laboratories (California, USA)
RTCA Software Pro	2.3.4	Agilent Technologies (California, USA)
Sequence Scanner Software	2.0	Applied Biosystems (subsidiary of Thermo Fisher Scientific, Massachusetts, USA)

Table 2.7 - Cell line information

Cell Line	Cell Type	Patient Details	Derivation	Culture Conditions	Supplier
A172	Continually-cultured adult glioblastoma	53-year-old male patient with glioblastoma.	Commercially available. Establishment described by Giard et al. 1977.	Adherent culture. Maintained in DMEM, 10% (v/v) FBS.	Kindly supplied by Peter Gunning of the Oncology Research Unit, University of New South Wales, Australia.
K562	Continually-cultured chronic myeloid leukaemia	53-year-old female with chronic myelogenous leukaemia.	Commercially available. Establishment described by Lozzio & Lozzio. 1975.	Suspension culture. Maintained in RPMI 1640, 2mM L-Glutamine, 10% (v/v) FBS.	Commercially available.
Kelly	Continually-cultured neuroblastoma	1-year-old female patient with Stage IV neuroblastoma tumour located in the brain.	Commercially available. Establishment described by Gilbert et al. 1982.	Adherent culture. Maintained in RPMI 1640, 10% (v/v) FBS.	Commercially available.
LA-N-2	Continually-cultured neuroblastoma	3-year-old female patient with Stage IV neuroblastoma.	Commercially available. Establishment described by	Adherent culture. Maintained in DMEM/F12, 2mM L-Glutamine, 10% (v/v) FBS.	Commercially available.

			Seeger et al. 1977.		
MCF-10A	Continually-cultured breast epithelium	36-year-old female patient with fibrocystic disease in the breasts.	Commercially available. Establishment described by Soule et al. 1990.	Adherent culture. Maintained in DMEM/F12, 5% (v/v) horse serum, 20ng/ml EGF, 0.5µg/ml hydrocortisone, 100ng/ml cholera toxin, 10µg/ml insulin.	Commercially available.
QIMR-SJH1 (SJH1)	Primary adult glioblastoma	72-year-old male patient with primary glioblastoma tumour resected from left temporal lobe. 45-day survival.	Established from surgical aspirate as described by Day et al. 2013.	Adherent culture. Maintained on 1% (v/v) Matrigel-coated surface in Glioma Neural Stem Medium (KnockOut™ DMEM/F12, StemPro™ Neural Supplement, 2mM L-Glutamine, 20ng/ml EGF, 10ng/ml FGF-2, 20ng/ml heparin, 1X penicillin-streptomycin).	Kindly supplied by Bryan Day, Brett Stringer and Andrew Boyd of the Sid Faithfull Brain Cancer Laboratory, QIMR-Berghofer Medical Research Institute, Australia.
QIMR-WK1 (WK1)	Primary adult glioblastoma	77-year-old male patient with primary glioblastoma tumour resected from right parietal occipital lobe. 121-day survival.	Established from surgical aspirate as described by Day et al. 2013.	Adherent culture. Maintained on 1% (v/v) Matrigel-coated surface in Glioma Neural Stem Medium.	Kindly supplied by Bryan Day, Brett Stringer and Andrew Boyd of the Sid Faithfull Brain Cancer Laboratory, QIMR-Berghofer Medical Research Institute, Australia.
SK-N-SH	Continually-cultured neuroblastoma	4-year-old female patient with Stage IV neuroblastoma.	Commercially available. Establishment described by	Adherent culture. Maintained in DMEM, 10% FBS.	Commercially available.

			Biedler et al. 1973.		
SU-DIPG-VI (DIPG6)	Primary diffuse intrinsic pontine glioma	7-year-old female patient with DIPG tumour located at the pons. 6-month survival.	Established from post-mortem autopsy sample, as described by Lin & Monje 2017.	Suspension culture. Maintained in Tumour Stem Medium (Neurobasal™ minus vitamin A, DMEM/F12, 1X B27 minus vitamin A, 1X MEM-NEAA, 1X GlutaMax, 10mM HEPES, 1mM sodium pyruvate, 1X antibiotic-antimycotic, 50µg/ml heparin, 20ng/ml EGF, 20ng/ml FGF-2, 10ng/ml PDGF-AA, 10ng/ml PDGF-BB).	Kindly supplied by Michelle Monje of the Monje Lab, Stanford University, USA.
SU-DIPG-XVII (DIPG17)	Primary diffuse intrinsic pontine glioma	8-year-old male patient with DIPG tumour located at the pons. 13-month survival.	Established from post-mortem autopsy sample, as described by Lin & Monje 2017.	Adherent culture. Maintained in Tumour Stem Medium.	Kindly supplied by Michelle Monje of the Monje Lab, Stanford University, USA.
SU-DIPG-XXI (DIPG21)	Primary diffuse intrinsic pontine glioma	7-year-old male patient with DIPG tumour located at the pons. 18-month survival.	Established from post-mortem autopsy sample, as described by Lin & Monje 2017.	Suspension culture. Maintained in Tumour Stem Medium.	Kindly supplied by Michelle Monje of the Monje Lab, Stanford University, USA.
SU-DIPG-XXIV (DIPG24)	Primary diffuse intrinsic pontine glioma	6-year-old female patient with DIPG tumour located at the	Established from post-mortem	Adherent culture. Maintained in Tumour Stem Medium.	Kindly supplied by Michelle Monje of the

		pons. 18-month survival.	autopsy sample, as described by Lin & Monje 2017.		Monje Lab, Stanford University, USA.
T Cells	Primary human T cells	Assorted healthy Blood Bank donors.	Isolated from healthy donor samples, enriched, and activated as described by Hsu et al. 2020.	Suspension culture. Active and transduced T cells maintained in T cell medium (CTS OpTimizer T cell expansion medium, 2.5% (v/v) CTS Immune Cell serum replacement, 10ng/ml IL-7, 5ng/ml IL-15).	Kindly supplied by Kenneth Hsu of the Advanced Cellular Therapeutics team, Kids Research, CHW, Australia.
U87-MG	Continually-cultured adult glioblastoma	Male patient of unknown age with malignant glioma, likely glioblastoma.	Commercially available. Characterised by Allen et al. 2016.	Adherent culture. Maintained in DMEM, 10% (v/v) FBS.	Commercially available.
WA-09 (H9)	Embryonic stem cells	-	Commercially available. Established from blastocyst-stage embryo as described by Thomson et al. 1998.	Adherent culture. Maintained on 10µg/ml vitronectin-coated flasks in TeSR-E8 complete culture medium.	Kindly supplied by Mirella Dottori of the Dottori Group, Illawarra Health & Medical Research Institute, Australia, with permission from WiCell, USA (Agreement #19-W0538).

Table 2.8 - Primary cell lines and patient-derived organoids (PDOs)

ID	Tumour Type	Patient Details	Established Cultures	Culture Conditions
NBL-9	Neuroblastoma	5-year-old female patient with left retro-peritoneal tumour.	2D Adherent	Adherent culture in DMEM/F12, 10% (v/v) heat-inactivated FBS, 1X B27 supplement, 1X MEM-NEAA, 20ng/ml EGF, 20ng/ml FGF-2, 500µM sodium pyruvate, 1% (v/v) penicillin/streptomycin.
MBL-10	Medulloblastoma Non-Wnt, Non-SHH subtype.	5-year-old female patient with posterior fossa/4th ventricular brain tumour.	2D Adherent, 3D PDO	Adherent culture in NSA Medium (Neurocult™ NS-A basal medium, Neurocult™ NS-A supplement, 20ng/ml EGF, 20ng/ml FGF-2, 2µg/ml heparin, 1% (v/v) penicillin/streptomycin, 500ng/ml amphotericin B). PDO culture in Glioblastoma Organoid Medium (50% DMEM/F12, 50% Neurobasal™ medium, 1X GlutaMax, 1X MEM-NEAA, 1% (v/v) penicillin/streptomycin, 1X N2 supplement, 1X B27 without vitamin A, 1X beta-mercaptoethanol, 2.5µg/ml insulin). Maintained in suspension in ultra-low attachment plates in New Brunswick™ s41i orbital shaking incubator at 70rpm.
PNET-17	Primitive neuroectodermal tumour (PNET)	14-year-old female patient with recurrent right temporal brain tumour.	3D PDO	PDO culture in Neurosphere Medium (KnockOut™ DMEM/F12, StemPro™ Neural Supplement, 2mM L-Glutamine, 20ng/ml EGF, 10ng/ml FGF-2, 1X penicillin-streptomycin).
MBL-23	Medulloblastoma Wnt subtype.	7-year-old female with 4th ventricular brain tumour.	2D Adherent, 3D PDO	Adherent culture in Neurosphere medium (KnockOut™ DMEM/F12, StemPro™ neural supplement, 20ng/ml EGF, 20ng/ml FGF-2, 1X GlutaMax, 1% (v/v) penicillin/streptomycin). PDO culture in ultra-low attachment plates in Neurosphere medium. Maintained in suspension under static incubation conditions.

eRMS-25	Embryonal rhabdomyosarcoma	19-month-old male patient with peritoneal metastatic disease.	2D Adherent	Adherent culture in Renaissance Essential Tumour Medium, 10% (v/v) FBS, 1% (v/v) penicillin/streptomycin, 500ng/ml amphotericin B, 20µg/ml gentamicin, 25 ng/ml cholera toxin).
PBL-31	Pineoblastoma	13-year-old female patient with pineal tumour.	3D PDO	PDO culture in Glioblastoma Organoid Medium. Maintained in suspension in ultra-low attachment plates in New Brunswick™ s41i orbital shaking incubator at 70rpm.
MGC-40	Mixed germ cell brain tumour- Majority embryonal carcinoma and significant focal germinoma.	16-year-old male patient with pineal tumour.	3D PDO	PDO culture in Glioblastoma Organoid Medium. Maintained in suspension in ultra-low attachment plates in New Brunswick™ s41i orbital shaking incubator at 70rpm.
pGBM-42	Glioblastoma	7-year-old male patient with frontal lobe brain tumour.	2D Adherent, 3D PDO	Adherent culture maintained on 1% (v/v) Matrigel-coated surface in Tumour Stem Medium. PDO culture in Glioblastoma Organoid Medium. Maintained in suspension in ultra-low attachment plates in New Brunswick™ s41i orbital shaking incubator at 70rpm.
ES-43	Ewing sarcoma	13-month-old male patient with liver metastasis.	3D PDO	PDO culture in Smooth Muscle Growth Medium (SmGM™-2 Smooth Muscle Cell Growth Medium -2 BulletKit, 1% (v/v) penicillin/streptomycin, 500ng/ml amphotericin B, 20µg/ml gentamicin). Maintained in suspension under static incubation conditions.
NBL-53	Neuroblastoma	6-year-old female patient with left suprarenal tumour.	3D PDO	PDO culture in Neuroblastoma Organoid Medium (DMEM/F12, 10% (v/v) BIT 9500 Serum Substitute, 5% (v/v) MEM-NEAA, 1X GlutaMax, 1X B27 supplement, 1X N2 supplement, 40ng/ml FGF-2, 20ngml EGF, 1X beta-mercaptoethanol).
pGBM-55	Glioblastoma	6-year-old male patient with right frontal lobe brain tumour. Diagnosed with constitutional mismatch repair deficiency (CMMRD) syndrome.	3D PDO	PDO culture in Glioblastoma Organoid Medium. Maintained in suspension in ultra-low attachment plates in New Brunswick™ s41i orbital shaking incubator at 70rpm.

Table 2.9 - gBlock Control DNA Fragments Design

Mutation	Type of Mutation	Wild-Type gBlock	Mutation gBlock
NM_198253.3 TERT c.1-124G>A p.Gly42Arg	Missense	ATAATAGGACATAATATTATCTGAAACTCATAT CATGAGGAGAGGATATAATCGCGGAAAGGAA GGGGAGGGGCTGGGAGGGCCCGGAGGGGGC TGGGCCATATACCCATAAATATTCATAACGGGA TATATTCCATATGGAGGAGGCGGAGCTGGAAG GTGAAGGGGCAGGACGGGTATCCATATCCCC AGTCCCTCCATCACGTGGGAAATATGGTCCTG GATGTCTGTATCCATGAATCCA	ATAATAGGACATAATATTATCTGAAACTCATATC ATGAGGAGAGGATATAATCGCGGAAAGGAAGG GGAGGGGCTGGGAGGGCCCGGAaGGGGCTGG GCCATATACCCATAAATATTCATAACGGGATATA TTCCATATGGAGGAGGCGGAGCTGGAAGGTGA AGGGGCAGGACGGGTATCCATATCCCCAGTCC CTCCATCACGTGGGAAATATGGTCCTGGATGTC TGTATCCATGAATCCA
NM_006231.4 POLE c.1366G>C p.Ala456Pro	Missense	CCCATGAGACATACAAAAAGGTAATGCCGCC TCGCTAGGTGAGCTACAGCTCGATTGTCACGT TAAGCTGGCCCCCGCTCCACCCAGCAGGCTG TGTCTCCGGGACACACGTGTTTTGTCCTGTGC CGGTCTCCTTACTGTGTGTGCGGCAGGCTGGT CAGGCCAGGCTTTGCTTTCTGTGCTTCACACT TGACCCTGGGCTCTTGATTTTTGATGGCCCTG CTCTCTGGCGTTCTCTCCTCAGACTCTGGCCA CGTATTCTGTGTCAGATGCTGTCGCCACTTAC TACCTGTACATGAAGTACGTCCACCCATTCAT CTTTGCTCTGTGCACCATTATTCCCATGGAGC CCGACGAGGTGAGCATTATCTGTCCTGTCGGC ACCCTGGCCTCCTCAGCCCTTGCCCCATTCCA AATGCACTGGAGCTGAATGGAGGTGGATGTC CCAGGAGTGCTGGCACCAGAGGCGGCGGTCT CGACTATACGCCCGTTTTCGGATC	CCCATGAGACATACAAAAAGGTAATGCCGCCT CGCTAGGTGAGCTACAGCTCGATTGTCACGTTA AGCTGGCCCCCGCTCCACCCAGCAGGCTGTGT CTCCGGGACACACGTGTTTTGTCCTGTGCCGG TCTCCTTACTGTGTGTGCGGCAGGCTGGTCAG GCCAGGCTTTGCTTTCTGTGCTTCACACTTGAC CCTGGGCTCTTGATTTTTGATGGCCCTGCTCTC TGGCGTTCTCTCCTCAGACTCTGCCCACGTATT CTGTGTCAGATGCTGTCGCCACTTACTACCTGT ACATGAAGTACGTCCACCCATTCATCTTTGCTC TGTGCACCATTATTCCCATGGAGCCCGACGAGG TGAGCATTATCTGTCCTGTCGGCACCCTGGCCT CCTCAGCCCTTGCCCCATTCCAAATGCACTGGA GCTGAATGGAGGTGGATGTCCCAGGAGTGCTG GCACCAGAGGCGGCGGTCTCGACTATACGCCC GTTTTCGGATC

NM_002834.5 PTPN11 c.1492C>T p.ARG498Trp	Missense	CCCATGAGACATACAAAAAGGTAATGCCGCC TCGCTAGGTGAGCTACAGCTCGATTGTCACGT TAAGCTGGCCCATTGCAACATGCTCAGTTAAA ACAGCAAAGACTAAATTAGCATTGTCTCTGAG TCCACTAAAAGTTGTGCATTAAACAACTTCAT CCTGGCTCTGCAGTTTCTCTTTATTCTTCATGA TGTTTCCTTCGTAGGTGTTGACTGCGATATTG ACGTTCCCAAAACCATCCAGATGGTGTGGTCT CAGAGGTCAGGGATGGTCCAGACAGAAGCA CAGTACCGATTTATCTATATGGCGGTCCAGCAT TATATTGAAACACTACAGCGCAGGATTGAAGA AGAGCAGGTACCAGCCTGAGGGCTGGCATGC GGATTCTCATTCTCTTGCTAGGCCTCTTGGATA CGCTCTCCTTTTGAGCAGGAGGACAGGCTCT GATAGACAACTGTTTGATTTCGGAAGGTCTCG ACTATACGCCCGTTTTCGGATC	CCCATGAGACATACAAAAAGGTAATGCCGCCT CGCTAGGTGAGCTACAGCTCGATTGTCACGTTA AGCTGGCCCATTGCAACATGCTCAGTTAAAAC AGCAAAGACTAAATTAGCATTGTCTCTGAGTCC ACTAAAAGTTGTGCATTAAACAACTTCATCCTG GCTCTGCAGTTTCTCTTTATTCTTCATGATGTTT CCTTCGTAGGTGTTGACTGCGATATTGACGTTC CCAAAACCATCCAGATGGTGCGGTCTCAGAGG TCAGGGATGGTCCAGACAGAAGCACAGTACCG ATTTATCTATATGGCGGTCCAGCATTATATTGAA ACACTACAGCGCAGGATTGAAGAAGAGCAGGT ACCAGCCTGAGGGCTGGCATGCGGATTCTCATT CTCTTGCTAGGCCTCTTGGATACGCTCTCCTTTT GAGCAGGAGGACAGGCTCTGATAGACAACTGT TTGATTTCGGAAGGTCTCGACTATACGCCCGTT TTCGGATC

Table 2.10 - Probes and Primers

Mutation	Type of Mutation	Primers	Probes
NM_198253.3 TERT c.1-124G>A p.Gly42Arg	Missense	TERT Forward: AAAGGAAGGGGAGGGGCT TERT Reverse: CTTCACCTTCCAGCTCCG	TERT c.1-124G (WT): [HEX] AGGGCCCGGAGGGGGCT [Iowa Black FQ] TERT c.1-124G>A: [6-FAM] AGGGCCCGGAaGGGGCTG [Iowa Black FQ]
NM_006231.4 POLE c.1366G>C p.Ala456Pro	Missense	POLE c.1366G (WT): [HEX] dHsaMDW1685846123 (Bio-Rad) POLE POLE c.1366G>C [6-FAM] dHsaMDM1685846121 (Bio-Rad)	
NM_002834.5 PTPN11 c.1492C>T p.ARG498Trp	Missense	PTPN11 c.1492C>T: Mutation Detection Single Tube [HEX/6-FAM] dHsaMDS580107299 (Bio-Rad)	
NM_002107.7 H3F3A c.83A>T p.Lys28Met	Missense	H3F3A c.83A (WT): [FAM] dHsaCP2500511 (Bio-Rad) H3F3A c.83A>T: [FAM] dHsaCP2500510 (Bio-Rad)	

Table 2.11 - Solutions & Buffers

Solution/Buffer	Final Concentration & Composition
0.05% PBS-T	0.05% (v/v) Triton X-100 in 1X PBS
0.1% Ponceau	0.1% (w/v) Ponceau-S, 5% (v/v) acetic acid in MilliQ H_2O
1% Matrigel solution	1% (v/v) Matrigel in DMEM-high glucose sodium pyruvate medium
10% SDS solution	10% (w/v) SDS in MilliQ H_2O
10X FACS buffer	137.4mM NaCl, 2.7mM KCl, 10.1mM KH_2HPO_4, 0.1% (w/v) BSA in MilliQ H_2O
10X PBS	1.4M NaCl, 0.03M KCl, 0.1M Na_2HPO_4 0.2mM KH_2PO_4 in MilliQ H_2O, pH adjusted to 7.4
10X SDS-PAGE transfer buffer	25mM Tris, 2M glycine in MilliQ H_2O, pH adjusted to 7.5 with HCl
10X TBS	1M Tris, 1.5M NaCl in MilliQ H_2O, pH adjusted to 7.5 with HCl
1X DNA sample dye	30% (v/v) glycerol, 1mM EDTA pH 8.0, 0.25% (w/v) bromophenol blue, 0.25% (w/v) xylene cyanol FF in MilliQ H_2O
1X MES/SDS running buffer	20X NuPAGE™ MES SDS running buffer in MilliQ H_2O
1X SDS-PAGE transfer buffer	10X SDS-PAGE transfer buffer, 20% (v/v) methanol, 0.005% (w/v) SDS in MilliQ H_2O
1X TAE buffer	40mM Tris, 20mM acetic acid, 1mM EDTA pH 8.0 in MilliQ H_2O
1X TBS-T	10X TBS, 0.1% (v/v) Tween-20 in MilliQ H_2O
4% PFA solution	4% (w/v) PFA in MilliQ H_2O, pH adjusted to 7.2 with NaOH
5X SDS-PAGE sample buffer	50% (v/v) glycerol, 250mM Tris pH (6.8), 25% (v/v) beta-mercaptoethanol, 10% (w/v) SDS) 0.05% (v/v) bromophenol blue
Collagen neutralising buffer	20% (v/v) 10X PBS, 100mM HEPES in MilliQ H_2O, pH adjusted to 7.3 with HCl
Immunofluorescence blocking buffer	10% (v/v) Donkey serum in 1X PBS

Immunofluorescence permeabilising buffer	0.3% (v/v) Triton X-100 in 1X PBS
Organoid lysis buffer	1% SDS (w/v), 8M urea, 100mM Tris-HCl (pH 8.0) in MilliQ H_2O
Western blocking buffer	5% (w/v) non-fat dry milk or 5% (w/v) BSA, 1X TBS, 0.1% (v/v) Tween-20

2.2 - Tissue culture

All cell lines used in this thesis were cultured in filter-capped 25cm^2 or 75cm^2 tissue culture flasks (Corning) at 37°C, 5% CO_2 in a humidified Forma Steri-Cycle™ incubator (Thermo Fisher Scientific), unless stated otherwise. Culture health and growth were routinely monitored using a CKX41 inverted phase-contrast microscope (Olympus LifeScience). Cells were passaged upon reaching approximately 80% confluence and sub-cultured at an appropriate ratio to fresh culture flasks. Continually-cultured and patient-derived cell lines were both used in this thesis. “Continually-cultured” refers to cell lines which have been repeatedly passaged in serum-containing medium and have experienced varying degrees of genetic drift from the original tissue sample. “Primary patient-derived” cell lines have been cultured in serum-free conditions at lower passage numbers, and are frequently validated against the primary tissue sample reference using short-tandem repeat (STR) profiling, performed by CellBank Australia (Children’s Medical Research Institute, Australia). Details of the cell lines used in this thesis, including patient data, establishment protocols, and culture conditions, are summarised in Table 2.7.

2.2.1 - Continually-Cultured Cell Line Maintenance

GBM cell lines A172 and U87-MG were maintained under adherent conditions in Dulbecco’s Minimum Eagle Medium (DMEM) supplemented with 10% foetal bovine serum (FBS). The continually-cultured breast epithelium cell line MCF-10A was maintained under

adherent conditions in DMEM/F12, 5% (v/v) horse serum, 20ng/ml EGF, 0.5µg/ml hydrocortisone, 100ng/ml cholera toxin, 10µg/ml insulin. Continually-cultured cells were passaged every 3-4 days with 0.05% (v/v) Trypsin-EDTA. Enzymatic activity was neutralised using equal volume medium, then cells were centrifugated at 300xg for five minutes and subcultured into fresh 75cm^2 flasks at a ratio of 1:4 for MCF-10A, 1:5 for A172, and 1:8 for U87-MG.

2.2.2 - Primary Patient-Derived Cell Line Maintenance

Four primary patient-derived DIPG cell lines were kindly provided by Prof. Michelle Monje (Stanford University, USA) and were established from post-mortem tissue samples, as previously published [Lin & Monje 2017]. All DIPG lines were maintained in 'Tumour Stem Medium (TSM)', comprising 50% (v/v) Neurobasal™ medium without vitamin A, 50% (v/v) DMEM/F12, 1X B27 supplement without vitamin A, 1X minimum essential medium non-essential amino acids (MEM-NEAA), 1X GlutaMax, 10mM HEPES, 1mM sodium pyruvate, 1X antibiotic-antimycotic, 50µg/ml heparin, 20ng/ml EGF, 20ng/ml FGF-2, 10ng/ml PDGF-AA, and 10ng/ml PDGF-BB. SU-DIPG-XVII (DIPG17) and SU-DIPG-XXIV (DIPG24) were maintained under adherent conditions, while SU-DIPG-VI (DIPG6) and SU-DIPG-XXI (DIPG21) formed neurospheres in suspension. Adherent lines were passaged by enzymatic detachment with accutase for 3 to 5 minutes, then neutralised with equal volume trypsin inhibitor. Neurosphere lines were collected in medium, pelleted by centrifugation at 200xg for 3 minutes, resuspended in accutase for a further 3 minutes to facilitate dissociation, then neutralised with equal volume trypsin inhibitor. Cell suspensions were centrifuged at 200xg for 3 minutes, and subcultured into fresh 25cm^2 culture flasks (Corning) at 1:4 to 1:5 ratio.

Primary patient-derived GBM lines SJH1 and WK1 were kindly supplied by Professor Bryan Day, Professor Andrew Boyd, and Dr Brett Stringer (Brain Cancer Research

Unit, QIMR-Berghofer Medical Research Institute, Australia). Establishment protocol from surgical aspirates and subsequent characterisation was previously reported [Day 2013, Stringer 2019]. Tissue culture flasks were coated with 1% (v/v) Matrigel in DMEM, high-glucose sodium pyruvate medium and incubated overnight at 4°C. Matrigel-coated flasks were rinsed twice with DPBS prior to culturing cells under adherent conditions in 'Glioma Neural Stem (GNS)' medium, consisting of KnockOut™ DMEM/F12, StemPro™ Neural Supplement, 2mM L-Glutamine, 1X penicillin-streptomycin, 20ng/ml heparin, 20ng/ml EGF, and 10ng/ml FGF-2. Cells were passaged every 3-4 days with accutase, neutralised with trypsin inhibitor, and centrifuged at 200xg for three minutes. Cells were subcultured into Matrigel-coated 25cm^2 flasks at ratios of 1:2 for SJH1 and 1:5 for WK1. To limit genetic drift, patient-derived cell lines were not maintained past 35 passages and were routinely validated by STR profiling.

2.2.3 - Human Embryonic Stem Cell (hESC) Maintenance

All experiments conducted with stem cells were performed in accordance with the National Statement on Ethical Conduct in Human Research (2007) under approval 2019/ETH00240 from the Sydney Children's Hospital Network (SCHN) Human Research and Ethics Committee (HREC). The human embryonic stem cell (hESC) line WA-09 (H9) was kindly supplied to our laboratory by Mirella Dottori (University of Wollongong, Australia; Agreement No. 19-W0538; WiCell, USA). H9 cells were maintained in TeSR™-E8™ culture medium as adherent colonies on vitronectin XF™-coated flasks. 10µg/ml Vitronectin-XF™ was prepared in CellAdhere™ dilution buffer (StemCell Technologies) and added to flasks at room temperature for 30 minutes, before rinsing twice with DPBS. Cells were detached from flasks by gently rinsing with DPBS and adding 0.5mM EDTA for 3.5 minutes at 37°C. EDTA was aspirated and colonies lifted from the flask with medium, then sub-cultured at 1:4 ratio. Complete medium changes were performed every second day, and

cells passaged every fourth day. Cultures were monitored daily to check for differentiation, based upon the phase-brightness, size, and density of colonies.

2.2.4 - Neuronal Differentiation of hESCs

H9 hESC culture medium was changed to TeSR™-E8™ with 10µM Y-27632 ROCK inhibitor an hour prior to passaging. Cells were passaged with pre-warmed accutase for 6 minutes at 37°C and collected in 1ml TeSR™-E8™/Y-27632, then centrifuged at 1000xg for 4 minutes. Cells were resuspended in STEMdiff™ SMADi Neural Induction medium supplemented with 10µM Y027632, and 2 x 10^6 cells were seeded to a Matrigel-coated well of a 6-well plate. Cells were fed daily with STEMdiff™ SMADi Neural Induction medium until Day 7, then subcultured 1:2. Passages were performed at days 14 and 21, after which the neural progenitor cells (hNPCs) were maintained in STEMdiff™ Neural Progenitor medium in a Matrigel-coated 25cm^2 tissue culture flask. At passage 3, hNPCs were characterised to confirm cell identity by positive PAX6 and SOX2 expression and absence of β-tubulin III, then expanded. Stocks were frozen back in STEMdiff™ Neural Progenitor Freezing Medium and stored in liquid nitrogen.

To differentiate hNPCs into neurons, cultureware was first coated with 15µg/ml poly-L-ornithine (PLO) solution for 30 minutes at 37°C, then 30µg/ml laminin overnight at 4°C. hNPCs were dissociated by accutase and seeded at a density of 1.5 x 10^4 – 3 x 10^4 cells/cm^2 in BrainPhys™ Neuronal Medium, supplemented with 1X NeuroCult™ SM1 neuronal supplement, 1X N2 supplement without vitamin A, 20ng/ml BDNF, 20ng/ml GDNF, 1mM dibutyryl cAMP, 200nM ascorbic acid, and 10mM glucose. Half medium changes were performed every 2-3 days, with cells being routinely evaluated for neuronal markers. Differentiation was continued for 28 days to confirm further neuronal maturation.

2.2.5 - Dorsal Cortical Organoid Generation

Two separate protocols were evaluated for the neural differentiation of stem cells and replicable generation of dorsal cortical organoids. The main protocol used for this thesis was previously described for hESCs, with minor alterations [Mattei 2018, Prior 2022]. Briefly, stem cell colonies were detached from flasks using 0.5mM EDTA for 3.5 minutes at 37°C and transferred in TeSR™-E8™ medium to 6-well plates coated overnight at 4°C with 30µg/ml laminin. After 24 hours, TeSR™-E8™ was replaced with neural induction medium (50% Neurobasal™ medium, 50% DMEM/F12, 1X B27 supplement without vitamin A, 1X N2 supplement, 1X insulin-transferrin-selenium sodium pyruvate (ITS) without vitamin A, 2mM GlutaMax, 0.3% (w/v) glucose) freshly supplemented with 0.1mM LDN193189 and 1µM SB-431524 for dual SMAD inhibition. Neural induction medium was refreshed daily for up to 7 days to allow for differentiation. NPCs were detached by 0.5mM EDTA and centrifuged at 200xg for 3 minutes, then seeded to a 96-well round-bottom ultra-low attachment plate in neural medium (Neurobasal™ medium, 1X B27 supplement without vitamin A, 1X N2 supplement, 1X ITS without vitamin A, 2mM GlutaMax) supplemented with 20ng/ml EGF and 20ng/ml FGF-2. Resulting organoids were cultured in static conditions for 10-14 days, with neural medium changed every 2-3 days. Once organoids approached approximately 500µm in diameter, they were transferred to 6-well ultra-low attachment plates (maximum 6 organoids per well) and cultured in an Eppendorf Brunswick™ s41i orbital shaking incubator set to 70rpm, 5% CO_2, and 37°C.

An alternative method for the generation of cortical organoids was investigated for comparison, adapted from a protocol by Pașca and Yoon [Pașca S & Yoon 2018]. H9 cells were cultured as adherent colonies in TeSR™-E8™, with 1% (v/v) DMSO added to the medium 48 hours prior to passage to prime the cells. On the day of passage, culture medium was changed to TeSR™-E8™ with 1% DMSO and 10µM Y-27632 for an hour. Colonies

were then dissociated in 1ml accutase for 6 minutes at 37°C and collected in 2ml TeSR™-E8™/Y-27632. Cells were centrifuged at 1000xg for 4 minutes, then seeded at 10,000 cells in 100µl TeSR™-E8™/Y-27632 per well of a 96-well round-bottom ultra-low attachment plate. After 24 hours incubation, 100µl TeSR™-E6™ medium supplemented with 2.5µM dorsomorphin and 10µM SB-431542 was added. Half media changes were performed daily with supplemented TeSR™-E6™ medium until day 6, when organoids were transferred to 6-well ultra-low attachment plates in 'neural medium 2' (Neurobasal™ medium without vitamin A, 1X B27 supplement without vitamin A, and 1X GlutaMax) supplemented with 20ng/ml EGF and 20ng/ml FGF-2. Daily medium changes were performed until day 16, then every second day until day 24. From day 25, EGF and FGF-2 were replaced with 20ng/ml BDNF and 20ng/ml NT-3. From day 43 onwards, growth factors were removed from the medium and orbital shaker speed was reduced to 56rpm. Organoids continued to be cultured in their respective conditions until day 120, whereupon culture medium was changed to BrainPhys™ Neuronal Medium, supplemented with 1X NeuroCult™ SM1 neuronal supplement, 1X N2 supplement without vitamin A, 20ng/ml BDNF, 20ng/ml GDNF, 0.1mM taurine, 200nM ascorbic acid, 1mM dibutyryl cAMP, 10mM glucose, and 1% (v/v) penicillin-streptomycin. Organoid culture was continued in these conditions until required. Organoid culture medium was routinely tested for presence of mycoplasma using LookOut® Mycoplasma PCR Detection Kit (Sigma-Aldrich).

2.3 - Generation of Tumour Spheroids

Tumour spheroids are 3D aggregates of tumour cells which form under non-adherent culture conditions, exhibiting a concentration gradient across which nutrients, growth factors, oxygen, drugs, and waste are distributed. Spheroids were generated from the primary patient-derived cell lines SJH1, WK1, DIPG17, and DIPG24. Cells were dissociated according to the aforementioned protocol and pelleted by centrifugation. Supernatant was discarded and the

cell pellet resuspended in medium. 10µl cell suspension was transferred to a 1.5ml Eppendorf tube containing an equal volume of 0.4% Trypan blue solution (Life Technologies). Following mixing by pipetting, 10µl was placed into the channel of a Bright-Line™ haemocytometer (Sigma-Aldrich) and cells manually counted across 4 grids, excluding stained cells signifying non-viable cells. Required number of cells was seeded into 100µl medium per well of a 96-well round-bottom ultra-low attachment plate (Corning) and incubated at 37°C, 5% CO_2 in static conditions for 4 days. Cells typically aggregated within 24 hours, but culture was extended to allow for greater cell-cell adhesion, appearance of well-defined borders, and to ensure spheroids could be handled as required without dissolution.

2.4 - Embedding of Tumour Spheroids in Hydrogels

Early experiments required embedding WK1 and SJH1 spheroids in a collagen hydrogel, providing an extracellular matrix scaffold to support tumour cell growth and migration. Tumour spheroids were generated in ultra-low attachment plates, with cell counts ranging from 7.5×10^3 to 2.5×10^4 cells per spheroid. Spheroids were grown for 4 days to allow for aggregation, and washed in DPBS prior to embedding. All work with matrices was performed on ice to prevent premature polymerisation. Collagen I stock was diluted to 1.7mg/ml and pH increased with neutralising buffer (see Table 2.11) for compatibility with cell culture. 40µl collagen was added to each well of a 96-well black flat-bottom plate, and spheroids transferred on top. An additional 40µl collagen was added to ensure spheroids were fully encapsulated, then incubated at 37°C for at least 5 minutes. Once collagen was polymerised, 100µl GNS medium was carefully added to each well and spheroids maintained under standard culture conditions until required.

2.5 - Formation of Assembloid Co-Cultures

In this context, 'assembloid' refers to the co-culture and engraftment of tumour spheroids with dorsal cortical organoids. Spheroids were formed by passaging lentiviral-transduced patient-derived cell lines (see Section 2.8) and seeding 1 x 10^4 cells in 100µl medium per well of a 96-well round bottom ultra-low attachment plate for 4 days. Concurrently, cortical organoids were cultured as previously described for 16 days post-neural induction. Scissors were used to cut P200 pipette tips and increase bore size, facilitating the transfer of 3D cultures. A single spheroid and organoid were transferred in 50% tumour medium, 50% neural medium to each well of a 96-well round bottom ultra-low attachment plate. Fusion occurred within 24 hours and assembloids were transferred in 500µl neural medium to a 24-well ultra-low attachment plate and maintained in the orbital shaking incubator for a further 6 days. Engraftment and invasion of the eGFP-luciferase-positive tumour cells into the brain organoid was monitored by imaging assembloids using the brightfield and FITC channels of the DMi8 inverted epifluorescence microscope system (Leica Biosystems).

2.6 - Establishment of Primary Cell Lines and Patient-Derived Organoids (PDOs)

Patient tumour samples were acquired by surgical biopsy or resection and kindly supplied for research purposes by the histopathology department of the Children's Hospital at Westmead (CHW). Tumour samples were stored at 4°C in 'transport medium' (DMEM, 10% (v/v) FBS, 1X penicillin/streptomycin, 1X amphotericin B) for no longer than 48 hours following surgery. Tissue was processed on ice in a biosafety cabinet by aspirating transport medium, rinsing twice in ice-cold DPBS, and quickly cutting the sample into pieces approximately 0.5mm in size with scalpels or dissection scissors. Fragments were resuspended into 80% FBS, 20% DMSO solution and stored in cryovials in liquid nitrogen.

Patient information was de-identified and consent to generate cell lines from the stored samples was obtained from patients' families by the Biospecimen Research Services group (formerly CHW Tumour Bank). Research was approved by the SCHN Human Research and Ethics Committee (2024/ETH01165).

Once consent was obtained, samples were thawed into pre-warmed DMEM high-glucose sodium pyruvate, then centrifuged at 300xg for 5 minutes. Tumour fragments were resuspended in culture medium combinations reported across the literature [Table 2.8], transferred to 96-well or 6-well ultra-low attachment plates, and cultured in an Eppendorf Brunswick™ s41i orbital shaking incubator set to 70rpm, 5% CO_2 and 37°C. Tumour recovery and self-organisation was typically observed within 2 weeks, and 3D cultures thereafter termed PDOs. Once PDOs exceeded 500µm in diameter, they were bisected using scalpels for propagation purposes and to limit necrosis. After 4 weeks, representative PDOs were collected, washed with DPBS, and fixed in 4% paraformaldehyde (PFA) for characterisation. Others were snap frozen at -80°C for nucleic acid extraction. Remaining PDOs were cut with scalpels to approximately 250µm diameter, resuspended in 90% medium, 10% DMSO solution, and cryopreserved in liquid nitrogen.

On occasions where abundant tumour tissue was available, concurrent attempts were made to establish 2D adherent cell lines using an optimised workflow [Chew 2023]. Tissue fragments not used for PDO formation were pelleted in a separate 50ml Falcon tube, excess volume of activated papain solution (0.08% (v/v) papain, 0.33mg/ml L-cysteine, 1µM UltraPure™ EDTA pH 8.0, UltraPure™ DNase/RNase-free distilled water) was added and incubated at 37°C for 20 minutes. Following incubation, 10mg/ml DNAse I was added to the tissue fragments and mixed thoroughly by pipetting, then fragments were resuspended in 20ml transport medium and centrifuged at 300xg for 5 minutes. Supernatant was aspirated and fragments resuspended in 5ml of ammonium-chloride-potassium (ACK) for 1 minute to

ensure lysis of red blood cells. Lysis buffer was quenched in 20ml ice-cold Hanks' Balanced Salt Solution (HBSS) and centrifuged at 300xg for 5 minutes at 4°C. Where significant volumes of solid tissue fragments were present following resuspension, enzymatic dissociation steps were repeated until a single-cell suspension could be achieved. Cells were then seeded in recommended culture medium to 96-well plates. Once adherence was confirmed, cells were gradually expanded to cultureware with larger surface area until maintenance could be performed in 25cm^2 flasks. Cell lines were then characterised and STR profiled against the reference tumour sample.

2.7 - Flow Cytometry

Cells were assessed for antigen surface expression by flow cytometry. Cells were enzymatically detached dependent upon cell line protocol, centrifuged at 300xg for 5 minutes, resuspended in culture medium, and counted by haemocytometer. Required cell count was transferred to FACS tubes and spun at 1400rpm for 5 minutes, supernatant discarded, and rinsed with 1X FACS buffer. Cells were centrifuged at 1400rpm for an additional 5 minutes, then resuspended in 100µl FACS buffer. 5µl of either PE-conjugated EphA2 antibody (BioLegend) or PE-conjugated Mouse IgG2b, κ isotype control (BD Biosciences) were added to the cells and vortexed. FACS tubes were covered in foil to protect from light and incubated at 4°C for 20 minutes. Cells were then washed in excess FACS buffer, centrifuged at 1400rpm for 5 minutes, and resuspended in 200µl FACS buffer for analysis.

Samples were processed using a FACS Canto II cytometer (BD Biosciences) and FlowJo software (FlowJo LLC). Samples were gated using forward scatter height (FSC-H) and forward scatter area (FSC-A) to exclude doublets, then side scatter area (SSC-A) and FSC-A to select for live cell populations. Isotype and positive controls allowed for gating of

PE-positive cells using the B530_30E-A fluorochrome detector, against which experimental samples were analysed for antigen expression.

2.8 - Lentiviral Vector (LVV) Transduction of Tumour Cell Lines

A lentiviral vector (LVV) was used to generate stable eGFP-luciferase-expressing GBM and DIPG cell lines. Lentiviral particle generation was performed by transducing a pLentipuro3/TO/V5-GW/EGFP-Firefly Luciferase vector (Addgene), together with psPAX2 packing and pMD2.G envelope vectors, into HEK293T cells. Culture medium was harvested after 48 hours and 72 hours, and virus particles purified and concentrated using a Vivaspin® Centrifugal Concentrator. This work was conducted by Dr Kenneth Hsu and Dr Yuyan Chen (Kids Research, Australia), in accordance with regulations set by the Office of the Gene Technology Regulator (OTGR, Department of Health and Aged Care, Australian Government) and approved by the CMRI and CHW Institutional Biosafety Committee (NL16/14).

Cells were transduced by seeding into 1% (v/v) Matrigel-coated 96-well plates, as previously described, and allowing for adherence overnight. 500µl fresh medium, containing the viral particles at calculated multiplicities of infection (MOI) and 0.5µl polybrene to enhance infection and transduction, was then added for 24 hours. A complete medium change was performed, and cells monitored for health and fluorescence using a DMi8 epifluorescence microscope system (Leica) with a FITC filter. Cells were sorted by eGFP expression by the Westmead Cytometry team (Westmead Institute for Medical Research, Australia), with upper and lower margins of expression excluded. Finally, transduced cells were expanded and biobanked, with STR profiling to ensure concordance with the original untransduced cell lines.

2.9 - Assessment of Tumour Cell Viability

2.9.1 - CellTiter-Glo 3D

Initial experiments assessed viability of tumour cells using CellTiter-Glo® 3D Viability Assay (Promega). Culture medium was removed from spheroids, which were washed once in DBPS before transferring to 96-well black flat-bottom plates. Maximal liquid was removed from the spheroid and replaced with 100µl CellTiter solution. Plates were agitated using the 'medium' orbital shaker function of the SpectraMax® iD3 microplate reader (Molecular Devices) for 5 minutes, then incubated at room temperature for 25 minutes. Luminescent signal was measured by the plate reader in relative light units (RLU).

2.9.2 - Bright-Glo - 2D Culture

Luciferase-expressing tumour cells were transferred to a 96-well black flat-bottom plate (Corning) in 100µl culture medium and incubated overnight to allow adherence. Bright-Glo™ Luciferase Assay System was thawed at room temperature an hour prior to use. 100µl Bright-Glo™ was added to the medium of each well and briefly mixed by pipetting, then incubated at room temperature for 3 minutes to ensure complete cell lysis. The luminescent signal, corresponding to luciferase expression and used as a *de facto* measurement of tumour cell viability, was recorded using the SpectraMax® iD3 microplate reader in RLU.

2.9.3 - Bright-Glo - 3D Culture

Tumour spheroids and assembloid co-cultures were transferred to 24-well black flat-bottom plates (Corning) in 150µl culture medium. Bright-Glo™ was thawed to room temperature, and 150µl added to each well for 1 minute, with brief mixing by pipetting. Due to complications measuring luminescence of 3D cultures by standard luminometers, we instead used the IVIS Lumina X5 preclinical imaging system (PerkinElmer). Photographic and luminescent images were acquired with 1 second exposure times and medium binning

every 30 seconds for 3 minutes. Following acquisition, ROIs of equal area were drawn for each well of the plate using the Living Image software. Luminescent signal within these ROIs was quantified by total flux (photons/second, p/s).

2.10 - CAR-T Cell Generation

The protocol for production of EphA2-directed CAR constructs and transduction to T cells was previously published by Hsu et al [Hsu 2021]. Normal donor buffy coats were obtained under a Material Supply Agreement from Australian Red Cross Lifeblood. Peripheral blood mononuclear cells (PBMCs) were isolated through centrifugation with Lymphoprep™ Density Gradient Medium (StemCell Technologies), and T cells enriched with the EasySep™ Human CD3 Positive Selection Kit (StemCell Technologies). T cells were cultured in CTS™ OpTimizer™ T Cell Expansion supplemented with CTS™ Immune Cell Serum Replacement (Thermo Fisher), 10ng/ml IL-7, and 5ng/ml IL-15. Activation via CD3 and CD28 was performed with T cell TransAct™ (Miltenyi BioTec) 24 hours before transduction with the EphA2 LVV. Transduced cells were then expanded for 8-10 days before cytotoxicity assays. CAR manufacture was conducted by Dr Kenneth Hsu, and T cell culture by Dr Yuyan Chen (Kids Research, Australia).

2.11 - CAR-T Cytotoxicity Assays

2.11.1 - 2D Culture

Efficacy of CAR-T treatment was assessed in 2D cultures using the xCELLigence Real-Time Cell Analysis (RTCA) system (Agilent Technologies). 16-well RTCA E-plates were coated with 1% (v/v) Matrigel, as previously described. Culture medium was added to each well, and E-plates transferred to RTCA analysers in a CO_2 incubator at 37°C. Electrical conductivity was confirmed via gold microelectrodes on the bottom surface of the E-plate wells using RTCA Software Pro. Patient-derived GBM and DIPG cell lines were passaged

and counted, and cells transferred to the E-plate. Real-time recordings were taken for 24 hours during cell adherence and equilibration to establish a baseline for cellular impedance. CAR-T cells were then added to the tumour cells at varying effector:target (E:T) ratios and measurements recorded for several days. Cytolysis was calculated in the software based upon changes to cellular impedance from the baseline values.

2.11.2 - 3D Culture

CAR-T treatment was administered to luciferase-expressing tumour spheroids 4 days post-formation and to assembloid co-cultures 7 days post-engraftment. Due to tumour cell proliferation between initial seeding and CAR-T treatment, E:T ratios were calculated by dissociating a representative number of cultures with Accutase for 10 minutes. Spheroids were dissociated to a single-cell suspension and counted by haemocytometer. Due to the mixed populations within the assembloids, cells were dissociated with accutase and centrifuged at 300xg for 3 minutes. The cell pellet was resuspended in 1ml FACS buffer and cells sorted for eGFP expression by the Westmead Cytometry team. Spheroids and assembloids were transferred to 24-well black flat-bottom plates in 75µl culture medium. CAR-T cells were added at calculated E:T ratios in 75µl T cell medium, and monitored for 72 hours. Cytotoxicity was then assessed by Bright-Glo assay using the IVIS preclinical imaging system.

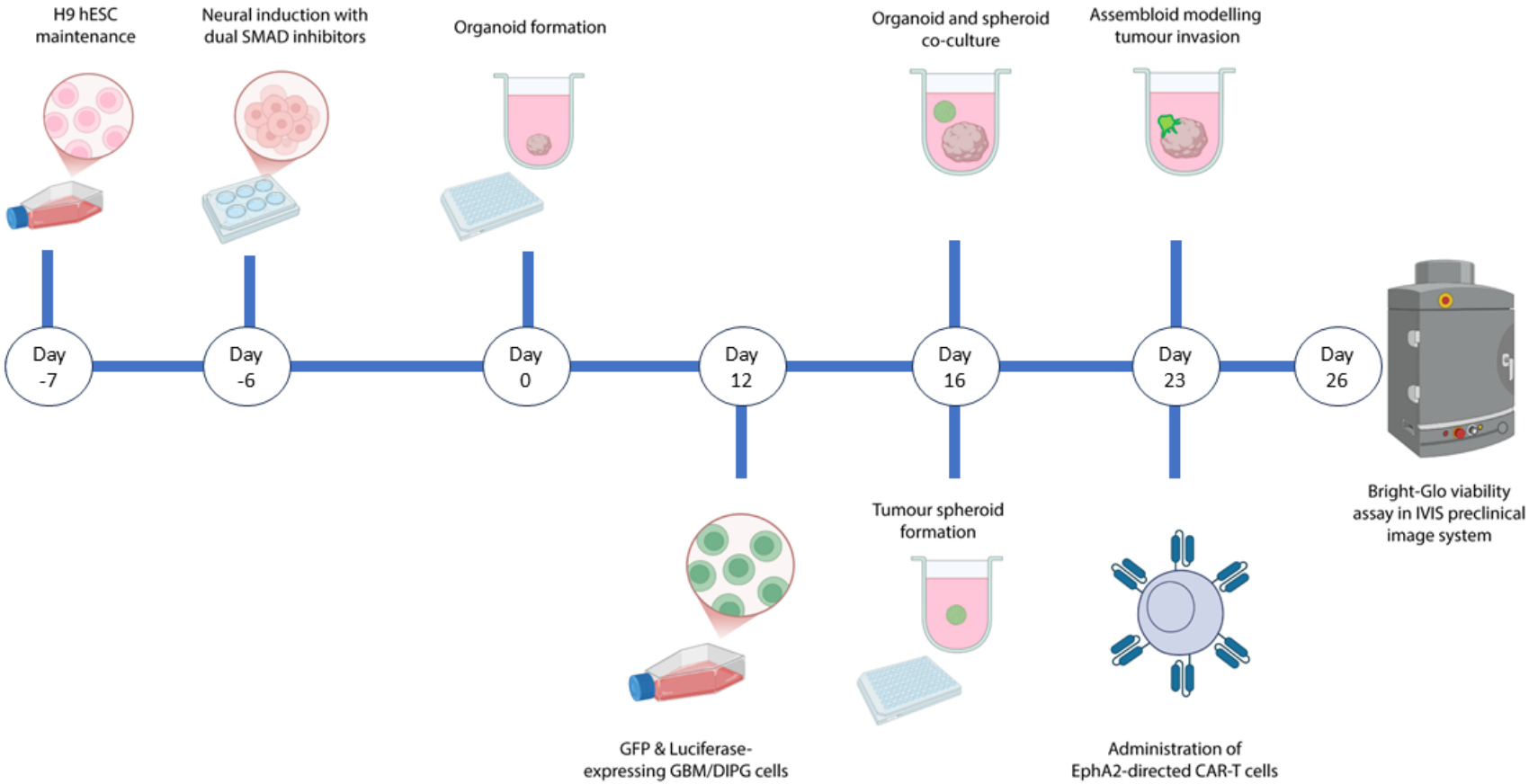

Figure 2.1 - Schematic of assembloid formation and CAR-T treatment. H9 hESCs are plated into laminin-coated wells and undergo neural induction with dual SMAD inhibitors for 7 days. Neural progenitors are harvested and transferred to ultra-low attachment plates, forming cortical organoids. Tumour spheroids are concurrently established from transduced HGG cell lines, then co-cultured with cortical organoids for a further week to ensure engraftment and invasion. Resulting assembloids are treated with CAR-T cells for 72h, then tumour cell viability measured using Bright-Glo assay and the IVIS X5 preclinical imaging system. Figure created in BioRender.

2.12 - Micro-Electrode Array (MEA)

2.12.1 - CytoView Plate Setup and MEA Recordings

Following 5 months of culture, organoids were randomly selected and transferred to CytoView MEA 6-well plates (Axion BioSystems) using a cut P1000 pipette tip. At the centre of each well of the CytoView 6-well plate is a poly(3,4-ethylenedioxythiophene) (PEDOT) electrode grid in an 8 x 8 arrangement, for a total of 64 electrodes per well. Maximal culture medium was removed and organoids carefully positioned on the PEDOT grid to cover as many electrodes as possible. Organoids were embedded in place by pipetting 20µl ice-cold growth factor-reduced Matrigel directly on top and incubating at 37°C for at least 5 minutes to allow for Matrigel polymerisation. 700µl culture medium could then be added without organoid displacement occurring.

MEA recordings were performed every 3-4 days using the Maestro Pro MEA system (Axion BioSystems). Culture medium was refreshed 24 hours prior to recording. Organoids were allowed to equilibrate in the Maestro Pro at 37°C, 5% CO_2 for at least 10 minutes. Raw data was then acquired with the Neural Spontaneous & Viability Real-Time module of the AxIS Navigator software version 3.7.3, at a sampling rate of 12.5kHz for 10 minutes. Subsequent identification of spike events was performed using a Butterworth filter of 200Hz to 3kHz and an adaptive threshold of ±6 standard deviations from the median background voltage to limit the inclusion of false positives. Individual electrodes were considered 'active' when more than 5 spike events were detected per minute across the duration of the recording. Bursting events were defined as a minimum of 5 spikes with a maximum inter-spike interval (ISI) of 100ms. Network bursts were defined as a minimum of 50 spikes with a maximum ISI of 100ms across at least 35% participating electrodes. Analysis of synchronous activity was calculated using a synchrony window of 20ms between events, using the Synchrony Index

measure [Paiva 2010]. All calculations were performed by the Neural Statistics Compiler within the AxIS Navigator software and compiled into a Comma-Separated Values (.csv) file. MEA recordings were performed until around day 180, after which organoids were rinsed from the plates, washed in DPBS, and snap-frozen on dry ice.

Table 2.12 - Electrophysiological Parameters

Parameter	Calculation
Spike Count	Total number of action potentials detected in a well over the duration of analysis.
Mean Firing Rate	Total number of spikes detected across all electrodes in a well divided by the duration of analysis, in Hz.
Number of Active Electrodes	Number of electrodes within a well detecting an average ≥5 spike events per minute over the duration of analysis.
Burst Count	Total number of bursts (≥5 spikes with maximum ISI of 100ms) across all electrodes over duration of analysis.
Burst Frequency	Total number of bursts detected across all electrodes in a well divided by the duration of analysis, in Hz.
Average Burst Duration	Mean of all electrode median burst durations in a well, in seconds.
ISI Coefficient of Variation	The coefficient of variation (standard deviation divided by mean) of the inter-spike interval (ISI; time between spikes) across active electrodes (≥5 spikes/minute).
Network ISI Coefficient of Variation	The coefficient of variation (standard deviation divided by mean) of the ISI for all recorded spikes in a well.
IBI Coefficient of Variation	The coefficient of variation (standard deviation divided by mean) of the inter-burst interval (IBI; time between bursts) across active electrodes (≥5 spikes/minute).
Network IBI Coefficient of Variation	The coefficient of variation (standard deviation divided by mean) of the IBI for all recorded bursts in a well.
Synchrony Index	A unitless measure of synchrony between spikes, ranging from 0 (asynchronous) to 1 (perfect synchrony).

2.12.2 - MEA Data Analysis

For analytical purposes, recordings of organoids with fewer than 5 spontaneous spike events detected per minute (i.e. <50 spikes/10 minutes) were considered electrically 'inactive', while those organoids with greater activity were reported as 'active'. Recordings of active organoids were assessed for spike count, mean firing rate, number of active electrodes, burst count, burst frequency, average burst duration, ISI coefficient of variation, network ISI coefficient of variation, inter-burst interval (IBI) coefficient of variation, network IBI coefficient of variation, and synchrony index, as defined in Table 2.12. Raster plots were generated using AxIS Metric Plotting Tool v2.5.0 for visualisation of electrode activity over the duration of recordings. Data was extracted from .csv files and plotted in GraphPad Prism software version 10.2.1. Statistical outliers were removed from the data set using the ROUT (Q = 1%) test. Mean values of each treatment group were compared against the expected mean values of untreated controls using an unpaired Student's t test. Statistical significance was determined with p-values ≤0.05.

2.12.3 - Cleaning of CytoView MEA Plates

CytoView MEA plates were re-used between technical replicates due to high consumable costs. As such, a protocol for cleaning the plates was followed to remove traces of organoids, Matrigel, culture medium and other debris. Organoids were removed by shear force pipetting, then culture medium was aspirated and wells rinsed twice with DPBS. Matrigel was digested using 0.05% Trypsin-EDTA incubated at 37°C for at least 30 minutes until no further residue was observed. Further washes were performed in triplicate with DPBS, 70% ethanol, and MilliQ water. Lastly, wells were coated in 0.1% (w/v) bovine serum albumin (BSA) for 30 minutes, then rinsed with MilliQ water three times, to provide a mild hydrophobic charge and facilitate embedding of organoids with Matrigel as described above.

2.13 - MEA Neurotoxicity Screen

Cortical organoids were generated by the described protocols and maintained until day 31, with any organoids exhibiting aberrant morphology removed. Organoids were randomly selected into experimental groups and treated with 50mM 200-proof pure ethyl alcohol (Sigma-Aldrich), 10µM acrylamide (Sigma-Aldrich), 10µM lorlatinib, 1µM lorlatinib (Selleckchem), 10µM gefitinib (Cell Signaling Technologies), or 10µM ibuprofen (Sigma-Aldrich). Culture medium was freshly supplemented with treatment compounds and full medium changes performed every 2-3 days throughout the experiment. At day 150, organoids were transferred in triplicate to CytoView plates, and electrophysiology recordings taken every 3-4 days until day 180. Organoids were then detached from the plates and snap-frozen for protein extraction and subsequent Western blotting. Organoids which were not selected for MEA recordings were maintained in ultra-low attachment plates for the remainder of the experiment, then incubated in 4% (w/v) PFA with agitation at 4°C overnight to allow for sufficient fixation. PFA was aspirated, organoids were washed three times in DPBS, then incubated in 20% (w/v) sucrose at 4°C overnight. Sucrose was removed and organoids transferred to Optimal Cutting Temperature (OCT) solution in Tissue-Tek cryomoulds (Sakura Finetek). Cryomoulds were stored at -80°C until required.

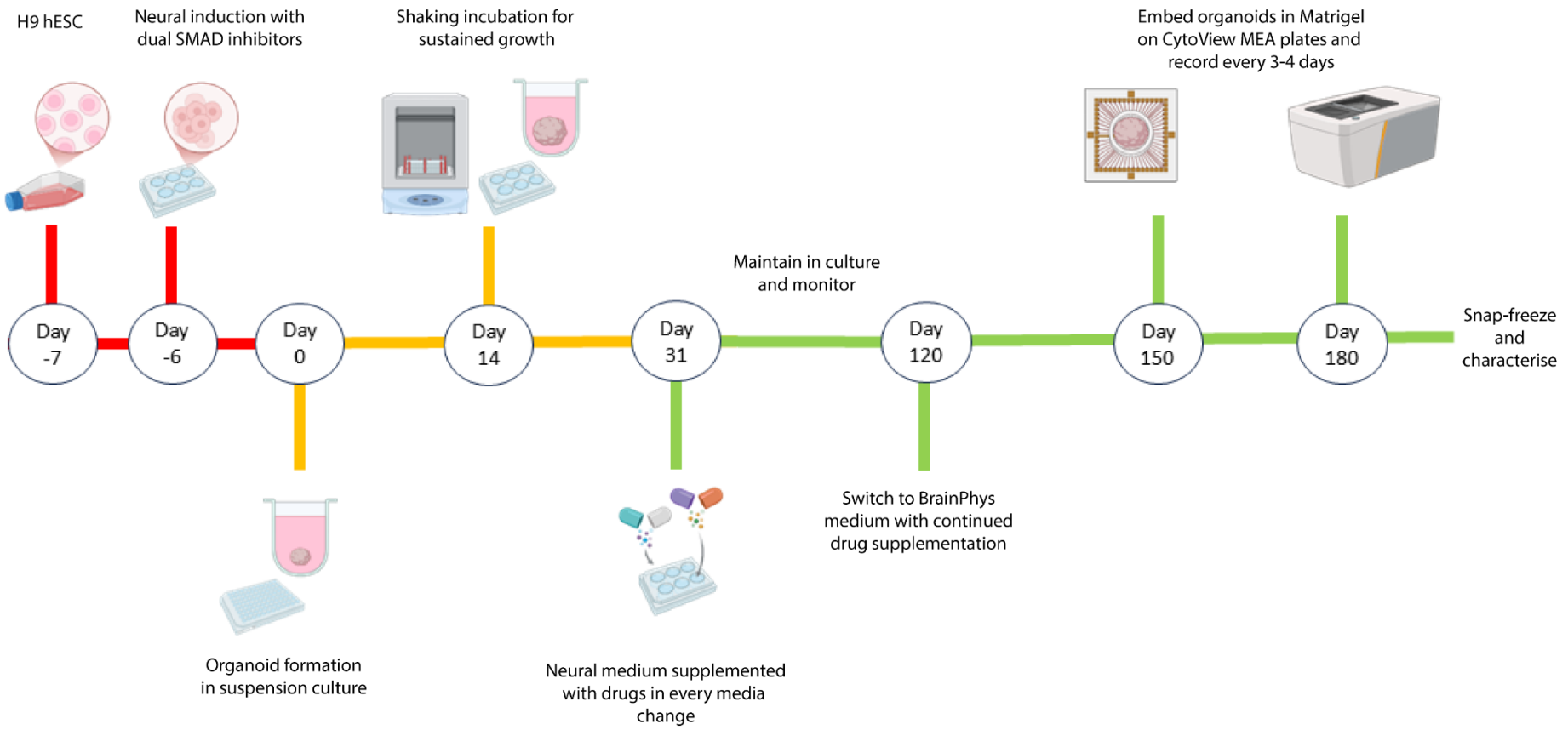

Figure 2.2 - Schematic of organoid neurotoxicity screen. Dorsal cortical organoids are generated by subjecting H9 hESCs to neural induction by dual SMAD inhibition (red). Organoids are maintained in ultra-low attachment plates in neural medium + EGF + bFGF for one month, during which plates are transferred to shaking incubator to limit hypoxia and necrosis. From Day 31 onwards, screened drugs are added to neural medium with every media change. At Day 120, neural medium is substituted with complete BrainPhys for further neuronal differentiation. Organoids are embedded in Matrigel onto the electrode array at Day 150, and MEA recordings performed every 3-4 days until Day 180. Figure created in BioRender.

2.14 - Cryosectioning Organoids

OCT blocks were cryosectioned using the CryoStar NX70 cryostat (Epredia). Cryostat chamber and blade temperatures were set to -15°C and adjusted if required during sectioning. Blocks were affixed to round 'chucks' using minimal volumes of room temperature OCT, allowed to reach chamber temperature, and placed upon the cryostat block head. When working with brain organoid tissue, section thickness was set to 16µm and cut sections gently applied to SuperFrost UltraPlus GOLD Adhesion slides (Epredia). Slides were kept at room temperature overnight and then stored long-term at -20°C.

2.15 - Immunofluorescence

Immunofluorescent staining was performed in a humidified slide chamber covered in foil to ensure slides were protected from light. Slides were thawed to room temperature, then marked with hydrophobic Advanced PAP pen (Sigma-Aldrich) to contain liquid to the section area and minimise waste. Sections were permeabilised with 0.3% (v/v) Triton 100-X for 10 minutes, then rinsed three times in 1X PBS. 10% (v/v) donkey serum was applied as blocking buffer for 1-2 hours, followed by three washes with PBS. Sections were incubated in primary antibody diluted to recommended concentrations in blocking buffer overnight at 4°C. Primary antibody was aspirated, sections rinsed three times with 0.05% Triton (v/v) in PBS (PBS-T), and secondary antibody applied at 1:500 for one hour. Secondary antibody was washed from slides with PBS-T, and tertiary staining applied with DAPI (4′,6-diamidino-2-phenylindole) for 30 minutes for nuclear localisation. Final washes with PBS-T and distilled water were performed in triplicate. 24x50mm glass coverslips (Dako) were applied to slides using Fluoromount aqueous mounting medium (Sigma-Aldrich) and allowed to dry overnight at room temperature protected from light**.** Slides were then stored at -20°C until required.

Imaging was performed using the Stellaris 5 confocal microscope system (Leica) and LAS X software. Objectives used for this project are detailed in Table 2.5. Excitation and emission parameters of the detectors were adjusted according to the Dye Assistant recommendations in order to limit cross-yield between fluorophore combinations. Image resolution was typically set to 2048x2048px and line average to 3 to reduce noise and image artefacts during acquisition. In order to image large structures, including whole organoids, the LAS X Navigator feature was utilised. ROIs were drawn around the perimeters of organoids and divided into tiles, which were stitched together automatically or using the Mosaic Merge function following acquisition. Project files containing all images and metadata were saved as .lif (Leica Image File) format. Acquired images were prepared for figure presentation in the FIJI distribution of ImageJ. Images were separated using the Split Channel option, and brightness and contrast histograms adjusted for clarity. Individual channels and merged composite images were then exported to .tiff format.

2.16 - Western Blotting

2.16.1 - Protein Extraction and Quantification

Fresh and snap-frozen organoids were dissociated to single-cell suspension by aspirating culture medium, rinsing twice with PBS, and resuspending in 300µl lysis buffer comprising 1% (w/v) sodium dodecyl sulphate (SDS), 8M urea, 100mM Tris-HCl (pH 8.0), supplemented with cOmplete mini protease inhibitor cocktail (Roche), 0.5M sodium fluoride (NaF), 100mM phenylmethylsulfonyl fluoride (PMSF), 100mM dithiothreitol (DTT), and 10mM sodium orthovanadate (Na_3VO_4). A single stainless-steel bead was added to each tube, which was then transferred to the TissueLyserII (QIAGEN). Tubes were run at 20Hz for 2 minutes to facilitate organoid dissociation. Beads were removed, solution briefly spun down, and supernatant collected into a 1.5ml Eppendorf tube on ice. The supernatant was sonicated

with a S-250A probe sonicator (Branson Ultrasonics) until fully homogenised, then centrifuged at 13000 rpm at 4°C for 20 minutes. Protein concentration from the lysates was measured against Pierce™ Bovine Serum Albumin Standards using Pierce™ BCA protein assay kit (Thermo Fisher). Prepared samples were incubated at 37°C for 30 minutes, then absorbance measured by the SpectraMax iD3 plate reader. Lysates were then stored at -80°C until required.

2.16.2 - Gel Electrophoresis, Transfer, and Imaging

Lysates were thawed on ice and mixed with 1X SDS-PAGE sample buffer (50% (v/v) glycerol, 250mM Tris (pH 6.8), 25% (v/v) beta-mercaptoethanol, 10% (w/v) SDS, 0.05% (v/v) bromophenol blue), then heated at 95°C for 5 minutes in a dry heating block. 20µg protein was loaded into wells of NuPAGE™ Bis-Tris 4-12% Mini Protein Gels (Invitrogen), with 10µl Novex™ Sharp Pre-Stained Protein Standards (Invitrogen) used as a reference ladder. Gels were immersed in 1X NuPAGE™ MES/SDS running buffer (Invitrogen) and electrophoresis run at 80V for 20 minutes, then 110-140V for 1-2 hours to allow for sufficient protein band separation. Gels were cut from the cartridge using a razor blade and placed onto Immobilon®-P PVDF membranes (Millipore) in cassettes between 4 layers of filter paper. Cassettes were immersed in tanks containing ice-cold 1X transfer buffer (2.5mM Tris, 200mM glycine, 20% (v/v) methanol, 0.005% (w/v) SDS in MilliQ water) and transfer run at 80V for 2 hours. Membranes were washed in methanol, dried for 15 minutes, re-hydrated in MilliQ water, and stained with Ponceau for band visualisation.

Following further washes in MilliQ water and 1X TBS to remove Ponceau staining, membranes were incubated for 30 minutes in blocking solution (5% (w/v) non-fat milk in 1X TBS-T). Blocking solution was rinsed off with 1X TBS-T in triplicate, then primary antibodies added and incubated at 4°C overnight with agitation. Primary antibodies were

removed and rinsed three times with 1X TBS-T, then horseradish peroxidase-conjugated secondary antibodies applied at room temperature for 1 hour. Following final washes with 1X TBS-T and TBS, SuperSignal™ West Pico PLUS chemiluminescent substrate (Thermo Fisher), comprising luminol and peroxide reagents, was added to the membranes at 1:1 ratio for 5 minutes.

Western blot imaging was conducted using the Odyssey® Fc imaging system (Li-Cor Biosciences). Total protein was visualised using the 700nm channel with 10-minute exposure, and the ladder visualised by exposing with the chemiluminescent channel for a further 2 minutes. Protein quantification was performed by comparing densitometry of bands against corresponding GAPDH loading controls with Image Studio software v6.0 (Li-Cor Biosciences).

2.17 - DNA Extraction

Tumour cells were passaged according to aforementioned protocols and pelleted by centrifugation. Medium was discarded, cells rinsed in DPBS, then centrifuged an additional time. Supernatant was removed and cell pellet snap-frozen on dry ice, then stored at -80°C until required. Cell pellet was thawed on ice and resuspended in 200µl PBS, then DNA extracted with QIAamp DNA Mini Kit (QIAGEN) according to manufacturer instructions. DNA was eluted in TE buffer and concentration quantified using Qubit 2.0 fluorometer (Invitrogen) against Qubit kit standards**.** Samples were stored at -20°C until required.

In PDOs and tumour tissue, nucleic acid extraction was performed using AllPrep® DNA/RNA Mini Kit (QIAGEN). DNA was eluted in TE buffer and RNA into nuclease-free water. PDO circulating tumour DNA (ctDNA) was acquired by collecting half of the culture medium during scheduled media changes. Debris was removed by centrifugation at 1500xg for 3 minutes, followed by centrifugation at 3000xg for 3 minutes. ctDNA was isolated using

the QIAamp Circulating Nucleic Acid Kit (QIAGEN) and eluted into AVE buffer according to manufacturer instructions. Quantification was performed using the Qubit 2.0 fluorometer and samples stored at -20°C until ddPCR analysis.

2.18 - Analysis of Tumour Mutational Profiles

2.18.1 - Probe and Primer Design

CHW clinical reports highlighted somatic mutations in two pGBM patients from whose tumour samples cell lines and PDOs were derived. The *TERT* mutation had no associated commercial assays available. Probe and primer design was performed with assistance by Dr Smadar Kahana-Edwin (Kids Research, Australia) with modifications suggested by Integrated DNA Technologies (Iowa, USA) and checked for regional similarity using BLAST (NCBI, USA). Commercial assays from Bio-Rad were used for the clinically reported *POLE* and *PTPN11* mutations, and for the *H3F3A* mutation for validation purposes. Probes and primers used for this thesis are detailed in Table 2.10.

2.18.2 - Polymerase Chain Reaction (PCR)

Agarose I powder (Amresco) was added to 1X TAE buffer in a flask and heated in 30 second intervals in a microwave until fully dissolved. The agarose solution was allowed to cool, then 1:10000 GelRed (Millipore) was added for fluorescent DNA staining. The 2% (w/v) agarose gel was poured into a mould, protected from light with foil, and allowed to set for 30 minutes. Due to unavailability of cell lines with the specific mutations of interest, gBlock DNA fragments were designed and supplied by Integrated DNA Technologies [Table 2.9] for use as controls. A master mix comprising primers, DNA polymerase, and dNTPs was made, and 50ng DNA per sample added. PCR was run for 40 cycles in a MiniAmp™ thermal cycler (Applied Biosystems), then 15µl product and 5µl DNA loading dye transferred to each well of the agarose gel. Quick-Load® 100bp DNA Ladder (NewEngland Biolabs, USA) was

run in a separate well for reference bands. Gel was immersed in 1X TAE buffer and electrophoresis performed at 120V for 40 minutes. Separated bands were visualised using the ChemiDoc imaging system (Bio-Rad).

2.18.3 - Droplet Digital Polymerase Chain Reaction (ddPCR)

Patient samples yielded lower concentrations of DNA than standard cell lines or gBlock controls, necessitating ddPCR methods for detection. Sample DNA was added to a master mix, comprising 1X ddPCR Supermix for Probes (No dUTP), 1X forward and reverse primers, 1X wild-type and mutant probes, and 2-5 units restriction enzyme, and made up to 22µl total with nuclease-free water. 20µl master mix and 70µl QX200 Droplet Generation Oil (Bio-Rad) were added to an eight-channel DG8 cartridge, and combined to form droplets with the QX200 Droplet Generator (Bio-Rad). 40µl droplets were transferred to a 96-well LoBind PCR plate (Eppendorf), which was then sealed with foil using the PX1 Plate Sealer to prevent droplet evaporation. PCR reaction was performed in the MiniAmp™ thermal cycler with programmed cycles, as outlined in Table 2.10. Once PCR was completed, fluorescent-tagged droplets were measured by the QX200 Droplet Reader (Bio-Rad) and data generated as a .qlp file. Data was analysed using QX Manager Software version 2.1 SE.

Table 2.13 - ddPCR Cycling Steps

Cycling Step	Temperature, ^{O}C	Time	Ramp Rate	Number of Cycles
Enzyme activation	95	10 min		1
Denaturation	94	30 sec	$2^{O}C$/sec	40
Annealing / extension	55	1 min		
Enzyme deactivation	98	10 min		1
Hold	4	Infinite	$1^{O}C$/sec	1

Functional assessment of kinase inhibitor neurotoxicity in cortical organoids

3

3.1 - Chapter Introduction

Kinases have widespread involvement in the key signalling pathways associated with tumourigenesis and cancer progression, but are also important in normal development and cellular functioning [Paul & Mukhopadhyay 2004, Cicenas 2018]. Kinase inhibitors are increasingly being approved for the management of various cancer types, particularly NSCLC and haematological malignancies [Kannaiyan & Mahadevan 2019], and additional indications are being sought in childhood cancers [Bellantoni & Wagner 2021]. Evidence from the clinic suggests that sustained kinase inhibition can prolong progression-free survival in some children with brain tumours, however the long-term systemic and neurological impacts remain unclear, and the key role of these enzymes in normal cellular function suggests that off-target effect effects are highly likely [Kilburn 2024, Manoharan 2023, Sheikh 2024].

Acute symptoms of neurotoxicity occur within a few days and generally resolve upon treatment completion. Unpredictable long-term sequelae do not present until months or years later, with wide-ranging impairments to cognition, socialisation, memory, and sleep function that more profoundly impact the quality-of-life of paediatric cancer survivors [Janelsins 2011,

Mounier 2020]. The pathophysiological mechanisms responsible are challenging to investigate with conventional preclinical models, such as neuronal cultures and animal models, due to their inadequate representation of the human brain.

Over the past decade, stem cell-derived cerebral organoids have gained prominence as a complex *in vitro* model resembling foetal brain tissue. hESCs or iPSCs are induced to differentiate into diverse neuronal and glial populations which self-organise into 3D brain-like structures, some of which are absent in animal models [Lancaster 2013, Qian 2019]. The presence of neural circuitry enables functional screening of organoids in response to acute neurotoxin exposure or drug administration. These assessments are mostly performed by micro-electrode array (MEA) systems which can continuously record electrical activity at a high spatiotemporal resolution [Trujillo 2019, Choi 2021].

The purpose of the research presented in this chapter was to further develop a dorsal cortical organoid protocol to exhibit spontaneous electrical activity detectable by MEA, then implement this model as a platform for a pilot test evaluating neurotoxicity of long-term kinase inhibitor use. Two exemplar tyrosine kinase inhibitors (TKIs) were analysed; the ALK inhibitor lorlatinib and EGFR inhibitor gefitinib.

Gefitinib (Iressa®) is a first-generation EGFR inhibitor which was initially approved for the treatment of advanced and metastatic NSCLC with specific *EGFR* mutations [Kazandjian 2016]. Gefitinib was subsequently evaluated at clinical trial for other *EGFR*-altered cancers, including HGGs, however no significant improvements to progression-free survival were noted due to poor brain penetrance and p-Gp-mediated efflux [Pollack 2011b]. Despite these limitations, gefitinib was included in this drug screen due to substantial clinical evidence indicating low neurotoxicity, making it a suitable reference for assessing CNS-focused safety profiling in organoid models. Clinical studies of NSCLC patients with brain

metastases reported neurotoxicity occurring in only 10% of cases. These side-effects were generally mild, including fatigue and insomnia, and were resolved by decreasing dose or upon cessation of treatment [Mok 2009, Hoe 2023]. The acceptable safety profile of gefitinib is supported by *in vitro* organoid models. Choe et al. showed that 10μM gefitinib selectively targeted tumour cells in a metastatic NSCLC assembloid model, and did not induce apoptosis in whole-brain cerebral organoids [Choe 2020].

Lorlatinib (Lorbrena®) is a third-generation ALK/ROS1 inhibitor for the treatment of ALK-positive NSCLC. Lorlatinib is designed to be more brain-penetrant than previous ALK TKIs, reducing the tight junctions between endothelial cells in the blood-brain barrier, and being less susceptible to efflux [Chen W 2020]. This increased brain penetrance is accompanied by CNS-specific toxicities, which have been consistently reported across multiple clinical trials for metastatic NSCLC. Neurotoxicity occurred in 35-39% of adult trial participants, with impairments to mood, working memory, attention, organisation, and speech, which generally resolved shortly after treatment [Shaw 2017, Bauer 2019, Solomon 2023, Liao 2023, Priantti 2024]. Shaw et al. noted that the median onset of these adverse events was between 6 to 7 weeks following commencement of treatment, though the range extended up to 452 days [Shaw 2017]. Preclinical experiments suggested that some of these side effects may be the result of disruption to ALK-mediated internalisation and regulation of dopamine D2 receptor (D2R), located in regions of the brain responsible for cognition, motor function, and motivation [Dutton 2017, He D & Lasek 2020]. Another *in vitro* study into the mechanisms of lorlatinib observed dose-dependent toxicity against neuron-like SY5Y cells [Chen W 2020].

These drugs were compared against known neurotoxins acrylamide and ethanol [Bu 2020, Lauvås 2022, Zhu 2017, Arzua 2020], as well as ibuprofen, which is indicated to have

neuroprotective properties [Iwata 2008, Medonça 2019], to assess their potential to disrupt brain organoid development and alter electrophysiology.

3.2 - Results

3.2.1 - Neural induction by dual SMAD inhibition generates dorsal cortical organoids

Guided protocols allow for the directed differentiation of region-specific organoids. Our department previously adopted a guided protocol for culturing dorsal forebrain cortical organoids which recapitulate early neocortical development [Mattei 2018, Prior 2022, Prior 2024]. To confirm cortical fate and experimental reproducibility, organoids were characterised after one month for neural progenitor and dorsal marker expression.

A defining feature of cortical organoids is the radial arrangement and apical polarisation of neural progenitor cells into rosette formations, resembling the neural tube from which brain and spinal cord are derived *in utero* [Knight 2018, Heide 2018]. Rosettes were observed by bright-field and phase-contrast imaging in the early stages of neural induction, increasing in size with organoid culture duration [Figure 3.1]. Immunofluorescent staining showed these regions resembled ventricular zones of developing brain, with the presence of radial glial cells exhibiting elongated nuclei and expression of SOX2, PAX6, and vimentin [Figure 3.2] [Noctor 2002, Lancaster 2013]. These progenitor cells are highly proliferative, as indicated by Ki67 staining, and give rise to Tbr2-expressing intermediate progenitors, as well as immature neurons which migrate from the ventricular zone to basal regions to form the cortical preplate [Figure 3.2B] [Li R 2017, Qian 2020]. Immature neurons are abundant throughout the organoid, expressing β-tubulin III and the dendritic marker MAP2, both of which regulate neuronal proliferation and differentiation into more mature populations [Figure 3.2B] [Korzhevskii 2012]. Overall, these findings confirmed that this

guided neural induction protocol [Mattei 2018] generated dorsal cortical organoids modelling corticogenesis.

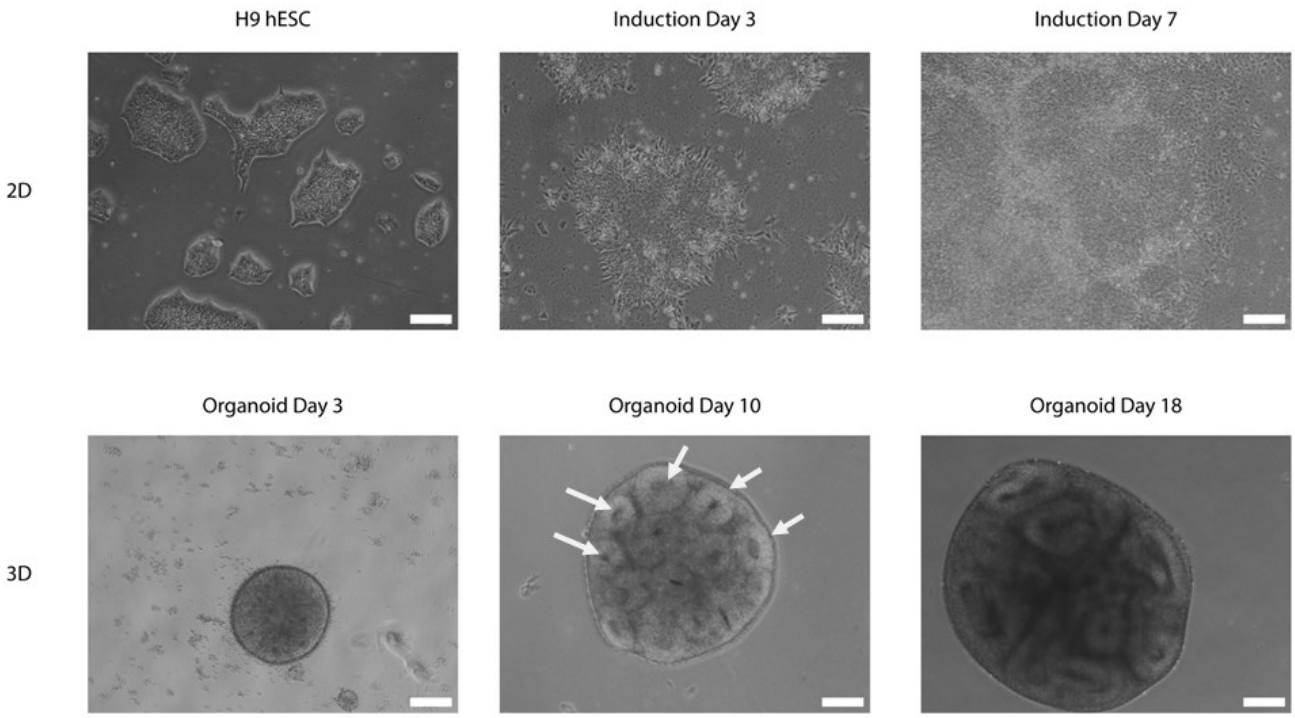

Figure 3.1 - Differentiation of H9 hESCs into dorsal cortical organoids.

Series of phase-contrast images showing stages of the neural induction protocol for generating dorsal cortical organoids. **2D.** H9 hESCs are cultured on vitronectin-coated flasks, forming phase-bright colonies. Cells are passaged onto laminin-coated plates and induced to neural fate with dual SMAD inhibitors. At Day 3, colonies expand in size and show signs of differentiation, with increased density and distinct individual cells at the periphery. Upon Day 7, layers of ectodermal-fated cells are ready to be harvested for suspension culture. **3D.** Neural progenitor cells aggregate into spheres under ultra-low attachment conditions. Several characteristic rosettes (highlighted by arrows) rapidly arrange within each organoid, and become visibly apparent by Day 10 as the organoid increases in size. Scale bars = 50μm.

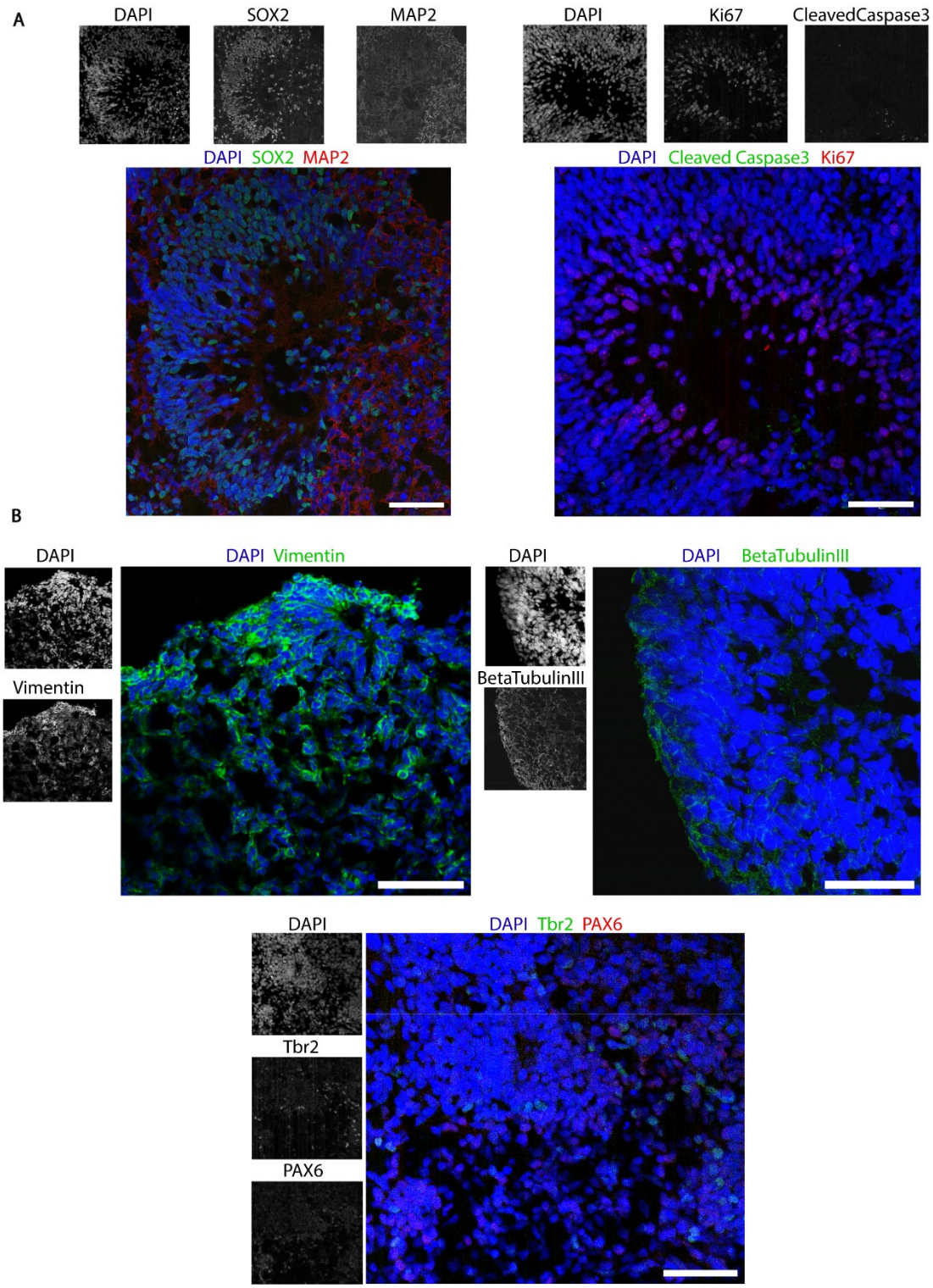

Figure 3.2 - Immunofluorescent images of cortical organoids highlight self-organisation and neural differentiation. A. Representative images of rosettes stained for radial glial progenitor cells (SOX2, green) and surrounding neuronal dendrites (MAP2, red). These areas are highly proliferative, as indicated by Ki67 (red). **B**. Differentiation gives rise to ventricular-zone progenitors (PAX6, Vimentin), intermediate progenitors (Tbr2), and immature neurons (β-Tubulin III) which migrate outwards from neural rosettes. Scale bars = 50μm.

3.2.2 - Mature cortical organoids exhibit spontaneous synchronised electrical activity

Before testing the effects of the kinase inhibitors on organoid function, it was necessary to first establish an assay for measuring their electrical activity. Since the development of electrical activity indicative of neural function requires aged organoids [Trujillo 2019], we tested extended culture to 3 months in neural medium, followed by an additional month in supplemented BrainPhys™ medium, as this has been reported to further drive neuronal differentiation to a physiologically representative state [Bardy 2015]. Organoids increased in size over time, with some finally exceeding 3mm diameter. Once culture duration reached 4 months total, organoids were plated in triplicate onto CytoView plates and assessed using the Maestro Pro MEA system, as described in Chapter 2.12 [Figure 3.3A].

Initial recordings of electrophysiology were performed for 5 minutes, after which data was exported and parameters selected for analysis [Table 2.12]. All organoids were considered electrically active using the default definition of ≥ 5 action potentials, or spikes, detected per minute. In addition, we also observed transient bursts in two organoids, whereby extended spiking activity with <100ms inter-spike intervals (ISI) was detected by a single electrode, followed by periods of relative quiescence. Bursting firing patterns are important in information processing and transmission, and the induction of neuronal plasticity [Shao 2021, Xie 2024].

Following confirmation that the aged organoids were electrophysiologically active, we then sought to determine the optimal culture length in BrainPhys™ medium and time points for MEA recordings. Mean firing rate (total spikes divided by recording duration) increased at day 137, regardless of media conditions [Figure 3.3B]. This was accompanied by the onset of synchronised activity, as demonstrated by repeated detection of spikes across

multiple electrodes simultaneously [Figure 3.3C] and an increase to the unitless synchrony index, suggesting the development of neural networks with functional synaptic connections. Additional MEA recordings were postponed due to COVID-19 isolation protocols, and resumed at day 175, upon which 1/3 organoids showed spontaneous activity, and both mean firing rate and synchrony index were diminished. Based upon these results, the neurotoxicity pilot test was designed to include multiple MEA recordings between day 150 and day 180, as detailed [Chapter 2.13] with the intent of capturing the likely period of peak activity. In line with other studies, we also extended the duration of recordings from 5 to 10 minutes.

While undertaking these experiments, variation in organoid size was noted. It was considered that larger organoids could obstruct detection of action potentials by the electrode array and thus skew the readings. To test this possibility, bright-field images were acquired of organoids embedded on CytoView plates at day 137 (n = 6), then surface area and maximal diameter calculated using ImageJ. When these values were normalised, no significant correlation was observed between measurements of organoid size and mean firing rate [Figure 3.4], confirming that organoid size did not affect the readings.

Pharmacological validation was independently conducted to exclude the possibility that MEA data resulted from background or instrument noise. Baseline electrical activity was measured in 5-month-old organoids (n = 6), then changes recorded following acute treatment with neurotransmitter antagonists that target the ionotropic receptors of neurons to inhibit electrical transmission. α-Amino-3-hydroxy-5-methyl-4-isoxazolepropionic acid (AMPA) and NMDA receptors facilitate excitatory signalling via binding to the neurotransmitter glutamate, which opens the intrinsic ion channel, leading to an influx of depolarising Na^{2+} ions into the neuron and promoting the firing of action potentials [Rao & Finkbeiner 2007]. Acute exposure of organoids to AMPA receptor antagonist cyanquixaline (CNQX) significantly reduced mean firing rate and eliminated bursting patterns. Similar effects were

observed following drug washout and exposure to the NMDA receptor antagonist D-2-amino-5-phosphonopentanoate (D-AP5), therefore showing the presence of functional excitatory receptors in the cortical organoids [Figure 3.5]. In contrast, $GABA_A$ receptors bind the inhibitory neurotransmitter GABA, allowing an influx of Cl^- ions which suppress neuronal excitability [Zhu S 2022]. Subsequent inhibition of $GABA_A$ receptors by bicuculline restored electrical activity, exceeding baseline values [Figure 3.5]. Thus, electrophysiology results were validated and indicated both excitatory and inhibitory neuronal signalling.

An alternative cortical organoid protocol was also explored, as detailed in Chapter 2.2.5, which sought to increase differentiation and reproducibility [Pașca S 2018]. However, no electrical activity was detected in that model, and so it was resolved to continue using the original methodology.

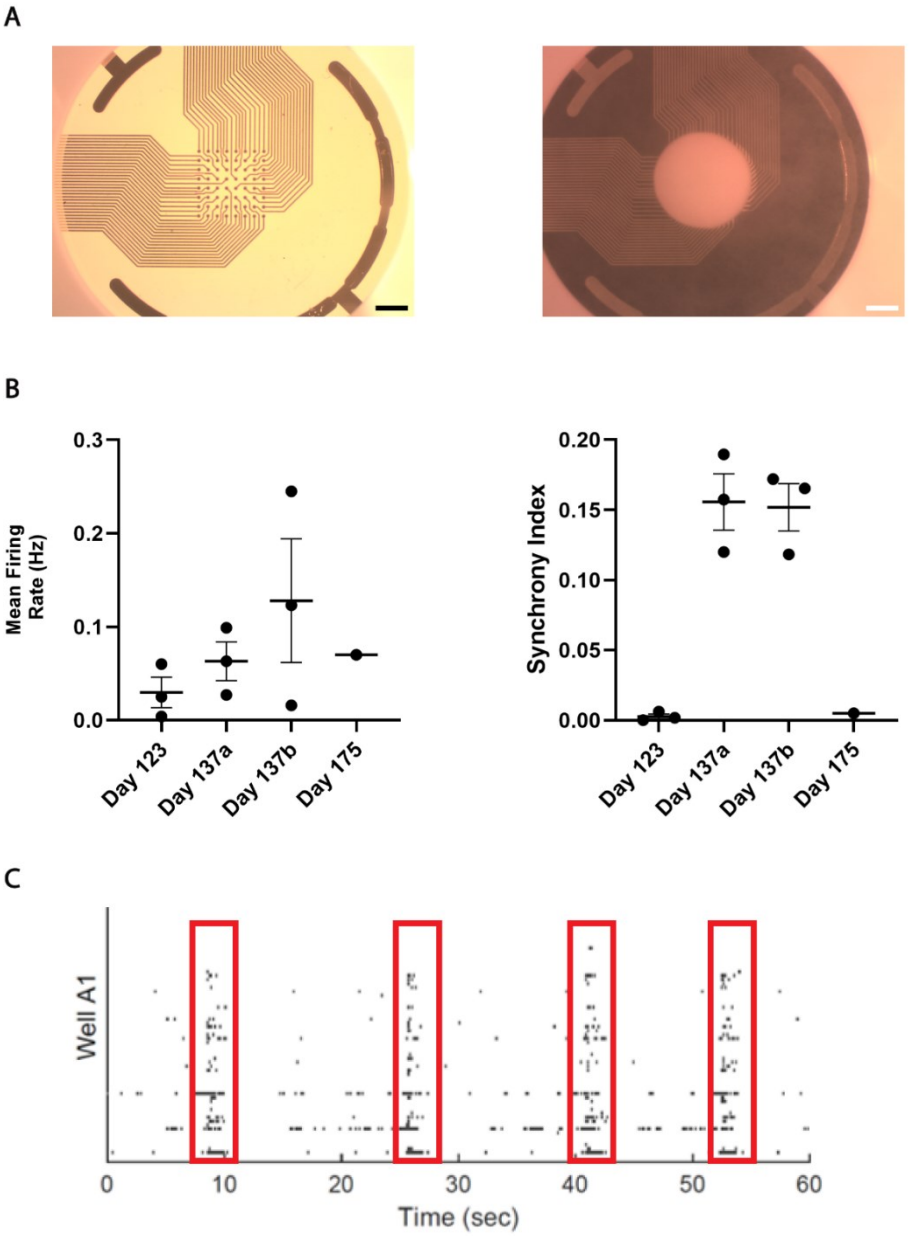

Figure 3.3 - Cortical organoids exhibit electrophysiology detectable by MEA.

A. Images showing the 8x8 PEDOT electrode array from a 6-well CytoView MEA plate. A representative organoid is embedded in place over the array at day 150. Scale bars = 1mm. **B.** Mean firing rates and synchrony index of organoids (n = 3) recorded at days 123, 137 (a = 3 months in neural medium and 6 weeks in BrainPhys; b = 4 months in neural medium and 2 weeks in BrainPhys), and 175. Higher mean firing rate means more spikes detected during recording, and increased synchrony index values refers to more synchronised activity. No statistical comparisons performed due to limited replicates. **C.** A raster plot visualising all spikes detected in a single organoid in 60 seconds. The 64 electrodes within the array are oriented along the y-axis. Spikes are represented by dots, and neuronal bursts by horizontal dashes. The red outlines highlight synchronised activity, where spikes and bursts are detected by multiple electrodes at the same time point. The pattern is repeated multiple times within the recording, indicating communication across a neural network.

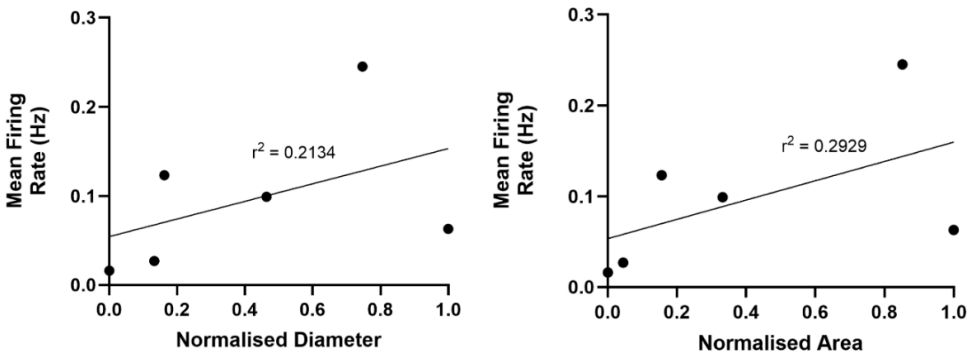

Figure 3.4 - Organoid size has minimal influence on detection of action potentials. Organoids (*n* = 6) were embedded on CytoView plates and imaged prior to recordings at day 137. Due to variance across calculated diameter and area, raw values were normalised from 0 to 1 by dividing each value by the maximum value in the dataset. Normalised measurements were compared against mean firing rate to determine correlation by linear regression.

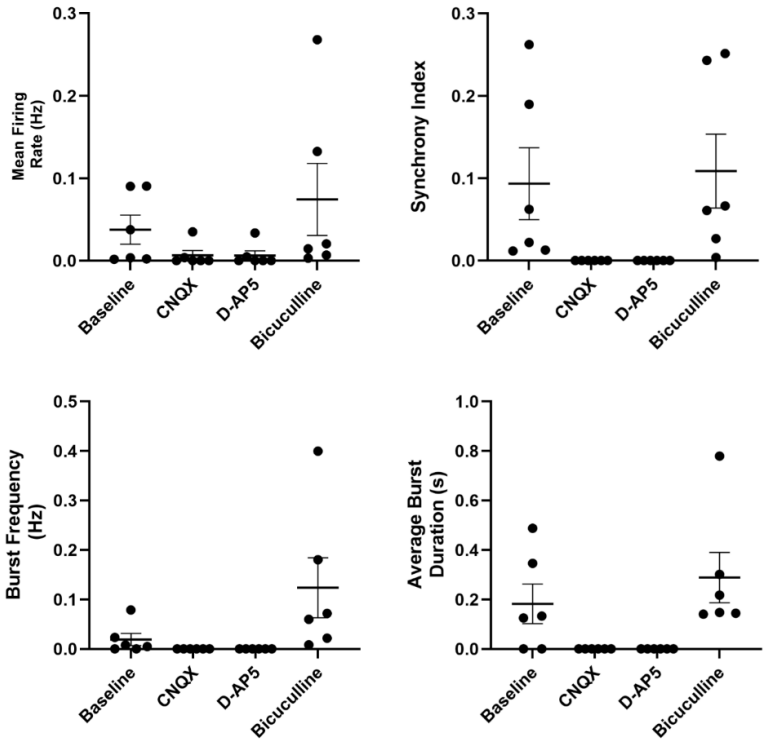

Figure 3.5 - Acute exposure to neurotransmitters validates organoid electrophysiology. 5-month-old cortical organoids (n = 6) were recorded by MEA to establish baseline electrical activity. Organoids were then sequentially treated for approximately 5 minutes with 20µM CNQX, 20µM D-AP5, and 20µM bicuculline, with drug wash-outs in triplicate between treatments. Antagonism of NDMA, AMPA, and $GABA_A$ receptors is demonstrated by changes to mean firing rate, bursting frequency and duration, and synchrony index. Error bars = mean ± SEM. No statistical significance was noted by paired t-test.

3.2.3 - Characterisation of cell types expressed in mature organoids

Neuronal and glial marker expression was next assessed to compare differentiation between immature (Day 31) and mature (Day 90 and Day 180) organoids. Protein was extracted from snap-frozen organoids and expression of differentiation markers compared by Western blot. SOX2 was detected in all samples, indicating the continuing persistence of neural progenitors. Low levels of GFAP indicated immature astrocytes with stem-like potential, while S100β expression showed mature astrocyte populations also present, particularly at latter time points [Figure 3.6] [Raponi 2009, Velasco 2019]. Notably, S100β expression also occurs in some oligodendrocytes [Du J 2021, Hernández-Ortega 2024].

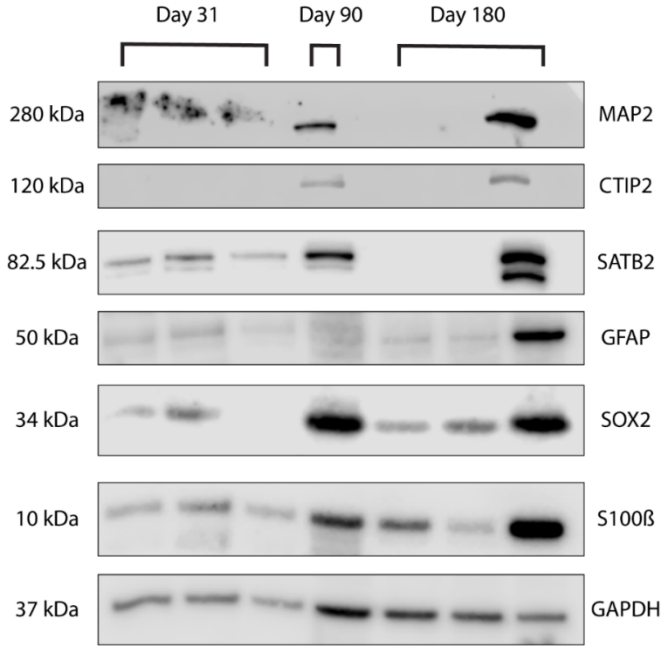

Figure 3.6 - Protein expression demonstrates variability in organoid neurodevelopment.
Protein extracted from snap-frozen organoids at Day 31 (n = 3), Day 90 (n = 1), and Day 180 (n = 3). Bands imaged in the chemiluminescent channel show protein expression of neuronal progenitors (SOX2), astrocytes (GFAP, S100ß), and mature neurons (CTIP2, SATB2, MAP2). GAPDH was used as a loading control.

In normal cortical development, immature neurons migrate from the inner ventricular zone and differentiate into distinct layers to form the cortical plate [Noctor 2002]. Early-born layer 5 neurons, characterised by CTIP2/BCL11B expression, are responsible for distributing information through cortical and subcortical regions, while late-born SATB2-expressing layer 4 neurons receive and process information from the periphery [Feldmeyer & Sakmann 2000]. Other studies suggest that both CTIP2 and SATB2 are expressed as early as one month into culture organoid culture, with CTIP2 expression significantly higher until 6 months, upon which SATB2 expression reaches approximately similar levels [Trujillo 2019, Qian 2020]. In contrast, immunoblots here showed the absence of CTIP2 in all organoids at day 31. CTIP2, SATB2, and MAP2 expression was observed in 1/3 organoids at day 180. The differences seen between organoids from the same development time-point likely represents the well-described heterogeneity that characterises these cultures [Qian 2019], and together with the range of electrical activity seen in the MEA readings, highlighted the need to analyse multiple organoids per condition in the pilot screen to account for this variance.

3.2.4 - Chronic exposure to kinase inhibitors and neurotoxins alters organoid electrophysiology

Having established the conditions for the development of electrical activity in the organoids, this model was next used to determine the feasibility and utility of organoids to detect potential neurotoxic effects of drug treatments. The pilot screen consisted of (1) untreated controls; (2) organoids treated with ibuprofen, as this has previously been suggested to have no adverse effects and therefore included to serve as a negative control for neurotoxicity [Wang Q 2022]; (3) the known neurotoxins acrylamide and ethanol, included as positive controls for neurotoxicity, and administered at concentrations (10μM and 55mM, respectively) reported in the literature to impair organoid function without causing complete loss of integrity [Renner 2021, Arzua 2020]; (4) gefitinib, administered at 10μM in line with

a previous study [Choe 2020]; and (5) lorlatinib, which was evaluated at 10μM and 1μM due to dose-dependent damage to 2D *in vitro* cell lines [Chen W 2020].

Based upon initial MEA results, and with the assumption that difference of least 10-20% would be required for statistical significance, it was calculated that 12-15 organoids were necessary per treatment condition. To manage limited culture capacity within the shaking incubator, experiments were spread across 5 technical replicates, each comprising 3 organoids per condition.

Overall, 111 cortical organoids were assessed by MEA as part of the neurotoxicity pilot screen [Table 3.1]. Measurements of electrophysiology were taken every 3-4 days, with an average of 7 recordings performed per organoid from days 150 to 180. As per the feasibility experiments, we considered an organoid to be electrically active when ≥5 spikes were detected per minute. When total number of electrically-active readings per condition were calculated and compared, it was revealed that there were significantly more examples of active organoids following treatment with gefitinib [Table 3.2]. Conversely, there were significantly fewer examples of active organoids following treatment with 10μM lorlatinib [Table 3.2]. The numbers of active recordings between the controls and all other treatments were not significantly different. Thus, this data suggests that both lorlatinib and gefitinib altered organoid electrophysiology.

Table 3.1 - Summary of MEA recordings by treatment condition

Condition	No. organoids evaluated	No. active recordings
Untreated	23	41/155 (26.45%)
Ibuprofen	13	38/98 (38.78%)
Acrylamide	15	30/112 (26.79%)
Ethanol	15	33/101 (32.67%)
10μM Lorlatinib	15	13/102 (12.75%)
1μM Lorlatinib	15	22/104 (21.15%)
Gefitinib	15	49/113 (43.36%)
Total	**111**	**226/785 (28.79%)**

Table 3.2 - Comparison of proportion of active recordings by Fisher's exact test

Comparison	Odds Ratio	p-value	Significance (P < 0.05)
Control vs Ibuprofen	0.59	0.07	NO
Control vs Acrylamide	1.02	>0.99	NO
Control vs Ethanol	0.77	0.40	NO
Control vs Lorlatinib (10μM)	2.552	0.0075	YES
Control vs Lorlatinib (1μM)	1.389	0.30	NO
Control vs Gefitinib	0.49	0.0085	YES

Next, drug effects on the capacity of neurons to generate and propagate action potentials was analysed. Organoids treated with gefitinib and ethanol exhibited a significantly higher mean firing rate, reflecting an increased number of spikes detected during recordings [Figure 3.7A]. As this was not associated with an increase in burst frequency, it appeared that gefitinib and ethanol enhanced tonic neuronal firing, which describes single spiking events occurring at regular intervals. Although burst frequency remained comparable to untreated controls, organoids treated with gefitinib showed a longer average burst duration [Figure 3.7A], which could reflect either increased excitatory or decreased inhibitory signalling. This can occur in response to specific stimuli, impaired glial cell function, altered synaptic plasticity, or changes in neural network connectivity [Tatti 2017]. Two parameters from the MEA analyses, the synchrony index (reports synchronicity of activity) and the coefficient of variation of ISI (reports the regularity of neuronal firing), provide information regarding synaptic function. No significant differences were observed in gefitinib-treated organoids for either parameter [Figure 3.7B-C], suggesting that the change in burst duration was not due to altered synaptic function. Furthermore, no detectable changes were reported in regularity of neuronal firing network-wide, as calculated by coefficient of variation of network ISI, thus suggesting that the burst duration did not reflect changes in network connectivity. Assessment of glial function through measurement of glial protein markers is addressed in the next section.

Conversely, long-term exposure to lorlatinib attenuated electrical activity. As previously described, fewer recordings of lorlatinib-treated organoids showed activity above the threshold. Mean firing rate in these recordings was comparable to untreated controls, but burst frequency was significantly decreased in organoids treated with 10μM lorlatinib, and bursts only occurred in half of recordings [Figure 3.7A]. The firing pattern in individual neurons was also more irregular in both lorlatinib conditions, as indicated by higher

coefficient of variation of ISI values, and this extended to network-wide firing in 1µM lorlatinib [Figure 3.7C]. The synchrony index was significantly increased in both 1µM lorlatinib and ibuprofen, and non-significantly in 10µM lorlatinib-treated organoids, though the latter measurements had considerable variance [Figure 3.7B]. This data is summarised in the table below [Table 3.3].

Table 3.3 - Summary table of electrical activity of drug-treated organoids

	Drug treatment					
	Ibuprofen	Ethanol	Acrylamide	Lorlatinib (10µM)	Lorlatinib (1µM)	Gefitinib
% Active Recordings						
Mean Firing Rate						
Burst Frequency						
Burst Duration						
Irregularity of Neuronal Firing						
Irregularity of Network Firing						
Synchronicity						

Grey – No change

Blue – Significant decrease.

Red – Significant increase.

Pink – Non-significant trend of increased activity

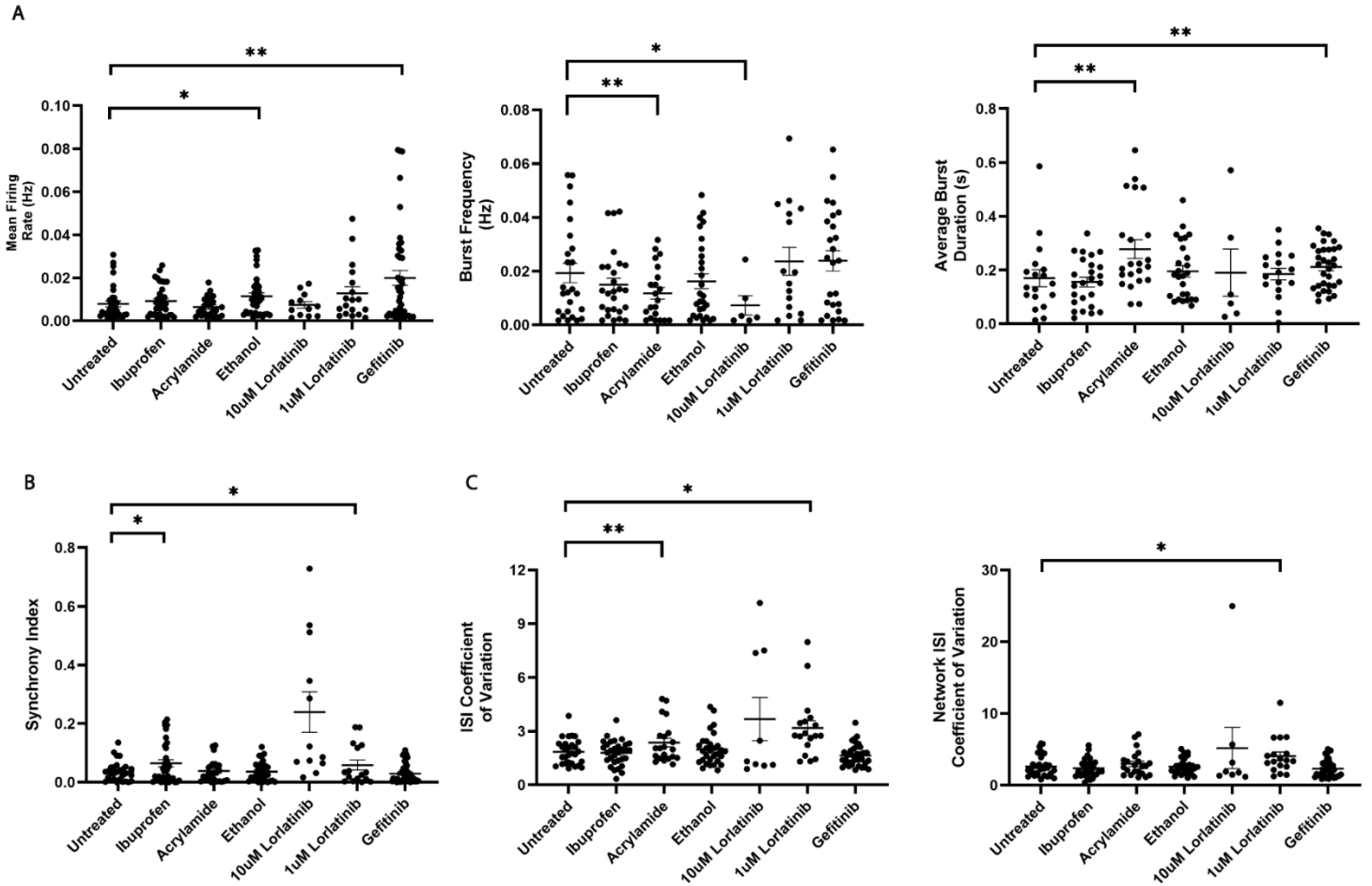

Figure 3.7 - Alterations to electrophysiological parameters of drug-treated organoids detected by MEA.

Compiled data of all MEA recordings (*n = 5* technical replicates) above the activity threshold of ≥5 spikes per minute. **A.** Neuronal function was assessed by mean firing rate and bursting parameters. **B.** Synchrony index was used as a parameter of synaptic function and signalling between neurons. **C.** Neural oscillations were evaluated at a single-neuron and network-wide scale by ISI coefficient of variation and network ISI coefficient of variation, respectively. Results were compared against untreated controls with unpaired t-test, * = $p<0.05$, **$p<0.02$. Error bars = mean ± SEM.

3.2.5 - Protein expression changes caused by chronic kinase inhibitor treatment

Electrophysiology was altered following the long-term exposure to both kinase inhibitors, so we next investigated the protein expression of organoids at day 180, comparing treatment conditions in replicates 1-3 by Western blot [Figure 3.8]. Late-stage neuronal (CTIP2, SATB2) and glial (GFAP) markers were assessed to determine whether long-term drug exposure impacted the differentiation of mature cell populations. We also evaluated activation of the ERK/MAPK and PI3K/Akt signalling pathways, as well as EGFR, due to their role in regulating neuronal proliferation, differentiation, survival, and synaptic plasticity [Fukunaga & Miyamoto 1998, Impey 1999, Chong 2005, Wang L 2017, Romano & Bucci 2020]. Protein expression levels were normalised against GAPDH loading controls using densitometry analysis [Figure 3.9].

Western blot analysis revealed variable protein expression between replicates, which precluded statistical comparison between the different conditions [Figures 3.8 and 3.9]. Instead, a descriptive analysis follows. Notably, there was limited expression of the late-stage neuronal marker CTIP2 under any condition, except replicate 3. In this same replicate, both CTIP2 and SATB2 were highly elevated in ibuprofen and 1μM lorlatinib-treated organoids. Moreover, there was also a noticeable increase in these markers, although not to the same extent in gefitinib and ethanol-treated conditions. These results suggest that, at least in this replicate, these conditions may stimulate neuronal maturation. The trend for the glial marker GFAP was either loss or decrease in all conditions relative to the untreated control. There were individual exceptions to this across the 3 replicates, but in no case was an increase seen in more than 1 replicate. Thus, this suggests that in this model, glial cells may be reduced by all treatments analysed.

In terms of signalling pathways, EGFR expression was consistently reduced in each treatment in at least 2/3 organoids. In contrast, total MAPK expression remained unchanged in the same proportion of organoids across conditions. Similarly, active MAPK, as measured by levels of phosphorylated (p)-MAPK, was unchanged, except in the acrylamide condition in which 2/3 organoids showed reduced MAPK activity. In 2/3 organoids, total Akt expression was increased in ibuprofen, decreased in acrylamide and ethanol, and unchanged in the other drug conditions. Active Akt, as determined by levels of phosphorylated (p)-Akt, was increased in 2/3 organoids exposed to ibuprofen and to either concentration of lorlatinib, while being unchanged in all other conditions.

Although variation between replicates prevents us from drawing firm conclusions, these findings hint that each treatment causes changes to differentiation and signalling in mature organoids. Overall, the data suggest that there are batch-dependent effects on cell types and signalling in the aged organoids, and future work will require larger numbers of organoids per replicate to overcome this variation, as was undertaken for the MEA experiments.

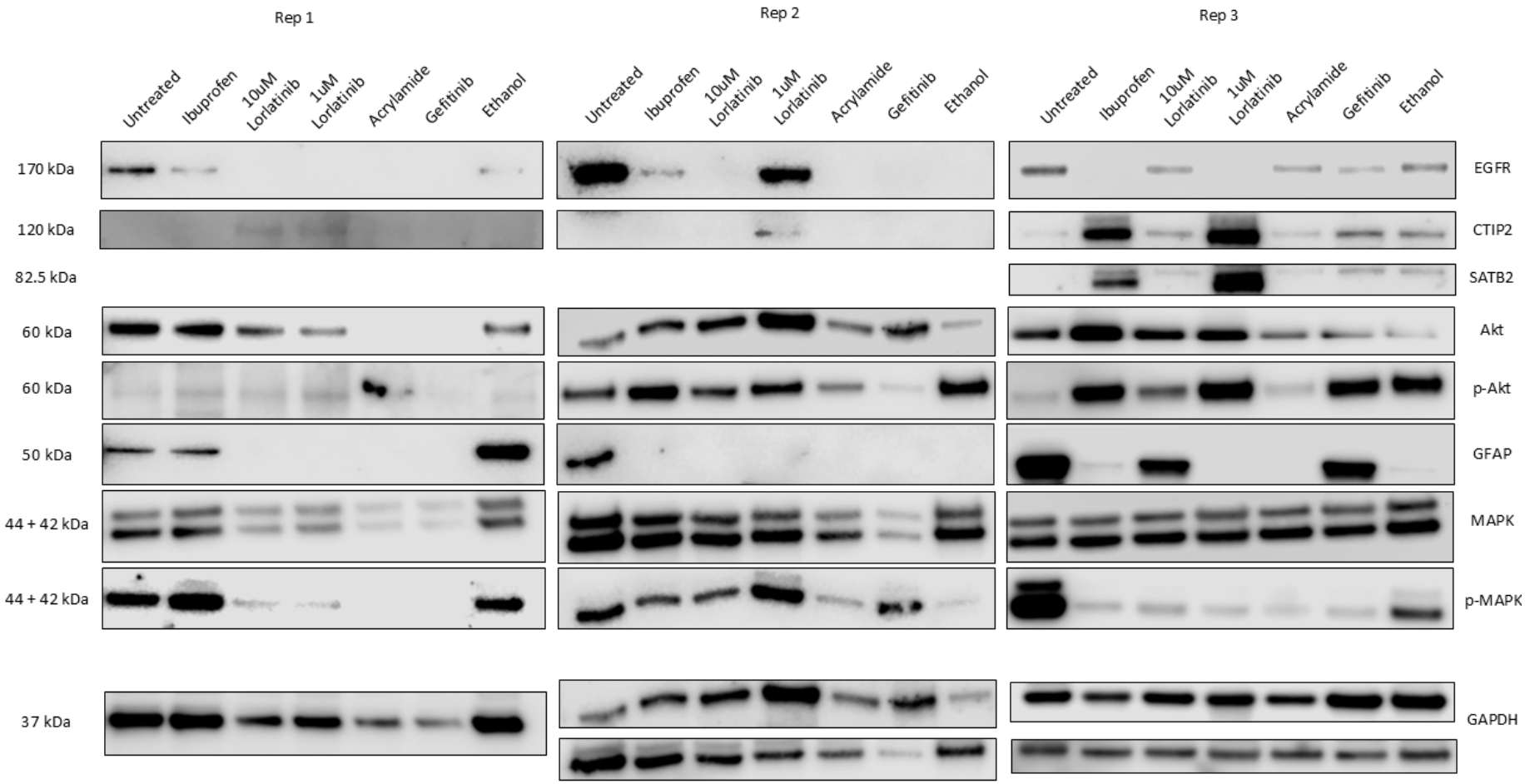

Figure 3.8 - Protein expression of drug-treated cortical organoids. Protein extracted from snap-frozen organoids from replicates 1-3 of the neurotoxicity screen. Bands imaged in the chemiluminescent channel show expression of cortical neurons (CTIP2, SATB2), astrocytes (GFAP), and markers of signalling pathways involved in neuronal and glial maintenance, proliferation, and differentiation (EGFR, Akt, phospho-Akt, MAPK, phospho-MAPK). GAPDH was used as a loading control (multiple shown where more than 1 membrane was used per replicate).

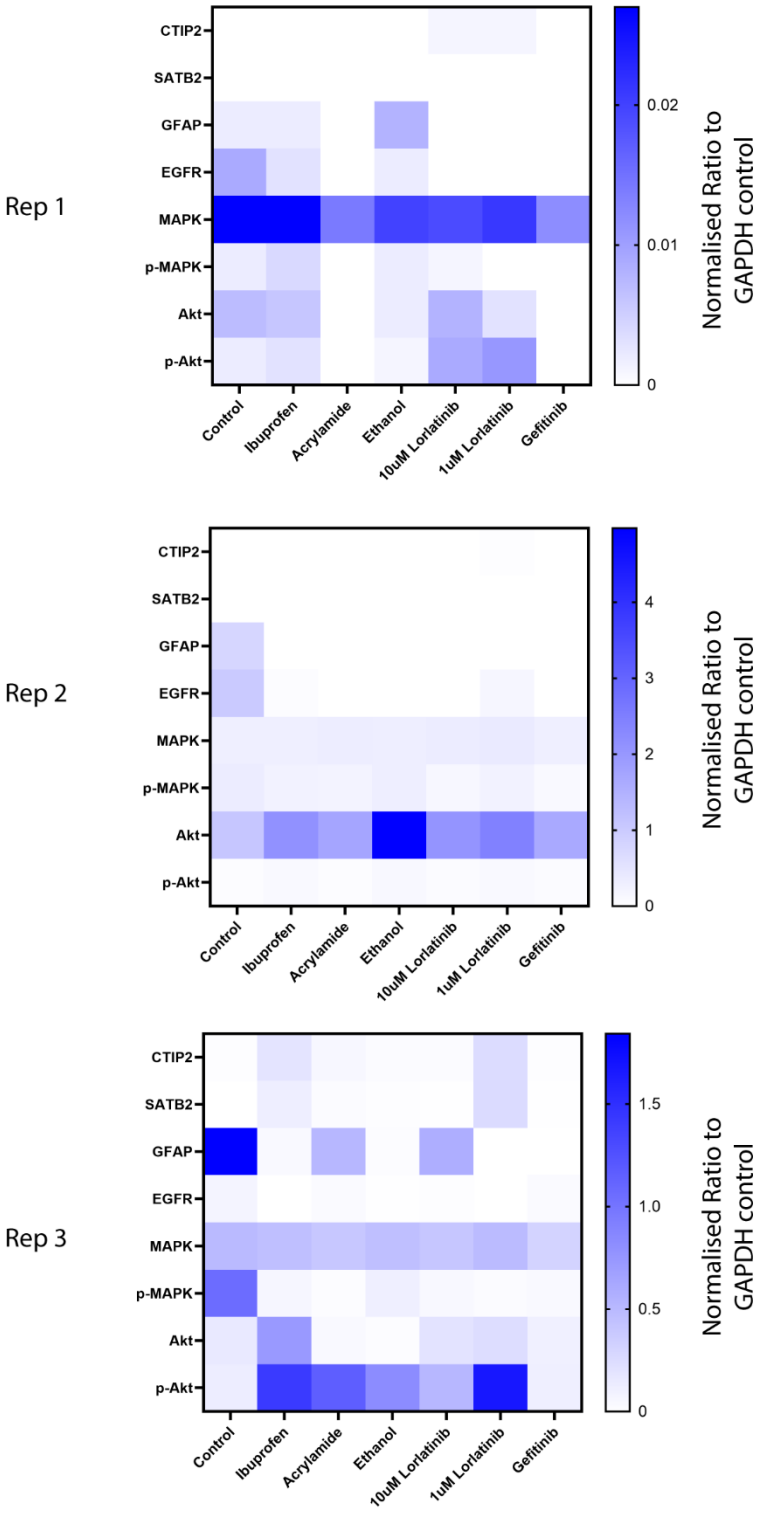

Figure 3.9 - Protein expression normalised against loading controls.

Densitometry analysis was performed to quantify and normalise protein expression against the GAPDH loading controls. Ratios were then compared across treatment conditions for each replicate 1-3.

3.3 - Chapter Discussion

The results of the pilot screen presented here demonstrate the feasibility of this approach for assessing neurotoxicity. Interestingly, the greatest changes were seen with the two kinase inhibitors, when compared with the control compound (ibuprofen) and the known neurotoxins (ethanol and acrylamide). Under the model conditions used here, acrylamide only significantly impacted bursting patterns, while ethanol treatment only significantly affected tonic neuronal firing. Furthermore, although ibuprofen was included as a bona-fide non-neurotoxic treatment, this drug significantly altered electrical synchronicity. Nonetheless, the findings suggest that chronic exposure to the targeted kinase inhibitors may indeed influence brain electrophysiology and warrants further research. Collectively, the data support the feasibility of the organoid screen, and expanding the analysis to include more drugs will provide deeper insights into their mechanisms of action in brain development and function.

3.3.1 - Cortical organoid generation and electrophysiology

This thesis demonstrated a protocol for culturing dorsal cortical organoids with complex electrophysiology, including spontaneous excitatory and inhibitory signalling, rapid bursting patterns, and synchronised activity across a neural network. Results provide a foundational basis for future research into functional screening. At least 40 studies on dorsal cortical organoids have been published in the literature [Mulder 2023], with many methodologies based on the early work of Pașca et al. [Pașca A 2015]. These approaches mostly involve seeding a precise number of stem cells into ultra-low attachment conditions to establish 3D embryoid bodies. Neuroectoderm formation is then typically prompted by dual SMAD inhibition targeting the BMP and TGF-β pathways, followed by the addition of a variety of morphogens and growth factors guiding differentiation. Research has shown that selection, concentration, and exposure duration of these small molecules can significantly

alter the differentiation and organisation of early-stage dorsal cortical organoids [Velasco 2019, Yoon 2019]. This is further exacerbated in studies maintaining organoids in matrix-supported culture, or supplementing growth medium with liquid ECM components, due to the secretion of additional growth factors and batch-to-batch variability [Tian 2020, Mulder 2023].

Dorsal cortical organoids mainly comprise numerous neural progenitors, excitatory glutamatergic neurons, inhibitory GABAergic interneurons, and mature astrocytes, all of which contribute to functional electrophysiology. Interactions between glutamatergic and GABAergic interneurons produce multi-frequency oscillatory responses, whereby individual neurons and neural networks engage in rhythmic activity, and which may lead to synchronisation [Stiefel & Ermentrout 2016]. Only small populations of inhibitory interneurons are generated locally in dorsal cortical organoids, with the majority originating in the ganglionic eminences of the ventral forebrain, then migrating to other brain regions [Delgado 2022]. Excitatory and inhibitory neurons laterally organise into cortical layers which process external sensory inputs and transmit information throughout the cortex and to distal regions, such as the thalamus and brain stem. Layer 4 and 5 neurons have been widely reported in dorsal cortical organoid models, including in this thesis by SATB2 and CTIP2 expression, although notably, SATB2 and CTIP2 expression were variable between mature organoids. Outer layers are less frequently characterised, potentially due to challenges in distinguishing overlapping layers which co-express markers. However, some studies have reported the presence of Cajal-Retzius cells and Reelin expression, both of which are responsible for organisation of cortical layers and indicative of cortical layer 1 [Qian 2020, Uzquiano 2022].

Astrocytes are the most abundant glial cell in the human brain and cerebral organoids, ranging from 15 to 53.5% of the total cell count in 6-month-old organoids [Pasca 2015, Yoon

2019, Trujillo 2019, Velasco 2019]. The ventricular radial glial cell marker PAX6 is highly expressed in early organoids [Prior 2022], and is a key transcription factor regulating differentiation of radial glial cells into cortical astrocytes [Heins 2002, Qin R 2024]. During initial stages of cortical development, large numbers of immature neurons and synapses are formed, confirmed here by the presence of SOX2 in the immature organoids. As neural networks are established and undergo maturation, excess synapses are directly pruned by astrocytic phagocytosis. Astrocytes then regulate action potential transmission between presynaptic and postsynaptic neurons through the release of Ca^{2+} ions, uptake of excitatory neurotransmitter glutamate, and other indirect mechanisms [Allen N 2012, Chung 2013, Sloan 2017, Liu X 2021].

Oligodendrocytes are the second-most prevalent glial population in cerebral organoids. They regulate the myelination of axons, and can alter this process in response to sensory inputs and neural network function to increase the speed and synchrony of action potential propagation [Munyeshyaka & Fields 2022]. OPCs typically emerge around 5-6 months into cortical organoid culture, but remain in an immature state [Madhavan 2018, Qian 2020]. It is hypothesised that oligodendrocyte maturation occurs slowly to maintain neuronal circuitry throughout a person's life, with individual myelinating oligodendrocytes persisting for decades [Hughes & Stockton 2021]. Recent protocols have enriched for mature oligodendrocytes at early culture time-points, but their impact on organoid electrophysiology has yet to be determined [Shaker 2021, Al-Mhanawi 2023].

Lastly, microglia are specialised glia which function as the immune cells of the brain, responding to neuronal injury and disease. During neural network development, astrocytes secrete TGF-β and upregulate neuronal expression of complement components C1q and C3, directing microglia to assist in pruning surplus synapses by phagocytosis [Schafer 2012]. Although whole-brain cerebral organoids develop populations of microglia, they are notably

absent in most cortical organoid models due to the SMAD inhibitor-mediated repression of mesodermal lineage, from which they are derived [Ormel 2018]. Integration can be achieved through the co-culture of cortical organoids with iPSC-derived microglia or myeloid precursor cells [Zhang W 2023]. The presence of microglia increases synchronisation and burst frequency in cortical organoids, indicating their retained role in synaptic development [Popova 2021]. The immunological implications of microglia-containing organoids are discussed further in Chapter 4.

In summary, populations of neuronal and glial populations vary between organoid modes, in turn impacting electrophysiological function [Zourray 2022]. While some early neural developmental processes appear to be accurately modelled by dorsal cortical organoids, the immaturity and underrepresentation of specific cell subtypes limits the recapitulation of postnatal brain structures.

3.3.2 - Assessment of organoid electrophysiology by MEA

Detection of electrophysiology from dorsal cortical organoids was performed using the commercial planar Maestro Pro MEA system. Importantly, this approach enabled the high-throughput assessment of entire neural networks in multiple organoids on a single plate. However, it is important to note that planar MEA systems were developed to evaluate the electrical activity of adherent neuronal and cardiomyocyte cells, which are cultured in direct contact with the electrode array. When the method is applied to 3D structures, such as the organoids analysed in this thesis, measurements can only be taken from the region touching the electrodes, and detection depth is restricted to approximately 100μm [Obien 2019]. This prevents the mapping of electrical activity from the entire organoid, including inner regions. In addition, organoids are required to be embedded into place with polymerised Matrigel or other matrices to immobilise them on the electrode grid. This may impede recordings by

creating gaps between the organoid and electrode, as well as leading to neurite outgrowth and morphological changes to the organoid over time [Trujillo 2019].

Several approaches have been taken to overcome problems with accessibility and electrode coverage when analysing 3D structures, although each comes with its own caveats. One method involves sectioning organoids by vibratome, followed by air-liquid interface culture, and electrophysiological analysis [Giandomenico 2019]. This increases diffusion of oxygen and nutrients in models susceptible to hypoxia and cell death, and allows measurements of otherwise inaccessible areas. Slices continue to show neuronal development and organisation, and retain electrical function. As these organoid slices are considerably thinner than their intact counterparts, there may also be less resistance encountered when measuring neuronal activity by MEA. However, sectioning organoids requires technical expertise, can physically break existing neural connections, and limits characterisation of the entire model [Giandomenico 2019, Qian 2020].

Recently, brain organoid slices have been assessed using commercial high-density complementary metal-oxide semiconductor (HD-CMOS) MEA systems, which feature arrays of thousands of platinum microelectrodes per mm^2. This results in significantly higher spatial resolution and signal-to-noise ratios, and enables the mapping of individual neurons and intracellular space within a network, rather than a broader population overview produced by sparser arrays, such as the one used in this thesis [Müller J 2015]. HD-MEAs have been used to assess network connectivity and calculate action potential propagation velocities from single neurons in brain organoid slices, demonstrating a level of detail unavailable from conventional planar MEA [Sharf 2022, Schröter 2022].

3D-MEA systems acknowledge the dimensionality of organoids, aiming to increase the surface contact area and gain greater insight into electrical activity. This can be achieved

through the fabrication of flexible polymer scaffolds that encapsulate organoids. Biocompatible materials with similar mechanical properties as organoids, such as stiffness, ensure greater conformal contact on all sides compared to rigid planar arrays [Lee J & Liu J 2025]. Several mesh and shell MEA systems have been described in the literature which envelop, roll, or fold around cerebral organoids and assembloids, and record electrical activity from multiple angles. [Park 2021, Huang Q 2022, Xiao 2024] Alternatively, shanks, spikes, or cantilevers may either be inserted into the organoid manually with micromanipulators, or organoids can be placed on top of the protrusions and allowed to settle over a few days. Recent advances in these systems have seen electrodes probe deeper into organoids, with measurements exceeding 100µm depth [Soscia 2020, Shin 2021, Phouphetlinthong 2023]. Yadav et al. demonstrated proof-of-concept of an array of 60 microelectrodes of different lengths, which were inserted into organoids and capable of monitoring electrophysiology at 35, 65, and 120µm depth simultaneously, thus providing a detailed understanding of layered inner circuitry [Yadav 2023]. Another option is to culture the organoid around the electrodes, such that they are effectively incorporated into the tissue. McDonald et al. demonstrated their mesh array was capable of integration and maintained organoid growth for up to a year without compromising culture morphology or function [McDonald 2023].

In many instances, authors reported that transitioning to 3D-MEA reveals active electrophysiology in organoids that had otherwise appeared inactive by 2D-MEA. From our own observations, activity above the threshold only occurred during 28.79% of recordings, and individual organoids often exhibited different firing rates between days 150-180. While this could be attributed to neurodevelopmental variability within the cortical organoid model, it can also be suggested that the acquired data was not fully representative of organoid function. Currently, there are no 3D-MEA systems available commercially. Once they are

developed into a commercial product, adopting this approach will likely provide even greater insight into organoid electrical conductivity.

3.3.3 - Chronic kinase inhibitor exposure induced greatest changes to electrophysiology

Functional screening of cortical organoids showed changes to electrophysiology resulting from long-term exposure to both TKIs. Gefitinib-treated organoids demonstrated significantly increased neuronal firing and longer bursting patterns, which was also observed in ethanol and acrylamide control conditions, respectively. Therefore, to gain potential insight into the mechanisms underpinning gefitinib effects on electrical activity, the known effects of ethanol and acrylamide on neurodevelopment are summarised below.

A common byproduct of food processing, the neurotoxicant acrylamide has been researched to determine its impact on neurodevelopment. Bu et al. treated one-month-old whole-brain cerebral organoids with 2-5mM acrylamide, reporting morphological changes compared to untreated controls. In addition to significant apoptosis, they noted an upregulation of the MAPK pathway – a finding that was not replicated in the present study - resulting in suppression of neuronal differentiation [Bu 2020]. At lower, physiologically-relevant concentrations, acrylamide and its metabolite glycidamide have less significant impacts on cell viability, but continue to impair neuronal differentiation and synapse formation, while driving increased astrocyte maturation [Renner 2021, Lauvås 2022]. The longer burst patterns of activity induced by acrylamide in the present study may indicate altered synapse formation.

Ethanol has likewise been investigated extensively, due to both social pervasiveness and established teratogenic effects with regards to cognitive and behavioural issues, such as FASD [Riley 2011]. In early-stage whole-brain organoids, ethanol exposure for 6-24 hours, at similar concentrations as was used here, caused apoptosis in neuronal populations, synapse

degeneration, and altered pathways relating to neurodevelopment and neurodegeneration [Zhu 2017, Arzua 2020]. In a separate study, one-month-old cortical organoids were treated with 100mM ethanol for one week, then culture continued in the absence of ethanol to determine how cortical development had been disrupted. The authors found that while early neuronal apoptosis stabilised over time, changes to cell populations persisted, with fewer deep-layer cortical neurons and more astrocytes than untreated controls 2 months later [Adams 2022]. These results might be explained by the sensitivity of oRGs to ethanol, causing premature astrocyte differentiation and impairment of neuronal migration to the cortical plate [Lü 2023]. Interestingly, Adams et al. reported that ethanol-treated cortical organoids exhibited decreased neuronal firing and burst frequency during MEA recordings [Adams 2022]. This is contrary to our own findings, albeit with considerable variations to experimental design, such as ethanol concentration, exposure length, and organoid culture duration. Clinical data reports that the excitatory or inhibitory influence of ethanol is dependent on brain region, typically either facilitating or inhibiting glutamate release and its receptors [Xiao C 2009, Perdue 2024]. Animal cortico-striatal models are more supportive of the results of our functional screen, suggesting that ethanol-induced impairment of inhibitory interneuron migration leads to an excitatory signalling imbalance [Bariselli & Lovinger 2021]. As previously mentioned, this process is frequently disrupted across several neurodevelopmental and neurodegenerative disorders, and could be a plausible mechanism by which gefitinib interferes in electrical signalling that is important for cortical development.

More profound disruption to cortical development was observed as a result of long-term lorlatinib treatment, with alterations to most electrophysiological parameters. Lorlatinib-treated organoids demonstrated spontaneous activity in the fewest number of MEA recordings of any condition, and while tonic neuronal firing remained consistent, the

frequency of complex bursts was significantly diminished. In particular, irregular over-synchronous neuronal firing distinguished lorlatinib from other treatment conditions, and is reminiscent of hypersynchronous firing patterns during epileptic seizures [Jiruska 2013]. The 'mossy fiber' hypothesis suggests that epileptic seizures occur due to aberrant formation of excitatory circuits from hippocampal mossy fibers, resulting in hyperexcitability. Alternatively, the 'dormant basket' hypothesis posits that a pathological decrease to excitatory signalling causes inhibitory GABAergic neurons to go dormant. When excitation does occur, the lack of inhibitory reciprocation causes excessive synchronous neuronal firing [Chauhan 2022]. The latter theory might be adapted here, explaining how lorlatinib-treated organoids displayed spontaneous activity less often than other organoids, while also accounting for the increased synchronicity of neuronal firing.

Notably, since commencing this work reports of the impacts of lorlatinib on cognitive function have emerged, focusing on standardised testing protocols, rather than relying on self-reported data, as well as expanding to paediatric patients. An observational study of 22 patients with metastatic NSCLC treated with lorlatinib reported neurocognitive testing at 2 weeks and 2 months after starting treatment. While verbal memory (recall of words) was significantly impaired at 2 weeks, all measurements of cognitive function were comparable to baseline values after 2 months [Schoenmaekers 2023]. Researchers did not follow-up with patients to investigate any long-term deficits which may have emerged at later time-points, but this would likely have been difficult due to disease progression. In paediatric patients, lorlatinib has been tested at phase I trial for relapsed and refractory ALK-positive neuroblastoma, both as a single agent and in combination with topotecan or cyclophosphamide. Goldsmith et al. showed mild, short-lived cognitive side effects in 2/33 (6%) paediatric patients and 4/15 (27%) adult patients, though adults received higher treatment doses and none of the patients presented with CNS metastases [Goldsmith 2023]. A

single case report has been published of lorlatinib being used to treat a 3-year-old patient with ALK-positive pHGG. Following successful clearance of both the initial tumour and a subsequent relapse, clinicians opted to maintain lorlatinib administration for as long as feasible, with no immediate treatment-associated deficits reported [Bagchi 2021]. Development of the approach presented in this thesis could help refine studies of potential neurotoxic side effects by identifying biomarkers or functional readouts that might determine patients at risk of neurotoxicity. This information would provide a window of opportunity to either consider using alternative non-neurotoxic therapies, or to use interventional strategies, as described in Chapter 1.2, to ameliorate neurotoxic effects.

While we can speculate as to the mechanisms by which organoid development and electrophysiology are impaired by gefitinib and lorlatinib, further advances to the model and methodology will be required before we can confidently predict neurotoxicity *in vivo*. Optimised organoid generation protocols, connectivity across brain regions, greater analytical coverage, physiologically-relevant drug concentrations, and incorporation of blood-brain barrier and efflux mechanisms must all be incorporated to sufficiently model human brain development and evaluate drug responses. Nonetheless, this research is a promising first step toward using 3D *in vitro* models to assess long-term safety profiles during drug development.

3.4 - Summary

Understanding the developmental processes of the human brain, and the mechanisms driving neurotoxicity, has remained challenging due to inadequate preclinical models. Detecting long-term neurotoxicity requires time-consuming longitudinal studies of large cohorts of patients, and there is no opportunity to alter the course for the patients under study. While the approach and model described here has its caveats, it offers a unique opportunity to identify potential neurotoxic effects in a greatly-reduced timeframe, providing the

opportunity to overcome neurocognitive deficits in patients. 3D cortical organoids recapitulate corticogenesis, displaying diverse cell populations which self-organise to mimic structures seen in late gestational and early postnatal neocortex. We presented a dorsal cortical organoid model that was cultured to maturation and developed complex electrophysiology, including functional neural networks. Despite the limitations of planar MEA for assessing 3D models, we observed that prolonged exposure to TKIs elicited significant alterations to organoid electrical activity which overlapped with effects from known neurotoxins. These results promote organoids as a platform for exploring the functional consequences of treatment-associated neurotoxicity.

Evaluating efficacy of EphA2 CAR-T cell therapy in 3D HGG models

4

4.1 - Chapter Introduction

Curative treatments against HGGs remain elusive due to their characteristic heterogeneity, diffuse infiltration through critical brain structures, and rapid recurrence. Single-target and combination chemotherapies have failed to demonstrate meaningful improvements to overall survival at clinical trial, despite apparent efficacy in preclinical *in vitro* and *in vivo* models [Dowden & Munro 2019, Huang M 2024]. This situation necessitates novel therapeutic options to overcome resistance mechanisms, as well as more representative preclinical models with which to evaluate these emerging treatments [Slika 2023].

As outlined in Chapter 1.1.4, following the success of CD19-directed CAR-T cell therapies in improving outcomes of treatment-resistant haematological malignancies, researchers have sought to translate these results to solid tumours. Although generally well-tolerated, efficacy of CAR-T therapy in adult HGG patients remains short-lived, with tumour heterogeneity and immunosuppressive responses being key limiting factors [O'Rourke 2017]. Studies have reported that some pHGGs, including DIPG, have altered immune components in the tumour microenvironment compared to their adult counterparts, which may render

them more susceptible to immunotherapies [Lin G 2018, Lieberman 2019, Njonkou 2022, Messiaen 2023]. Early-stage phase I and II clinical trials are ongoing in paediatric patients targeting a range of TAAs, such as HER2, GD2, and B7-H3 [Vitanza 2021, Majzner 2022, Vitanza 2023].

Another key therapeutic target is EphA2, which is overexpressed in several cancer types, including brain tumours [Binda 2012]. Non-canonical ligand-independent activation of EphA2 promotes self-renewal, increased motility, and invasion in glioma stem-like cells, corresponding to an aggressive phenotype and poorer outcomes in GBM patients [Wilson K 2021]. The highly conserved nature of ephrin receptors and the low expression in normal brain tissue further present EphA2 as a promising candidate for directed therapies. Our unit (the Children's Cancer Research Unit at CHW) developed an EphA2-directed CAR-T cell therapy demonstrating preclinical efficacy against paediatric osteosarcoma and Ewing sarcoma, and has received approval to commence recruitment for a phase I clinical trial. Our focus then turned toward other potential applications for this CAR construct.

Research presented in this thesis evaluated the efficacy of EphA2 CAR-T cell therapy against 3D *in vitro* models of GBM and DIPG. Tumour spheroid models aggregating from patient-derived cell lines provided dimensionality and a concentration gradient lacking in conventional monolayer cultures. Co-cultures with cortical organoids incorporated normal brain tissue to more closely resemble tumour invasion *in vivo*. An optimised protocol was developed for the quantification of tumour viability within these models in response to CAR-T treatment, with the aim of producing replicable results more accurately predicting response in human participants at clinical trial.

4.2 - Results

4.2.1 - EphA2 is differentially expressed in GBM and DIPG cell lines

Initial work conducted by our department characterised the EphA2 expression profiles of GBM and DIPG cell lines to determine appropriate candidates for therapy. In their PhD thesis, Dr Victoria Prior used immunofluorescence to observe membrane-bound EphA2 in adult patient-derived WK1 GBM monolayers [Prior 2022]. EphA2 expression was retained when WK1 cells were cultured under 3D conditions, forming tumour spheroids. Localisation at the cell surface facilitates binding of the CAR-T cells to the target antigen, thus suggesting the accessibility of EphA2 to CAR-T treatment in both 2D and 3D models.

Flow cytometry analyses confirmed differential expression of EphA2 across a panel of continually-cultured and patient-derived GBM and DIPG cell lines (performed by Dr Jody MacLeod, Dr Yuyan Chen, Teah Goodhand) [Figure 4.1]. Mean fluorescence intensity (MFI) was calculated from the geometric mean of stained EphA2-positive cells, indicating relative antigen abundance. MFI levels were highest in the patient-derived cell lines, expressing EphA2 at higher concentrations than continually-cultured A172 and U87-MG cells. As patient-derived cell lines are considered more representative of their primary tumours than continually-cultured cells, *in vitro* EphA2 expression is expected to closely reflect expression levels *in situ.* Patient-derived cell lines WK1, DIPG17, and DIPG24 were therefore selected as representative cell lines for further analysis.

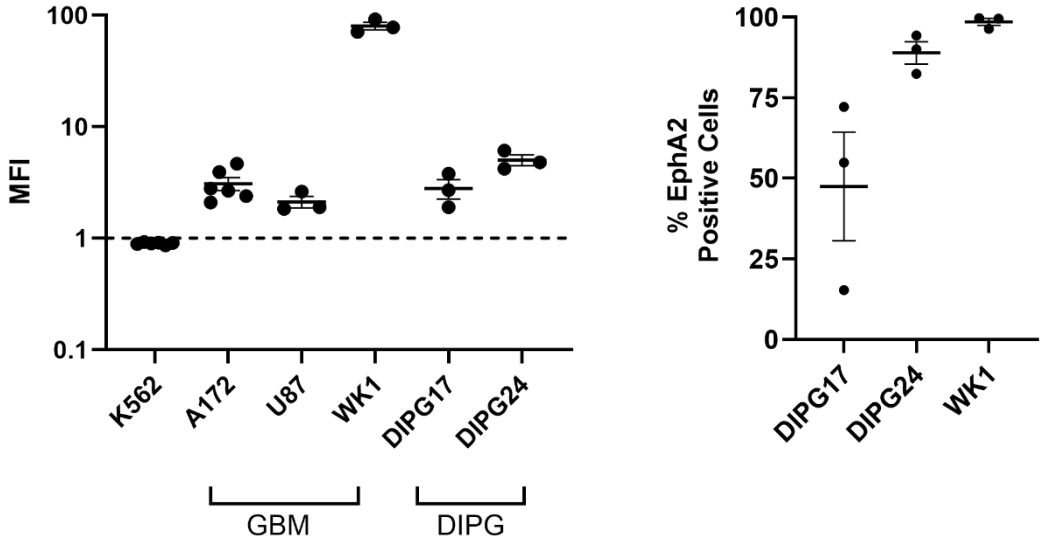

Figure 4.1 - EphA2 is differentially expressed between GBM and DIPG cell lines.

Continually-cultured and patient-derived GBM and DIPG cell lines were analysed for EphA2 expression by flow cytometry. Data points represent experimental replicates at different passages (K562 and A172 *n* = 6; U87, WK1, DIPG17, and DIPG24 *n* = 3). Mean fluorescence intensity (MFI) was calculated using the geometric mean of detected fluorophore intensity. In instances where MFI was below 1 (indicated by the horizontal dotted line), cells were considered negative for EphA2 surface expression. K562 was used as an EphA2-negative control cell line. % expression was determined by the number of live cells positive for the PE fluorophore-tagged EphA2 antibody. Error bars = mean ± SEM.

Data kindly supplied by Dr Jody MacLeod, Dr Yuyan Chen and Teah Goodhand.

4.2.2 - EphA2 CAR-T cells efficiently target pHGG in 2D conditions

Assessment of CAR-T efficacy was first performed against 2D monolayer cultures (experiments performed by Dr Jody MacLeod and Dr Yuyan Chen). Although tumour cells are highly sensitive under these conditions due to homogenous exposure to treatment, results provided a preliminary indication as to whether the CAR-T cell therapy was capable of targeting and killing GBM and DIPG cells. Cytotoxicity assays were conducted using the xCELLigence platform, which provided real-time analysis of cell viability based upon electrical impedance. The unitless parameter, Cell Index, increased as cells adhered to the wells and proliferated. Baseline recordings of monolayers were taken at 24 hours, followed by exposure to either CAR-T cells or untransduced control T cells lacking the CAR construct. Subsequent decreases to Cell Index indicated loss of adhesion, with visual observation suggestive of apoptosis, and values were converted to % cytolysis when compared to baseline measurements.

Treatments were administered at a range of Effector (E, CAR-T cells): Target (T, tumour cells) ratios from 1:1 to 1:27. Minimal non-specific cytotoxicity occurred from untransduced T cells across all cell lines, and no effects were observed following CAR-T treatment in EphA2-negative control cell line NIH-3T3. Significant killing was noted in all EphA2-expressing cell lines at 1:1 E:T ratio, with almost complete cell death in all replicates after 48 hours [Figure 4.2]. Lower CAR-T cell concentrations resulted in a delayed response, but 1:9 and 1:27 E:T ratios remained efficacious and cleared the majority of the tumour cells within 96 hours [Supplementary Figure 4.1]. Overall, the EphA2-directed CARs were shown to be capable of efficiently killing HGG cell lines under adherent conditions, and research therefore proceeded to 3D *in vitro* models to compare the efficacy of CAR-T cells between 2D and 3D models.

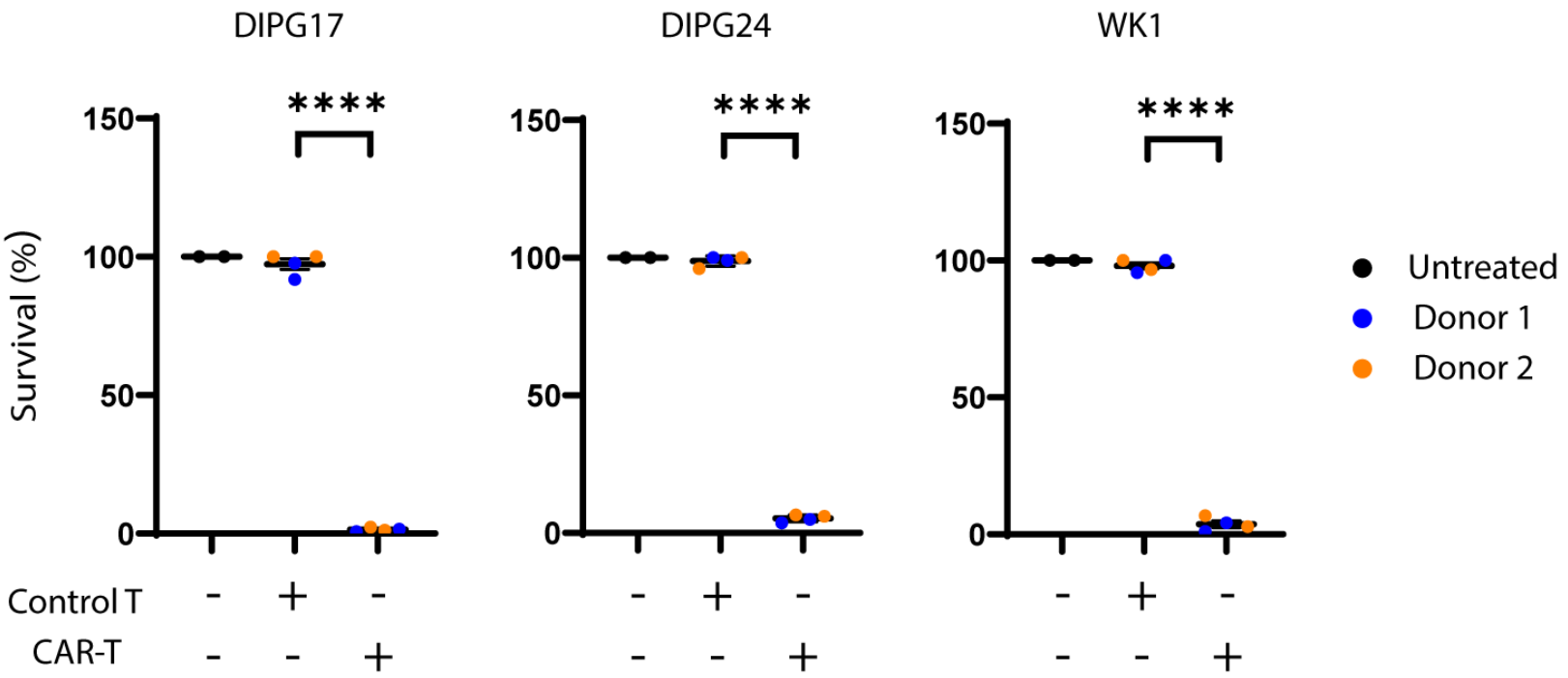

Figure 4.2 - Patient-derived HGG cell lines are efficiently killed by EphA2-directed CAR-T cells under 2D conditions.

Target cell lines DIPG17, DIPG24, and WK1 were cultured as adherent monolayers on xCELLigence E-plates, monitoring viability over time. Tumour cells were treated with either EphA2 CAR-T cells or untransduced control T cells from two separate healthy donors ($n = 2$). Treatment was added at 1:1 E:T ratio for 48h. Cell Index was compared to baseline recordings to calculate % survival. Results were analysed using unpaired t-test, ****$p<0.0001$. T cells for generating CAR-T cells were from independent donors (indicated by donor number) to test for donor-specific differences in T cell efficacy.

4.2.3 - Measurement of 3D viability required assay optimisation

As the xCELLigence system was only capable of measuring the viability of 2D adherent monolayers, the transition to 3D culture models required different methods. Selection criteria for commercial viability assays were ease of protocol, linear association between cell count and assay readout, and applicability across culture conditions and models.

CellTiter-Glo® 3D (Promega) was tested first due to its frequent application in research literature. The assay comprises a lysis buffer and ATP-binding substrate, producing a luminescent signal corresponding to the number of viable cells. WK1 spheroids were formed by seeding cells in ultra-low attachment plates at a range of cell counts. A maximum of 2.5 x 10^4 cells was used to prevent establishment of a necrotic core which could obfuscate viability recordings. Standard curves were generated showing strong association between cell count and luminescent signal measured in relative light units (RLU) by a luminometer. Spheroids were also embedded into collagen matrices to mimic cell-ECM interactions, and standard curves repeated in these conditions [Figure 4.3B]. Luminescent signal remained proportional to cell count, however RLU values from embedded spheroids were considerably lower than spheroids in suspension, indicating either incomplete lysis or signal interference by the collagen matrix. Furthermore, concerns were raised that CellTiter-Glo® 3D would not be sufficient in more complex 3D models, such as assembloids, where overall cell count would be more variable between biological replicates and viability of separate cell populations would not be distinguishable.

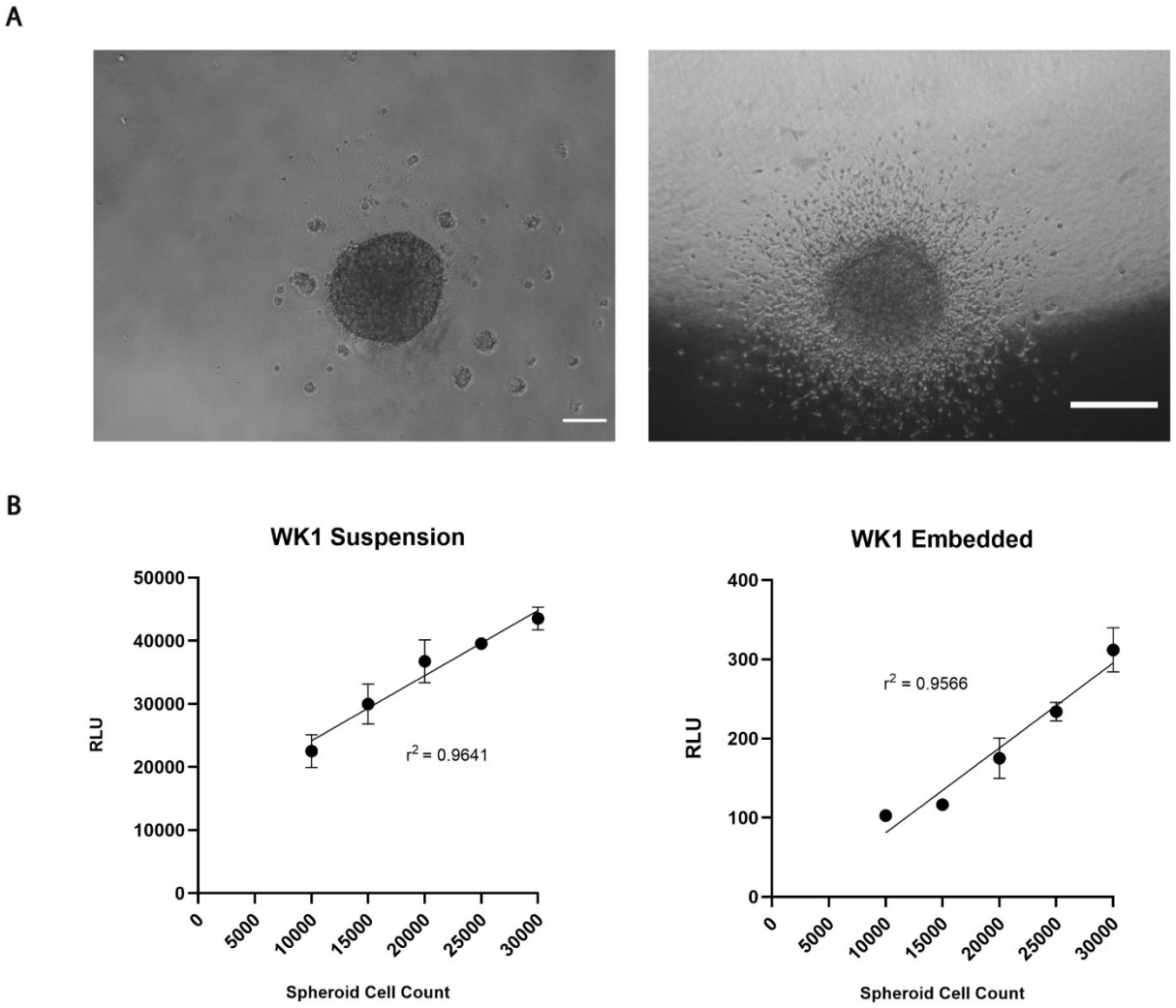

Figure 4.3 - Tumour spheroid viability recorded by CellTiter-Glo 3D assay. A. Representative images of WK1 spheroids comprising 7.5 x 10^3 cells, cultured in ultra-low attachment plate (left) or embedded in collagen gel for 24h (right). Embedded tumour spheroids exhibit outgrowth as cells invade into the ECM. Scale bars = 100µm. **B.** Spheroids were subjected to CellTiter-Glo 3D assay, with RLU values corresponding to the number of viable cells. Values are mean ± SEM, *n* = 3.

An alternative protocol was implemented in which the patient-derived cell lines were transduced using a lentiviral vector (LVV) encoding both luciferase and an eGFP reporter. Following transduction, expansion, and sorting, cells were imaged with the DMi8 epifluorescence microscope system. Unexpectedly, acquired images showed nuclear localisation of eGFP which was maintained in both 2D adherent cells and 3D spheroids. Standardly, eGFP should be expressed throughout the cytoplasm, however morphology was not altered compared to untransduced cells, and the presence of eGFP confirmed successful transduction. Viability of transduced cells was therefore then measured using the Bright-Glo™ Luciferase Assay System (Promega). Bright-Glo is a lytic assay containing luciferin substrate which oxidises in the presence of oxygen and ATP. Luciferase catalyses luciferin oxidation, causing the emission of luminescent signal equating to viability.

Luminescence of transduced cells (referred to here as WK1-luc) was quantified using a luminometer to determine the relationship between cell number and luminescent signal. When WK1-luc spheroids were treated with Bright-Glo and luminescence measured, only a moderate linear relationship (r^2= 0.7385) was observed between cell count and luminescent signal. Higher cell count did not always lead to increased luminescent signal, with decreases in mean RLU from $1x10^4$ to $1.5x10^4$ cells and from $2x10^4$ to $2.5x10^4$ cells, and high variance noted between spheroids of the same size [Supplementary Figure 4.2]. Despite visual confirmation of cell lysis in plate wells, thorough pipette mixing of assay reagents, increased assay incubation time, and use of an alternative luciferase-positive cell line, issues persisted across technical replicates. Hypothesising that the plate reader was insufficient for measuring 3D culture viability using the Bright-Glo assay, an alternative luminescence quantification method was next tested.

The IVIS Lumina X5 preclinical imaging system (PerkinElmer) enables high-throughput imaging of fluorescent or luminescent 3D structures. Although primarily used for

tracking tumour development in animal models, *in vitro* applications have been reported [Zhang Y 2024]. Photographic images of spheroids with a luminescent overlay were acquired at 30 second intervals, and regions of interest (ROIs) drawn to encompass each well. As the area of each ROI was the same across the plate, total flux (photons/second, p/s) was selected as the unit of measurement. WK1-luc spheroids were assessed by Bright-Glo with the IVIS platform, and demonstrated strong correlation between spheroid cell count and total flux [Figure 4.5]. Importantly, no luminescent signal was produced by luciferase-negative cells, so SJH1, DIPG17, and DIPG24 cells were also transduced and analysed (SJH1-luc and DIPG24-luc transduced by Dr Yuyan Chen), and this method was used for subsequent experiments.

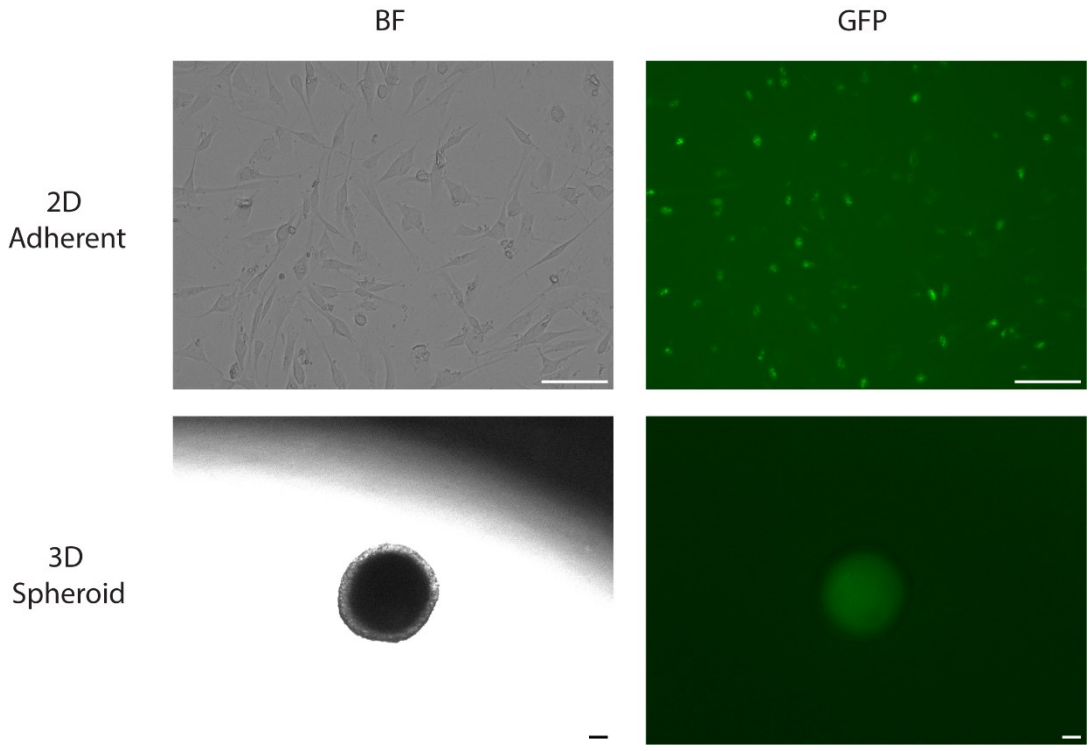

Figure 4.4 - eGFP expression in patient-derived cell lines.

Representative images of DIPG17-luc cells cultured as 2D adherent monolayer and 3D tumour spheroid. Bright-field (BF) images show cells retained original morphology post-transduction. Epifluorescence images with a FITC filter enabled monitoring of the eGFP reporter. 2.5X magnification, scale bars = 100µm (3D spheroids), 500µm (2D adherent).

A

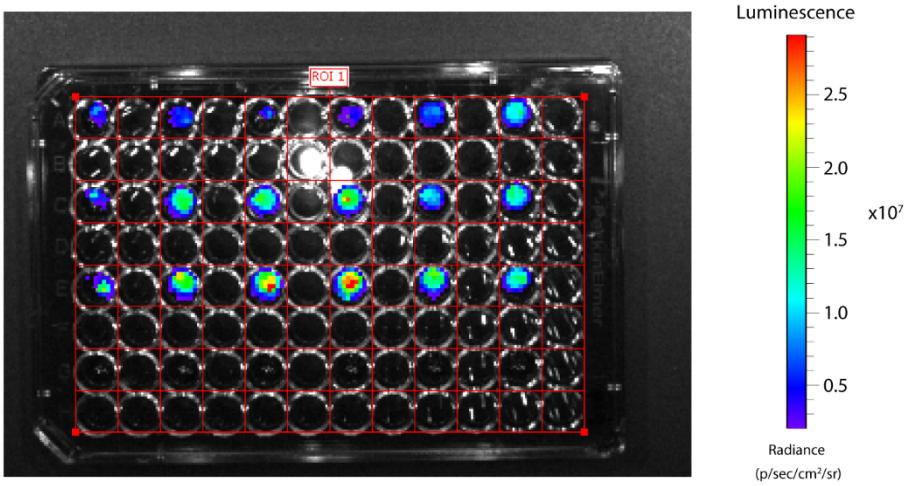

B

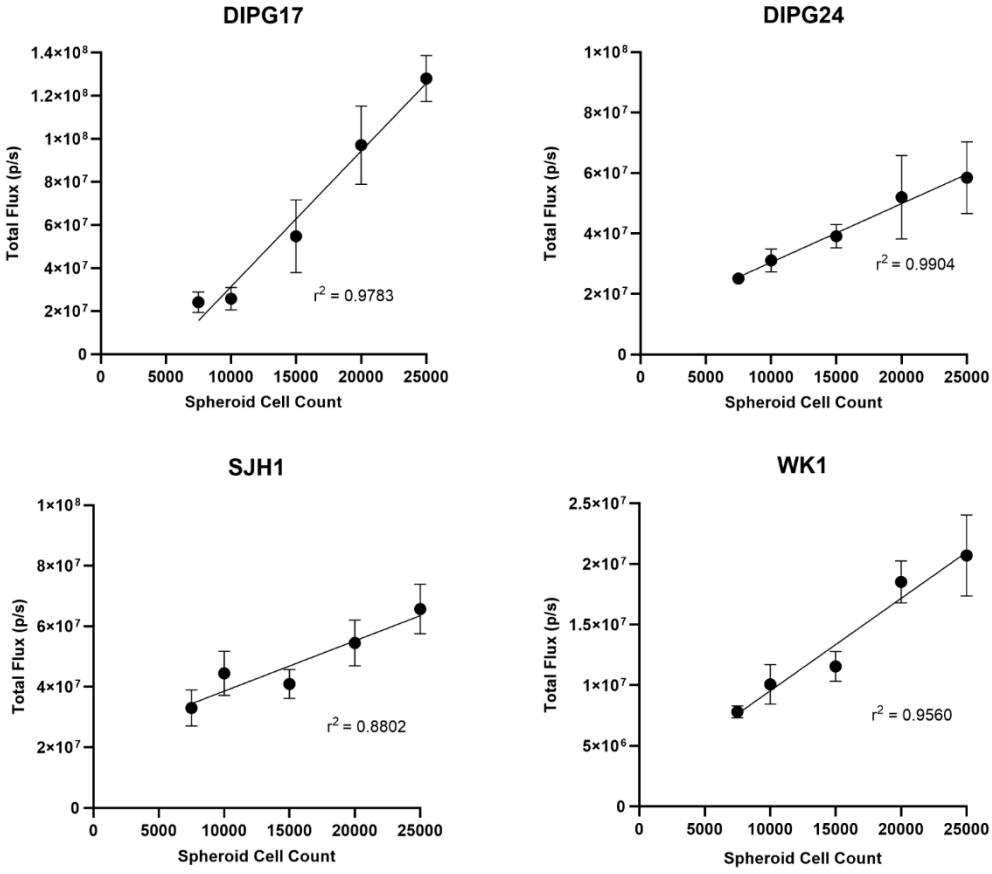

Figure 4.5 - Luciferase expression recorded with IVIS preclinical image system. (A) Representative photograph of DIPG17 spheroids with luminescent overlay acquired 3 minutes post-substrate addition by IVIS system. Colour scale corresponds to luminescent signal in radiance (p/sec/cm^2/sr). 12 x 8 ROI grid was drawn over the plate wells to define regions in which total flux (p/s) was calculated. **(B)** Graphs show linear association between spheroid cell count and total flux. Variable signal intensity was recorded between cell lines. Values are mean ± SEM, n = 3.

4.2.4 - Cell line- and donor-dependent CAR-T efficacy against tumour spheroids

A concentration gradient forms in 3D spheroid cultures**,** with outer proliferative layers receiving higher concentrations of nutrients, growth factors, and oxygen from their environment, and inner layers receiving lower concentrations, giving rise to quiescence and necrosis. In a similar manner, the drug concentrations vary through the spheroid, with decreasing concentrations closer to the core, in turn decreasing overall sensitivity to treatment. Prior to evaluating CAR-T efficacy in tumour spheroids, it was anticipated that adjustments to the E:T ratio and treatment duration would be required to achieve a response comparable to that observed in 2D monolayers.

Luciferase-expressing cells were seeded at $1.5x10^4$ cells and maintained for 96 hours for aggregation to form spheroids. To account for proliferation when calculating E:T ratios, representative spheroids were dissociated and mean cell counts obtained. Based on these calculations, CAR-T cells were added to spheroids at ~2:1 E:T ratio and monitored daily. As allogeneic CAR-T cell therapies are known to have variable potency dependent upon the donor, CAR-T cells and untransduced T cells from multiple donors were used for a comprehensive assessment of efficacy.

Bright-field images showed spheroids gradually losing integrity upon CAR-T cell exposure over 72 hours, with several segments of the spheroid breaking apart from the main structure [Figure 4.6A]. For visual confirmation that this process was being driven by treatment, CAR-T cells and control T cells were stained with CellTracker™ Deep Red fluorescent probes (Thermo Fisher) prior to co-culture with spheroids. Epifluorescence imaging revealed the tagged CAR-T cells penetrating spheroids within 24 hours, and present throughout inner regions after 72 hours. Untransduced T cells were noted in spheroids after

72 hours, but accumulated in far fewer numbers and did not prompt substantial disruption of spheroid stability [Figure 4.6B].

Imaging results informed the decision to measure tumour spheroid viability 72 hours post-treatment using the Bright-Glo assay and IVIS system. Variability in spheroid size was highlighted by total flux measurements of untreated control spheroids; hence a minimum of three spheroids were assessed per condition, per experiment. CAR-T treatment induced significant cytotoxicity across all cell lines to varying extent, and differences were noted between T cell donors. DIPG17-luc appeared the most sensitive to EphA2 CARs, with near-complete killing in all replicates (Donor 1; $p = 0.0003$, Donor 2; $p = 0.0002$). WK1-luc spheroids were equally sensitive across both donors (Donor 1; $p = 0.0267$, Donor 2; $p = 0.0022$), however statistically significant results were only achieved with one donor against DIPG24-luc spheroids (Donor 1; $p = 0.0008$) [Figure 4.7]. Non-specific effects from untransduced T cells were observed in both DIPG17-luc and WK1-luc spheroids. Interestingly, DIPG24-luc exposed to control T cells from two separate donors showed increased total flux values compared to untreated spheroids. Overall, greater resistance to treatment was observed in 3D spheroids than 2D monolayers.

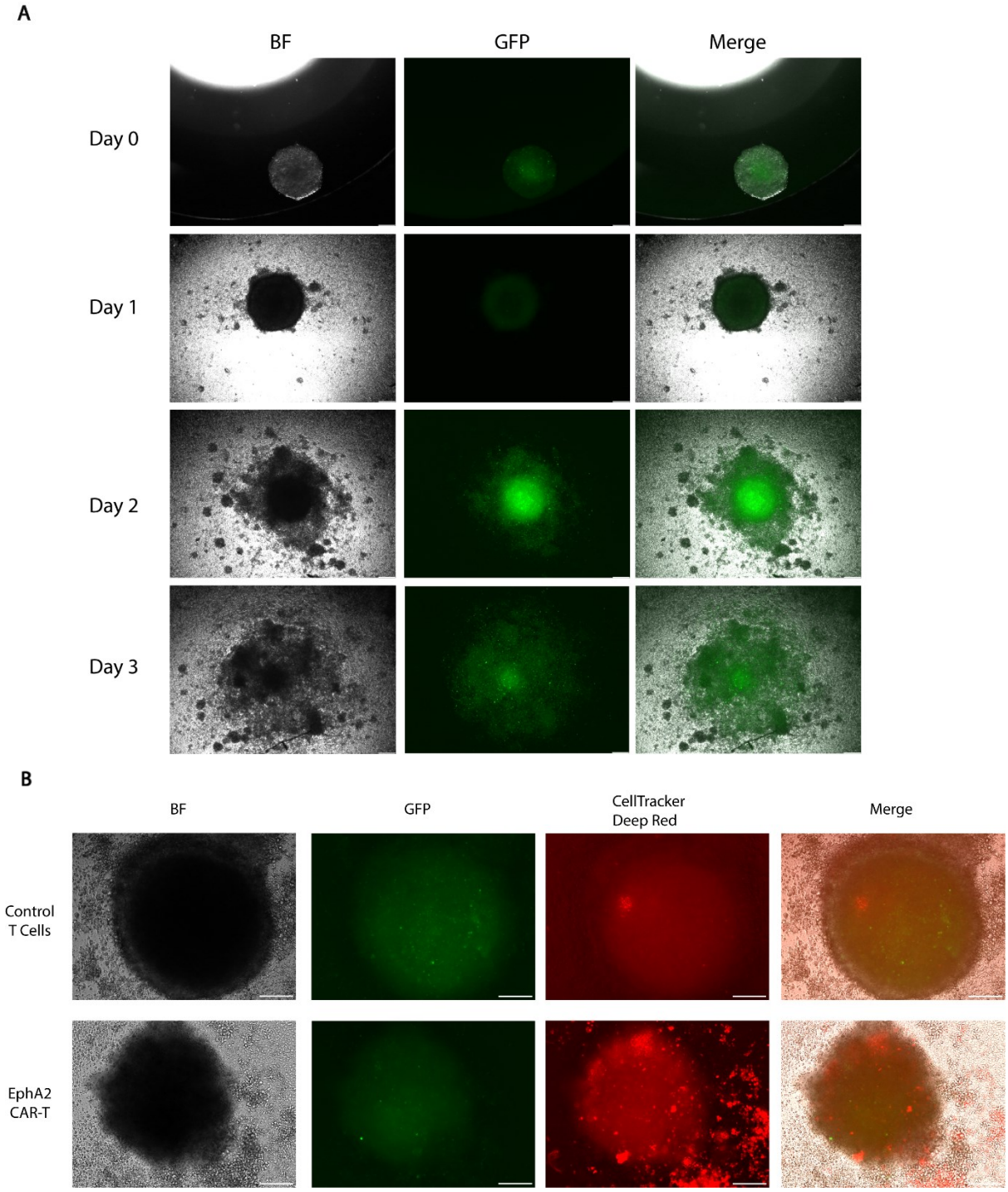

Figure 4.6 - CAR-T cells target and kill cells grown as tumour spheroids. (A) DIPG24-luc spheroids (n = 3) were treated with EphA2 CAR-T cells at 2:1 E:T ratio. Images show representative response over 72h treatment duration with disruption and dispersal of tumour bulk. **(B)** T cells were tagged with CellTracker Deep Red fluorescent probes and added to DIPG17-luc spheroids. Images were acquired at 72h demonstrating CAR-T cell (red) infiltration and disruption of spheroid integrity. Scale bars = 200µm.

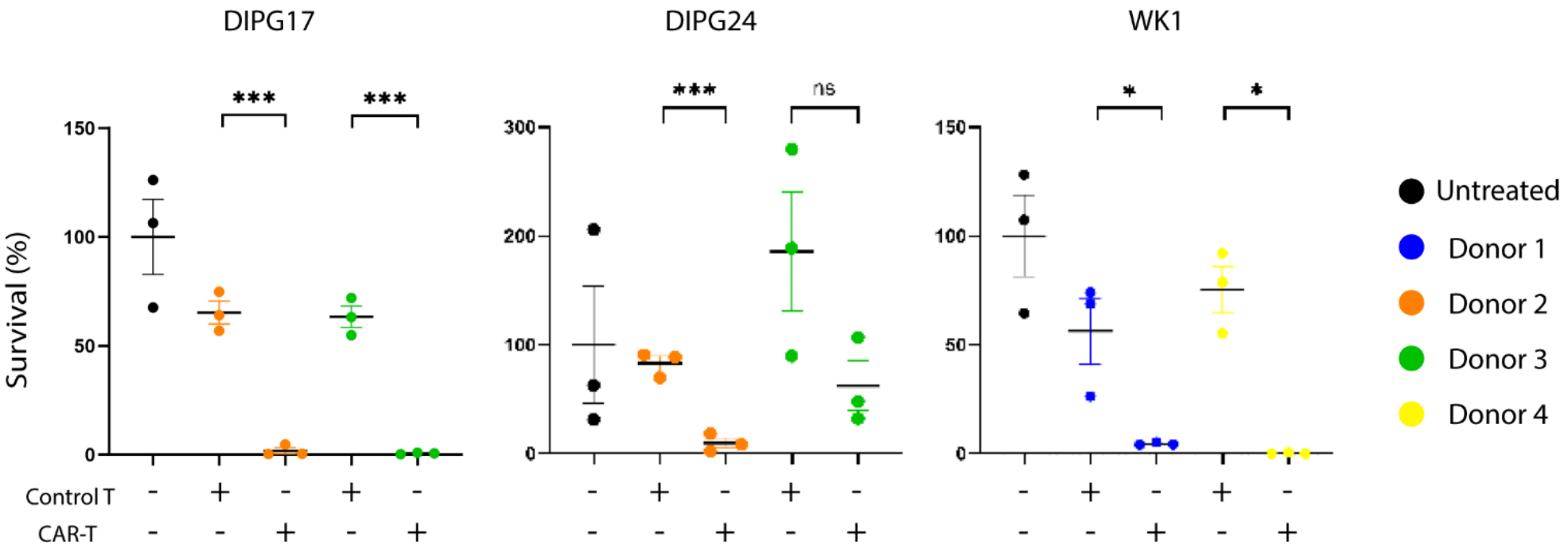

Figure 4.7 - Cell line- and donor-dependent responses in 3D tumour spheroids.

Tumour spheroids were treated 2:1 with EphA2 CAR-T cells or control T cells for 72h, and viability measured using Bright-Glo and IVIS preclinical image system. Survival was calculated by comparing total flux (p/s) relative to mean values of untreated spheroids. Data was collected from $n = 1$ independent experiment with $n = 3$ spheroids per condition per cell line. Results were analysed using unpaired t-test, with statistical significance denoted by *p<0.05, **p<0.02, and ***p<0.0005. Error bars indicate mean ± SEM.

4.2.5 - Decreased treatment sensitivity in assembloid co-culture models

The use of 2D adherent monolayers and 3D spheroids presumes the existence of tumour cells in isolation. As discussed in Chapter 1.3.4, tumour spheroids and cortical organoids can be co-cultured to form assembloids, accounting for the invasive nature of pHGGs and changes to signalling pathways that occur in the *vivo* brain tumour microenvironment [Prior 2024]. Assembloids also provide a brain-like tissue mimetic through which CAR-T cells must infiltrate to reach target cells, modelling a key obstacle in their translation to treatment of solid tumours *in vivo*. Therefore, the efficacy of EphA2 CAR-T cells was next assessed in luciferase-expressing HGG lines co-cultured with cortical organoids in assembloid models.

Cortical organoids were generated as outlined in Chapter 3 and cultured for 16 days. Coinciding with the final 4 days of cortical organoid generation, separate tumour spheroids were formed. Subsequently, the spheroids were added to organoids to form assembloids, monitored by eGFP imaging. Within 24 hours, DIPG24-luc and WK1-luc cells began disseminating through adjacent regions of the organoid. After 7 days, the tumour spheroid structures were no longer distinguishable and tumour cells had infiltrated throughout the organoid. Conversely, DIPG17-luc exhibited minimal invasion and spheroids largely retained their structure engrafted to the organoid [Figure 4.8].

Initial luminescence recordings from the IVIS showed higher total flux values in control assembloids compared to matched control spheroids cultured for the same duration. Literature has reported upregulation of growth regulation genes when tumour cells invaded and formed networks within GBM-cerebral organoid co-cultures [Krieger 2020]**.** Therefore, it was hypothesised that the increased luminescent signal observed in the assembloid might be due to increased tumour proliferation within the brain-like microenvironment. However,

when assembloids and spheroids were separately dissociated and sorted for GFP expression, there were no significant differences in cell count between the two models, thus proliferation does not appear to be different between the two culture conditions and cannot explain the higher luminescence seen in the control assembloids. Nonetheless, confirmation of target cell count informed an accurate estimation of E:T ratios for assembloid treatment.

When grown as spheroids, DIPG17-luc cells displayed the greatest sensitivity to CAR-T treatment, so the 2:1 E:T ratio was maintained when treating DIPG17 assembloids. Decreased sensitivity to CAR-T treatment was observed in assembloids, with CAR-T cells derived from only one donor causing statistically significant cytotoxicity. We tested a 2:1 E:T ratio in DIPG24 assembloids without effect, prompting an increase to 10:1. Higher effector concentrations led to more efficient CAR-T response, though matched concentration of untransduced T cells also resulted in increased non-specific killing, but importantly this effect was significantly less than that induced in the presence of the CAR-T cells. A range of E:T ratios were tested against WK1 assembloids however no significant cytotoxicity was observed by Bright-Glo assay and response did not improve with increasing E:T ratio, despite the appearance of cellular debris shed from assembloids [Figure 4.9].

To verify that the luciferase reporter was continuing to function as intended, WK1-luc spheroids and adherent monolayers were acutely treated with hydrogen peroxide, sodium hypochlorite, or ethanol, or treated for 24 hours with doxorubicin. Total flux values were reduced upon doxorubicin treatment, and luminescent signal completely eliminated following chemical exposure, indicating that the reporter remained functional [Figure 4.10].

We investigated whether the decreased treatment sensitivity in assembloids was caused by the inability of CAR-T cells to penetrate the culture and reach target tumour cells. T cells were stained with CellTracker™ Deep Red probes as previously outlined, then added

to DIPG17 assembloids in which spheroid and organoid boundaries remained relatively discrete. After 24 hours, assembloids were fixed, cryosectioned, and imaged with the epifluorescence microscope. CAR-T cells tagged with CellTracker were localised within the eGFP-positive tumour spheroid regions of the assembloid, with minimal off-target presence in the cortical organoid. As with spheroid-only imaging, control T cells were mostly absent and confined to the outer perimeter [Figure 4.11]. These results suggested CAR-T cells were capable of accumulating in the tumour with limited targeting of adjacent normal tissue.

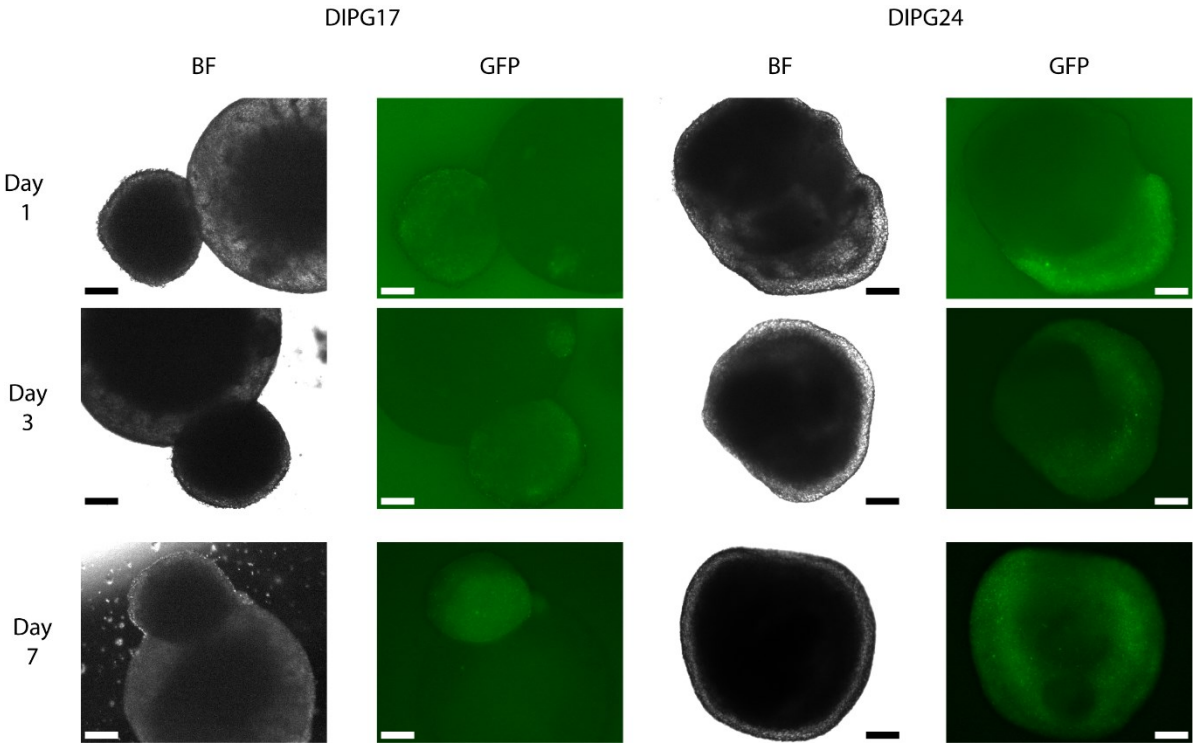

Figure 4.8 - Tumour cells display differential patterns of invasion through organoids. Epifluorescence imaging of live assembloids over 7 days of co-culture. Tumour spheroid invasion into the cortical organoid component was monitored every 1-2 days by eGFP expression. Images displayed are representative of n = 18 assembloids per cell line. Scale bars = 200µm.

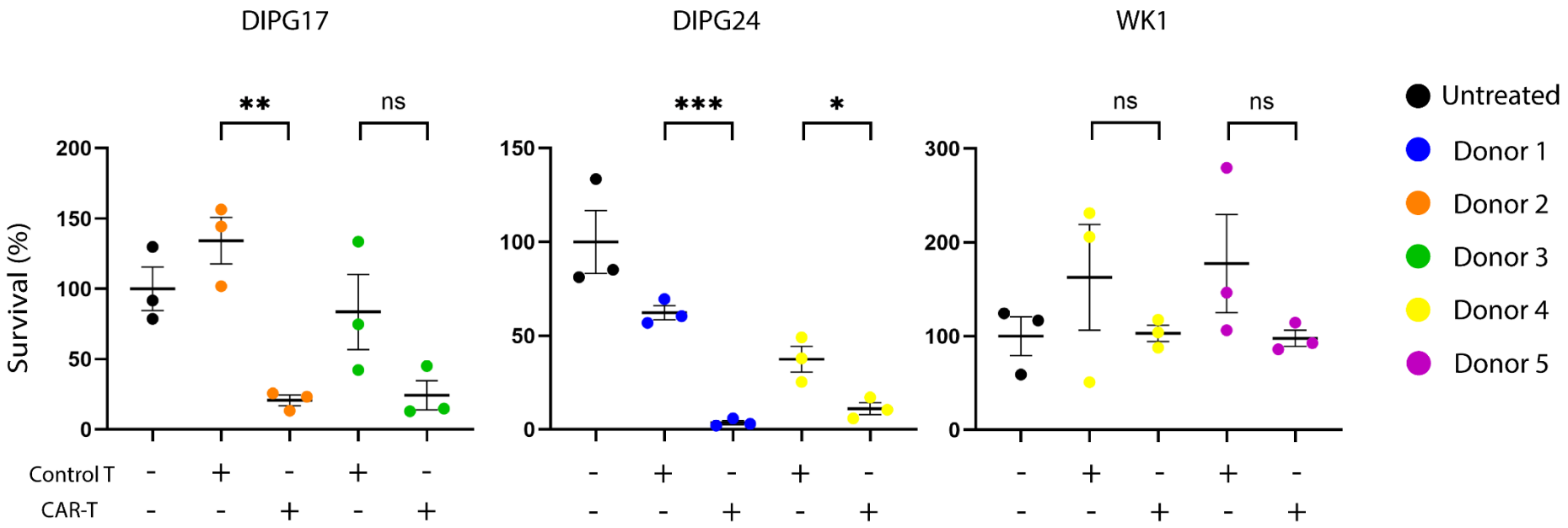

Figure 4.9 - Assembloid co-cultures demonstrated increased resistance to CAR-T treatment.

Assembloids were treated with CAR-T cells or control T cells at 2:1 (DIPG17), 6:1 (WK1), and 10:1 (DIPG24) E:T ratios for 72h. Survival was calculated by comparing total flux (p/s) relative to mean values of untreated spheroids. Data was collected from $n = 1$ independent experiment with $n = 3$ assembloids per condition per cell line. Results were analysed using unpaired t-test, with statistical significance denoted by *$p<0.05$, **$p<0.02$, and ***$p<0.0005$. Error bars indicate mean ± SEM.

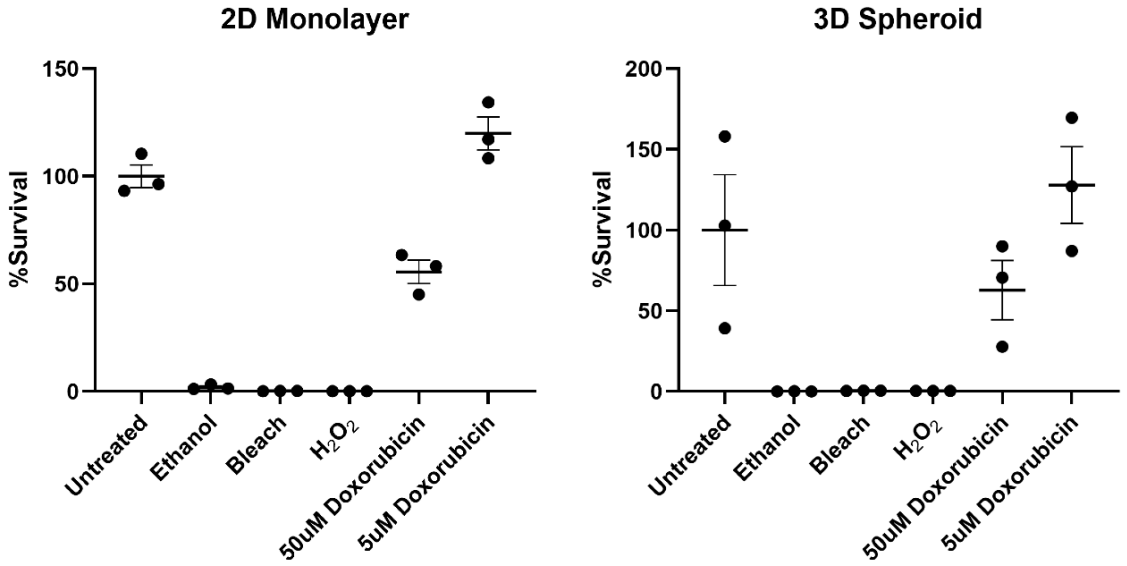

Figure 4.10 - Bright-Glo luminescent signal corresponds to cell viability.

Bright-Glo luminescent signal was validated against WK1-luc cells treated with ethanol, bleach, hydrogen peroxide H_2O_2, and 50μM and 5μM doxorubicin. 1 x 10^4 cells were seeded as 2D monolayers and 3D spheroids, then exposed to conditions for 24h. Bright-Glo assay was added and signal recorded in the IVIS preclinical imaging system. Survival was calculated by comparing total flux (p/s) relative to mean values of untreated conditions. $n = 1$ independent experiment with $n = 3$ adherent/spheroidal cultures per condition. Errors bars indicate mean ± SEM.

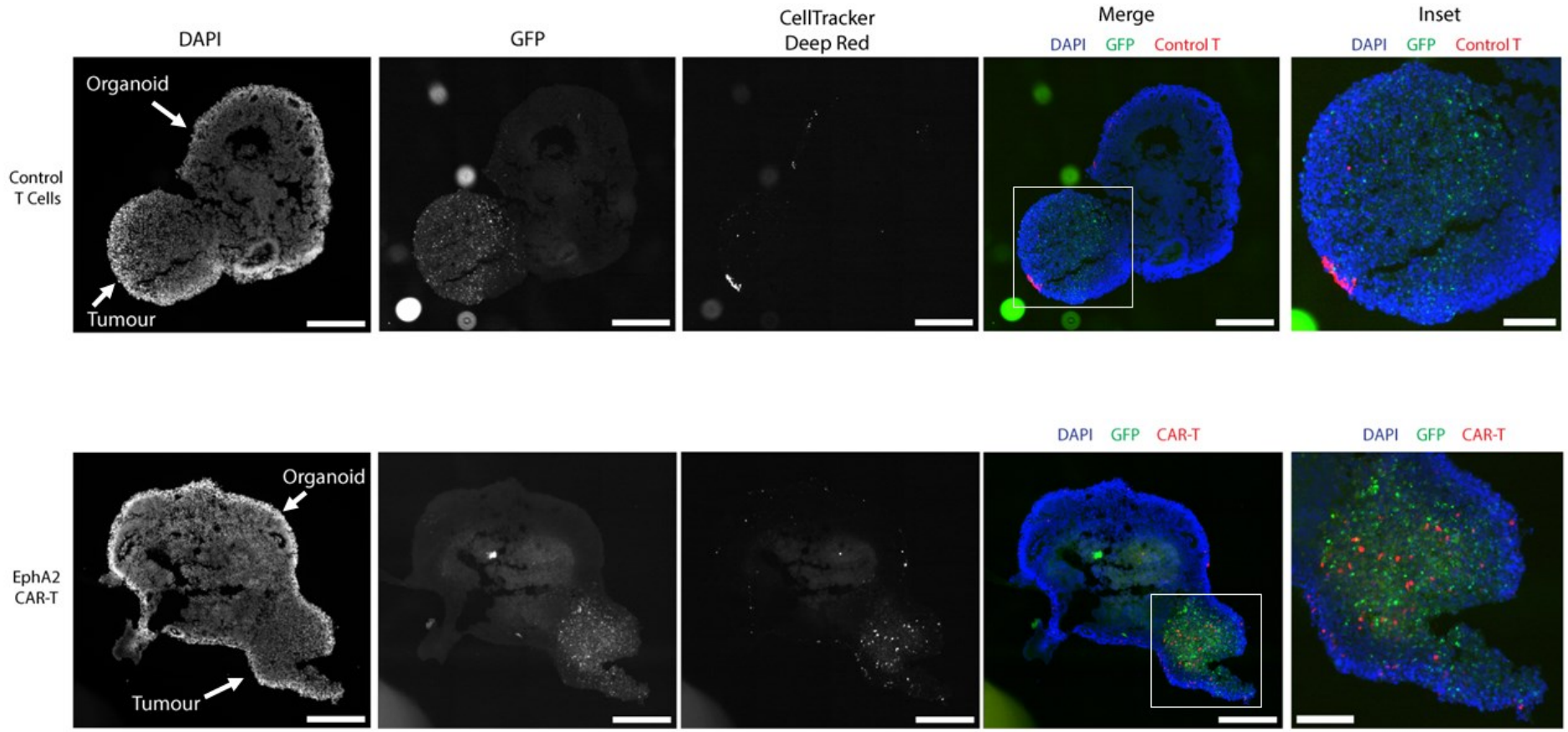

Figure 4.11 - EphA2 CAR-T cells target tumour component of assembloids. Epifluorescence images of DIPG17 assembloids following 24h treatment with 2:1 CellTracker™-tagged CAR-T cells or control T cells. Assembloids were fixed in PFA, cryosectioned, and nuclei stained with DAPI (blue) to assist with visualisation. Images show CAR-T cells (red) infiltrating the GFP-expressing tumour (green) of the assembloid, while remaining largely absent in the remaining cortical organoid component. $n = 3$ assembloids for both CAR-T cells and control T cells. Scale bars = 250µm (whole assembloid images), 100µm (inset images).

4.2.6 - T-cell mediated cytotoxicity confirmed by cytokine release

T lymphocytes recognise target antigens, switching to an activated state, forming an immunological synapse with the target cells, and secreting cytokines to recruit the endogenous immune response and induce cytotoxicity. Pro-inflammatory cytokines, such as interleukins IL-2, IL-6, and IL-17A, interferon-gamma (IFN- γ), and tumour necrosis factor alpha (TNF-α), promote T cell proliferation and survival, activate macrophages, and induce apoptosis in tumour cells. Direct cytotoxic mechanisms also include the release of secretory granules containing perforin and granzyme proteins. Perforin forms pores in the target cell membrane, through which granzymes are trafficked and induce apoptosis in the target cell [Voskoboinik 2015, Silveira 2022].

To confirm that tumour cell death in spheroids and assembloids resulted from CAR-T cell-mediated cytotoxicity, culture medium was collected from representative spheroids and assembloids 24 hours post-administration. Cytokine concentrations were then quantified using the LEGENDplex™ human CD8/NK multiplex panel (BioLegend), utilising fluorescence-encoded beads to simultaneously characterise expression of 13 proteins by flow cytometry (performed by Dr Suat Dervish, Westmead Cytometry).

Highly elevated levels of IFN-γ confirmed potent CAR-T activation in treated cultures, while CTL-mediated cytotoxicity was evidenced by increased concentration of granzymes and perforin. Expression and secretion of interleukins and TNF-α in CAR-treated cultures were suggestive of induction of inflammatory responses that would lead to subsequent T cell activation, proliferation, and differentiation *in vivo* [Figure 4.12]. In summary, cytokine results confirmed EphA2 CAR-T cells were effectively activated, responsible for inducing apoptosis and cytolysis in target tumour cells, and demonstrating potential for endogenous immune cell recruitment and persistent response.

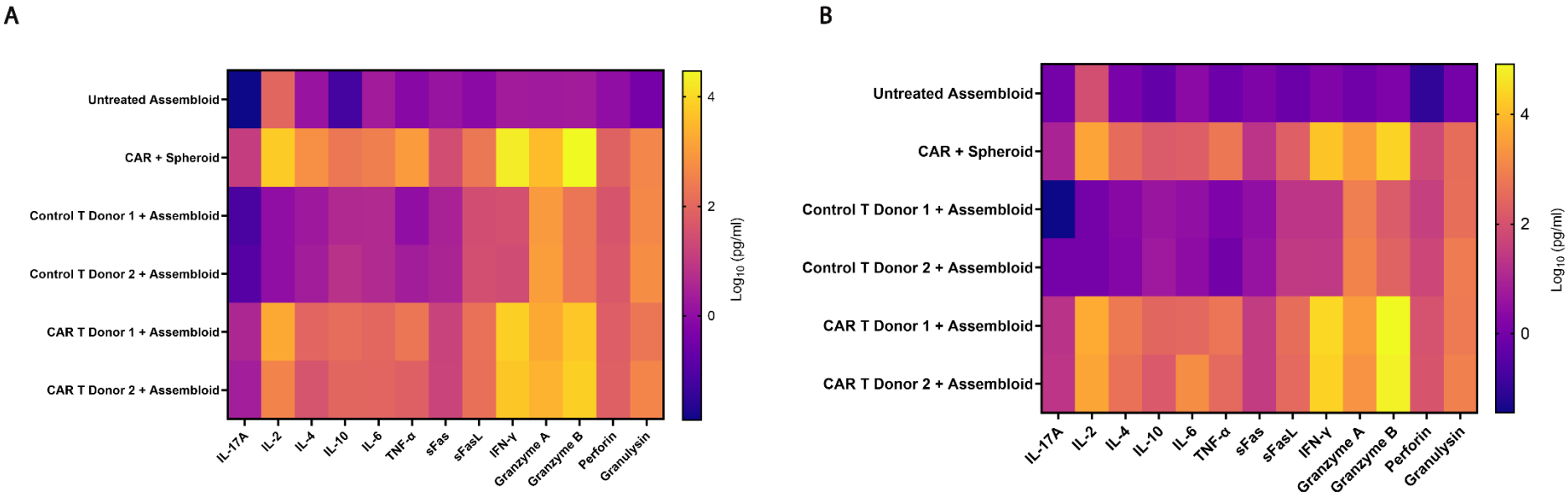

Figure 4.12 - CAR-T activation and cytotoxicity indicated by cytokine release. Heat maps showing normalised concentrations of pro-inflammatory and pro-apoptotic cytokines associated with T cell activation and cytotoxicity. **A.** 7.5 x 10^3 WK1-luc cells were seeded as spheroids, and either cultured separately or added to cortical organoids to form assembloids. CAR-T and untransduced control T cells were added at 2:1 E:T ratio. **B.** 1.5 x 10^4 WK1-luc cells were cultured as spheroids and in assembloids, and treated with CAR-T and untransduced control T cells at 3:1 E:T ratio. Culture medium was collected 24h post-administration and cytokine concentration measured with the LEGENDplex™ human CD8/NK multiplex panel. n = 1 independent replicate.

4.3 - Chapter Discussion

Elevated EphA2 expression in HGG has prompted the development of therapeutic interventions to inhibit kinase activity or direct treatment to EphA2 antigen-expressing tumour cells. Our EphA2 CAR-T cell therapy demonstrated *in vitro* efficacy against DIPG and GBM patient-derived cell lines, as evidenced by an optimised viability assay and cytokine release. Although 2D monolayers were efficiently cleared by CAR-T cells, treatment sensitivity was reduced when tumour cells were cultured as 3D spheroids. Model complexity was advanced through the use of assembloid co-cultures to better represent the complexity of the brain tumour microenvironment *in vivo*, leading to a further decrease in treatment sensitivity.

4.3.1 - EphA2 CAR-T cell design and manufacture

In this thesis, GBM and DIPG cell lines were efficiently killed by EphA2-directed CAR-T cells under 2D monolayer conditions. Significant cytolysis was measured across all replicates, with near-complete killing observed within 24 hours at 1:1 and 1:3 E:T ratios, and within 72 hours for more dilute CAR-T cell concentrations. These results align with data from other EphA2 CAR-T cell therapies tested against *in vitro* models of glioma [Table 4.1].

While comparisons of efficacy between studies is complicated by differences in experimental design, this research demonstrated some improvements over previously published work. In the literature, continually-cultured cell lines comprised the majority of target cells against which therapies were evaluated. These included glioma cell lines U87, U251, and U323, as well as leukaemia cell lines BV173 and K562 which were transduced to express the target antigens. As discussed in Chapter 1.3.1, continually-cultured cell lines do not adequately represent the primary tumour sample, and decades of sub-culture have driven clonal selection, loss of heterogeneity, and cell line variability between institutions. Patient-

derived lines used here are routinely validated against the original tumour sample, retaining much of their original heterogeneity, and treatment responses are expected to more closely resemble effects *in situ.*

Different methodologies have been implemented to measure viability of glioma cells *in vitro* across publications. Chromium release assays were considered the gold standard in T cell cytotoxicity assays and feature in early EphA2 CAR-T studies. In these studies, target tumour cells are loaded with radioactive ^{51}Cr isotopes which are released into culture medium upon cell death and quantified with a gamma counter. When measuring cytotoxicity induced by EphA2 CARs, chromium release assays were performed 4 hours post-treatment. Although significant differences were observed between treatment conditions, researchers extrapolated data assuming cytotoxicity would persist until complete killing occurred treatment [Chow 2013, Yi Z 2018]. In instances where patient-derived cell lines are used, heterogeneous cellular population and antigen expression could lead to some survival otherwise unaccounted for. Furthermore, under certain conditions, treatment concentrations as high as 40:1 were required to elicit a significant response detectable with this method [Chow 2013].

Chromium release assays have since been superseded by non-radioactive approaches with improved signal-to-noise ratio and which provide viability measurements at multiple time points, including real-time cell analysis (RTCA) systems and bio-luminescent imaging [Cerignoli 2018, Karimi 2014]. Recent EphA2 CAR-T studies have used these methodologies, thus allowing for comparison with the results presented in this thesis. For example, An et al. evaluated efficacy of CAR constructs specific to separate EphA2 epitopes using xCELLigence and luciferase-based imaging methods. When treating U251, U373, and U87 cell lines, their optimal CAR required between 2.5:1 and 10:1 E:T ratios to clear tumour cells *in vitro* [An 2021]. These concentrations were maintained when assessing CARs with B cell stimulation in a follow-up study from the same group [Zhang Y 2024]. We attained

comparable levels of cytotoxicity against adherent cells at much lower E:T ratios, suggesting our EphA2 CAR-T cell therapy has a more potent effect than those previously described in the literature. Another possible explanation is that the patient-derived cell lines used in this thesis were more sensitive to treatment than continually-cultured cell lines which may have adopted strategies to resist cell death following prolonged culture.

Various factors in the design and manufacture of CARs may account for the differences between our data and other reported findings. These include the affinity of the single-chain variable fragment (scFv) to the target antigen, selection of costimulatory domains, differences in donor T cell populations, and culture conditions during expansion.

The second-generation CAR construct used here comprised a synthetic 4H5 scFv specific to EphA2, located upstream from a IgG1-derived short spacer region. Initial EphA2 CARs used a CH2CH3 spacer, however the presence of Fc receptor binding sites made T cells susceptible to inhibition by Fc receptor-expressing immune cells, and so were removed from subsequent designs. In mouse models, this modification to the spacer region yielded similar treatment efficacy at a 20-fold lower dosage, reducing the risk of CRS and related side effects [Chow 2013, Yi Z 2018]. Intracellular costimulatory domains enhance CAR-T cell cytotoxicity and survival, as well as activate signalling pathways responsible for immune cell recruitment and cytokine release. When designing EphA2 CARs, researchers have used combinations of CD3, CD28, CD134, and 4-1BB (CD137). In other constructs and cancer types, such as CD19 CARs for leukaemia, selection of different costimulatory molecules has conferred more rapid cytotoxicity or improved persistence of CAR-T cells [Zhao X 2020]. The cost of manufacturing and assessing multiple treatments simultaneously is often prohibitive, and has not been extensively investigated in EphA2 CAR-T cells targeting glioma. A single study by Yi et al. compared CD28 and 4-1BB EphA2 CARs against U373 GBM cells, observing no differences to cytotoxicity or persistence in either *in vitro* or *in vivo*

xenograft models. As 4-1BB has been shown to improve persistence in other cancer models, the authors opted for CD28 instead, citing potential safety concerns [Yi Z 2018]. Our CAR construct was initially designed for sarcomas, and comprises both CD3ζ and 4-1BB costimulatory domains. The only clinical trial described to-date for EphA2 CARs against adult recurrent GBM used the same combination, reporting moderate CRS in two patients which resolved following dexamethasone treatment, and no neurotoxicity. CAR-T cells were shown to expand 7-10 days following intravenous administration, and persisted for at least 4 weeks in CSF [Lin Q 2021]. While safety and persistence of CD3ζ and 4-1BB CARs appears acceptable, more research is required to determine co-stimulation for optimal efficacy in this context.

Another major determinant in treatment efficacy is the cellular composition of CAR-T therapies. PBMCs are isolated from peripheral blood, then T cells are activated and enriched by plate-bound antibodies or antibody-coated magnetic beads, with the latter preferred due to increased activation and generation of less differentiated and less senescent T cells [Stock 2019]. Once enriched, T cells are expanded and their phenotype analysed prior to cytotoxicity assessment. The CD4:CD8 ratio of administered CAR-T cells is an important factor in treatment response, particularly *in vivo*. A balance is required between the cytokine production and proliferative capacity of CD4+ cells and the specific cytolytic activity of CD8+ cells to constitute an ideal CAR-T product [Turtle 2016, Galli & Bellesi 2023]. The proportion and health of CD4+ and CD8+ cells varies between individuals, depending upon variables such as age, antigen exposure, and the history of lymphodepletion therapies for autologous donors. Ensuring precise CD4+ and CD8+ counts adds to manufacturing cost and complexity, and has not been conducted for *in vitro* assessment of EphA2 CAR-T cells against glioma [Table 4.2].

More recently, there has been a focus on selecting for specific T cell subpopulations, particularly naïve-like T cells (T_N) and stem cell memory-like T cells (T_{SCM}). These cell types are closely associated with self-renewal, survival, and differentiation into various effector cells upon antigen recognition [Locke 2020]. High expression of $T_{N/SCM}$ improves treatment persistence *in vivo*, leading to a greater overall response against leukaemia and lymphoma cells than more differentiated CAR-T populations [Arcangeli 2022, Wang Y 2023]. In contrast, $T_{N/SCM}$ were less effective in killing CD19+ leukaemia cells *in vitro* than unselected bulk CAR-T cells [Arcangeli 2022]. Variance in these T cell subtypes likely contributed to differences in EphA2 CAR efficacy, however the characterisation of $T_{N/SCM}$ cells is under-reported and not performed in this thesis. Further research to optimise EphA2 CAR-T cell composition may be required when progressing to mouse models to address the issue of glioma recurrence frequently observed *in vivo*.

Table 4.1 - Cytotoxicity assays evaluating EphA2 CAR-T cell therapies against *in vitro* models of glioma

***In Vitro* Culture Models**	**Cell Lines**	**E:T Ratios**	***In Vitro* Viability Measurement**	**Treatment Duration**	**Efficacy Details**	**Authors**
2D adherent, 3D neurospheres	U373.eGFP.FFLuc, U87.eGFP.FFLuc, Primary GBM cells	Adherent: 5:1, 10:1, 20:1, 40:1 Neurospheres : 10:1	Adherent: Chromium-51 (^{51}Cr) release assay Neurospheres: GFP expression by microscopy and FACS analysis	Adherent: 4 hours Neurospheres: 4-6 days	Significant killing against U373 ($P < 0.0004$) and U87 ($P < 0.002$)	Chow 2013
2D adherent	U373.eGFP.FFLuc, A549, EphA2-expressing BV173	10:1	^{51}Cr release assay, in absence or presence of rituximab and complement	4 hours	No significant difference in cytotoxicity between costimulatory domains	Yi Z 2018
2D adherent	EphA2-expressing K562	0.1:1, 0.3:1, 1:1	Calcein-AM	4 hours	Significant dose-dependent lysis (0.1:1; $P < 0.01$, 0.3:1 and 1:1; $P < 0.0001$).	Lin Q 2021
2D adherent	U251.eGFP.FFLuc, U373.eGFP.FFLuc,	1:1, 2.5:1, 5:1, 10:1	xCELLigence	24 hours	Significant differences between CARs binding EphA2 epitopes	An Z 2021
2D adherent	IL13Rα1-, IL13Rα2-, and EphA2-expressing K562, U373.eGFP.FFLuc	1:1, 2:1, 3:1, 4:1, 5:1, 10:1, 15:1, 20:1	LDH release assay	24 hours	Improved cytotoxicity from TanCARs targeting both IL13 and EphA2 compared to single-specificity CARs.	Muhammad N 2022

2D adherent	U251.eGFP.FFLuc, U373.eGFP.FFLuc, Autologous B cells	1:1, 5:1, 10:1 with target cells 1:1 with B cells	Luciferase via IVIS imaging, LDH release assay, xCELLigence	24 hours (LDH) 70 hours (xCELLigence)	CAR-T cells stimulated by B cells exhibited higher cytotoxicity and persistence.	Zhang Y 2024

Table 4.2 - EphA2 CAR-T Manufacturing and Expansion Protocols

Donor T Cells	Enrichment	CAR Sequence	CAR Transduction	CAR-T Cell Population	T Cell Culture Medium	Authors
PBMCs derived from normal healthy donors	OKT3 and CD28 antibody-coated plates. 50-100 U/ml IL-2	4H5 EphA2 scFv upstream from IgG1-CH2CH3 domain, CD28 transmembrane domain, and CD28 and CD3-ζ co-stimulatory endodomains.	SFG retroviral vector. Median 73.2% CAR expression.	43.4% CD4+ 61.3% CD8+	RPMI or DMEM, 10% FBS, 2mM GlutaMax	Chow 2013
PBMCs derived from normal healthy donors	OKT3 and CD28 antibody-coated plates. 10ng/ml IL-7, 5ng/ml IL-15	4H5 EphA2 scFv upstream from IgG1 short-spacer domain, CD28 or CD8α transmembrane domain, and CD28ζ, 4-1BBζ, or CD28.4-1BBζ endodomain.	RD114-pseudotyped retroviral particles on RetroNectin-coated plates.	CD4:CD8 ratio of 1:3	RPMI or DMEM, 10% FBS, 2mM GlutaMax	Yi Z 2018
PBMCs derived from three GBM patients for autologous CAR-T cell manufacture	CD3/CD28 CTS Dynabeads 200U/ml IL-2	EphA2 scFV, CD8 hinge and transmembrane domain, 4-1BB and CD3-ζ co-stimulatory endodomains.	Lentiviral vector with puromycin cassette. 5-12.8% transduction efficiency	Mean 0.149 CD4:CD8 ratio. Mean 94.36% CD28+ Mean 87.11% CD62L+	TexMACS™, 200U/ml IL-2	Lin Q 2021

PBMCs derived from normal healthy donors	CD3/CD28 beads	D2-1A7 or D2-1B1 EphA2 scFv, CD28 transmembrane domain, CD28.41-BBζ co-stimulatory endodomain.	SFG retroviral vector. Approximately 30% transduction efficiency.	Not directly specified - similar CD4:CD8 ratio between the two EphA2 epitope-targeting CARs.	X-VIVO™15 serum-free medium, 5% GemCell™ human serum AB, IL-2	An Z 2021
PBMCs derived from normal healthy donors	CD8+ T Cell Isolation Kit, LS Column, MidiMACS Separator. 2µg/ml soluble anti-CD3, 1µg/ml soluble anti-CD28, 100U/ml IL-2	IL13(4MS) and EphA2 (4H5) with (GGGS)3 linker in a single scFv, CD8a leader sequence, CD28 transmembrane domain, CD28, CD134, and CD3ζ co-stimulatory domains.	Lentiviral vector. Mean 89.3% TanCAR expression.	Selected for CD8+	RPMI, 10% FBS, 2mM GlutaMax	Muhammad 2022
PBMCs derived from normal healthy donors	CD3/CD28 beads	D2-1A7 EphA2 scFv, CD28 transmembrane domain, CD28.41-BBζ co-stimulatory endodomain.	SFG retroviral vector.	3.3% CD4+ CD45RO+ T_{cm} unstimulated CAR-T cells. 7.9% CD4+ CD45RO+ T_{cm} CAR-T cells stimulated with B cells	X-VIVO™15 serum-free medium, 5% GemCell™ human serum AB, IL-2	Zhang Y 2024

4.3.2 - Transitioning from 2D to 3D tumour spheroids

CAR-T therapies demonstrate efficient killing of adherent tumour cells, however these 2D models do not sufficiently account for the challenges of trafficking CAR-T cells through the solid tumour microenvironment. 3D tumour spheroids and assembloid co-cultures address this issue by presenting a concentration gradient and physical barrier through which effector cells must penetrate in order to achieve complete cytotoxicity, resembling obstacles encountered *in vivo* [Pampaloni 2007].

Tumour spheroids have been extensively investigated across numerous cancer types, and are known to present greater treatment resistance than adherent monolayers, as observed in both conventional chemotherapies and CAR-T cell therapies. Spheroids are increasingly being incorporated into drug development workflows, but concerns remain regarding reproducibility, standardised assays, and throughput [Jensen & Teng 2020, Han 2021]. We presented a luciferase-based platform which was successfully applied to GBM and DIPG cell lines, and allowed for reproducible and high-throughput assessment of viability.

As expected, all three cell lines exhibited less sensitivity to CAR-T therapy when cultured as spheroids. Adherent monolayers were completely killed within 24 hours, but CAR-T cells tagged with CellTracker™ were shown to have only reached the outer layers of imaged spheroids over the same duration. Once treatment dose and duration were increased, CAR-T cells were capable of infiltrating the inner core and greater cytotoxicity was measured as a result.

The transition to spheroidal cultures highlighted differential treatment responses between cell lines. DIPG17-luc exhibited the lowest EphA2 expression by intensity and population percentage in the flow cytometry panel, but spheroids were more sensitive to CAR-T treatment than DIPG24-luc and WK1-luc. These findings are contrary to reports in

the literature stating antigen density (which fluorophore intensity relates to) correlates with CAR-T efficacy [Majzner 2020, Walker 2017]. Spheroid size and morphological features appeared consistent across cell lines, and no clear associations could be drawn between treatment response and the clinical outcomes of the primary tumours from which cell lines were established to provide an explanation [Table 2.7].

We also investigated cytotoxicity of CARs derived from five T cell donors, with differences in effect observed between donors. This may be attributed to variance in donor characteristics, CD4:CD8 ratio, and T cell subtypes, as previously discussed. Results demonstrated that CAR-T cells from an individual donor could produce different responses between cell lines. For example, 'Donor 3' CARs induced significant killing in DIPG17-luc spheroids, but not in DIPG24-luc, whereas 'Donor 2' CARs performed equally in both cell lines. This may have implications for allogeneic CAR-T cell therapy, such as necessitating a screen of the CAR-T product against primary tumour cells prior to infusion into a patient.

4.3.3 - Assembloid co-cultures

Spheroids demonstrated key advantages over adherent monolayers, but they only model tumour tissue in isolation and do not account for the normal brain tissue through which CAR-T cells must be trafficked *in vivo*, a factor which contributes to the lack of success in solid tumours. This complex brain tumour microenvironment was recapitulated by co-culturing tumour spheroids with early-stage cortical organoids. Previous research from our lab and other institutes has shown that tumour cells infiltrate through organoid tissue, activate signalling pathways similar to those *in vivo*, and can serve as a platform for evaluating chemotherapies and radiation [Linkous 2019, Prior 2024]. We therefore sought to determine their suitability in assessing CAR-T therapies.

Our results confirmed that CAR-T efficacy was attenuated in assembloids compared with tumour spheroids. DIPG17 assembloids exhibited significant cell death at the same 2:1 E:T ratio used to treat DIPG17-luc spheroids. However, this cytotoxicity in DIPG17 assembloids was observed only with CAR-T cells derived from a single donor. In contrast, a substantial increase in the E:T ratio from 2:1 to 10:1 was required to achieve a similar killing effect in DIPG24 assembloids. Cytokine analysis also showed diminished CAR-T activation and effect in DIPG24 assembloids, compared to CAR-T-treated DIPG24-luc spheroids, with lower secretion of IFN-γ and granzyme B when the same E:T ratio was administered. No significant response could be achieved in WK1 assembloids, with around half of tumour cells persisting despite increasing CAR-T dose. Although antigen loss and escape are not characteristic of EphA2 [Chow 2013], we were unable to confirm whether antigen expression was altered in WK1 assembloids by flow cytometry due to difficulties with sample processing, therefore necessitating further work in this area. Another possibility is that resistance in the WK1 cells may be caused by CAR-T-induced upregulation of immune checkpoint proteins, as previously reported in GBM cells treated with EphA2 CARs [An 2021]. Future research should investigate this further as it could present the possibility of combination therapy with immune checkpoint inhibitors. Patterns of tumour cell invasion may also explain the distinction between cell lines, with DIPG24 and WK1 invading throughout the organoid, whereas DIPG17 remained discrete on the periphery and therefore more accessible to CAR-T cells. Alternative approaches, such as the ‘mosaic’ co-culture model which prompts the formation of multifocal tumour sites within the organoid, are potential options to test whether reduced CAR-T efficacy is due to the normal brain tissue barrier [Prior 2024].

In addition to evaluating on-target efficacy, we monitored for off-target neurotoxicity using cortical organoids and assembloids. In adults, EphA2 expression is low or absent across

normal tissues, with the exception of proliferative epithelial cells, due to the role of EphA2 in tissue development and regeneration [Walker-Daniels 2003]. Clinical trials investigating therapies targeting EphA2, including CAR-T cells, have shown no observable neurotoxicity, suggesting an acceptable safety profile [Lin Q 2021]. In results presented here, CAR-T cells tagged with CellTracker fluorescent probes mostly localised to the tumour component of DIPG17 assembloids, and had minimal presence in the organoid. CAR-T treatment did not markedly alter individual organoid morphology compared to untreated controls. Previous unpublished proteomic data of assembloids suggested potential upregulation of EphA2 expression in organoid regions adjacent to tumour cells, possibly caused by heightened inflammation or hypoxia in the microenvironment [O'Neill, Chen, Prior, unpublished data]. The details concerning this expression change are unclear, and it remains to be determined whether CAR-T cells are capable of recognising the EphA2 epitope on these 'normal' cells.

4.3.4 - Proposed refinements to assembloid methodology

This research has demonstrated that assembloid co-cultures allow for the therapeutic screening of CAR-T cells against HGGs, and produce results more indicative of *in vivo* response than conventional 2D culture systems. Modifications to the protocol described here could be made to further mimic brain architecture, tumour behaviour and invasion, and the innate immune system, thereby better informing the drug development process.

A key limitation in the context of immunotherapeutic screening is the lack of endogenous immune cells in our assembloids. In the brain tumour microenvironment, microglia and tumour-associated macrophages (TAMs) release cytokines which promote inflammation, inhibit cytotoxic T lymphocyte function and viability, and recruit myeloid-derived suppressor cells (MDSCs) and regulatory T cells (T_{reg}) which further diminish the immune response and promote tumour survival [Pallarés-Moratalla & Bergers 2024].

Increased immune infiltrate has been associated with reduced CAR-T cell therapy efficacy in GBM patients [O'Rourke 2017], but remains challenging to effectively model *in vitro* and *in vivo* [Khan F 2023].

Microglia are often absent in region-specific brain organoids due to the repression of mesodermal differentiation by dual-SMAD inhibition, selecting for endodermal lineage. Undirected protocols without these restrictions can spontaneously develop innate microglia, but with variable proportions and functionality [Ormel 2018]. Several strategies have been adopted to standardise microglial expression across organoid models, including those generated with SMAD inhibitors. The most common method to-date involves differentiating microglia from iPSCs or PBMCs and co-culturing them with established organoids, though this is limited by microglial heterogeneity and challenges in maintaining cellular proportions. Alternatively, microglia progenitor/myeloid precursor cells can be seeded together with NPCs which have already undergone neural induction. NPCs will self-aggregate and develop into organoids containing a precise ratio of microglia [Zhang W 2023]. Sarnow et al. used the latter approach to generate immunocompetent DIPG assembloid cultures, termed microglia-containing brain organoid tumour fusions (MiCBO-TF). The authors reported highly-motile mature microglia migrating through both brain and tumoural compartments, and which enhanced DIPG invasion [Sarnow 2024]. Incorporation of microglia likely represents the next step in modelling the tumour microenvironment in assembloids. We hypothesise that doing so would further increase treatment resistance to EphA2 CAR-T activity, while presenting the opportunity to characterise and target tumour-associated immunosuppression by microglia.

TAMs are a diverse collection of macrophages present in the tumour microenvironment. While early efforts delineated TAMs as either M1 (anti-tumour) or M2 (pro-tumour), more recent research suggests variable function dependent upon cytokine release and individual tumoural identity [Pittet 2022]. Characterisation has mainly focused on

breast and colorectal cancers, however TAM markers such as TREM2 have been correlated with worse outcomes in brain tumour patients [Khantakova 2022]. TAMs may be isolated through dissociation of primary patient tumour tissue, or present in PDOs, however these methods are often restricted by small sample size and variable tumour content [Cassetta 2016]. Alternatively, iPSCs or PBMCs can be differentiated into macrophages which are then induced to a TAM-like phenotype through exposure to cytokines or conditioned medium from cancer cell culture [Heideveld 2020]. Another study showed that monocytes could infiltrate NSCLC tumour spheroids, displaying TAM features and susceptibility to treatment with cisplatin, paclitaxel, and an immunomodulatory drug [Rebelo 2018]. While this approach has been considered for the incorporation of TAMs into 3D brain tumour models, further work is required to address concerns relating to ECM composition, cytokine concentrations, and the role of specific TAM subtypes in glioma [Akins 2020].

In GBM, MDSCs have been demonstrated to suppress cytotoxic T lymphocyte activity through several mechanisms, most notably the release of arginase, in turn decreasing availability of L-arginase required for T cell function [Raychaudhuri 2011]. Other prominent mechanisms include the secretion of ROS to directly inhibit T cell growth and induce apoptosis, and the upregulation of indoleamine 2,3-dioxygenase (IDO1) to disrupt the availability of tryptophan for T cell activation and proliferation [Mi 2020]. Characterisation of MDSCs has highlighted numerous subtypes yet to be fully elucidated, however highly metabolic early MDSCs (E-MDSCs) have been identified as targets for recruitment by stem-like GBM cells, and high expression of E-MDSCs is associated with poorer clinical prognosis [Jackson C 2025]. Protocols have been developed to isolate and expand MDSCs from PBMCs via stimulation with granulocyte macrophage colony stimulating factor (GM-CSF), but potential *in vitro* applications have yet to be fully explored [Singh & Rieber 2020]. Similarly, T_{reg} cells can be enriched from PBMCs by CD3 and CD28 stimulation in the

presence of IL-2, retaining their capacity to inhibit $CD4^+$ T cell activity [Hoffmann 2004]. Both patient-derived and continually-cultured GBM cell lines secrete soluble factors, particularly CCL2, which promote T_{reg} migration to the tumour site [Crane 2012]. Although secretion of CCL2 was shown to increase in response to radiation treatment of GBM cells, this did not correspond to increased T_{reg} migration [Vasco 2013]. To the best of our knowledge, most research into the impact of T_{reg} expression on immunosuppression has focused on *in vivo* and patient models, and has yet to be incorporated into 3D *in vitro* models of glioma.

Additional changes to the organoid culture protocols could more accurately model the tumour microenvironment and tumour behaviour. Our assembloid model comprises early-stage organoids committed to a dorsal cortical lineage and consisting of neural progenitors, and immature neuronal and glial populations. In Chapter 3, we showed that extending culture duration led to increased organoid size and differentiation to mature cellular populations and structures, resembling later stages of prenatal brain development. We can hypothesise that cell-cell interactions, tumour cell behaviour, and responses to treatment would be altered as a result of these changes in microenvironment. This is partially supported by Linkous et al., who found that glioma stem cells added to whole-brain organoids (GLICO model) at 1-month and 4-month time-points displayed differences in proliferation and invasion, though the relevance of these findings remains uncertain [Linkous 2019]. It is important to scrutinise the practicality of this approach however, as longer culture duration would reduce experimental throughput and increase inter-organoid variability.

The organoid component of the assembloid could also be modified to take into consideration the regions of the brain in which the tumour arises. Cortical organoids are a suitable platform for GBM, which most frequently occurs in the cerebral hemispheres, including the cerebral cortex. However, DIPG originates in the pons and can disseminate into

the medulla oblongata, thalamus, and cerebellum. DIPG proliferation and invasion is believed to be partially facilitated by neuron-glioma interactions and the formation of synaptic connections, as has been reported in other HGGs [Plessier 2017, Kluiver 2020, Venkatesh 2019]. Inclusion of these neuronal populations, such as noradrenergic neurons, and related cellular architecture may therefore induce more representative invasion and behaviour in DIPG cultures. Brainstem and pontine-specific organoid protocols have recently been reported, and could be applied to assembloids for this purpose [Eura 2020, Bessler 2023].

Patient-derived cell lines were used as the target for EphA2 CAR-T therapy. Although more representative than continually-cultured glioma cell lines used in other studies, limitations persist here which can be addressed. The focus of this thesis is on modelling the paediatric tumour microenvironment, however the WK1 GBM cell line used was established from adult disease, and treatment responses likely altered due to molecular differences with pGBM. We sought to address this discrepancy by establishing a primary cell line – pGBM-42 - from a patient tumour sample, kindly supplied by the CHW histopathology department [Table 2.8]. Initially, these cells were highly proliferative and could be expanded for at least three passages without noticeable changes to growth or morphology. Characterisation by flow cytometry showed EphA2 expression in the majority of cells, with a comparable MFI to DIPG and DIPG24, suggesting pGBM42 eligibility for CAR-T treatment [Supplementary Figure 4.3]. Unfortunately, following LVV transduction for eGFP and luciferase at a range of MOIs, culture health was adversely impacted and cells became senescent on two separate occasions. Time constraints prevented additional attempts or 2D viability assessment by xCELLigence.

Another option to constitute the tumour portion of assembloids are brain tumour PDOs. These 3D cultures retain the cellular heterogeneity and architecture of the primary tumour, including ECM and immune cell infiltrate, and avoid many of the selective pressures

from adherent cell line establishment [Neal 2018]. CAR-T treatments targeting EGFRvIII and Podoplanin (PDPN) have demonstrated potent efficacy in GBM PDOs, based upon immunohistochemical analyses [Jacob 2020, Diener 2022]. More robust viability measures, such as the luciferase transduction protocol described in this chapter, have been implemented in PDOs of other tumour types, but typically require dissociation beforehand, leading to potential loss of cellular populations [Jobin 2024]. These results indicate that GBM and DIPG PDOs could potentially be utilised to screen EphA2 CAR-T therapy alongside tumour spheroids. Assembloid models containing brain tumour PDOs have been proposed, but are yet to be successfully generated [Mei 2024]. We successfully established PDOs from several patient tumour samples, as detailed in the next chapter, but therapeutic screening was considered outside of the scope of this research.

4.4 - Summary

In vitro cytotoxicity assays are predominantly conducted against cells cultured under 2D conditions due to low cost and perceived experimental reproducibility. Adherent monolayers fail to recapitulate key characteristics of the tumour microenvironment *in vivo* however, and exhibit unrepresentative treatment sensitivity that often leads to failure in the latter stages of drug development. These issues are partially resolved by the transition to 3D tumour spheroids, and our data showed cell line- and donor-dependent differences upon treatment with EphA2 CAR-T cell therapy which were not apparent from 2D results. We subsequently increased resistance through the use of assembloid co-cultures, which incorporate brain tissue mimetics to more accurately model HGG invasion, as well as introducing an additional obstacle to CAR-T trafficking. EphA2 CAR-T cells were capable of specifically targeting tumour cells within the complex culture, as evidenced by cytotoxicity assays and cytokine release. These results demonstrate the utility of 3D *in vitro* models, and indicate that our EphA2 CAR-T warrants further investigation in HGGs, particularly DIPG.

Detection of tumour mutational profiles from PDO ctDNA

5

5.1 - Chapter Introduction

PDOs are derived from biopsy samples, surgical resection, and circulating tumour cells, recapitulating many of the histological features and genetic alterations present in the primary tumour. Successful propagation supplies researchers with additional material for genomic analysis and drug screening, facilitating personalised therapy selection for precision medicine [Driehuis 2020]. However, a key obstacle in the formation of PDOs is the limited availability of biopsy material, particularly in paediatric cancers where smaller specimens are collected to minimise patient burden [Interiano 2015]. Furthermore, when biopsy is performed, the tumour sample must first be prioritised for essential diagnostic analyses, including histological assessment and the identification of clinically-relevant mutations. As a result, limited tissue is available for PDO generation, which can restrict efforts to create patient-specific models for therapeutic screening.

Inspired by liquid biopsy, in which ctDNA is sampled from bodily fluids [Poulet 2019], recent studies have showed that ctDNA can be detected in culture medium within a few days of PDO establishment. Using highly-sensitive droplet digital PCR (ddPCR), samples are partitioned into thousands of nanolitre-sized droplets, then amplified, and

detected with fluorescent probes, ensuring rapid and specific characterisation of known hotspot mutations. Researchers showed that ctDNA sampled from PDOs had high concordance with the mutational profile of the primary tumour [Dantes 2020]. The quick turnaround provides the necessary genetic information for diagnosis and therapy selection, while also retaining PDOs as a resource for drug screening to identify tailored treatment options for the patient.

At present, mutational profiling of ctDNA has only been demonstrated in pancreatic and gastric PDOs [Dantes 2020, Hennig 2022]. Therefore, this chapter sought to determine the feasibility of this approach in brain cancer models, including pHGG PDOs.

5.2 - Results

5.2.1 - PDOs established from paediatric patient tumour samples

Between August 2018 and January 2023, CHW histopathology kindly supplied this research with 61 patient tumour samples, comprising fine-needle aspirates, open biopsy samples, and surgical resection specimens. Tissue was processed as described in Chapter 2.6, then stored in liquid nitrogen while consent for research was sought by the Biospecimen Repository Services team (formerly CHW Tumour Bank). Consent was granted by the families of 35/61 patients (57.3% consent rate), while 24/61 families either declined consent or did not respond to queries. A decision was also made to not approach the families of two DIPG patients who had died to avoid further emotional distress, and samples collected from these patients were appropriately discarded.

Upon thawing tumour samples, culture establishment workflow prioritised the formation of 3D models, following published protocols for GBM, neuroblastoma, and sarcoma PDOs [Jacob 2020a, Fusco 2019, He 2020]. When excess tissue was available, concurrent efforts were made to establish 2D adherent cell lines. Attempts to culture patient-

derived models were conducted using 26 of the available tissue samples [Supplementary Table 5.1], with the remainder excluded due to excessive culture medium costs, inadequate volume, or selection for other research projects.

We used standard criteria to distinguish between tissue fragments remaining in suspension and PDO establishment, namely maintained tissue integrity for at least 2 weeks, development of spheroidal morphology with well-defined boundaries, and verifiable growth [Jacob 2020b]. Based upon these criteria, PDOs were successfully cultured from 8/25 tissue samples (32% establishment rate). Deidentified patient data, tumour characteristics, and culture conditions are outlined in Table 2.8. Success rate varied between tumour entities, with high-grade brain tumours proving most receptive to culture. PDOs were formed from 3/3 pGBM samples, as well as medulloblastoma, pineoblastoma, PNET, and a mixed germ cell brain tumour. In contrast, the LGG pilocytic astrocytoma failed to demonstrate any growth across 3 attempts. Non-CNS tumour results were generally unfavourable, with PDOs established from a single instance of metastatic Ewing sarcoma [Figure 5.1].

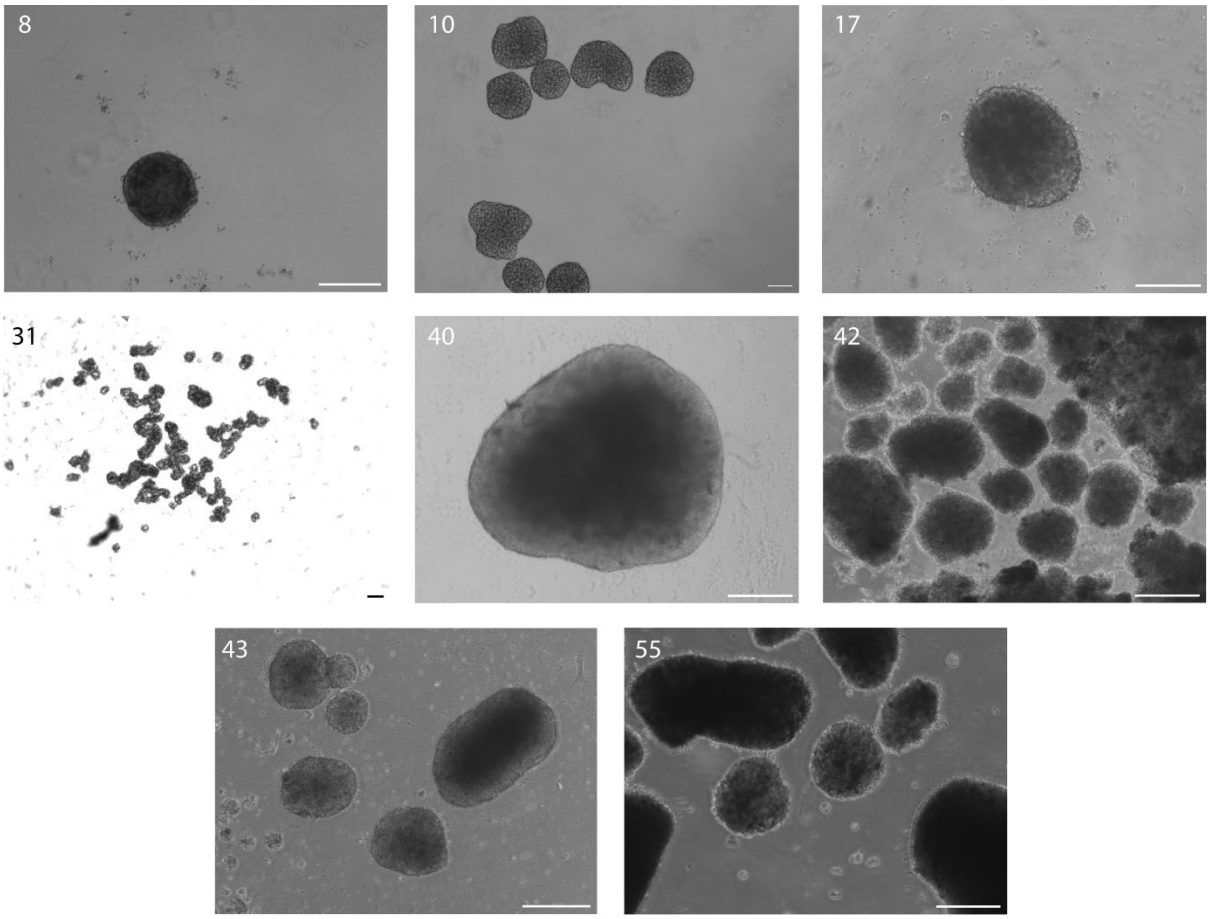

Figure 5.1 - Establishment of PDOs from patient tumour samples.

Phase-contrast and bright-field images of PDO models displaying characteristic rounded morphology and well-defined borders. PDOs were successfully established from tumour samples from patient #8 (pGBM), #10 (medulloblastoma), #17 (PNET), #31 (pineoblastoma), #40 (mixed germ cell brain tumour), #42 (pGBM), #43 (Ewing sarcoma liver metastasis), and #55 (pGBM). Scale bars = 100µm.

Dr Bhavna Padhye (Cancer Centre for Children in Westmead) compiled clinical reports of the primary tumours of enrolled patients to identify the clinically-relevant mutations for each individual. Clinically-reported mutations were identified in two cases where PDOs were successfully established – pGBM-42 and pGBM-55. PDO pGBM-55 was derived from a patient diagnosed with constitutional mismatch repair deficiency (CMMRD) and ultramutated pGBM, and pathogenic mutations to *POLE* (NM_996231.4; *POLE* c.1366G>C) and *PTPN11* (NM_002834.5; *PTPN11* c.1492C>T). A single nucleotide variant in the *TERT* promoter (NM_198253.3; *TERT* c.1-124G>A) was described in the patient sample from which PDO pGBM-42 was established. Clinical reports specifically described both cases as 'H3 wild-type'.

Next, the cellular identity and populations in pGBM-42 were analysed by immunofluorescence, following fixation and cryosectioning. Note that there was insufficient material for pGBM-55 immunostaining. pGBM-42 displayed expression of glial cell (GFAP, MAP2) and neural progenitor markers (NESTIN, ß-tubulin III, SOX2) [Figure 5.2A-D], both associated in the literature with GBM PDOs [Jacob 2020a]. Interestingly, few proliferative regions were observed by Ki67 expression, while apoptotic cells (cleaved caspase 3) were distributed through the PDO [Figure 5.2F]. The presence of apoptotic cells may be explained by the culture duration at the time of fixation (approximately 28 days) and relatively large diameter of the PDOs limiting nutrient intake.

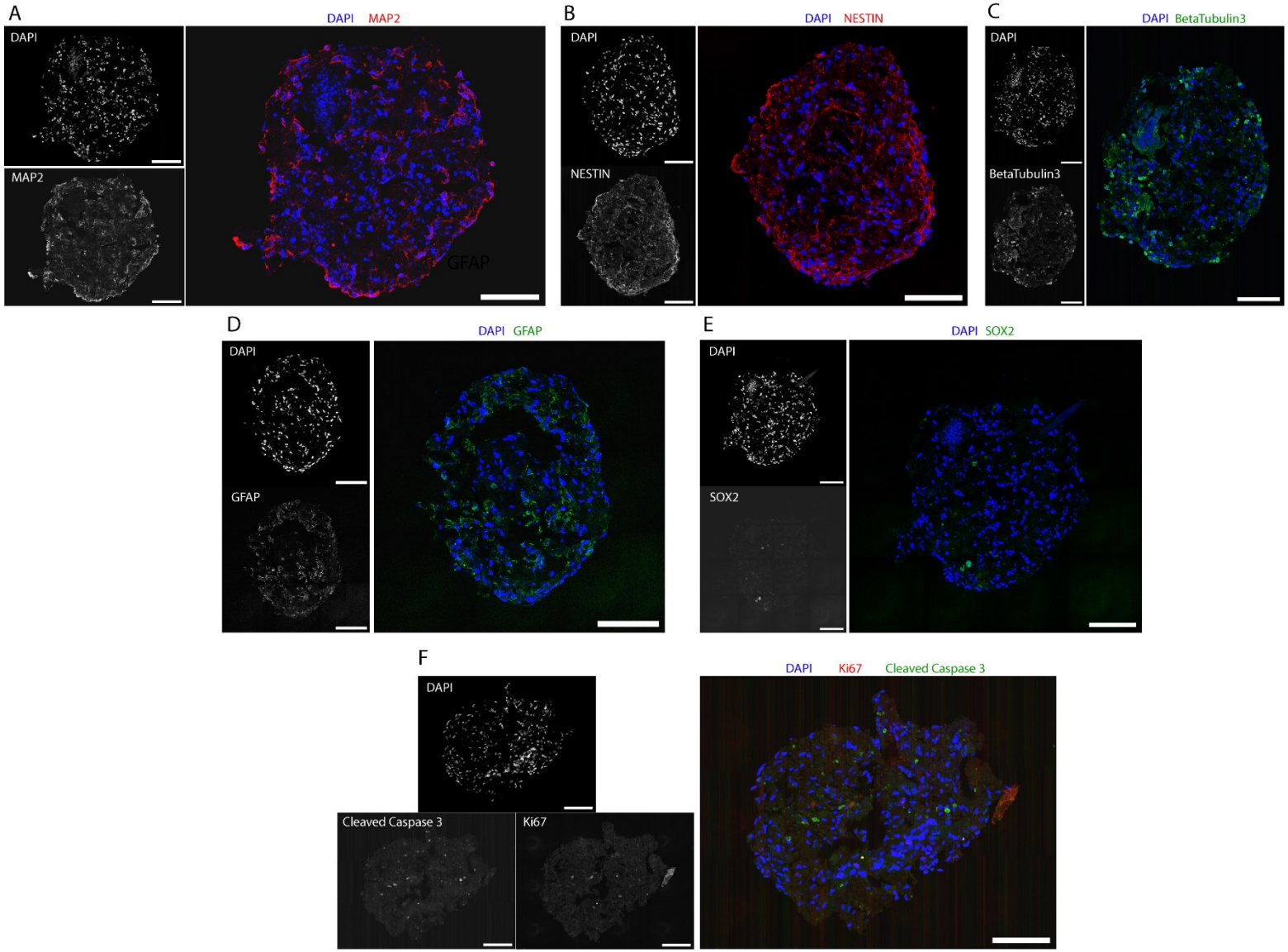

Figure 5.2 - Immunofluorescence images of pGBM-42 PDO populations.

Representative images of pGBM-42 PDO cryosections (n = 2 PDOs). Separated channels are displayed in greyscale, while composite images show nuclei stained with DAPI (blue) and markers of interest (green, red). Scale bars = 200µm.

5.2.2 - H3.3 K27M mutations detectable in DIPG spheroid ctDNA

Due to the precious nature of the PDO samples and the desire to preserve the material, DIPG tumour spheroids were instead initially used to test the feasibility of collecting and evaluating glioma ctDNA. Apoptotic and necrotic cell death are believed to be the main sources of ctDNA, so spheroids were seeded in excess of 5 x 10^4 cells and culture duration extended to intentionally compromise spheroid integrity. After 28 days, culture medium was collected, then ctDNA isolated and quantified. DIPG17 and DIPG24 spheroid medium yielded 1.55-8.06ng/µl (mean 4.74ng/µl, n = 5 spheroids) and 0.852-1.54ng/µl ctDNA (mean 1.22ng/µl, n = 4 spheroids), respectively.

To test the ability to detect tumour-associated mutations in the cfDNA harvested from spheroid media, the extracted DNA samples were probed for the hotspot driver mutation H3.3 K27M, which both cell lines are known to harbour [Qin 2017]. ddPCR was performed using validated commercial probes and primers for wild-type H3 and the K27M substitution. gDNA extracted from adherent DIPG cells served as positive controls for the H3.3 K27M mutation, and the breast epithelial cell line MCF10A, which lacks this mutation, and non-template controls (NTCs) were used as negative controls.

ddPCR analysis of extracted gDNA from DIPG17 and DIPG24 confirmed that they were positive for both mutant H3.3 K27M and wild-type H3 sequences. Variant allele frequency (VAF) was determined by the percentage of droplets containing DNA with the mutant sequence versus droplets containing the wild-type DNA sequence. Detection of the mutation differed between cell lines cultured as adherent monolayers, with 67.9% positivity in DIPG17 and 49.6% in DIPG24 (n = 3 technical replicates). Both sequences were also detected in ctDNA isolated from DIPG17 and DIPG24 spheroid media. However, fewer positive droplets were detected in the ctDNA preparations than in the gDNA extracts,

potentially owing to variable concentrations between samples [Figure 5.3]. Mean VAF in DIPG17 spheroids and DIPG24 spheroids was 55.2% and 65.88%, respectively (n = 3 technical replicates). MCF10A control samples consisted of wild-type sequences exclusively, while no sequences were detected in the NTCs. These results demonstrated the presence of ctDNA matching the mutational profile of the DIPG cell lines investigated, and thus this method was next tested in cfDNA isolated from PDOs.

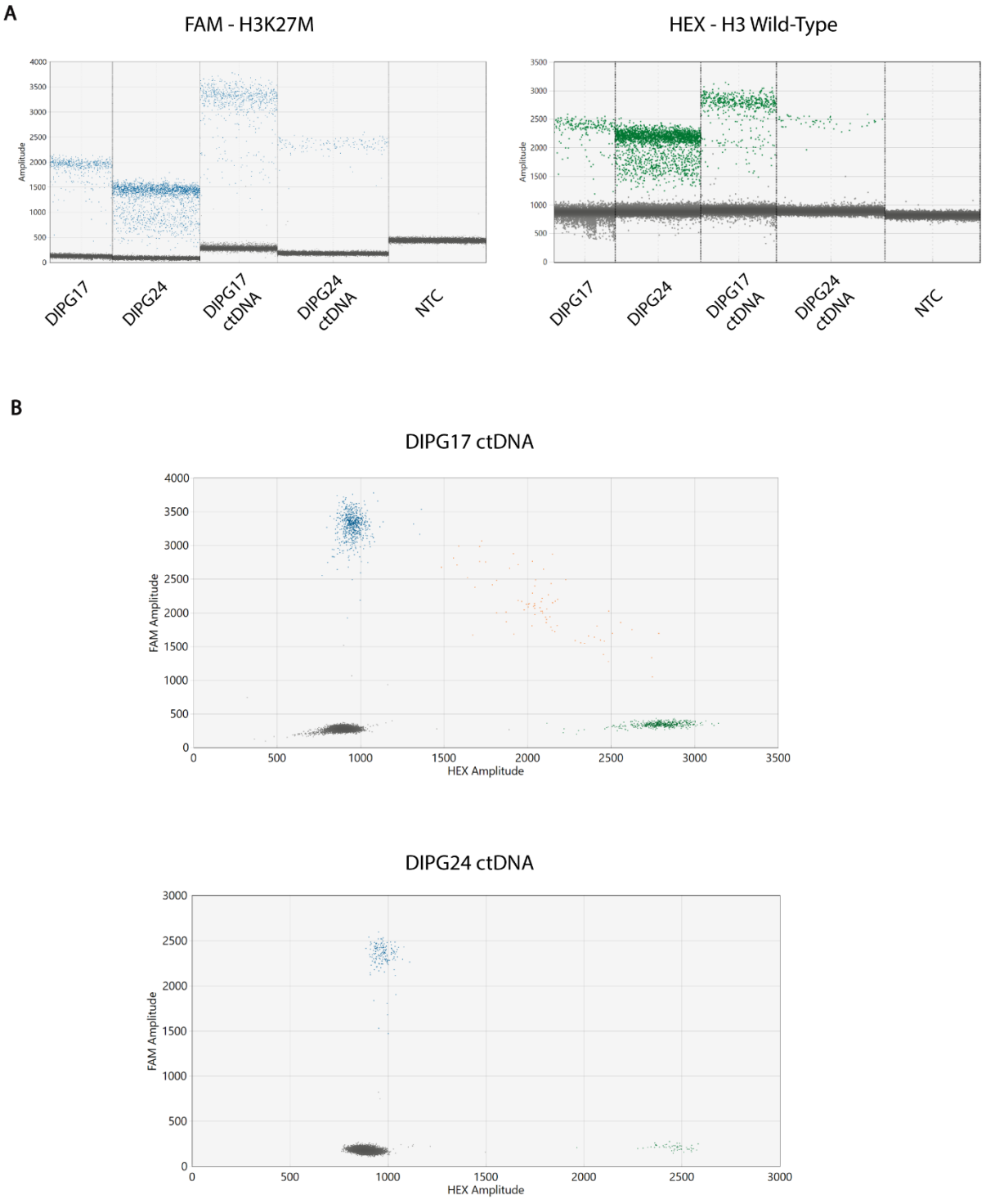

Figure 5.3 - Detection of H3.3 K27M in DIPG cfDNA by ddPCR. A. Amplitude plots for the FAM and HEX fluorophore channels, displaying H3.3 K27M mutation (FAM) and H3 wild-type (HEX) sequence positivity across adherent DIPG and ctDNA samples. **B.** Scatter plots showing amplitude distribution for droplets positive for H3.3K27M mutant (blue) and H3 wild-type (green), and droplets positive for both sequences (orange, DIPG17 ctDNA). Negative droplets (grey) contained neither fluorescent-tagged sequence.

5.2.3 - Detection of clinically-relevant mutations in PDO ctDNA

ctDNA isolated from culture medium of the PDOs was quantified by Qubit fluorometer (pGBM-42; 0.88ng/µl, pGBM-55; 2.88ng/µl). Matching gDNA samples were collected from both of the original tumour tissue samples and snap-frozen PDOs to allow for comparison across models. Commercial assays were available for the clinically-relevant *POLE* and *PTPN11* mutations that were reported for pGBM-55, and custom probes and primers were designed for the *TERT* mutation for pGBM-42 [Table 2.10]. In the absence of cell lines with these mutations to use as controls for mutant and wild-type sequences, synthetic double-stranded DNA fragments (gBlocks) were used instead [Table 2.9].

The presence of the *POLE* and *PTPN11* mutations was compared between tumour tissue gDNA, PDO gDNA, and PDO ctDNA extracts. Both mutant sequences were detected across all pGBM-55 samples by ddPCR (n = 1 technical replicate) [Figure 5.4]. Furthermore, all samples tested negative for H3.3 K27M, with only wild-type H3 sequences present [Figure 5.4C]. Combined, these results indicated that sampled ctDNA from pGBM-55 had a tumoural identity reflecting the primary tumour. VAF values also showed similarity to clinical reports, however more replicates would be necessary for statistical analysis [Table 5.1].

Table 5.1 - Comparison between VAF from clinical reports and pGBM-55 samples

Mutation	Primary Tumour VAF	pGBM-55 Tissue VAF	pGBM-55 PDO VAF	pGBM-55 ctDNA VAF
PTPN c.1492C>T	25%	14.17%	29.62%	21.21%
POLE c.1366G>C	44%	41.17%	50%	37.53%

Next, pGBM-42 was analysed for the *TERT* c.1-124G>A mutation and wild-type sequences across tumour tissue gDNA, adherent cell line gDNA, PDO gDNA, and PDO ctDNA. Neither mutant nor wild-type sequences in the relevant *TERT* region were detected by ddPCR. It was considered that this might reflect the high GC content contained within this DNA sequence, which could lead to probe mismatches and hinderance of DNA polymerase activity. To address this question, conventional PCR was performed with the probe and primer set. Although the positive gBlock controls were both detected, no bands were displayed from pGBM-42 tissue gDNA [Supplementary Figure 5.1]. We also repeated ddPCR using a gradient of annealing temperatures, however sequences were only detected from gBlock controls, and 2D amplitude plots could not delineate between wild-type and mutant sequences [Supplementary Figure 5.2]. Thus, the data suggested that the probes were unable to discriminate *TERT* sequence in the DNA extracts.

We considered that there may have been a problem in the sample preparation for pGBM-42. To rule out this possibility, we analysed the H3.3 K27M status across the pGBM-42 samples, and confirmed the presence of wild-type H3 in all samples, and the absence of mutant H3 [Figure 5.5]. This data was consistent with the clinically-reported genotype for this patient, therefore confirming the integrity of the DNA extracts. In addition, this data provides an independent corroboration of the ability to detect patient-relevant DNA sequences in media harvested from PDOs.

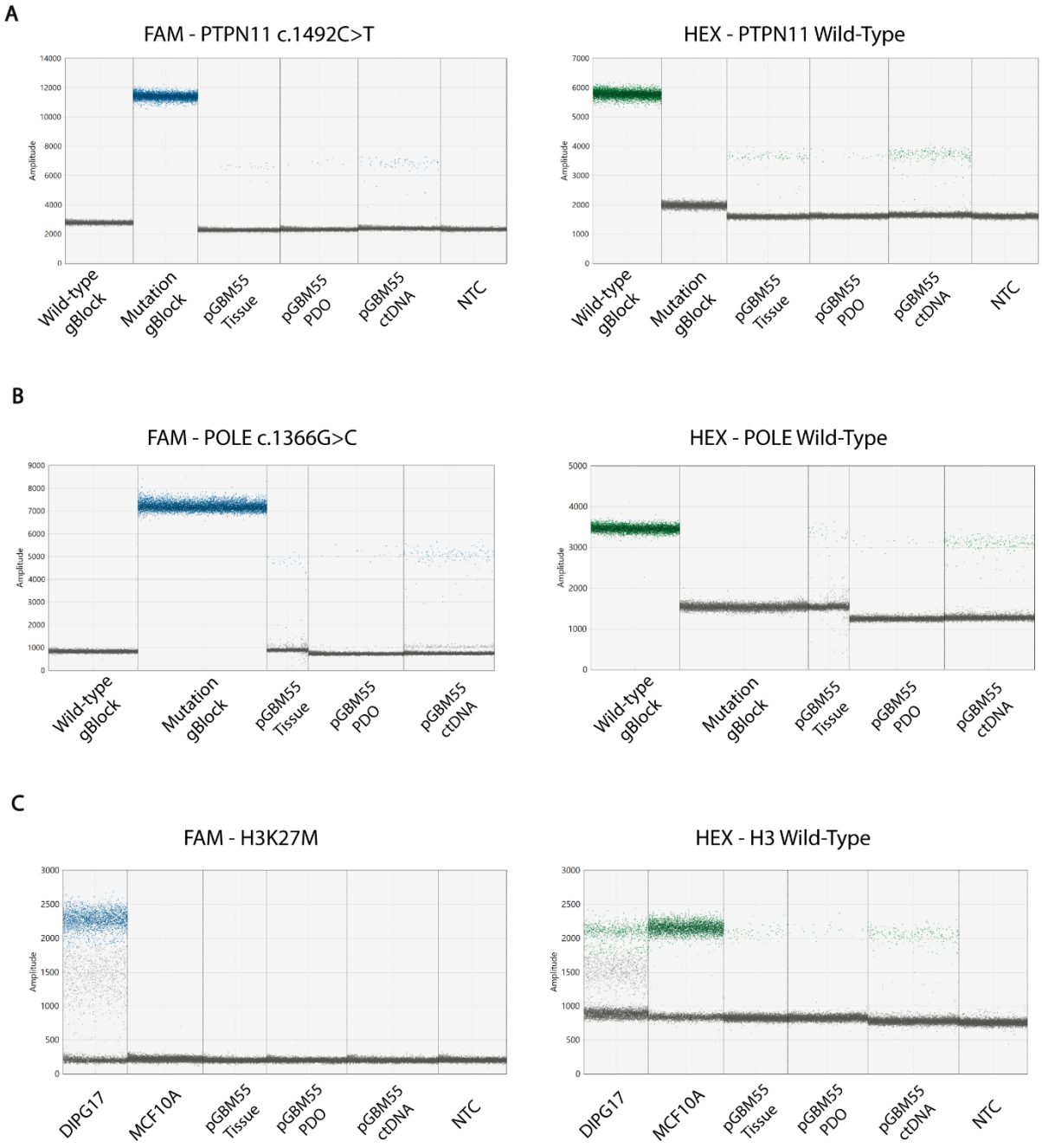

Figure 5.4 - Characterisation of mutational profile of pGBM-55 samples. Amplitude plots of the FAM and HEX fluorophores, indicating mutation and wild-type sequences, respectively. Positive droplets (blue, green) were determined by thresholding against gBlock controls and gDNA from DIPG17 and MCF10A adherent cell lines (n = 1 technical replicate).

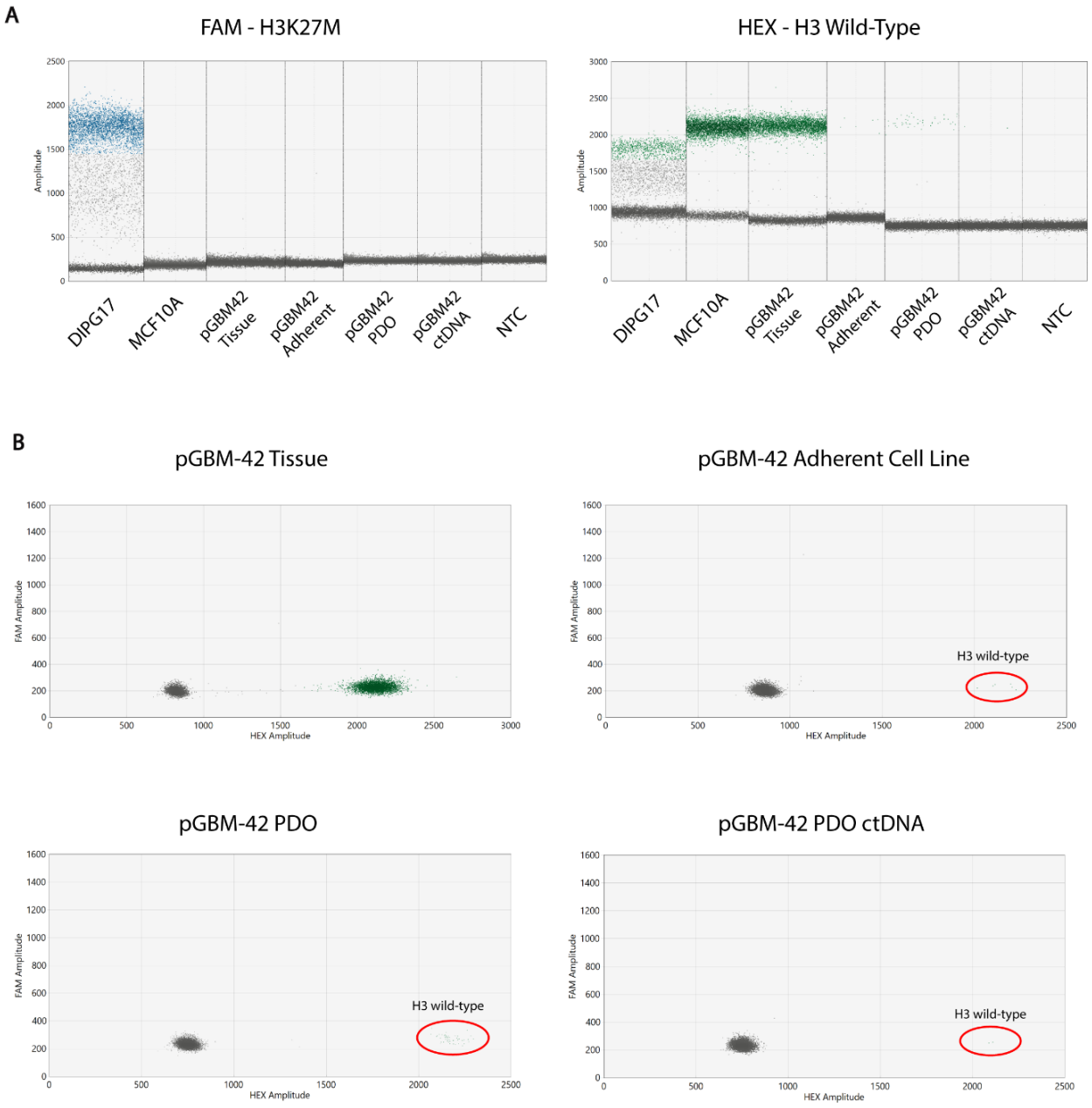

Figure 5.5 - Wild-type H3 detected across pGBM-42 samples. A. Amplitude plots of the FAM and HEX fluorophores, indicating H3K27M mutation and wild-type H3 sequences, respectively. **B.** Scatter plots show the presence of wild-type H3 (green) in pGBM-42 tumour tissue, the primary adherent cell line, PDOs, and ctDNA *(n* = 1 technical replicate).

5.3 - Chapter Discussion

PDOs were established from several paediatric tumour samples, with success mostly focused in high-grade brain tumours. These models were capable of long-term culture and propagation, and pGBM PDOs displayed disease-associated markers observed by immunofluorescence. ctDNA was shed from DIPG tumour spheroids and pGBM PDOs into culture medium and exhibited similar mutational profiles as the primary tumour when assessed by ddPCR.

5.3.1 - Factors influencing culture of PDOs

The establishment of PDOs remains challenging due to the complex variables surrounding individual patient samples, handling and processing procedures, and the lack of standardised culture maintenance protocols. Tissue sample size and composition are among the most important factors when establishing patient-derived culture models. Sample volumes exceeding $1cm^3$ are generally preferred due to the higher chance of including viable cells and capturing intratumoural heterogeneity [Vilgelm 2020]. This may not be possible depending upon the sample acquisition method, such as core biopsies, and the number of diagnostic procedures that must be prioritised before a portion of tissue is provided for research purposes [Driehuis 2020, Bae 2022, Thorel 2024]. Conversely, larger samples acquired from open surgical resection may also pose a problem for researchers as patients will have typically undergone treatment with radiotherapy and chemotherapies beforehand, leading to necrosis and calcification of the tumoural site [Driehuis 2020]. This was observed here in some of the neuroblastoma samples collected for cell line and PDO generation.

Short-term storage and transportation of tumour samples is also crucial to ensure that tissue does not undergo degradation and cells remain viable. In ideal circumstances, the sample should be immediately placed into culture medium after resection and transferred on

ice for processing. This requires prior knowledge of the individual case, prospective enrolment and consenting of the patient to the study, and communication with the surgical and pathology teams. The majority of samples in this study were received opportunistically where spare material was available following allocation to other diagnostic and research groups. Most samples were transferred to our department within 48 hours of surgery, however some exceeded this time-frame, particularly during COVID-19 pandemic lockdowns when staff shortages were encountered. Evidence from the literature indicates that PDO establishment rates significantly decline when culture is delayed more than 2 days post-surgery [Fisch 2024].

Upon receiving samples, they were processed by mechanical dissociation, then cryopreserved until retrospective consenting was completed. Although cell stress signatures were elevated in some tumour types thawed from liquid nitrogen storage, studies have found no significant differences in culture establishment rates between fresh and properly cryopreserved tumour tissue, including GBM [Wu 2021, Restivo 2022, Valyi-Nagy 2021]. Likewise, cellular architecture and drug responses appear consistent across PDOs derived from fresh or stored tumour material [Chen P 2024].

Once tissue is processed, optimal culture conditions are required to facilitate PDO growth and propagation. The variable success rates reported in this thesis suggests that the approaches used were ideal for high-grade brain tumours, but cannot necessarily be applied in the same manner to all tumour types. In some instances, minor modifications to the protocol may be sufficient to improve outcomes. For example, Abdullah et al. overcame the challenges of maintaining patient-derived models of LGGs by reducing incubator oxygen concentration to 5%. The physiologically-relevant hypoxic conditions yielded an 87% success rate from WHO grade I-III tumours, whereas PDOs from the same patient specimens failed to thrive at standard O_2 levels [Abdullah 2022]. These results were published after our unsuccessful

attempts to culture pilocytic astrocytoma samples, but offers a promising avenue for any future research in this area. In other non-CNS tumours, optimal conditions often remain disputed. Contrasting culture medium compositions are reported in the literature, as researchers speculate on the growth factors and morphogens required to improve culture survival. An imbalance can have ramifications on PDO development, including unrepresentative gene enrichment, and the potential for stromal populations outcompeting tumour cells, leading to culture senescence [Bae 2022, Hogenson 2022]. Multiple media recipes can be tested simultaneously for comparison purposes if tumour tissue volume is adequate, but this may dramatically increase experimental expenses. This was an influential factor in our decision to not pursue ovarian tumour PDOs, despite receiving two consented patient samples, as different combinations of hormonal supplements used across papers would have proven cost-prohibitive [Chan 2023].

5.3.2 - Mutational profiling of pHGG ctDNA

Biopsies inform clinicians and researchers of actionable therapeutic targets, and allow for the monitoring of disease progression in recurrent and refractory tumours. However, the proximity of pHGGs, particularly DIPG, to critical midline regions means that conventional biopsy techniques carry inherent neurological risk and are conducted at the discretion of surgical teams. Recently, liquid biopsies have offered new opportunities in this area, with studies showing that H3K27M and BRAF_V600E mutations can be detected from the plasma, serum, cystic fluid, and CSF samples of pHGG patients [Huang TY 2017, Panditharatna 2018, Izquierdo 2021]. Early detection of these biomarkers guides clinical strategy and is an important criterion for clinical trial enrolment. Cantor et al. progressed this work by observing that changes in H3K27M VAF values from CSF ctDNA were indicative of patient response to ONC201 treatment during a phase I clinical trial. Researchers also noted

H3K27M VAF increases prior to tumour progression in half of cases, further adding to the potential clinical utility of liquid biopsies in pHGGs [Cantor 2022].

Patient-derived models are known to shed ctDNA into culture medium with minimal contamination of normal cfDNA, and conserve the mutational profile of the primary tumour [Dantes 2020, Hennig 2022]. *In vitro* model differentiation, as well as drug screening responses, can also be monitored by changes in the ctDNA [Silver 2023, Silver 2024]. Use of these models provides a rapid source of additional information to clinicians, without adding to patient burden. While this approach has been demonstrated in other *in vitro* models of tumours and normal tissue types, to the best of our knowledge, our research investigated the first application in pHGG.

We first investigated the feasibility of evaluating ctDNA by collecting and analysing DIPG spheroid medium using ddPCR. This method has been utilised in multiple clinical trials to monitor disease progression in DIPG patients by measuring H3K27M frequency [Stallard 2018, Panditharatna 2018, Mueller 2019 Cantor 2022, Patel J 2024]. We confirmed consistent expression of H3.3 K27M across all DIPG17 and DIPG24 samples, including ctDNA, then progressed to investigating other somatic changes in pGBM-42 and pGBM-55 samples.

The clinical report for pGBM-55 highlighted mutations to *POLE* and *PTPN11*. *POLE* is involved in the proofreading of DNA replication, and deficits are associated with an ultramutated cancer phenotype and high tumour burden [Das A 2022, Erson-Omay 2015]. Accordingly, this patient had >400 mutations per megabase of DNA, and later developed another tumour with additional mutations to *TP53* and *FGFR1*. *POLE* cannot be directly targeted, however detection of alterations to this gene alerts clinicians to the probability of disease recurrence. Furthermore, it is hypothesised that *POLE*-mutated tumours are susceptible to immune checkpoint inhibition due to increased neoantigen load, though this

has yet to be fully explored due to small patient cohorts [Howitt 2015, Lukas 2018]. *PTPN11* encodes for SHP2, and mutations lead to an overactivation of the RAS/MAPK pathway, driving tumour cell proliferation. *PTPN11* mutations may therefore be targetable by MEK inhibitors, but this has so far only been demonstrated in preclinical models of pHGG [Ferguson 2016, Campbell 2021]. The presence of both *POLE* and *PTPN11* mutations was confirmed across tumour tissue samples, PDOs, and ctDNA, with broadly comparable VAF values as those described in clinical reports. As ctDNA can be collected and analysed by ddPCR within the first few days of culture, we propose a hypothetical scenario in which these results could be applied to design a preclinical therapeutic screen for MEK inhibition and immune checkpoint inhibition against PDOs upon expansion, informing clinical decision-making for the individual patient.

A single mutation in the *TERT* promoter region was reported in pGBM-42. Telomeres are located at the ends of chromosomes and are responsible for maintaining chromosomal integrity. As cells progress through the cell cycle repeatedly, telomeres shorten, eventually leading to cell senescence and death. *TERT* mutations activate the enzyme telomerase, causing the reparation of telomeres and indefinitely extending cell replication [Shammas 2011]. *TERT* alterations occur in a wide-range of cancers, with the C228T and C250T mutations reported in approximately 70-80% of GBM cases [Olympios 2021]. Commercial ddPCR assays are available for these specific sequences, and have been used to characterise ctDNA isolated from HGG patients [Fontanilles 2020, Ge 2020]. The *TERT* mutation in pGBM-42 is not the same as that detected in the commercially available kits and therefore required custom-designed probes and primers. We were unable to detect the relevant sequences in any of the patient-derived samples. Potentially, this may be due to high GC content, leading to non-specific amplification. While the presence of ctDNA was confirmed by known wild-type H3 status, lack of detection of the *TERT* mutation underlines a drawback

of using PCR-based methodologies for detecting allelic variants. An alternative analytical method here would be whole-genome next-generation sequencing (NGS), which has seen limited clinical use in liquid biopsies of DIPG [Panditharatna 2018]. Although the reported *TERT* VAF (39%) is within the purported limit of detection, NGS is expensive, requires higher DNA concentrations, and takes longer to perform than ddPCR, potentially curtailing their future applications for analysing PDO ctDNA [Patel J 2024].

5.4 - Summary

PDOs derived from patient samples resemble the cellular structure and populations of the primary tumour, offering a more representative *in vitro* model than adherent monolayers or tumour spheroids. The development of standardised generation protocols has improved culture success rates, as demonstrated here by the establishment of high-grade paediatric brain tumour PDOs, however further research is required to expand these advances to other cancers. Our results showed that 3D *in vitro* models of pHGGs, including pGBM PDOs, shed detectable quantities of ctDNA which can be isolated from culture medium and evaluated by ddPCR. Somatic mutations exhibited in ctDNA matched the profiles of the primary tumours, supporting its potential for providing a rapid source of additional genetic information to clinicians to assist in delivering precision medicine.

Discussion

6

6.1 - Thesis Summary

2D cultures inadequately represent *in vivo* tumour and brain microenvironments, but remain widely used in research due to their relative affordability, ease of use, and the perception of inter-study reproducibility. These apparent benefits often undermine the overall drug development process by advancing poor candidates likely to fail at clinical trial, further inflating costs and delaying improvements to patient outcomes [Dowden & Munro 2019]. Researchers are transitioning to 3D *in vitro* models to improve trial success rates, with ongoing efforts to determine suitable applications, standardise model composition, and increase throughput [Jensen & Teng 2020]. In this thesis, we established 3D tumour spheroid, cortical organoid, assembloid, and PDO models which were used to evaluate therapeutic safety and efficacy profiles, as well as exploring a potential role in clinical diagnosis and precision medicine.

In Chapter 3, we progressed an existing protocol for generating dorsal cortical organoids, observing the emergence of complex neural networks characterised by MEA. We then developed a pilot screen to assess the functional consequences of long-term TKI administration on organoid neurodevelopment. Results demonstrated significant alterations to electrophysiological parameters, as well as dysregulated activation of MAPK signalling implicated in neuronal development. These results suggest that mature cortical organoids can be used to measure neurotoxicity caused by chronic treatment exposure. We propose that

further refinements to reproducibility, scalability, and detection method could lead to the incorporation of this approach into the drug development process to predict long-term side effects that would not otherwise be evident from 2D neuronal assays or animal models. This would inform clinicians in advance to select alternative treatments where possible, or to prescribe the early adoption of intervention strategies to mitigate cognitive deficits in paediatric cancer survivors.

Cortical organoids were then co-cultured with patient-derived DIPG and GBM tumour spheroids to form assembloids in Chapter 4. These models were previously used in our department to visualise DIPG invasion into normal brain tissue, and proteomic analysis had indicated similarities to the *in vivo* brain tumour microenvironment [Prior 2024]. Research presented here investigated the utility of assembloids in assessing response to a novel EphA2 CAR-T cell therapy. Treatment efficiently cleared 2D monolayers, however sensitivity diminished with increasing model complexity, and spheroids and assembloids required higher treatment dose and duration for significant tumour killing to occur. CAR-T cells were trafficked through organoids and released pro-inflammatory and effector cytokines to induce cytotoxicity and propagate the immune response. The data confirmed the suitability of assembloids in evaluating treatment efficacy and suggests that this model more accurately reflects likely patient responses than conventional models. Consequently, the drug development process could be streamlined by selecting more promising therapeutic options, alleviating the reliance on animal models, and preventing the progression of ill-suited candidates to clinical trial.

Lastly, Chapter 5 focused on the establishment of PDOs from patient tumour tissue samples. High-grade brain tumours were more amenable to 3D culture conditions than other paediatric cancers, and we successfully formed PDOs from two pGBM patient samples. PDOs displayed histological features characteristic of pGBM, and shed ctDNA into culture

medium. ddPCR analysis confirmed the presence of clinically-relevant mutations in ctDNA from both PDOs, demonstrating for the first time the feasibility of this method in glioma. These findings highlighted an additional diagnostic application for PDOs, and advocates for the allocation of tumour tissue for culture to maximise information acquisition for personalised medicine.

6.2 - Future Directions

This study has advanced our understanding of 3D *in vitro* models and examined their applications in both normal brain and HGGs. Future research should build upon these findings to explore the applications of these models in other contexts, as well as improve model standardisation and experimental throughput.

Our research focused on therapeutic screening for neurotoxicity in cortical organoids and treatment efficacy in assembloids, with the potential for expansion to other compounds of interest. For example, long-term use of BRAF/MEK inhibitors, such as selumetinib, and the combination therapy of dabrafenib and trametinib, has shown promise in treating paediatric LGGs [Fangusaro 2019. Bouffet 2023]. Given the extended survival rates associated with these tumours, assessing their long-term neurotoxic effects is of particular interest and could be examined using our organoid assay. In assembloids, we successfully trialled EphA2 CAR-T cells against pHGG assembloids, and our department is now considering exploring the use of bispecific CAR-T cells to widen tumour coverage. Specifically, CARs that simultaneously target both EphA2 and IL13Rα2, as has been reported in the literature [Muhammad 2022, Kashyap & Salman 2024], are likely to represent the next stage of this research.

From a technical perspective, increased control and throughput could be achieved by utilising bio-fabrication techniques, such as microfluidics. Microfluidic systems culture spheroids in hydrogel compartments in parallel to channels of nutrients, growth factors,

drugs, and waste which can continuously diffuse across a concentration gradient, enabling long-term culture [Vadivelu 2017]. Standard microfluidic devices are manufactured with polydimethylsiloxane (PDMS) as it can be readily mixed with cross-linking agents to alter its mechanical properties [Friend & Yeo 2010]. Alternatively, other hydrogels can be selected for their rigidity/stiffness, pore size, and other properties depending upon the desired microenvironment [Orcheston-Findlay 2021]. Thousands of cultures can be maintained simultaneously with higher reproducibility than manual methods, addressing concerns of heterogeneity in spheroids, organoids, and PDOs [Xie R 2024]. Microfluidics has been used to treat GBM spheroids with EGFRvIII CAR-T cells [Huang J 2022], facilitate acute neurotoxicity screening against whole-brain and cortical organoids [Yin 2018. Cui 2020, Cui 2022, Ao 2020, Wang Y 2018b], and standardise PDO establishment [Thorel 2024]. Furthermore, the incorporation of distinct layers of endothelial cells, astrocytes, and pericytes in microfluidic chambers has been shown to effectively mimic the blood-brain barrier and to induce vascularisation [Wevers 2018, Huang J 2022, Straehla 2022]. Although traditionally expensive due to the need for silicon moulding and clean-room assembly, advances in stereolithography and additive manufacturing-based 3D printing have enabled the production of microfluidic devices using biocompatible thermoplastics and resins, making them more affordable and accessible [Su 2023]. Thus, microfluidics offers a promising avenue for scaling up our research and enhancing the recapitulation of the *in vivo* microenvironment.

Regarding analytical methodologies, machine learning systems have been trained from stock image libraries to assess the morphological features of 3D culture models. These networks then automate selection of appropriate cultures for assays or conduct high-throughput data analysis. For example, researchers have developed systems that calculate the area and circularity of tumour spheroids and initiate transfer to new plates [Grexa 2021]. Other approaches have been employed for label-free analysis of spheroid and organoid

viability, measuring responses to treatment based upon structural integrity and spheroid volume [Abd El-Sadek 2024, Bell 2025]. This allows for scheduled recordings of viability without compromising the culture, as occurs when using end-stage lytic assays, such as those used in this thesis. Strong correlations are reported between conventional live/dead staining and automated label-free methods across tens of thousands of spheroids [Chiang 2024]. While these automated methods could significantly increase experimental throughput and reduce time and bias from analysis, they currently remain constrained by lengthy training requirements and variability between data sets.

6.3 - Thesis Conclusion

pHGGs are fatal brain tumours characterised by rapid, diffuse infiltration through critical brain regions. No curative therapies exist for pHGGs, with management options restricted to palliative radiation and largely ineffective chemotherapy. Despite numerous preclinical studies advancing promising candidates, clinical trials have repeatedly failed to demonstrate benefits in patients. These shortcomings have been blamed on insufficient preclinical models, including 2D monolayers and animal models, which do not adequately recapitulate the human normal brain and brain tumour microenvironments. 3D *in vitro* models have been proposed as alternatives to overcome these obstacles. The work presented here highlighted the utility of 3D models in measuring CAR-T cell efficacy against pHGGs, predicting neurotoxicity induced by long-term kinase inhibitor treatment, and enabling rapid profiling and identification of actionable targets. Results clearly demonstrated the advantages of 3D culture over conventional models, and provides a foundation for further research to improve patient outcomes.

References

Abd El-Sadek, I., Morishita, R., Mori, T., Makita, S., Mukherjee, P., Matsusaka, S., & Yasuno, Y. (2024). Label-free visualization and quantification of the drug-type-dependent response of tumor spheroids by dynamic optical coherence tomography. Scientific reports, 14(1), 3366.

Abdullah, K. G., Bird, C. E., Buehler, J. D., Gattie, L. C., Savani, M. R., Sternisha, A. C., Xiao, Y., Levitt, M. M., Hicks, W. H., & Li, W. (2022). Establishment of patient-derived organoid models of lower-grade glioma. Neuro-Oncology, 24(4), 612-623.

Adams, J. W., Negraes, P. D., Truong, J., Tran, T., Szeto, R. A., Guerra, B. S., Herai, R. H., Teodorof-Diedrich, C., Spector, S. A., & Del Campo, M. (2023). Impact of alcohol exposure on neural development and network formation in human cortical organoids. Molecular psychiatry, 28(4), 1571-1584.

Agarwal, S., Sane, R., Gallardo, J. L., Ohlfest, J. R., & Elmquist, W. F. (2010). Distribution of gefitinib to the brain is limited by P-glycoprotein (ABCB1) and breast cancer resistance protein (ABCG2)-mediated active efflux. Journal of Pharmacology and Experimental Therapeutics, 334(1), 147-155.

Ahmed, N., Brawley, V., Hegde, M., Bielamowicz, K., Kalra, M., Landi, D., Robertson, C., Gray, T. L., Diouf, O., & Wakefield, A. (2017). HER2-specific chimeric antigen receptor–modified virus-specific T cells for progressive glioblastoma: a phase 1 dose-escalation trial. JAMA oncology, 3(8), 1094-1101.

Ahmed, S., Chauhan, V. M., Ghaemmaghami, A. M., & Aylott, J. W. (2019). New generation of bioreactors that advance extracellular matrix modelling and tissue engineering. Biotechnology letters, 41(1), 1-25.

Ajithkumar, T., Avanzo, M., Yorke, E., Tsang, D. S., Milano, M. T., Olch, A. J., Merchant, T. E., Dieckmann, K., Mahajan, A., & Fuji, H. (2024). Brain and Brain Stem Necrosis After Reirradiation for Recurrent Childhood Primary Central Nervous System Tumors: A PENTEC Comprehensive Review. International Journal of Radiation Oncology, Biology, Physics, 119(2), 655-668.

Ajithkumar, T., Parkinson, C., Shamshad, F., & Murray, P. (2007). Ifosfamide encephalopathy. Clinical oncology, 19(2), 108-114.

Akins, E. A., Aghi, M. K., & Kumar, S. (2020). Incorporating tumor-associated macrophages into engineered models of glioma. Iscience, *23*(12).

Alentorn, A., Marie, Y., Carpentier, C., Boisselier, B., Giry, M., Labussiere, M., Mokhtari, K., Hoang-Xuan, K., Sanson, M., & Delattre, J.-Y. (2012). Prevalence, clinico-pathological value, and co-occurrence of PDGFRA abnormalities in diffuse gliomas. Neuro-Oncology, 14(11), 1393-1403.

Alessi, I., Caroleo, A. M., de Palma, L., Mastronuzzi, A., Pro, S., Colafati, G. S., Boni, A., Della Vecchia, N., Velardi, M., & Evangelisti, M. (2022). Short and long-term toxicity in pediatric cancer treatment: central nervous system damage. Cancers, 14(6), 1540.

Allen, M., Bjerke, M., Edlund, H., Nelander, S., & Westermark, B. (2016). Origin of the U87MG glioma cell line: Good news and bad news. Science translational medicine, 8(354), 354re353-354re353.

Allen, N. J., Bennett, M. L., Foo, L. C., Wang, G. X., Chakraborty, C., Smith, S. J., & Barres, B. A. (2012). Astrocyte glypicans 4 and 6 promote formation of excitatory synapses via GluA1 AMPA receptors. Nature, 486(7403), 410-414.

Al-Mhanawi, B., Marti, M. B., Morrison, S. D., Gupta, P., Alani, M., Noakes, P. G., Wolvetang, E. J., & Shaker, M. R. (2023). Protocol for generating embedding-free brain organoids enriched with oligodendrocytes. STAR protocols, 4(4), 102725.

Álvarez-Torres, M. d. M., López-Cerdán, A., Andreu, Z., de la Iglesia Vayá, M., Fuster-Garcia, E., García-García, F., & García-Gómez, J. M. (2023). Vascular differences between IDH-wildtype glioblastoma and astrocytoma IDH-mutant grade 4 at imaging and transcriptomic levels. NMR in Biomedicine, 36(11), e5004.

An, D., Kim, K., & Kim, J. (2014). Microfluidic system based high throughput drug screening system for curcumin/TRAIL combinational chemotherapy in human prostate cancer PC3 cells. Biomolecules & therapeutics, 22(4), 355.

An, Z., Aksoy, O., Zheng, T., Fan, Q.-W., & Weiss, W. A. (2018). Epidermal growth factor receptor and EGFRvIII in glioblastoma: signaling pathways and targeted therapies. Oncogene, 37(12), 1561-1575.

An, Z., Hu, Y., Bai, Y., Zhang, C., Xu, C., Kang, X., Yang, S., Li, W., & Zhong, X. (2021). Antitumor activity of the third generation EphA2 CAR-T cells against glioblastoma is associated with interferon gamma induced PD-L1. Oncoimmunology, 10(1), 1960728.

Anderson, F. S., & Kunin-Batson, A. S. (2009). Neurocognitive late effects of chemotherapy in children: the past 10 years of research on brain structure and function. Pediatric blood & cancer, 52(2), 159-164.

Andres, A. L., Gong, X., Di, K., & Bota, D. A. (2014). Low-doses of cisplatin injure hippocampal synapses: a mechanism for ‘chemo’brain? Experimental neurology, 255, 137-144.

Antonucci, L., Canciani, G., Mastronuzzi, A., Carai, A., Del Baldo, G., & Del Bufalo, F. (2022). CAR-T therapy for pediatric high-grade gliomas: peculiarities, current investigations and future strategies. Frontiers in Immunology, 13, 867154.

Arnone, C. M., Polito, V. A., Mastronuzzi, A., Carai, A., Diomedi, F. C., Antonucci, L., Petrilli, L. L., Vinci, M., Ferrari, F., & Salviato, E. (2021). Oncolytic adenovirus and gene therapy with EphA2-BiTE for the treatment of pediatric high-grade gliomas. Journal for immunotherapy of cancer, 9(5), e001930.

Arrieta, V. A., Dmello, C., McGrail, D. J., Brat, D. J., Lee-Chang, C., Heimberger, A. B., Chand, D., Stupp, R., & Sonabend, A. M. (2023). Immune checkpoint blockade in glioblastoma: from tumor heterogeneity to personalized treatment. The Journal of clinical investigation, 133(2).

Arrillaga-Romany, I., Gardner, S. L., Odia, Y., Aguilera, D., Allen, J. E., Batchelor, T., Butowski, N., Chen, C., Cloughesy, T., & Cluster, A. (2024). ONC201 (Dordaviprone) in Recurrent H3 K27M–Mutant Diffuse Midline Glioma. Journal of Clinical Oncology, 42(13), 1542-1552.

Arzua, T., Yan, Y., Jiang, C., Logan, S., Allison, R. L., Wells, C., Kumar, S. N., Schäfer, R., & Bai, X. (2020). Modeling alcohol-induced neurotoxicity using human induced pluripotent stem cell-derived three-dimensional cerebral organoids. Translational psychiatry, 10(1), 1-21.

Australian Childhood Cancer Registry, C. C. Q. (2023). Australian Childhood Cancer Statistics Online (1983-2020)

Australian Institute of Health & Welfare (2023). Cancer data in Australia. https://www.aihw.gov.au/reports/cancer/cancer-data-in-australia Accessed: 20th February 2025

Bachoo, R. M., Maher, E. A., Ligon, K. L., Sharpless, N. E., Chan, S. S., You, M. J., Tang, Y., DeFrances, J., Stover, E., & Weissleder, R. (2002). Epidermal growth factor receptor and Ink4a/Arf: convergent mechanisms governing terminal differentiation and transformation along the neural stem cell to astrocyte axis. Cancer cell, 1(3), 269-277.

Bae, J., Choi, Y. S., Cho, G., & Jang, S. J. (2022). The patient-derived cancer organoids: Promises and challenges as platforms for cancer discovery. Cancers, 14(9), 2144.

Bagchi, A., Orr, B. A., Campagne, O., Dhanda, S., Nair, S., Tran, Q., Christensen, A. M., Gajjar, A., Furtado, L. V., & Vasilyeva, A. (2021). Lorlatinib in a child with ALK-fusion–positive high-grade glioma. New England journal of medicine, 385(8), 761-763.

Bagley, J. A., Reumann, D., Bian, S., Lévi-Strauss, J., & Knoblich, J. A. (2017). Fused cerebral organoids model interactions between brain regions. Nature methods, 14(7), 743-751.

Bardy, C., Van Den Hurk, M., Eames, T., Marchand, C., Hernandez, R. V., Kellogg, M., Gorris, M., Galet, B., Palomares, V., & Brown, J. (2015). Neuronal medium that supports basic synaptic functions and activity of human neurons in vitro. Proceedings of the National Academy of Sciences, 112(20), E2725-E2734.

Bariselli, S., & Lovinger, D. M. (2021). Corticostriatal circuit models of cognitive impairments induced by fetal exposure to alcohol. Biological psychiatry, 90(8), 516-528.

Baruchel, S., Sharp, J. R., Bartels, U., Hukin, J., Odame, I., Portwine, C., Strother, D., Fryer, C., Halton, J., & Egorin, M. J. (2009). A Canadian paediatric brain tumour consortium

(CPBTC) phase II molecularly targeted study of imatinib in recurrent and refractory paediatric central nervous system tumours. European Journal of Cancer, 45(13), 2352-2359.

Batra, V., Sands, S. A., Holmes, E., Geyer, J. R., Yates, A., Becker, L., Burger, P., Gilles, F., Wisoff, J., & Allen, J. C. (2014). Long-term survival of children less than six years of age enrolled on the CCG-945 phase III trial for newly-diagnosed high-grade glioma: a report from the Children's Oncology Group. Pediatric blood & cancer, 61(1), 151-157.

Bauer, T. M., Felip, E., Solomon, B. J., Thurm, H., Peltz, G., Chioda, M. D., & Shaw, A. T. (2019). Clinical management of adverse events associated with lorlatinib. The Oncologist, 24(8), 1103-1110.

Bautista, F., Paoletti, X., Rubino, J., Brard, C., Rezai, K., Nebchi, S., Andre, N., Aerts, I., De Carli, E., & van Eijkelenburg, N. (2021). Phase I or II study of ribociclib in combination with topotecan-temozolomide or everolimus in children with advanced malignancies: arms A and B of the AcSé-ESMART trial. Journal of Clinical Oncology, 39(32), 3546-3560.

Becher, O. J., Gilheeney, S. W., Khakoo, Y., Lyden, D. C., Haque, S., De Braganca, K. C., Kolesar, J. M., Huse, J. T., Modak, S., & Wexler, L. H. (2017). A phase I study of perifosine with temsirolimus for recurrent pediatric solid tumors. Pediatric blood & cancer, 64(7), e26409.

Bell, L., Simonneau, C., Zanini, C., Kassianidou, E., Zundel, C., Neff, R., Steinhuber, B., Tecilla, M., Odermatt, A., & Villaseñor, R. (2025). Advanced tissue technologies of blood-brain barrier organoids as high throughput toxicity readouts in drug development. Heliyon, 11(1).

Bellantoni, A. J., & Wagner, L. M. (2021). Pursuing precision: Receptor tyrosine kinase inhibitors for treatment of pediatric solid tumors. Cancers, 13(14), 3531.

Bessler, N., Moreno, C. R., Wezenaar, A., Dommann, N., Keramati, F., Ariese, H., Honhoff, C., de Blank, S., Román, M. B., & Alieva, M. (2023). P07. 07. B INDUCTION AND TARGETING OF DIFFUSE MIDLINE GLIOMA IN A NOVEL HUMAN PONTINE ORGANOID MODEL. Neuro-Oncology, 25(Suppl 2), ii52.

Biasoli, D., Kahn, S. A., Cornélio, T., Furtado, M., Campanati, L., Chneiweiss, H., Moura-Neto, V., & Borges, H. (2013). Retinoblastoma protein regulates the crosstalk between autophagy and apoptosis, and favors glioblastoma resistance to etoposide. Cell death & disease, 4(8), e767-e767.

Biedler, J. L., Helson, L., & Spengler, B. A. (1973). Morphology and growth, tumorigenicity, and cytogenetics of human neuroblastoma cells in continuous culture. Cancer research, 33(11), 2643-2652.

Binda, E., Visioli, A., Giani, F., Lamorte, G., Copetti, M., Pitter, K. L., Huse, J. T., Cajola, L., Zanetti, N., & DiMeco, F. (2012). The EphA2 receptor drives self-renewal and tumorigenicity in stem-like tumor-propagating cells from human glioblastomas. Cancer cell, 22(6), 765-780.

Bjerke, L., Mackay, A., Nandhabalan, M., Burford, A., Jury, A., Popov, S., Bax, D. A., Carvalho, D., Taylor, K. R., & Vinci, M. (2013). Histone H3. 3 mutations drive pediatric glioblastoma through upregulation of MYCN. Cancer discovery, 3(5), 512-519.

Bohn, A., Braley, A., Rodriguez de la Vega, P., Zevallos, J. C., & Barengo, N. C. (2018). The association between race and survival in glioblastoma patients in the US: a retrospective cohort study. PLoS One, 13(6), e0198581.

Bouffet, E., Hansford, J. R., Garrè, M. L., Hara, J., Plant-Fox, A., Aerts, I., Locatelli, F., Van Der Lugt, J., Papusha, L., & Sahm, F. (2023). Dabrafenib plus trametinib in pediatric glioma with BRAF V600 mutations. New England journal of medicine, 389(12), 1108-1120.

Brennan, C. W., Verhaak, R. G., McKenna, A., Campos, B., Noushmehr, H., Salama, S. R., Zheng, S., Chakravarty, D., Sanborn, J. Z., & Berman, S. H. (2013). The somatic genomic landscape of glioblastoma. Cell, 155(2), 462-477.

Brown, C. E., Hibbard, J. C., Alizadeh, D., Blanchard, M. S., Natri, H. M., Wang, D., Ostberg, J. R., Aguilar, B., Wagner, J. R., & Paul, J. A. (2024). Locoregional delivery of IL-13Rα2-targeting CAR-T cells in recurrent high-grade glioma: a phase 1 trial. Nature medicine, 30(4), 1001-1012.

Brown, R. T., Madan-Swain, A., Walco, G. A., Cherrick, I., Ievers, C. E., Conte, P. M., Vega, R., Bell, B., & Lauer, S. J. (1998). Cognitive and academic late effects among children previously treated for acute lymphocytic leukemia receiving chemotherapy as CNS prophylaxis. Journal of pediatric psychology, 23(5), 333-340.

Bu, Q., Huang, Y., Li, M., Dai, Y., Fang, X., Chen, K., Liu, Q., Xue, A., Zhong, K., & Huang, Y. (2020). Acrylamide exposure represses neuronal differentiation, induces cell apoptosis and promotes tau hyperphosphorylation in hESC-derived 3D cerebral organoids. Food and Chemical Toxicology, 144, 111643.

Buczkowicz, P., Hoeman, C., Rakopoulos, P., Pajovic, S., Letourneau, L., Dzamba, M., Morrison, A., Lewis, P., Bouffet, E., & Bartels, U. (2014). Genomic analysis of diffuse intrinsic pontine gliomas identifies three molecular subgroups and recurrent activating ACVR1 mutations. Nature Genetics, 46(5), 451-456.

Buizer, A. I., de Sonneville, L. M., van den Heuvel–Eibrink, M. M., & Veerman, A. J. (2005). Chemotherapy and attentional dysfunction in survivors of childhood acute lymphoblastic leukemia: effect of treatment intensity. Pediatric blood & cancer, 45(3), 281-290.

Buizer, A. I., de Sonneville, L. M., & Veerman, A. J. (2009). Effects of chemotherapy on neurocognitive function in children with acute lymphoblastic leukemia: a critical review of the literature. Pediatric blood & cancer, 52(4), 447-454.

Cakir, B., Xiang, Y., Tanaka, Y., Kural, M. H., Parent, M., Kang, Y.-J., Chapeton, K., Patterson, B., Yuan, Y., & He, C.-S. (2019). Engineering of human brain organoids with a functional vascular-like system. Nature methods, 16(11), 1169-1175.

Camp, J. G., Badsha, F., Florio, M., Kanton, S., Gerber, T., Wilsch-Bräuninger, M., Lewitus, E., Sykes, A., Hevers, W., & Lancaster, M. (2015). Human cerebral organoids recapitulate gene expression programs of fetal neocortex development. Proceedings of the National Academy of Sciences, 112(51), 15672-15677.

Campbell, B. B., Galati, M. A., Stone, S. C., Riemenschneider, A. N., Edwards, M., Sudhaman, S., Siddaway, R., Komosa, M., Nunes, N. M., & Nobre, L. (2021). Mutations in the RAS/MAPK Pathway Drive Replication Repair–Deficient Hypermutated Tumors and Confer Sensitivity to MEK Inhibition. Cancer discovery, 11(6), 1454-1467.

Campo-Soria, C., Chang, Y., & Weiss, D. S. (2006). Mechanism of action of benzodiazepines on GABAA receptors. British journal of pharmacology, 148(7), 984-990.

Cancer Genome Atlas Research Network. (2008). Comprehensive genomic characterization defines human glioblastoma genes and core pathways. Nature, 455(7216), 1061-1068.

Cantor, E., Wierzbicki, K., Tarapore, R. S., Ravi, K., Thomas, C., Cartaxo, R., Nand Yadav, V., Ravindran, R., Bruzek, A. K., & Wadden, J. (2022). Serial H3K27M cell-free tumor DNA (cf-tDNA) tracking predicts ONC201 treatment response and progression in diffuse midline glioma. Neuro-Oncology, 24(8), 1366-1374.

Carvalho, D. M., Richardson, P. J., Olaciregui, N., Stankunaite, R., Lavarino, C., Molinari, V., Corley, E. A., Smith, D. P., Ruddle, R., & Donovan, A. (2022). Repurposing vandetanib plus everolimus for the treatment of ACVR1-mutant diffuse intrinsic pontine glioma. Cancer discovery, 12(2), 416-431.

Casanova, M. F., Casanova, E. L., Frye, R. E., Baeza-Velasco, C., LaSalle, J. M., Hagerman, R. J., Scherer, S. W., & Natowicz, M. R. (2020). Secondary vs. idiopathic autism. In (Vol. 11, pp. 297): Frontiers Media SA.

Cassetta, L., Noy, R., Swierczak, A., Sugano, G., Smith, H., Wiechmann, L., & Pollard, J. W. (2016). Isolation of mouse and human tumor-associated macrophages. In 'Tumor Microenvironment: Study Protocols (pp. 211-229)'. Springer International Publishing.

Castel, D., Kergrohen, T., Tauziède-Espariat, A., Mackay, A., Ghermaoui, S., Lechapt, E., Pfister, S. M., Kramm, C. M., Boddaert, N., & Blauwblomme, T. (2020). Histone H3 wild-type DIPG/DMG overexpressing EZHIP extend the spectrum diffuse midline gliomas with PRC2 inhibition beyond H3-K27M mutation. Acta neuropathologica, 139, 1109-1113.

Castel, D., Philippe, C., Calmon, R., Le Dret, L., Truffaux, N., Boddaert, N., Pagès, M., Taylor, K. R., Saulnier, P., & Lacroix, L. (2015). Histone H3F3A and HIST1H3B K27M mutations define two subgroups of diffuse intrinsic pontine gliomas with different prognosis and phenotypes. Acta neuropathologica, 130, 815-827.

Castellino, S. M., Tooze, J. A., Flowers, L., Hill, D. F., McMullen, K. P., Shaw, E. G., & Parsons, S. K. (2012). Toxicity and efficacy of the acetylcholinesterase (AChe) inhibitor donepezil in childhood brain tumor survivors: a pilot study. Pediatric blood & cancer, 59(3), 540-547.

Cavaletti, G., & Marmiroli, P. (2010). Chemotherapy-induced peripheral neurotoxicity. Nature Reviews Neurology, 6(12), 657-666.

Cerignoli, F., Abassi, Y. A., Lamarche, B. J., Guenther, G., Santa Ana, D., Guimet, D., Zhang, W., Zhang, J., & Xi, B. (2018). In vitro immunotherapy potency assays using real-time cell analysis. PLoS One, 13(3), e0193498.

Chaicharoenaudomrung, N., Kunhorm, P., & Noisa, P. (2019). Three-dimensional cell culture systems as an in vitro platform for cancer and stem cell modeling. World journal of stem cells, 11(12), 1065.

Chambers, S. M., Fasano, C. A., Papapetrou, E. P., Tomishima, M., Sadelain, M., & Studer, L. (2009). Highly efficient neural conversion of human ES and iPS cells by dual inhibition of SMAD signaling. Nature biotechnology, 27(3), 275-280.

Chan, W. S., Mo, X., Ip, P. P. C., & Tse, K. Y. (2023). Patient-derived organoid culture in epithelial ovarian cancers—Techniques, applications, and future perspectives. Cancer medicine, 12(19), 19714-19731.

Chauhan, P., Philip, S. E., Chauhan, G., & Mehra, S. (2022). The anatomical basis of seizures.

Chen, H. I., Song, H., & Ming, G. l. (2019). Applications of human brain organoids to clinical problems. Developmental Dynamics, 248(1), 53-64.

Chen, P., Zhou, J.-B., Chu, X.-P., Feng, Y.-Y., Zeng, Q.-B., Lei, J.-H., Wong, K.-P., Chan, T.-I., Lam, C.-W., & Zhu, W.-L. (2024). Establishing a cryopreserved biobank of living tumor tissues for drug sensitivity testing. Bioactive Materials.

Cheung, Y. T., Brinkman, T. M., Mulrooney, D. A., Mzayek, Y., Liu, W., Banerjee, P., Panoskaltsis-Mortari, A., Srivastava, D., Pui, C. H., & Robison, L. L. (2017). Impact of sleep, fatigue, and systemic inflammation on neurocognitive and behavioral outcomes in long-term survivors of childhood acute lymphoblastic leukemia. Cancer, 123(17), 3410-3419.

Cheung, Y. T., Edelmann, M. N., Mulrooney, D. A., Green, D. M., Chemaitilly, W., John, N., Robison, L. L., Hudson, M. M., & Krull, K. R. (2016). Uric acid and neurocognitive function in survivors of childhood acute lymphoblastic leukemia treated with chemotherapy only. Cancer Epidemiology, Biomarkers & Prevention, 25(8), 1259-1267.

Chew, N., Habarakada, D., Firestein, R., & Daniel, P. (2023). A protocol to establish cell line models from rare pediatric solid tumors. STAR protocols, 4(3), 102537.

Chiang, C.-C., Anne, R., Chawla, P., Shaw, R. M., He, S., Rock, E. C., Zhou, M., Cheng, J., Gong, Y.-N., & Chen, Y.-C. (2024). Deep learning unlocks label-free viability assessment of cancer spheroids in microfluidics. Lab on a Chip, 24(12), 3169-3182.

Choe, M. S., Kim, J. S., Yeo, H. C., Bae, C. M., Han, H. J., Baek, K., Chang, W., Lim, K. S., Yun, S. P., & Shin, I. S. (2020). A simple metastatic brain cancer model using human embryonic stem cell-derived cerebral organoids. The FASEB Journal, 34(12), 16464-16475.

Choi, J. S., Lee, H. J., Rajaraman, S., & Kim, D.-H. (2021). Recent advances in three-dimensional microelectrode array technologies for in vitro and in vivo cardiac and neuronal interfaces. Biosensors and Bioelectronics, 171, 112687.

Chong, Z., Li, F., & Maiese, a., K. (2005). Activating Akt and the brain's resources to drive cellular survival and prevent inflammatory injury. Histology and histopathology, 20(1), 299.

Chow, K. K., Naik, S., Kakarla, S., Brawley, V. S., Shaffer, D. R., Yi, Z., Rainusso, N., Wu, M.-F., Liu, H., & Kew, Y. (2013). T cells redirected to EphA2 for the immunotherapy of glioblastoma. Molecular Therapy, 21(3), 629-637.

Chung, W.-S., Clarke, L. E., Wang, G. X., Stafford, B. K., Sher, A., Chakraborty, C., Joung, J., Foo, L. C., Thompson, A., & Chen, C. (2013). Astrocytes mediate synapse elimination through MEGF10 and MERTK pathways. Nature, 504(7480), 394-400.

Cicenas, J., Zalyte, E., Bairoch, A., & Gaudet, P. (2018). Kinases and cancer. In (Vol. 10, pp. 63): MDPI.

Coffman, K. T., Hu, M., Carles-Kinch, K., Tice, D., Donacki, N., Munyon, K., Kifle, G., Woods, R., Langermann, S., & Kiener, P. A. (2003). Differential EphA2 epitope display on normal versus malignant cells. Cancer research, 63(22), 7907-7912.

Cohen, K. J., Heideman, R. L., Zhou, T., Holmes, E. J., Lavey, R. S., Bouffet, E., & Pollack, I. F. (2011). Temozolomide in the treatment of children with newly diagnosed diffuse intrinsic pontine gliomas: a report from the Children's Oncology Group. Neuro-Oncology, 13(4), 410-416.

Cohen, K. J., Pollack, I. F., Zhou, T., Buxton, A., Holmes, E. J., Burger, P. C., Brat, D. J., Rosenblum, M. K., Hamilton, R. L., & Lavey, R. S. (2011). Temozolomide in the treatment of high-grade gliomas in children: a report from the Children's Oncology Group. Neuro-Oncology, 13(3), 317-323.

Conklin, H. M., Reddick, W. E., Ashford, J., Ogg, S., Howard, S. C., Morris, E. B., Brown, R., Bonner, M., Christensen, R., & Wu, S. (2010). Long-term efficacy of methylphenidate in enhancing attention regulation, social skills, and academic abilities of childhood cancer survivors. Journal of Clinical Oncology, 28(29), 4465-4472.

Corrò, C., Novellasdemunt, L., & Li, V. S. (2020). A brief history of organoids. American Journal of Physiology-Cell Physiology, 319(1), C151-C165.

Crane, C. A., Ahn, B. J., Han, S. J., & Parsa, A. T. (2012). Soluble factors secreted by glioblastoma cell lines facilitate recruitment, survival, and expansion of regulatory T cells: implications for immunotherapy. Neuro-oncology, 14(5), 584-95.

Cui, K., Wang, Y., Zhu, Y., Tao, T., Yin, F., Guo, Y., Liu, H., Li, F., Wang, P., & Chen, Y. (2020). Neurodevelopmental impairment induced by prenatal valproic acid exposure shown with the human cortical organoid-on-a-chip model. Microsystems & nanoengineering, 6(1), 49.

Cui, K., Chen, W., Cao, R., Xie, Y., Wang, P., Wu, Y., Wang, Y., & Qin, J. (2022). Brain organoid-on-chip system to study the effects of breast cancer derived exosomes on the neurodevelopment of brain. Cell Regeneration, 11(1), 7.

da Hora, C. C., Schweiger, M. W., Wurdinger, T., & Tannous, B. A. (2019). Patient-derived glioma models: from patients to dish to animals. Cells, 8(10), 1177.

Dang, J., Tiwari, S. K., Agrawal, K., Hui, H., Qin, Y., & Rana, T. M. (2021). Glial cell diversity and methamphetamine-induced neuroinflammation in human cerebral organoids. Molecular psychiatry, 26(4), 1194-1207.

Dantes, Z., Yen, H.-Y., Pfarr, N., Winter, C., Steiger, K., Muckenhuber, A., Hennig, A., Lange, S., Engleitner, T., & Öllinger, R. (2020). Implementing cell-free DNA of pancreatic cancer patient–derived organoids for personalized oncology. Jci Insight, 5(15).

Das, A., Sudhaman, S., Morgenstern, D., Coblentz, A., Chung, J., Stone, S. C., Alsafwani, N., Liu, Z. A., Karsaneh, O. A. A., & Soleimani, S. (2022). Genomic predictors of response to PD-1 inhibition in children with germline DNA replication repair deficiency. Nature medicine, 28(1), 125-135.

Das, K. K., & Kumar, R. (2017). Pediatric glioblastoma. Exon Publications, 297-312.

Day, B. W., Stringer, B. W., Al-Ejeh, F., Ting, M. J., Wilson, J., Ensbey, K. S., Jamieson, P. R., Bruce, Z. C., Lim, Y. C., & Offenhäuser, C. (2013). EphA3 maintains tumorigenicity and is a therapeutic target in glioblastoma multiforme. Cancer cell, 23(2), 238-248.

Dekkers, J. F., Wiegerinck, C. L., De Jonge, H. R., Bronsveld, I., Janssens, H. M., De Winter-de Groot, K. M., Brandsma, A. M., De Jong, N. W., Bijvelds, M. J., & Scholte, B. J. (2013). A functional CFTR assay using primary cystic fibrosis intestinal organoids. Nature medicine, 19(7), 939-945.

Del Baldo, G., Carai, A., Abbas, R., Cacchione, A., Vinci, M., Di Ruscio, V., Colafati, G. S., Rossi, S., Diomedi Camassei, F., & Maestro, N. (2022). Targeted therapy for pediatric diffuse intrinsic pontine glioma: a single-center experience. Therapeutic Advances in Medical Oncology, 14, 17588359221113693.

Del Baldo, G., Del Bufalo, F., Pinacchio, C., Carai, A., Quintarelli, C., De Angelis, B., Merli, P., Cacchione, A., Locatelli, F., & Mastronuzzi, A. (2023). The peculiar challenge of bringing CAR-T cells into the brain: Perspectives in the clinical application to the treatment of pediatric central nervous system tumors. Frontiers in Immunology, 14, 1142597.

Delgado, R. N., Allen, D. E., Keefe, M. G., Mancia Leon, W. R., Ziffra, R. S., Crouch, E. E., Alvarez-Buylla, A., & Nowakowski, T. J. (2022). Individual human cortical progenitors can produce excitatory and inhibitory neurons. Nature, 601(7893), 397-403.

Di Lullo, E., & Kriegstein, A. R. (2017). The use of brain organoids to investigate neural development and disease. Nature Reviews Neuroscience, 18(10), 573-584.

Diener, L., Goedert, N., Schulz, T., Monoranu, C., Ernestus, R., Hagemann, C., Löhr, M., Nerreter, T., & Dufner, V. (2022). P06. 04. B Efficacy of Podoplanin-CAR-T Cells in ex vivo Patient Derived Glioblastoma Organoids. Neuro-Oncology, 24(Supplement_2), ii38-ii38.

Dietrich, J. (2020). Neurotoxicity of cancer therapies. CONTINUUM: Lifelong Learning in Neurology, 26(6), 1646-1672.

Dowden, H., & Munro, J. (2019). Trends in clinical success rates and therapeutic focus. Nat Rev Drug Discov, 18(7), 495-496.

Driehuis, E., Kretzschmar, K., & Clevers, H. (2020). Establishment of patient-derived cancer organoids for drug-screening applications. Nature protocols, 15(10), 3380-3409.

Du, J., Yi, M., Zhou, F., He, W., Yang, A., Qiu, M., & Huang, H. (2021). S100B is selectively expressed by gray matter protoplasmic astrocytes and myelinating oligodendrocytes in the developing CNS. Molecular Brain, 14, 1-11.

Du, W., & Searle, J. S. (2009). The rb pathway and cancer therapeutics. Current drug targets, 10(7), 581-589.

Duchatel, R. J., Jackson, E. R., Parackal, S. G., Kiltschewskij, D., Findlay, I. J., Mannan, A., Staudt, D. E., Thomas, B. C., Germon, Z. P., & Laternser, S. (2024). PI3K/mTOR is a therapeutically targetable genetic dependency in diffuse intrinsic pontine glioma. The Journal of clinical investigation, 134(6).

Dutton III, J. W., Chen, H., You, C., Brodie, M. S., & Lasek, A. W. (2017). Anaplastic lymphoma kinase regulates binge-like drinking and dopamine receptor sensitivity in the ventral tegmental area. Addiction biology, 22(3), 665-678.

Edelmann, M. N., Krull, K. R., Liu, W., Glass, J. O., Ji, Q., Ogg, R. J., Sabin, N. D., Srivastava, D. K., Robison, L. L., & Hudson, M. M. (2014). Diffusion tensor imaging and neurocognition in survivors of childhood acute lymphoblastic leukaemia. Brain, 137(11), 2973-2983.

Erson-Omay, E. Z., Çağlayan, A. O., Schultz, N., Weinhold, N., Omay, S. B., Özduman, K., Köksal, Y., Li, J., Serin Harmancı, A., & Clark, V. (2015). Somatic POLE mutations cause an

ultramutated giant cell high-grade glioma subtype with better prognosis. Neuro-Oncology, 17(10), 1356-1364.

Esemen, Y., Awan, M., Parwez, R., Baig, A., Rahman, S., Masala, I., Franchini, S., & Giakoumettis, D. (2022). Molecular pathogenesis of glioblastoma in adults and future perspectives: A systematic review. International Journal of Molecular Sciences, 23(5), 2607.

Eura, N., Matsui, T. K., Luginbühl, J., Matsubayashi, M., Nanaura, H., Shiota, T., Kinugawa, K., Iguchi, N., Kiriyama, T., & Zheng, C. (2020). Brainstem organoids from human pluripotent stem cells. Frontiers in Neuroscience, 14, 538.

Fangusaro, J. (2012). Pediatric high grade glioma: a review and update on tumor clinical characteristics and biology. Frontiers in Oncology, 2, 105.

Fangusaro, J., Onar-Thomas, A., Poussaint, T. Y., Wu, S., Ligon, A. H., Lindeman, N., Banerjee, A., Packer, R. J., Kilburn, L. B., & Goldman, S. (2019). Selumetinib in paediatric patients with BRAF-aberrant or neurofibromatosis type 1-associated recurrent, refractory, or progressive low-grade glioma: a multicentre, phase 2 trial. The Lancet Oncology, 20(7), 1011-1022.

Feins, S., Kong, W., Williams, E. F., Milone, M. C., & Fraietta, J. A. (2019). An introduction to chimeric antigen receptor (CAR) T-cell immunotherapy for human cancer. American journal of hematology, 94(S1), S3-S9.

Feldmeyer, D., & Sakmann, B. (2000). Synaptic efficacy and reliability of excitatory connections between the principal neurones of the input (layer 4) and output layer (layer 5) of the neocortex. The Journal of Physiology, 525(1), 31-39.

Ferguson, S. D., Xiu, J., Weathers, S.-P., Zhou, S., Kesari, S., Weiss, S. E., Verhaak, R. G., Hohl, R. J., Barger, G. R., & Reddy, S. K. (2016). GBM-associated mutations and altered protein expression are more common in young patients. Oncotarget, 7(43), 69466.

Fernström, E., Jarfelt, M., Blomstrand, M., Lannering, B., Axelsson, M., Wasling, P., Björk-Eriksson, T., Zetterberg, H., & Kalm, M. (2024). CSF biomarkers of neurotoxicity in childhood cancer survivors after cranial radiotherapy or surgery. Annals of Clinical and Translational Neurology, 11(9), 2382-2391.

Finlay, J. L., Boyett, J. M., Yates, A. J., Wisoff, J. H., Milstein, J. M., Geyer, J. R., Bertolone, S. J., McGuire, P., Cherlow, J. M., & Tefft, M. (1995). Randomized phase III trial in childhood high-grade astrocytoma comparing vincristine, lomustine, and prednisone with the eight-drugs-in-1-day regimen. Childrens Cancer Group. Journal of Clinical Oncology, 13(1), 112-123.

Fisch, A.-S., Pestana, A., Sachse, V., Doll, C., Hofmann, E., Heiland, M., Obermueller, T., Heidemann, J., Dommerich, S., & Schoppe, D. (2024). Feasibility analysis of using patient-derived tumour organoids for treatment decision guidance in locally advanced head and neck squamous cell carcinoma. European Journal of Cancer, 213, 115100.

Fontanilles, M., Marguet, F., Beaussire, L., Magne, N., Pépin, L.-F., Alexandru, C., Tennevet, I., Hanzen, C., Langlois, O., & Jardin, F. (2020). Cell-free DNA and circulating TERT promoter mutation for disease monitoring in newly-diagnosed glioblastoma. Acta neuropathologica communications, 8, 1-10.

Fontoura, J. C., Viezzer, C., Dos Santos, F. G., Ligabue, R. A., Weinlich, R., Puga, R. D., Antonow, D., Severino, P., & Bonorino, C. (2020). Comparison of 2D and 3D cell culture models for cell growth, gene expression and drug resistance. Materials Science and Engineering: C, 107, 110264.

Force, L. M., Abdollahpour, I., Advani, S. M., Agius, D., Ahmadian, E., Alahdab, F., Alam, T., Alebel, A., Alipour, V., & Allen, C. A. (2019). The global burden of childhood and adolescent cancer in 2017: an analysis of the Global Burden of Disease Study 2017. The Lancet Oncology, 20(9), 1211-1225.

Fortin, J., Tian, R., Zarrabi, I., Hill, G., Williams, E., Sanchez-Duffhues, G., Thorikay, M., Ramachandran, P., Siddaway, R., & Wong, J. F. (2020). Mutant ACVR1 arrests glial cell differentiation to drive tumorigenesis in pediatric gliomas. Cancer cell, 37(3), 308-323. e312.

Foster, M. T., Hennigan, D., Grayston, R., van Baarsen, K., Sunderland, G., Millward, C. P., Lalgudi Srinivasan, H., Ferguson, D., Totimeh, T., Pizer, B., & Mallucci, C. (2021). Reporting morbidity associated with pediatric brain tumor surgery: are the available scoring systems sufficient? Journal of neurosurgery. Pediatrics, 27(5), 556-565. https://doi.org/10.3171/2020.9.peds20556

Foty, R. (2011). A simple hanging drop cell culture protocol for generation of 3D spheroids. JoVE (Journal of Visualized Experiments)(51), e2720.

Frederico, S. C., Hancock, J. C., Brettschneider, E. E., Ratnam, N. M., Gilbert, M. R., & Terabe, M. (2021). Making a cold tumor hot: the role of vaccines in the treatment of glioblastoma. Frontiers in Oncology, 11, 672508.

Friend, J., & Yeo, L. (2010). Fabrication of microfluidic devices using polydimethylsiloxane. Biomicrofluidics, 4(2).

Fukunaga, K., & Miyamoto, E. (1998). Role of MAP kinase in neurons. Molecular neurobiology, 16, 79-95.

Fusco, P., Parisatto, B., Rampazzo, E., Persano, L., Frasson, C., Di Meglio, A., Leslz, A., Santoro, L., Cafferata, B., & Zin, A. (2019). Patient-derived organoids (PDOs) as a novel in vitro model for neuroblastoma tumours. BMC cancer, 19, 1-11.

Galli, E., Bellesi, S., Pansini, I., Di Cesare, G., Iacovelli, C., Malafronte, R., Maiolo, E., Chiusolo, P., Sica, S., & Sorà, F. (2023). The CD4/CD8 ratio of infused CD19-CAR-T is a prognostic factor for efficacy and toxicity. British Journal of Haematology, 203(4), 564-570.

Ge, J., Liu, M. Y., Li, L., Deng, Q., Liu, F., Luo, Y., Wang, L., Yao, G., Zhu, D., & Lu, H. (2020). Detection of IDH1 and TERT promoter mutations with droplet digital PCR in diffuse gliomas. International Journal of Clinical and Experimental Pathology, 13(2), 230.

Gehring, K., Patwardhan, S., Collins, R., Groves, M., Etzel, C., Meyers, C., & Wefel, J. (2012). A randomized trial on the efficacy of methylphenidate and modafinil for improving cognitive functioning and symptoms in patients with a primary brain tumor. Journal of neuro-oncology, 107, 165-174.

Genschaft, M., Huebner, T., Plessow, F., Ikonomidou, V. N., Abolmaali, N., Krone, F., Hoffmann, A., Holfeld, E., Vorwerk, P., & Kramm, C. (2013). Impact of chemotherapy for childhood leukemia on brain morphology and function. PLoS One, 8(11), e78599.

Geoerger, B., Kieran, M. W., Grupp, S., Perek, D., Clancy, J., Krygowski, M., Ananthakrishnan, R., Boni, J. P., Berkenblit, A., & Spunt, S. L. (2012). Phase II trial of temsirolimus in children with high-grade glioma, neuroblastoma and rhabdomyosarcoma. European Journal of Cancer, 48(2), 253-262.

Geraghty, A. C., Gibson, E. M., Ghanem, R. A., Greene, J. J., Ocampo, A., Goldstein, A. K., Ni, L., Yang, T., Marton, R. M., Paşca, S. P., Greenberg, M. E., Longo, F. M., & Monje, M. (2019). Loss of Adaptive Myelination Contributes to Methotrexate Chemotherapy-Related

Cognitive Impairment. Neuron, 103(2), 250-265.e258. https://doi.org/10.1016/j.neuron.2019.04.032

Giandomenico, S. L., Mierau, S. B., Gibbons, G. M., Wenger, L. M., Masullo, L., Sit, T., Sutcliffe, M., Boulanger, J., Tripodi, M., & Derivery, E. (2019). Cerebral organoids at the air–liquid interface generate diverse nerve tracts with functional output. Nature neuroscience, 22(4), 669-679.

Giard, D. J., Aaronson, S. A., Todaro, G. J., Arnstein, P., Kersey, J. H., Dosik, H., & Parks, W. P. (1973). In vitro cultivation of human tumors: establishment of cell lines derived from a series of solid tumors. Journal of the National Cancer Institute, 51(5), 1417-1423.

Gibson, E. M., Nagaraja, S., Ocampo, A., Tam, L. T., Wood, L. S., Pallegar, P. N., Greene, J. J., Geraghty, A. C., Goldstein, A. K., & Ni, L. (2019). Methotrexate chemotherapy induces persistent tri-glial dysregulation that underlies chemotherapy-related cognitive impairment. Cell, 176(1-2), 43-55. e13.

Gilbert, F., Balaban, G., Moorhead, P., Bianchi, D., & Schlesinger, H. (1982). Abnormalities of chromosome 1p in human neuroblastoma tumors and cell lines. Cancer genetics and cytogenetics, 7(1), 33-42.

Goldsmith, K. C., Park, J. R., Kayser, K., Malvar, J., Chi, Y.-Y., Groshen, S. G., Villablanca, J. G., Krytska, K., Lai, L. M., & Acharya, P. T. (2023). Lorlatinib with or without chemotherapy in ALK-driven refractory/relapsed neuroblastoma: phase 1 trial results. Nature medicine, 29(5), 1092-1102.

Goyco Vera, D., Waghela, H., Nuh, M., Pan, J., & Lulla, P. (2024). Approved CAR-T therapies have reproducible efficacy and safety in clinical practice. Human Vaccines & Immunotherapeutics, 20(1), 2378543.

Grexa, I., Diosdi, A., Harmati, M., Kriston, A., Moshkov, N., Buzas, K., Pietiäinen, V., Koos, K., & Horvath, P. (2021). SpheroidPicker for automated 3D cell culture manipulation using deep learning. Scientific reports, 11(1), 14813.

Grill, J., Massimino, M., Bouffet, E., Azizi, A. A., McCowage, G., Cañete, A., Saran, F., Le Deley, M.-C., Varlet, P., & Morgan, P. S. (2018). Phase II, open-label, randomized, multicenter trial (HERBY) of bevacizumab in pediatric patients with newly diagnosed high-grade glioma. Journal of Clinical Oncology, 36(10), 951-958.

Grundy, T. J., De Leon, E., Griffin, K. R., Stringer, B. W., Day, B. W., Fabry, B., Cooper-White, J., & O'Neill, G. M. (2016). Differential response of patient-derived primary glioblastoma cells to environmental stiffness. Scientific reports, 6(1), 1-10.

Gururangan, S., Chi, S. N., Young Poussaint, T., Onar-Thomas, A., Gilbertson, R. J., Vajapeyam, S., Friedman, H. S., Packer, R. J., Rood, B. N., & Boyett, J. M. (2010). Lack of efficacy of bevacizumab plus irinotecan in children with recurrent malignant glioma and diffuse brainstem glioma: a Pediatric Brain Tumor Consortium study. Journal of Clinical Oncology, 28(18), 3069-3075.

Ham, S. W., Jeon, H.-Y., Jin, X., Kim, E.-J., Kim, J.-K., Shin, Y. J., Lee, Y., Kim, S. H., Lee, S. Y., & Seo, S. (2019). TP53 gain-of-function mutation promotes inflammation in glioblastoma. Cell Death & Differentiation, 26(3), 409-425.

Han, S. J., Kwon, S., & Kim, K. S. (2021). Challenges of applying multicellular tumor spheroids in preclinical phase. Cancer cell international, 21, 1-19.

Hashemi, M., Etemad, S., Rezaei, S., Ziaolhagh, S., Rajabi, R., Rahmanian, P., Abdi, S., Koohpar, Z. K., Rafiei, R., & Raei, B. (2023). Progress in targeting PTEN/PI3K/Akt axis in glioblastoma therapy: Revisiting molecular interactions. Biomedicine & Pharmacotherapy, 158, 114204.

He, A., Huang, Y., Cheng, W., Zhang, D., He, W., Bai, Y., Gu, C., Ma, Z., He, Z., & Si, G. (2020). Organoid culture system for patient-derived lung metastatic osteosarcoma. Medical Oncology, 37, 1-9.

He, D., & Lasek, A. W. (2020). Anaplastic lymphoma kinase regulates internalization of the dopamine D2 receptor. Molecular pharmacology, 97(2), 123-131.

Heide, M., Huttner, W. B., & Mora-Bermúdez, F. (2018). Brain organoids as models to study human neocortex development and evolution. Current opinion in cell biology, 55, 8-16.

Heideveld, E., Horcas-Lopez, M., Lopez-Yrigoyen, M., Forrester, L. M., Cassetta, L., & Pollard, J. W. (2020). Methods for macrophage differentiation and in vitro generation of human tumor associated-like macrophages. Methods in Enzymology, 632, 113-131.

Heins, N., Malatesta, P., Cecconi, F., Nakafuku, M., Tucker, K. L., Hack, M. A., Chapouton, P., Barde, Y.-A., & Götz, M. (2002). Glial cells generate neurons: the role of the transcription factor Pax6. Nature neuroscience, 5(4), 308-315.

Hennig, A., Baenke, F., Klimova, A., Drukewitz, S., Jahnke, B., Brückmann, S., Secci, R., Winter, C., Schmäche, T., & Seidlitz, T. (2022). Detecting drug resistance in pancreatic cancer organoids guides optimized chemotherapy treatment. The Journal of pathology, 257(5), 607-619.

Hernández-Ortega, K., Canul-Euan, A. A., Solis-Paredes, J. M., Borboa-Olivares, H., Reyes-Muñoz, E., Estrada-Gutierrez, G., & Camacho-Arroyo, I. (2024). S100B actions on glial and neuronal cells in the developing brain: An overview. Frontiers in Neuroscience, 18, 1425525.

Hertler, C., Felsberg, J., Gramatzki, D., Le Rhun, E., Clarke, J., Soffietti, R., Wick, W., Chinot, O., Ducray, F., & Roth, P. (2023). Long-term survival with IDH wildtype

glioblastoma: first results from the ETERNITY Brain Tumor Funders' Collaborative Consortium (EORTC 1419). European Journal of Cancer, 189, 112913.

Hill, D. E., Ciesielski, K., Sethre-Hofstad, L., Duncan, M. H., & Lorenzi, M. (1997). Visual and Verbal Short-Term Memory Deficits in Childhood Leukemia Survivors After Intrathecal Chemotheraphy. Journal of pediatric psychology, 22(6), 861-870.

Hingorani, A. D., Kuan, V., Finan, C., Kruger, F. A., Gaulton, A., Chopade, S., Sofat, R., MacAllister, R. J., Overington, J. P., & Hemingway, H. (2019). Improving the odds of drug development success through human genomics: modelling study. Scientific reports, 9(1), 18911.

Hoeman, C. M., Cordero, F. J., Hu, G., Misuraca, K., Romero, M. M., Cardona, H. J., Nazarian, J., Hashizume, R., McLendon, R., & Yu, P. (2019). ACVR1 R206H cooperates with H3. 1K27M in promoting diffuse intrinsic pontine glioma pathogenesis. Nature communications, 10(1), 1023.

Hoffman, L. M., Veldhuijzen van Zanten, S. E., Colditz, N., Baugh, J., Chaney, B., Hoffmann, M., Lane, A., Fuller, C., Miles, L., & Hawkins, C. (2018). Clinical, radiologic, pathologic, and molecular characteristics of long-term survivors of diffuse intrinsic pontine glioma (DIPG): a collaborative report from the International and European Society for Pediatric Oncology DIPG Registries. Journal of Clinical Oncology, 36(19), 1963-1972.

Hoffmann, P., Eder, R., Kunz-Schughart, L. A., Andreesen, R., & Edinger, M. (2004). Large-scale in vitro expansion of polyclonal human CD4+ C25high regulatory T cells. Blood, 104(3), 895-903.

Hogenson, T. L., Xie, H., Phillips, W. J., Toruner, M. D., Li, J. J., Horn, I. P., Kennedy, D. J., Almada, L. L., Marks, D. L., & Carr, R. M. (2022). Culture media composition influences

patient-derived organoid ability to predict therapeutic responses in gastrointestinal cancers. Jci Insight, 7(22).

Hou, X., Li, M., Wu, G., Feng, W., Su, J., Jiang, H., Jiang, G., Chen, J., Zhang, B., & You, Z. (2023). Gefitinib plus chemotherapy vs gefitinib alone in untreated EGFR-Mutant non–small cell lung Cancer in patients with brain metastases: the GAP BRAIN open-label, randomized, multicenter, phase 3 study. JAMA network open, 6(2), e2255050-e2255050.

Howitt, B. E., Shukla, S. A., Sholl, L. M., Ritterhouse, L. L., Watkins, J. C., Rodig, S., Stover, E., Strickland, K. C., D'Andrea, A. D., & Wu, C. J. (2015). Association of polymerase e–mutated and microsatellite-instable endometrial cancers with neoantigen load, number of tumor-infiltrating lymphocytes, and expression of PD-1 and PD-L1. JAMA oncology, 1(9), 1319-1323.

Hsu, K., Middlemiss, S., Saletta, F., Gottschalk, S., McCowage, G. B., & Kramer, B. (2021). Chimeric Antigen Receptor-modified T cells targeting EphA2 for the immunotherapy of paediatric bone tumours. Cancer Gene Therapy, 28(3), 321-334.

Huang, J., Li, Y. B., Charlebois, C., Nguyen, T., Liu, Z., Bloemberg, D., Zafer, A., Baumann, E., Sodja, C., & Leclerc, S. (2022). Application of blood brain barrier models in pre-clinical assessment of glioblastoma-targeting CAR-T based immunotherapies. Fluids and Barriers of the CNS, 19(1), 38.

Huang, M., Li, S., Li, P., Kang, Z., Zhang, B., & Li, W. (2024). Drug clinical trials on high-grade gliomas: challenges and hopes. Cancer Biology & Medicine, 20(12), 947.

Huang, Q., Tang, B., Romero, J. C., Yang, Y., Elsayed, S. K., Pahapale, G., Lee, T.-J., Morales Pantoja, I. E., Han, F., & Berlinicke, C. (2022). Shell microelectrode arrays (MEAs) for brain organoids. Science advances, 8(33), eabq5031.

Huang, T. Y., Piunti, A., Lulla, R. R., Qi, J., Horbinski, C. M., Tomita, T., James, C. D., Shilatifard, A., & Saratsis, A. M. (2017). Detection of Histone H3 mutations in cerebrospinal fluid-derived tumor DNA from children with diffuse midline glioma. Acta neuropathologica communications, 5, 1-12.

Huang, W.-K., Wong, S. Z. H., Pather, S. R., Nguyen, P. T., Zhang, F., Zhang, D. Y., Zhang, Z., Lu, L., Fang, W., & Chen, L. (2021). Generation of hypothalamic arcuate organoids from human induced pluripotent stem cells. Cell stem cell, 28(9), 1657-1670. e1610.

Hughes, E. G., & Stockton, M. E. (2021). Premyelinating oligodendrocytes: mechanisms underlying cell survival and integration. Frontiers in cell and developmental biology, 9, 714169.

Hwang, T. J., Carpenter, D., Lauffenburger, J. C., Wang, B., Franklin, J. M., & Kesselheim, A. S. (2016). Failure of Investigational Drugs in Late-Stage Clinical Development and Publication of Trial Results. JAMA Internal Medicine, 176(12), 1826-1833. https://doi.org/10.1001/jamainternmed.2016.6008

Ikonomidou, C. (2018). Chemotherapy and the pediatric brain. Molecular and cellular pediatrics, 5(1), 8.

Impey, S., Obrietan, K., & Storm, D. R. (1999). Making new connections: role of ERK/MAP kinase signaling in neuronal plasticity. Neuron, 23(1), 11-14.

Interiano, R. B., Loh, A. H., Hinkle, N., Wahid, F. N., Malkan, A. D., Bahrami, A., Jenkins, J. J., Mao, S., Wu, J., & Proctor, K. (2015). Safety and diagnostic accuracy of tumor biopsies in children with cancer. Cancer, 121(7), 1098-1107.

Iroegbu, J. D., Ijomone, O. K., Femi-Akinlosotu, O. M., & Ijomone, O. M. (2021). ERK/MAPK signalling in the developing brain: Perturbations and consequences. Neuroscience & Biobehavioral Reviews, 131, 792-805.

Iwata, Y., Nicole, O., Zurakowski, D., Okamura, T., & Jonas, R. A. (2010). Ibuprofen for neuroprotection after cerebral ischemia. The Journal of thoracic and cardiovascular surgery, 139(2), 489-493.

Izquierdo, E., Proszek, P., Pericoli, G., Temelso, S., Clarke, M., Carvalho, D. M., Mackay, A., Marshall, L. V., Carceller, F., & Hargrave, D. (2021). Droplet digital PCR-based detection of circulating tumor DNA from pediatric high grade and diffuse midline glioma patients. Neuro-Oncology Advances, 3(1), vdab013.

Jackson, C., Cherry, C., Bom, S., Dykema, A. G., Wang, R., Thompson, E., Zhang, M., Li, R., Ji, Z., & Hou, W. (2025) Distinct myeloid-derived suppressor cell populations in human glioblastoma. Science, 387(6731), eabm5214.

Jackson, E. R., Duchatel, R. J., Staudt, D. E., Persson, M. L., Mannan, A., Yadavilli, S., Parackal, S., Game, S., Chong, W. C., & Jayasekara, W. S. N. (2023). ONC201 in combination with paxalisib for the treatment of H3K27-altered diffuse midline glioma. Cancer research, 83(14), 2421-2437.

Jacob, F., Ming, G.-l., & Song, H. (2020). Generation and biobanking of patient-derived glioblastoma organoids and their application in CAR T cell testing. Nature protocols, 15(12), 4000-4033.

Jacob, F., Salinas, R. D., Zhang, D. Y., Nguyen, P. T., Schnoll, J. G., Wong, S. Z. H., Thokala, R., Sheikh, S., Saxena, D., & Prokop, S. (2020). A patient-derived glioblastoma organoid model and biobank recapitulates inter-and intra-tumoral heterogeneity. Cell, 180(1), 188-204. e122.

Jakacki, R. I., Cohen, K. J., Buxton, A., Krailo, M. D., Burger, P. C., Rosenblum, M. K., Brat, D. J., Hamilton, R. L., Eckel, S. P., & Zhou, T. (2016). Phase 2 study of concurrent radiotherapy and temozolomide followed by temozolomide and lomustine in the treatment of children with high-grade glioma: a report of the Children's Oncology Group ACNS0423 study. Neuro-Oncology, 18(10), 1442-1450.

Jäkel, S., & Dimou, L. (2017). Glial cells and their function in the adult brain: a journey through the history of their ablation. Frontiers in cellular neuroscience, 11, 24.

Janelsins, M. C., Kohli, S., Mohile, S. G., Usuki, K., Ahles, T. A., & Morrow, G. R. (2011). An update on cancer- and chemotherapy-related cognitive dysfunction: current status. Seminars in oncology, 38(3), 431-438. https://doi.org/10.1053/j.seminoncol.2011.03.014

Jarmolowicz, D. P., Gehringer, R., Lemley, S. M., Sofis, M. J., Kaplan, S., & Johnson, M. A. (2019). 5-Fluorouracil impairs attention and dopamine release in rats. Behavioural brain research, 362, 319-322. https://doi.org/10.1016/j.bbr.2019.01.007

Jensen, C., & Teng, Y. (2020). Is it time to start transitioning from 2D to 3D cell culture? Frontiers in Molecular Biosciences, 7, 33.

Jiao, L., & Liu, X. (2015). Structural basis of histone H3K27 trimethylation by an active polycomb repressive complex 2. science, 350(6258), aac4383.

Jiruska, P., De Curtis, M., Jefferys, J. G., Schevon, C. A., Schiff, S. J., & Schindler, K. (2013). Synchronization and desynchronization in epilepsy: controversies and hypotheses. The Journal of Physiology, 591(4), 787-797.

Jobin, C., Harvey, M., Lacouture, A., Weidmann, C., Neveu, B., Pouliot, F., & Audet-Walsh, É. (2024). Protocol for transducing human primary epithelial prostate cells and patient-derived organoids with high efficiency. STAR protocols, 5(3), 103200.

Kadoshima, T., Sakaguchi, H., Nakano, T., Soen, M., Ando, S., Eiraku, M., & Sasai, Y. (2013). Self-organization of axial polarity, inside-out layer pattern, and species-specific progenitor dynamics in human ES cell–derived neocortex. Proceedings of the National Academy of Sciences, 110(50), 20284-20289.

Kannaiyan, R., & Mahadevan, D. (2018). A comprehensive review of protein kinase inhibitors for cancer therapy. Expert review of anticancer therapy, 18(12), 1249-1270.

Kanu, O. O., Hughes, B., Di, C., Lin, N., Fu, J., Bigner, D. D., Yan, H., & Adamson, C. (2009). Glioblastoma multiforme oncogenomics and signaling pathways. Clinical medicine. Oncology, 3, CMO. S1008.

Kapałczyńska, M., Kolenda, T., Przybyła, W., Zajączkowska, M., Teresiak, A., Filas, V., Ibbs, M., Bliźniak, R., Łuczewski, Ł., & Lamperska, K. (2018). 2D and 3D cell cultures–a comparison of different types of cancer cell cultures. Archives of medical science, 14(4), 910-919.

Karimi, M. A., Lee, E., Bachmann, M. H., Salicioni, A. M., Behrens, E. M., Kambayashi, T., & Baldwin, C. L. (2014). Measuring cytotoxicity by bioluminescence imaging outperforms the standard chromium-51 release assay. PLoS One, 9(2), e89357.

Karschnia, P., Parsons, M. W., & Dietrich, J. (2019). Pharmacologic management of cognitive impairment induced by cancer therapy. The Lancet Oncology, 20(2), e92-e102.

Kashyap, D., & Salman, H. (2024). Targeting Interleukin-13 Receptor α2 and EphA2 in Aggressive Breast Cancer Subtypes with Special References to Chimeric Antigen Receptor T-Cell Therapy. International Journal of Molecular Sciences, 25(7), 3780.

Kasper, L. H., & Baker, S. J. (2020). Invited Review: Emerging functions of histone H3 mutations in paediatric diffuse high-grade gliomas. Neuropathology and applied neurobiology, 46(1), 73-85.

Kaur, B., Khwaja, F. W., Severson, E. A., Matheny, S. L., Brat, D. J., & Van Meir, E. G. (2005). Hypoxia and the hypoxia-inducible-factor pathway in glioma growth and angiogenesis. Neuro-Oncology, 7(2), 134-153.

Kazandjian, D., Blumenthal, G. M., Yuan, W., He, K., Keegan, P., & Pazdur, R. (2016). FDA approval of gefitinib for the treatment of patients with metastatic EGFR mutation–positive non–small cell lung cancer. Clinical cancer research, 22(6), 1307-1312.

Kelley, M. R., Jiang, Y., Guo, C., Reed, A., Meng, H., & Vasko, M. R. (2014). Role of the DNA base excision repair protein, APE1 in cisplatin, oxaliplatin, or carboplatin induced sensory neuropathy. PLoS One, 9(9), e106485.

Khan, F., Pang, L., Dunterman, M., Lesniak, M. S., Heimberger, A. B., & Chen, P. (2023). Macrophages and microglia in glioblastoma: heterogeneity, plasticity, and therapy. The Journal of clinical investigation, 133(1).

Khantakova, D., Brioschi, S., & Molgora, M. (2022). Exploring the impact of TREM2 in tumor-associated macrophages. Vaccines, 10(6), 943.

Kickingereder, P., Sahm, F., Radbruch, A., Wick, W., Heiland, S., Deimling, A. v., Bendszus, M., & Wiestler, B. (2015). IDH mutation status is associated with a distinct hypoxia/angiogenesis transcriptome signature which is non-invasively predictable with rCBV imaging in human glioma. Scientific reports, 5(1), 16238.

Kilburn, L. B., Khuong-Quang, D.-A., Hansford, J. R., Landi, D., van der Lugt, J., Leary, S. E., Driever, P. H., Bailey, S., Perreault, S., & McCowage, G. (2024). The type II RAF

inhibitor tovorafenib in relapsed/refractory pediatric low-grade glioma: the phase 2 FIREFLY-1 trial. Nature medicine, 30(1), 207-217.

Kim, J., Hong, S.-P., Lee, S., Lee, W., Lee, D., Kim, R., Park, Y. J., Moon, S., Park, K., & Cha, B. (2023). Multidimensional fragmentomic profiling of cell-free DNA released from patient-derived organoids. Human Genomics, 17(1), 96.

Kluiver, T., Alieva, M., Van Vuurden, D., Wehrens, E. J., & Rios, A. C. (2020). Invaders exposed: understanding and targeting tumor cell invasion in diffuse intrinsic pontine glioma. Frontiers in Oncology, 10, 92.

Knight, G. T., Lundin, B. F., Iyer, N., Ashton, L. M., Sethares, W. A., Willett, R. M., & Ashton, R. S. (2018). Engineering induction of singular neural rosette emergence within hPSC-derived tissues. Elife, 7, e37549.

Knight, K. R. G., Kraemer, D. F., & Neuwelt, E. A. (2005). Ototoxicity in children receiving platinum chemotherapy: underestimating a commonly occurring toxicity that may influence academic and social development. Journal of Clinical Oncology, 23(34), 8588-8596.

Kobolak, J., Teglasi, A., Bellak, T., Janstova, Z., Molnar, K., Zana, M., Bock, I., Laszlo, L., & Dinnyes, A. (2020). Human induced pluripotent stem cell-derived 3d-neurospheres are suitable for neurotoxicity screening. Cells, 9(5), 1122.

Korshunov, A., Schrimpf, D., Ryzhova, M., Sturm, D., Chavez, L., Hovestadt, V., Sharma, T., Habel, A., Burford, A., & Jones, C. (2017). H3-/IDH-wild type pediatric glioblastoma is comprised of molecularly and prognostically distinct subtypes with associated oncogenic drivers. Acta neuropathologica, 134, 507-516.

Kortüm, F., Das, S., Flindt, M., Morris-Rosendahl, D. J., Stefanova, I., Goldstein, A., Horn, D., Klopocki, E., Kluger, G., & Martin, P. (2011). The core FOXG1 syndrome phenotype

consists of postnatal microcephaly, severe mental retardation, absent language, dyskinesia, and corpus callosum hypogenesis. Journal of medical genetics, 48(6), 396-406.

Korzhevskii, D., Karpenko, M., & Kirik, O. (2012). Microtubule-associated proteins as indicators of differentiation and the functional state of nerve cells. Neuroscience and Behavioral Physiology, 42, 215-222.

Koschmann, C., Calinescu, A.-A., Nunez, F. J., Mackay, A., Fazal-Salom, J., Thomas, D., Mendez, F., Kamran, N., Dzaman, M., & Mulpuri, L. (2016). ATRX loss promotes tumor growth and impairs nonhomologous end joining DNA repair in glioma. Science translational medicine, 8(328), 328ra328-328ra328.

Koschmann, C., Zamler, D., MacKay, A., Robinson, D., Wu, Y.-M., Doherty, R., Marini, B., Tran, D., Garton, H., & Muraszko, K. (2016). Characterizing and targeting PDGFRA alterations in pediatric high-grade glioma. Oncotarget, 7(40), 65696.

Krieger, T. G., Tirier, S. M., Park, J., Jechow, K., Eisemann, T., Peterziel, H., Angel, P., Eils, R., & Conrad, C. (2020). Modeling glioblastoma invasion using human brain organoids and single-cell transcriptomics. Neuro-Oncology, 22(8), 1138-1149.

Kung, C.-P., & Weber, J. D. (2022). It's getting complicated—a fresh look at p53-MDM2-ARF triangle in tumorigenesis and cancer therapy. Frontiers in cell and developmental biology, 10, 818744.

Labuhn, M., Jones, G., Speel, E. J., Maier, D., Zweifel, C., Gratzl, O., Van Meir, E. G., Hegi, M. E., & Merlo, A. (2001). Quantitative real-time PCR does not show selective targeting of p14ARF but concomitant inactivation of both p16INK4A and p14ARF in 105 human primary gliomas. Oncogene, 20(9), 1103-1109.

Laetsch, T. W., Ludwig, K., Williams, P. M., Roy-Chowdhuri, S., Patton, D. R., Coffey, B., Reid, J. M., Piao, J., Saguilig, L., & Alonzo, T. A. (2024). Phase II Study of Samotolisib in Children and Young Adults With Tumors Harboring Phosphoinositide 3-Kinase/Mammalian Target of Rapamycin Pathway Alterations: Pediatric MATCH APEC1621D. JCO Precision Oncology, 8, e2400258.

Lago, C., Federico, A., Leva, G., Mack, N. L., Schwalm, B., Ballabio, C., Gianesello, M., Abballe, L., Giovannoni, I., & Reddel, S. (2023). Patient-and xenograft-derived organoids recapitulate pediatric brain tumor features and patient treatments. EMBO molecular medicine, 15(12), e18199.

Lancaster, M. A., Renner, M., Martin, C.-A., Wenzel, D., Bicknell, L. S., Hurles, M. E., Homfray, T., Penninger, J. M., Jackson, A. P., & Knoblich, J. A. (2013). Cerebral organoids model human brain development and microcephaly. Nature, 501(7467), 373-379.

Langhans, S. A. (2018). Three-dimensional in vitro cell culture models in drug discovery and drug repositioning. Frontiers in pharmacology, 9, 6.

Lauvås, A. J., Lislien, M., Holme, J. A., Dirven, H., Paulsen, R. E., Alm, I. M., Andersen, J. M., Skarpen, E., Sørensen, V., & Macko, P. (2022). Developmental neurotoxicity of acrylamide and its metabolite glycidamide in a human mixed culture of neurons and astrocytes undergoing differentiation in concentrations relevant for human exposure. Neurotoxicology, 92, 33-48.

Lee, A., Arasaratnam, M., Chan, D. L. H., Khasraw, M., Howell, V. M., & Wheeler, H. (2020). Anti-epidermal growth factor receptor therapy for glioblastoma in adults. Cochrane Database of Systematic Reviews (5).

Lee, C.-T., Chen, J., Kindberg, A. A., Bendriem, R. M., Spivak, C. E., Williams, M. P., Richie, C. T., Handreck, A., Mallon, B. S., & Lupica, C. R. (2017). CYP3A5 mediates effects

of cocaine on human neocorticogenesis: studies using an in vitro 3D self-organized hPSC model with a single cortex-like unit. Neuropsychopharmacology, 42(3), 774-784.

Lee, D. W., Santomasso, B. D., Locke, F. L., Ghobadi, A., Turtle, C. J., Brudno, J. N., Maus, M. V., Park, J. H., Mead, E., & Pavletic, S. (2019). ASTCT consensus grading for cytokine release syndrome and neurologic toxicity associated with immune effector cells. Biology of blood and marrow transplantation, 25(4), 625-638.

Lee, J., & Liu, J. (2025). Flexible and stretchable bioelectronics for organoids. Med-X, 3(1), 5.

Leek, R., Grimes, D. R., Harris, A. L., & McIntyre, A. (2016). Methods: using three-dimensional culture (spheroids) as an in vitro model of tumour hypoxia. Tumor microenvironment, 167-196.

Li, R., Sun, L., Fang, A., Li, P., Wu, Q., & Wang, X. (2017). Recapitulating cortical development with organoid culture in vitro and modeling abnormal spindle-like (ASPM related primary) microcephaly disease. Protein & cell, 8(11), 823-833.

Liao, D., Zhang, J., Yan, T., Chen, S., Li, W., Shangguan, D., & She, Z. (2023). Recent Advances in the Management of Adverse Events Associated with Lorlatinib. OncoTargets and Therapy, 731-738.

Lieberman, N. A., DeGolier, K., Kovar, H. M., Davis, A., Hoglund, V., Stevens, J., Winter, C., Deutsch, G., Furlan, S. N., & Vitanza, N. A. (2019). Characterization of the immune microenvironment of diffuse intrinsic pontine glioma: implications for development of immunotherapy. Neuro-Oncology, 21(1), 83-94.

Lin, G. L., & Monje, M. (2017). A protocol for rapid post-mortem cell culture of diffuse intrinsic pontine glioma (DIPG). Journal of visualized experiments: JoVE(121), 55360.

Lin, G. L., Nagaraja, S., Filbin, M. G., Suvà, M. L., Vogel, H., & Monje, M. (2018). Non-inflammatory tumor microenvironment of diffuse intrinsic pontine glioma. Acta neuropathologica communications, 6, 1-12.

Lin, Q., Ba, T., Ho, J., Chen, D., Cheng, Y., Wang, L., Xu, G., Xu, L., Zhou, Y., & Wei, Y. (2021). First-in-human trial of EphA2-redirected CAR T-cells in patients with recurrent glioblastoma: a preliminary report of three cases at the starting dose. Frontiers in Oncology, 11, 694941.

Linkous, A., Balamatsias, D., Snuderl, M., Edwards, L., Miyaguchi, K., Milner, T., Reich, B., Cohen-Gould, L., Storaska, A., & Nakayama, Y. (2019). Modeling patient-derived glioblastoma with cerebral organoids. Cell reports, 26(12), 3203-3211. e3205.

Liu, F., Huang, J., & Liu, Z. (2019). Vincristine impairs microtubules and causes neurotoxicity in cerebral organoids. Neuroscience, 404, 530-540.

Liu, I., Jiang, L., Samuelsson, E. R., Marco Salas, S., Beck, A., Hack, O. A., Jeong, D., Shaw, M. L., Englinger, B., & LaBelle, J. (2022). The landscape of tumor cell states and spatial organization in H3-K27M mutant diffuse midline glioma across age and location. Nature Genetics, 54(12), 1881-1894.

Liu, K.-W., Feng, H., Bachoo, R., Kazlauskas, A., Smith, E. M., Symes, K., Hamilton, R. L., Nagane, M., Nishikawa, R., & Hu, B. (2011). SHP-2/PTPN11 mediates gliomagenesis driven by PDGFRA and INK4A/ARF aberrations in mice and humans. The Journal of clinical investigation, 121(3), 905-917.

Liu, X., Ying, J., Wang, X., Zheng, Q., Zhao, T., Yoon, S., Yu, W., Yang, D., Fang, Y., & Hua, F. (2021). Astrocytes in neural circuits: key factors in synaptic regulation and potential targets for neurodevelopmental disorders. Frontiers in Molecular Neuroscience, 14, 729273.

Locke, F. L., Rossi, J. M., Neelapu, S. S., Jacobson, C. A., Miklos, D. B., Ghobadi, A., Oluwole, O. O., Reagan, P. M., Lekakis, L. J., & Lin, Y. (2020). Tumor burden, inflammation, and product attributes determine outcomes of axicabtagene ciloleucel in large B-cell lymphoma. Blood advances, 4(19), 4898-4911.

Lomeli, N., Di, K., Czerniawski, J., Guzowski, J. F., & Bota, D. A. (2017). Cisplatin-induced mitochondrial dysfunction is associated with impaired cognitive function in rats. Free Radical Biology and Medicine, 102, 274-286. https://doi.org/https://doi.org/10.1016/j.freeradbiomed.2016.11.046

Lonjaret, L., Guyonnet, M., Berard, E., Vironneau, M., Peres, F., Sacrista, S., Ferrier, A., Ramonda, V., Vuillaume, C., Roux, F. E., Fourcade, O., & Geeraerts, T. (2017). Postoperative complications after craniotomy for brain tumor surgery. Anaesth Crit Care Pain Med, 36(4), 213-218. https://doi.org/10.1016/j.accpm.2016.06.012

Louis, D. N., Perry, A., Reifenberger, G., Von Deimling, A., Figarella-Branger, D., Cavenee, W. K., Ohgaki, H., Wiestler, O. D., Kleihues, P., & Ellison, D. W. (2016). The 2016 World Health Organization classification of tumors of the central nervous system: a summary. Acta neuropathologica, 131, 803-820.

Loureiro, L. V. M., Neder, L., Callegaro-Filho, D., de Oliveira Koch, L., Stavale, J. N., & Malheiros, S. M. F. (2020). The immunohistochemical landscape of the VEGF family and its receptors in glioblastomas. Surgical and Experimental Pathology, 3, 1-8.

Lozzio, C. B., & Lozzio, B. B. (1975). Human chronic myelogenous leukemia cell-line with positive Philadelphia chromosome.

Lü, L., Yuan, F., Fan, H., Li, Y., Liu, J., Feng, W., Zhang, H.-G., & Chen, S.-Y. (2023). Ethanol exposure disrupted the formation of radial glial processes and impaired the

generation and migration of outer radial glial cells in forebrain organoids derived from human embryonic stem cells. Experimental neurology, 362, 114325.

Lukas, R. V., Rodon, J., Becker, K., Wong, E. T., Shih, K., Touat, M., Fassò, M., Osborne, S., Molinero, L., & O'Hear, C. (2018). Clinical activity and safety of atezolizumab in patients with recurrent glioblastoma. Journal of neuro-oncology, 140, 317-328.

Lulla, R. R., Buxton, A., Krailo, M. D., Lazow, M. A., Boue, D. R., Leach, J. L., Lin, T., Geller, J. I., Kumar, S. S., & Nikiforova, M. N. (2024). Vorinostat, temozolomide or bevacizumab with irradiation and maintenance BEV/TMZ in pediatric high-grade glioma: A Children's Oncology Group Study. Neuro-Oncology Advances, 6(1), vdae035.

Luo, J., Junaid, M., Hamid, N., Duan, J.-J., Yang, X., & Pei, D.-S. (2022). Current understanding of gliomagenesis: from model to mechanism. International Journal of Medical Sciences, 19(14), 2071.

Machon, O., Backman, M., Krauss, S., & Kozmik, Z. (2005). The cellular fate of cortical progenitors is not maintained in neurosphere cultures. Molecular and Cellular Neuroscience, 30(3), 388-397.

Mackay, A., Burford, A., Carvalho, D., Izquierdo, E., Fazal-Salom, J., Taylor, K. R., Bjerke, L., Clarke, M., Vinci, M., & Nandhabalan, M. (2017). Integrated molecular meta-analysis of 1,000 pediatric high-grade and diffuse intrinsic pontine glioma. Cancer cell, 32(4), 520-537. e525.

Madhavan, M., Nevin, Z. S., Shick, H. E., Garrison, E., Clarkson-Paredes, C., Karl, M., Clayton, B. L., Factor, D. C., Allan, K. C., & Barbar, L. (2018). Induction of myelinating oligodendrocytes in human cortical spheroids. Nature methods, 15(9), 700-706.

Majzner, R. G., Ramakrishna, S., Yeom, K. W., Patel, S., Chinnasamy, H., Schultz, L. M., Richards, R. M., Jiang, L., Barsan, V., & Mancusi, R. (2022). GD2-CAR T cell therapy for H3K27M-mutated diffuse midline gliomas. Nature, 603(7903), 934-941.

Majzner, R. G., Rietberg, S. P., Sotillo, E., Dong, R., Vachharajani, V. T., Labanieh, L., Myklebust, J. H., Kadapakkam, M., Weber, E. W., & Tousley, A. M. (2020). Tuning the antigen density requirement for CAR T-cell activity. Cancer discovery, 10(5), 702-723.

Malumbres, M., & Barbacid, M. (2009). Cell cycle, CDKs and cancer: a changing paradigm. Nature reviews cancer, 9(3), 153-166.

Manoharan, N., Liu, K. X., Mueller, S., Haas-Kogan, D. A., & Bandopadhayay, P. (2023). Pediatric low-grade glioma: Targeted therapeutics and clinical trials in the molecular era. Neoplasia, 36, 100857.

Mariani, J., Coppola, G., Zhang, P., Abyzov, A., Provini, L., Tomasini, L., Amenduni, M., Szekely, A., Palejev, D., & Wilson, M. (2015). FOXG1-dependent dysregulation of GABA/glutamate neuron differentiation in autism spectrum disorders. Cell, 162(2), 375-390.

Mattei, C., Alshawaf, A., D'Abaco, G., Nayagam, B., & Dottori, M. (2018). Generation of neural organoids from human embryonic stem cells using the rotary cell culture system: effects of microgravity on neural progenitor cell fate. Stem cells and development, 27(12), 848-857.

McDonald, M., Sebinger, D., Brauns, L., Gonzalez-Cano, L., Menuchin-Lasowski, Y., Mierzejewski, M., Psathaki, O.-E., Stumpf, A., Wickham, J., & Rauen, T. (2023). A mesh microelectrode array for non-invasive electrophysiology within neural organoids. Biosensors and Bioelectronics, 228, 115223.

Mei, J., Liu, X., Tian, H. X., Chen, Y., Cao, Y., Zeng, J., Liu, Y. C., Chen, Y., Gao, Y., & Yin, J. Y. (2024). Tumour organoids and assembloids: Patient-derived cancer avatars for immunotherapy. Clinical and Translational Medicine, 14(4), e1656.

Mendonça, L. S., Nóbrega, C., Tavino, S., Brinkhaus, M., Matos, C., Tomé, S., Moreira, R., Henriques, D., Kaspar, B. K., & Pereira de Almeida, L. (2019). Ibuprofen enhances synaptic function and neural progenitors proliferation markers and improves neuropathology and motor coordination in Machado–Joseph disease models. Human Molecular Genetics, 28(22), 3691-3703.

Messiaen, J., Jacobs, S. A., & De Smet, F. (2023). The tumor micro-environment in pediatric glioma: friend or foe? Frontiers in Immunology, 14, 1227126.

Mi, Y., Guo, N., Luan, J., Cheng, J., Hu, Z., Jiang, P., Jin, W., & Gao, X. (2020). The emerging role of myeloid-derived suppressor cells in the glioma immune suppressive microenvironment. Frontiers in Immunology, 11, 737.

Miklja, Z., Yadav, V. N., Cartaxo, R. T., Siada, R., Thomas, C. C., Cummings, J. R., Mullan, B., Stallard, S., Paul, A., & Bruzek, A. K. (2020). Everolimus improves the efficacy of dasatinib in PDGFRα-driven glioma. The Journal of clinical investigation, 130(10), 5313-5325.

Miyoshi, G., Ueta, Y., Natsubori, A., Hiraga, K., Osaki, H., Yagasaki, Y., Kishi, Y., Yanagawa, Y., Fishell, G., & Machold, R. P. (2021). FoxG1 regulates the formation of cortical GABAergic circuit during an early postnatal critical period resulting in autism spectrum disorder-like phenotypes. Nature communications, 12(1), 1-17.

Mok, T. S., Wu, Y.-L., Thongprasert, S., Yang, C.-H., Chu, D.-T., Saijo, N., Sunpaweravong, P., Han, B., Margono, B., & Ichinose, Y. (2009). Gefitinib or carboplatin–paclitaxel in pulmonary adenocarcinoma. New England journal of medicine, 361(10), 947-957.

Mounier, N. M., Abdel-Maged, A. E.-S., Wahdan, S. A., Gad, A. M., & Azab, S. S. (2020). Chemotherapy-induced cognitive impairment (CICI): An overview of etiology and pathogenesis. Life sciences, 258, 118071.

Mueller, S., Jain, P., Liang, W. S., Kilburn, L., Kline, C., Gupta, N., Panditharatna, E., Magge, S. N., Zhang, B., & Zhu, Y. (2019). A pilot precision medicine trial for children with diffuse intrinsic pontine glioma—PNOC003: A report from the Pacific Pediatric Neuro-Oncology Consortium. International journal of cancer, 145(7), 1889-1901.

Muguruma, K., Nishiyama, A., Kawakami, H., Hashimoto, K., & Sasai, Y. (2015). Self-organization of polarized cerebellar tissue in 3D culture of human pluripotent stem cells. Cell reports, 10(4), 537-550.

Muhammad, N., Wang, R., Li, W., Zhang, Z., Chang, Y., Hu, Y., Zhao, J., Zheng, X., Mao, Q., & Xia, H. (2022). A novel TanCAR targeting IL13Rα2 and EphA2 for enhanced glioblastoma therapy. Molecular Therapy-Oncolytics, 24, 729-741.

Mulder, L. A., Depla, J. A., Sridhar, A., Wolthers, K., Pajkrt, D., & Vieira de Sá, R. (2023). A beginner's guide on the use of brain organoids for neuroscientists: a systematic review. Stem cell research & therapy, 14(1), 87.

Mulhern, R. K., Khan, R. B., Kaplan, S., Helton, S., Christensen, R., Bonner, M., Brown, R., Xiong, X., Wu, S., & Gururangan, S. (2004). Short-term efficacy of methylphenidate: a randomized, double-blind, placebo-controlled trial among survivors of childhood cancer. Journal of Clinical Oncology, 22(23), 4795-4803.

Müller, J., Ballini, M., Livi, P., Chen, Y., Radivojevic, M., Shadmani, A., Viswam, V., Jones, I. L., Fiscella, M., & Diggelmann, R. (2015). High-resolution CMOS MEA platform to study neurons at subcellular, cellular, and network levels. Lab on a Chip, 15(13), 2767-2780.

Muller, P. A., & Vousden, K. H. (2014). Mutant p53 in cancer: new functions and therapeutic opportunities. Cancer cell, 25(3), 304-317.

Munyeshyaka, M., & Fields, R. D. (2022). Oligodendroglia are emerging players in several forms of learning and memory. Communications Biology, 5(1), 1148.

Nath, S., & Devi, G. R. (2016). Three-dimensional culture systems in cancer research: Focus on tumor spheroid model. Pharmacology & therapeutics, 163, 94-108.

Neal, J. T., Li, X., Zhu, J., Giangarra, V., Grzeskowiak, C. L., Ju, J., Liu, I. H., Chiou, S.-H., Salahudeen, A. A., & Smith, A. R. (2018). Organoid modeling of the tumor immune microenvironment. Cell, 175(7), 1972-1988. e1916.

Nicolas, S., Abdellatef, S., Haddad, M. A., Fakhoury, I., & El-Sibai, M. (2019). Hypoxia and EGF stimulation regulate VEGF expression in human glioblastoma multiforme (GBM) cells by differential regulation of the PI3K/Rho-GTPase and MAPK pathways. Cells, 8(11), 1397.

Nishimura, K., Inoue, T., Yoshimoto, K., Taniguchi, T., Kitamura, Y., & Agata, K. (2011). Regeneration of dopaminergic neurons after 6-hydroxydopamine-induced lesion in planarian brain. Journal of neurochemistry, 119(6), 1217-1231.

Njonkou, R., Jackson, C. M., Woodworth, G. F., & Hersh, D. S. (2022). Pediatric glioblastoma: mechanisms of immune evasion and potential therapeutic opportunities. Cancer Immunology, Immunotherapy, 71(8), 1813-1822.

Nobusawa, S., Watanabe, T., Kleihues, P., & Ohgaki, H. (2009). IDH1 mutations as molecular signature and predictive factor of secondary glioblastomas. Clinical cancer research, 15(19), 6002-6007.

Noctor, S. C., Flint, A. C., Weissman, T. A., Wong, W. S., Clinton, B. K., & Kriegstein, A. R. (2002). Dividing precursor cells of the embryonic cortical ventricular zone have

morphological and molecular characteristics of radial glia. Journal of Neuroscience, 22(8), 3161-3173.

Notaras, M., Lodhi, A., Barrio-Alonso, E., Foord, C., Rodrick, T., Jones, D., Fang, H., Greening, D., & Colak, D. (2021). Neurodevelopmental signatures of narcotic and neuropsychiatric risk factors in 3D human-derived forebrain organoids. Molecular psychiatry, 26(12), 7760-7783.

O'Rourke, D. M., Nasrallah, M. P., Desai, A., Melenhorst, J. J., Mansfield, K., Morrissette, J. J., Martinez-Lage, M., Brem, S., Maloney, E., & Shen, A. (2017). A single dose of peripherally infused EGFRvIII-directed CAR T cells mediates antigen loss and induces adaptive resistance in patients with recurrent glioblastoma. Science translational medicine, 9(399), eaaa0984.

Obien, M. E. J., Hierlemann, A., & Frey, U. (2019). Accurate signal-source localization in brain slices by means of high-density microelectrode arrays. Scientific reports, 9(1), 788.

Ohgaki, H., & Kleihues, P. (2013). The definition of primary and secondary glioblastoma. Clinical cancer research, 19(4), 764-772.

Okada, H., Low, K. L., Kohanbash, G., McDonald, H. A., Hamilton, R. L., & Pollack, I. F. (2008). Expression of glioma-associated antigens in pediatric brain stem and non-brain stem gliomas. Journal of neuro-oncology, 88, 245-250.

Olympios, N., Gilard, V., Marguet, F., Clatot, F., Di Fiore, F., & Fontanilles, M. (2021). TERT promoter alterations in glioblastoma: a systematic review. Cancers, 13(5), 1147.

Orcheston-Findlay, L., Bax, S., Utama, R., Engel, M., Govender, D., & O'Neill, G. (2021). Advanced spheroid, tumouroid and 3D bioprinted in-vitro models of adult and paediatric glioblastoma. International Journal of Molecular Sciences, 22(6), 2962.

Ormel, P. R., Vieira de Sá, R., Van Bodegraven, E. J., Karst, H., Harschnitz, O., Sneeboer, M. A., Johansen, L. E., van Dijk, R. E., Scheefhals, N., & Berdenis van Berlekom, A. (2018). Microglia innately develop within cerebral organoids. Nature communications, 9(1), 4167.

Ostrom, Q. T., Price, M., Neff, C., Cioffi, G., Waite, K. A., Kruchko, C., & Barnholtz-Sloan, J. S. (2022). CBTRUS statistical report: primary brain and other central nervous system tumors diagnosed in the United States in 2015–2019. Neuro-Oncology, 24(Supplement_5), v1-v95.

Ozone, C., Suga, H., Eiraku, M., Kadoshima, T., Yonemura, S., Takata, N., Oiso, Y., Tsuji, T., & Sasai, Y. (2016). Functional anterior pituitary generated in self-organizing culture of human embryonic stem cells. Nature communications, 7(1), 10351.

Padovani, L., André, N., Constine, L. S., & Muracciole, X. (2012). Neurocognitive function after radiotherapy for paediatric brain tumours. Nat Rev Neurol, 8(10), 578-588. https://doi.org/10.1038/nrneurol.2012.182

Pagani, L. S. (2014). Environmental tobacco smoke exposure and brain development: the case of attention deficit/hyperactivity disorder. Neuroscience & Biobehavioral Reviews, 44, 195-205.

Paiva, A. R., Park, I., & Príncipe, J. C. (2010). A comparison of binless spike train measures. Neural Computing and Applications, 19, 405-419.

Pallares-Moratalla, C., & Bergers, G. (2024). The ins and outs of microglial cells in brain health and disease. Frontiers in Immunology, 15, 1305087.

Pamies, D., Block, K., Lau, P., Gribaldo, L., Pardo, C. A., Barreras, P., Smirnova, L., Wiersma, D., Zhao, L., & Harris, G. (2018). Rotenone exerts developmental neurotoxicity in a human brain spheroid model. Toxicology and applied pharmacology, 354, 101-114.

Pampaloni, F., Reynaud, E. G., & Stelzer, E. H. (2007). The third dimension bridges the gap between cell culture and live tissue. Nature reviews Molecular cell biology, 8(10), 839-845.

Panditharatna, E., Kilburn, L. B., Aboian, M. S., Kambhampati, M., Gordish-Dressman, H., Magge, S. N., Gupta, N., Myseros, J. S., Hwang, E. I., & Kline, C. (2018). Clinically relevant and minimally invasive tumor surveillance of pediatric diffuse midline gliomas using patient-derived liquid biopsy. Clinical cancer research, 24(23), 5850-5859.

Park, Y., Franz, C. K., Ryu, H., Luan, H., Cotton, K. Y., Kim, J. U., Chung, T. S., Zhao, S., Vazquez-Guardado, A., & Yang, D. S. (2021). Three-dimensional, multifunctional neural interfaces for cortical spheroids and engineered assembloids. Science advances, 7(12), eabf9153.

Paşca, A. M., Sloan, S. A., Clarke, L. E., Tian, Y., Makinson, C. D., Huber, N., Kim, C. H., Park, J.-Y., O'rourke, N. A., & Nguyen, K. D. (2015). Functional cortical neurons and astrocytes from human pluripotent stem cells in 3D culture. Nature methods, 12(7), 671-678.

Pasca, S., & Yoon, S.-J. (2018). Feeder-free, Xeno-free generation of cortical spheroids from human pluripotent stem cells.

Passaro, A. P., & Stice, S. L. (2021). Electrophysiological analysis of brain organoids: current approaches and advancements. Frontiers in Neuroscience, 14, 622137.

Patel, A. P., Fisher, J. L., Nichols, E., Abd-Allah, F., Abdela, J., Abdelalim, A., Abraha, H. N., Agius, D., Alahdab, F., Alam, T., Allen, C. A., Anber, N. H., Awasthi, A., Badali, H., Belachew, A. B., Bijani, A., Bjørge, T., Carvalho, F., Catalá-López, F.,…Fitzmaurice, C. (2019). Global, regional, and national burden of brain and other CNS cancer, 1990–2016: a systematic analysis for the Global Burden of Disease Study 2016. The Lancet Neurology, 18(4), 376-393. https://doi.org/https://doi.org/10.1016/S1474-4422(18)30468-X

Patel, J., Aittaleb, R., Doherty, R., Gera, A., Lau, B., Messinger, D., Wadden, J., Franson, A., Saratsis, A., & Koschmann, C. (2024). Liquid biopsy in H3K27M diffuse midline glioma. Neuro-Oncology, 26(Supplement_2), S101-S109.

Paul, M. K., & Mukhopadhyay, A. K. (2004). Tyrosine kinase–role and significance in cancer. International Journal of Medical Sciences, 1(2), 101.

Pearson, A. D., DuBois, S. G., Macy, M. E., de Rojas, T., Donoghue, M., Weiner, S., Knoderer, H., Bernardi, R., Buenger, V., & Canaud, G. (2024). Paediatric Strategy Forum for Medicinal Product Development of PI3-K, mTOR, AKT and GSK3β Inhibitors in Children and Adolescents with Cancer. European Journal of Cancer, 114145.

Peng, G., Wang, Y., Ge, P., Bailey, C., Zhang, P., Zhang, D., Meng, Z., Qi, C., Chen, Q., & Chen, J. (2021). The HIF1α-PDGFD-PDGFRα axis controls glioblastoma growth at normoxia/mild-hypoxia and confers sensitivity to targeted therapy by echinomycin. Journal of Experimental & Clinical Cancer Research, 40, 1-16.

Perdue, M. V., Ghasoub, M., Long, M., DeMayo, M. M., Bell, T. K., McMorris, C. A., Dewey, D., Gibbard, W. B., Tortorelli, C., & Harris, A. D. (2025). Altered markers of brain metabolism and excitability are associated with executive functioning in young children exposed to alcohol in utero. Metabolic Brain Disease, 40(1), 1-15.

Pham, M. T., Pollock, K. M., Rose, M. D., Cary, W. A., Stewart, H. R., Zhou, P., Nolta, J. A., & Waldau, B. (2018). Generation of human vascularized brain organoids. Neuroreport, 29(7), 588.

Phouphetlinthong, O., Partiot, E., Bernou, C., Sebban, A., Gaudin, R., & Charlot, B. (2023). Protruding cantilever microelectrode array to monitor the inner electrical activity of cerebral organoids. Lab on a Chip, 23(16), 3603-3614.

Pittet, M. J., Michielin, O., & Migliorini, D. (2022) Clinical relevance of tumour-associated macrophages. Nature Reviews Clinical Oncology, 19(6), 402-421.

Plessier, A., Le Dret, L., Varlet, P., Beccaria, K., Lacombe, J., Meriaux, S., Geffroy, F., Fiette, L., Flamant, P., & Chretien, F. (2017). New in vivo avatars of diffuse intrinsic pontine gliomas (DIPG) from stereotactic biopsies performed at diagnosis. Oncotarget, 8(32), 52543.

Pollack, I. F., Hamilton, R. L., Sobol, R. W., Nikiforova, M. N., Lyons-Weiler, M. A., LaFramboise, W. A., Burger, P. C., Brat, D. J., Rosenblum, M. K., & Holmes, E. J. (2011). IDH1 mutations are common in malignant gliomas arising in adolescents: a report from the Children's Oncology Group. Child's Nervous System, 27, 87-94.

Pollack, I. F., Jakacki, R. I., Blaney, S. M., Hancock, M. L., Kieran, M. W., Phillips, P., Kun, L. E., Friedman, H., Packer, R., & Banerjee, A. (2007). Phase I trial of imatinib in children with newly diagnosed brainstem and recurrent malignant gliomas: a Pediatric Brain Tumor Consortium report. Neuro-Oncology, 9(2), 145-160.

Pollack, I. F., Stewart, C. F., Kocak, M., Poussaint, T. Y., Broniscer, A., Banerjee, A., Douglas, J. G., Kun, L. E., Boyett, J. M., & Geyer, J. R. (2011). A phase II study of gefitinib and irradiation in children with newly diagnosed brainstem gliomas: a report from the Pediatric Brain Tumor Consortium. Neuro-Oncology, 13(3), 290-297.

Popova, G., Soliman, S. S., Kim, C. N., Keefe, M. G., Hennick, K. M., Jain, S., Li, T., Tejera, D., Shin, D., & Chhun, B. B. (2021). Human microglia states are conserved across experimental models and regulate neural stem cell responses in chimeric organoids. Cell stem cell, 28(12), 2153-2166. e2156.

Poulet, G., Massias, J., & Taly, V. (2019). Liquid biopsy: general concepts. Acta cytologica, 63(6), 449-455.

Priantti, J. N., Vilbert, M., de Moraes, F. C. A., Madeira, T., de Lima Santiago, E. M., Leighl, N. B., Cavalcante, L., & Karim, N. F. A. (2024). Neurocognitive adverse events related to lorlatinib in non-small cell lung cancer: a systematic review and meta-analysis. Cancers, 16(14), 2611.

Prior, V. G. (2022). Developing 3-dimensional in vitro models to investigate interactions between high-grade glioma and the tumour microenvironment. The University of Sydney.

Prior, V. G., Maksour, S., Miellet, S., Hulme, A. J., Chen, Y., Mirzaei, M., Wu, Y., Dottori, M., & O'Neill, G. M. (2024). Parsing the effect of co-culture with brain organoids on Diffuse Intrinsic Pontine Glioma (DIPG) using quantitative proteomics. The International Journal of Biochemistry & Cell Biology, 174, 106617.

Qayed, M., Cash, T., Tighiouart, M., MacDonald, T. J., Goldsmith, K. C., Tanos, R., Kean, L., Watkins, B., Suessmuth, Y., & Wetmore, C. (2020). A phase I study of sirolimus in combination with metronomic therapy (CHOAnome) in children with recurrent or refractory solid and brain tumors. Pediatric blood & cancer, 67(4), e28134.

Qian, X., Nguyen, H. N., Song, M. M., Hadiono, C., Ogden, S. C., Hammack, C., Yao, B., Hamersky, G. R., Jacob, F., & Zhong, C. (2016). Brain-region-specific organoids using mini-bioreactors for modeling ZIKV exposure. Cell, 165(5), 1238-1254.

Qian, X., Song, H., & Ming, G.-l. (2019). Brain organoids: advances, applications and challenges. Development, 146(8), dev166074.

Qian, X., Su, Y., Adam, C. D., Deutschmann, A. U., Pather, S. R., Goldberg, E. M., Su, K., Li, S., Lu, L., & Jacob, F. (2020). Sliced human cortical organoids for modeling distinct cortical layer formation. Cell stem cell, 26(5), 766-781. e769.

Qin, E. Y., Cooper, D. D., Abbott, K. L., Lennon, J., Nagaraja, S., Mackay, A., Jones, C., Vogel, H., Jackson, P. K., & Monje, M. (2017). Neural precursor-derived pleiotrophin mediates subventricular zone invasion by glioma. Cell, 170(5), 845-859. e819.

Qin, R., Zhang, Y., Yang, Y., Chen, J., Huang, L., Xu, W., Qin, Q., Liang, X., Lai, X., & Huang, X. (2024). Decoding single-cell molecular mechanisms in astrocyte-to-iN reprogramming via Ngn2-and Pax6-mediated direct lineage switching. European Journal of Medical Research, 29(1), 390.

Quadrato, G., Nguyen, T., Macosko, E. Z., Sherwood, J. L., Min Yang, S., Berger, D. R., Maria, N., Scholvin, J., Goldman, M., & Kinney, J. P. (2017). Cell diversity and network dynamics in photosensitive human brain organoids. Nature, 545(7652), 48-53.

Rahban, M., Joushi, S., Bashiri, H., Saso, L., & Sheibani, V. (2024). Characterization of prevalent tyrosine kinase inhibitors and their challenges in glioblastoma treatment. Frontiers in Chemistry, 11, 1325214.

Raponi, E., Agenes, F., Delphin, C., Assard, N., Baudier, J., Legraverend, C., & Deloulme, J. C. (2007). S100B expression defines a state in which GFAP-expressing cells lose their neural stem cell potential and acquire a more mature developmental stage. Glia, 55(2), 165-177.

Raychaudhuri, B., Rayman, P., Ireland, J., Ko, J., Rini, B., Borden, E. C., Garcia, J., Vogelbaum, M. A., & Finke, J. (2011). Neuro-oncology, 13(2), 591-599.

Rebelo, S. P., Pinto, C., Martins, T. R., Harrer, N., Estrada, M. F., Loza-Alvarez, P., Cabeçadas, J., Alves, P. M., Gualda, E. J., Sommergruber, W., & Brito, C. (2018). 3D-3-culture: A tool to unveil macrophage plasticity in the tumour microenvironment. Biomaterials, 163, 185-197.

Reifenberger, G., Liu, L., Ichimura, K., Schmidt, E. E., & Collins, V. P. (1993). Amplification and overexpression of the MDM2 gene in a subset of human malignant gliomas without p53 mutations. Cancer research, 53(12), 2736-2739.

Renner, H., Becker, K. J., Kagermeier, T. E., Grabos, M., Eliat, F., Günther, P., Schöler, H. R., & Bruder, J. M. (2021). Cell-type-specific high throughput toxicity testing in human midbrain Organoids. Frontiers in Molecular Neuroscience, 14.

Restivo, G., Tastanova, A., Balázs, Z., Panebianco, F., Diepenbruck, M., Ercan, C., Preca, B.-T., Hafner, J., Weber, W. P., & Kurzeder, C. (2022). Live slow-frozen human tumor tissues viable for 2D, 3D, ex vivo cultures and single-cell RNAseq. Communications Biology, 5(1), 1144.

Reumann, D., Krauditsch, C., Novatchkova, M., Sozzi, E., Wong, S. N., Zabolocki, M., Priouret, M., Doleschall, B., Ritzau-Reid, K. I., & Piber, M. (2023). In vitro modeling of the human dopaminergic system using spatially arranged ventral midbrain–striatum–cortex assembloids. Nature methods, 20(12), 2034-2047.

Reynolds, B. A., & Weiss, S. (1992). Generation of neurons and astrocytes from isolated cells of the adult mammalian central nervous system. science, 255(5052), 1707-1710.

Riley, E. P., Infante, M. A., & Warren, K. R. (2011). Fetal alcohol spectrum disorders: an overview. Neuropsychology review, 21, 73-80.

Romano, R., & Bucci, C. (2020). Role of EGFR in the Nervous System. Cells, 9(8), 1887.

Sakaguchi, H., Kadoshima, T., Soen, M., Narii, N., Ishida, Y., Ohgushi, M., Takahashi, J., Eiraku, M., & Sasai, Y. (2015). Generation of functional hippocampal neurons from self-organizing human embryonic stem cell-derived dorsomedial telencephalic tissue. Nature communications, 6(1), 1-11.

Samarasinghe, R. A., Miranda, O. A., Buth, J. E., Mitchell, S., Ferando, I., Watanabe, M., Allison, T. F., Kurdian, A., Fotion, N. N., & Gandal, M. J. (2021). Identification of neural oscillations and epileptiform changes in human brain organoids. Nature neuroscience, 24(10), 1488-1500.

Sandström, J., Eggermann, E., Charvet, I., Roux, A., Toni, N., Greggio, C., Broyer, A., Monnet-Tschudi, F., & Stoppini, L. (2017). Development and characterization of a human embryonic stem cell-derived 3D neural tissue model for neurotoxicity testing. Toxicology in Vitro, 38, 124-135.

Sarnow, K., Majercak, E., Qurbonov, Q., Cruzeiro, G. A., Jeong, D., Harque, I. A., Khalil, A., Baird, L. C., Filbin, M. G., & Tang, X. (2024). Neuroimmune-competent human brain organoid model of Diffuse Midline Glioma. Neuro-Oncology, noae245.

Sato, T., Vries, R. G., Snippert, H. J., Van De Wetering, M., Barker, N., Stange, D. E., Van Es, J. H., Abo, A., Kujala, P., & Peters, P. J. (2009). Single Lgr5 stem cells build crypt-villus structures in vitro without a mesenchymal niche. Nature, 459(7244), 262-265.

Schafer, D. P., Lehrman, E. K., Kautzman, A. G., Koyama, R., Mardinly, A. R., Yamasaki, R., Ransohoff, R. M., Greenberg, M. E., Barres, B. A., & Stevens, B. (2012). Microglia sculpt postnatal neural circuits in an activity and complement-dependent manner. Neuron, 74(4), 691-705.

Schoenmaekers, J., Dijkstra, J., van der Wekken, A., Paats, M., Broen, M., Brandts, L., Dingemans, A.-M., & Hendriks, L. (2024). In-depth Analysis of Lorlatinib-related neurocognitive Adverse Events in Patients With Non–small-cell Lung Cancer. Clinical lung cancer, 25(2), 168-174. e161.

Scholz, S., Lewis, K., Saulich, F., Endres, M., Boehmerle, W., & Huehnchen, P. (2022). Induced pluripotent stem cell-derived brain organoids as potential human model system for chemotherapy induced CNS toxicity. Frontiers in Molecular Biosciences, 9, 1006497.

Schröter, M., Wang, C., Terrigno, M., Hornauer, P., Huang, Z., Jagasia, R., & Hierlemann, A. (2022). Functional imaging of brain organoids using high-density microelectrode arrays. MRS bulletin, 47(6), 530-544.

Seeger, R. C., Rayner, S. A., Banerjee, A., Chung, H., Laug, W. E., Neustein, H. B., & Benedict, W. F. (1977). Morphology, growth, chromosomal pattern, and fibrinolytic activity of two new human neuroblastoma cell lines. Cancer research, 37(5), 1364-1371.

Shaker, M. R., Pietrogrande, G., Martin, S., Lee, J.-H., Sun, W., & Wolvetang, E. J. (2021). Rapid and efficient generation of myelinating human oligodendrocytes in organoids. Frontiers in cellular neuroscience, 15, 631548.

Shammas, M. A. (2011). Telomeres, lifestyle, cancer, and aging. Current Opinion in Clinical Nutrition & Metabolic Care, 14(1), 28-34.

Shao, J., Liu, Y., Gao, D., Tu, J., & Yang, F. (2021). Neural burst firing and its roles in mental and neurological disorders. Frontiers in cellular neuroscience, 15, 741292.

Sharf, T., Van Der Molen, T., Glasauer, S. M., Guzman, E., Buccino, A. P., Luna, G., Cheng, Z., Audouard, M., Ranasinghe, K. G., & Kudo, K. (2022). Functional neuronal circuitry and oscillatory dynamics in human brain organoids. Nature communications, 13(1), 4403.

Shaw, A. T., Felip, E., Bauer, T. M., Besse, B., Navarro, A., Postel-Vinay, S., Gainor, J. F., Johnson, M., Dietrich, J., & James, L. P. (2017). Lorlatinib in non-small-cell lung cancer with ALK or ROS1 rearrangement: an international, multicentre, open-label, single-arm first-in-man phase 1 trial. The Lancet Oncology, 18(12), 1590-1599.

Sheikh, S. R., Klesse, L. J., Mangum, R., Bui, A., Siegel, B. I., Abdelbaki, M. S., & Patel, N. J. (2024). The role of MEK inhibition in pediatric low-grade gliomas. Frontiers in Oncology, 14, 1503894.

Shi, Y., Kirwan, P., & Livesey, F. J. (2012). Directed differentiation of human pluripotent stem cells to cerebral cortex neurons and neural networks. Nature protocols, 7(10), 1836-1846.

Shi, Y., Kirwan, P., Smith, J., MacLean, G., Orkin, S. H., & Livesey, F. J. (2012). A human stem cell model of early Alzheimer's disease pathology in Down syndrome. Science translational medicine, 4(124), 124ra129-124ra129.

Shin, H., Jeong, S., Lee, J.-H., Sun, W., Choi, N., & Cho, I.-J. (2021). 3D high-density microelectrode array with optical stimulation and drug delivery for investigating neural circuit dynamics. Nature communications, 12(1), 492.

Sil, S., Periyasamy, P., Thangaraj, A., Chivero, E. T., & Buch, S. (2018). PDGF/PDGFR axis in the neural systems. Molecular Aspects of Medicine, 62, 63-74.

Silveira, C. R. F., Corveloni, A. C., Caruso, S. R., Macêdo, N. A., Brussolo, N. M., Haddad, F., Fernandes, T. R., de Andrade, P. V., Orellana, M. D., & Guerino-Cunha, R. L. (2022). Cytokines as an important player in the context of CAR-T cell therapy for cancer: Their role in tumor immunomodulation, manufacture, and clinical implications. Frontiers in Immunology, 13, 947648.

Silver, B., Gerrish, K., & Tokar, E. (2023). Cell-free DNA as a potential biomarker of differentiation and toxicity in cardiac organoids. Elife, 12, e83532.

Silver, B. B., Brooks, A., Gerrish, K., & Tokar, E. J. (2024). Isolation and Characterization of Cell-Free DNA from Cerebral Organoids. International Journal of Molecular Sciences, 25(10), 5522.

Singla, A. K., Madan, R., Gupta, K., Goyal, S., Kumar, N., Sahoo, S. K., Uppal, D. K., & Ahuja, C. K. (2021). Clinical behaviour and outcome in pediatric glioblastoma: current scenario. Radiation oncology journal, 39(1), 72.

Slika, H., Karimov, Z., Alimonti, P., Abou-Mrad, T., De Fazio, E., Alomari, S., & Tyler, B. (2023). Preclinical models and technologies in Glioblastoma Research: evolution, current state, and future avenues. International Journal of Molecular Sciences, 24(22), 16316.

Sloan, S. A., Darmanis, S., Huber, N., Khan, T. A., Birey, F., Caneda, C., Reimer, R., Quake, S. R., Barres, B. A., & Paşca, S. P. (2017). Human astrocyte maturation captured in 3D cerebral cortical spheroids derived from pluripotent stem cells. Neuron, 95(4), 779-790. e776.

Solomon, B. J., Bauer, T. M., Mok, T. S., Liu, G., Mazieres, J., de Marinis, F., Goto, Y., Kim, D.-W., Wu, Y.-L., & Jassem, J. (2023). Efficacy and safety of first-line lorlatinib versus crizotinib in patients with advanced, ALK-positive non-small-cell lung cancer: updated analysis of data from the phase 3, randomised, open-label CROWN study. The Lancet Respiratory Medicine, 11(4), 354-366.

SongTao, Q., Lei, Y., Si, G., YanQing, D., HuiXia, H., XueLin, Z., LanXiao, W., & Fei, Y. (2012). IDH mutations predict longer survival and response to temozolomide in secondary glioblastoma. Cancer science, 103(2), 269-273.

Soscia, D. A., Lam, D., Tooker, A. C., Enright, H. A., Triplett, M., Karande, P., Peters, S. K., Sales, A. P., Wheeler, E. K., & Fischer, N. O. (2020). A flexible 3-dimensional microelectrode array for in vitro brain models. Lab on a Chip, 20(5), 901-911.

Soule, H. D., Maloney, T. M., Wolman, S. R., Peterson Jr, W. D., Brenz, R., McGrath, C. M., Russo, J., Pauley, R. J., Jones, R. F., & Brooks, S. (1990). Isolation and characterization of a spontaneously immortalized human breast epithelial cell line, MCF-10. Cancer research, 50(18), 6075-6086.

Sposto, R., Ertel, I. J., Jenkin, R., Boesel, C. P., Venes, J. L., Ortega, J. A., Evans, A. E., Waral, W., & Hammond, D. (1989). The effectiveness of chemotherapy for treatment of high grade astrocytoma in children: results of a randomized trial: a report from the Childrens Cancer Study Group. Journal of neuro-oncology, 7, 165-177.

Stallard, S., Savelieff, M. G., Wierzbicki, K., Mullan, B., Miklja, Z., Bruzek, A., Garcia, T., Siada, R., Anderson, B., & Singer, B. H. (2018). CSF H3F3A K27M circulating tumor DNA copy number quantifies tumor growth and in vitro treatment response. Acta neuropathologica communications, 6, 1-4.

Stiefel, K. M., & Ermentrout, G. B. (2016). Neurons as oscillators. Journal of neurophysiology, 116(6), 2950-2960.

Stock, S., Schmitt, M., & Sellner, L. (2019). Optimizing manufacturing protocols of chimeric antigen receptor T cells for improved anticancer immunotherapy. International Journal of Molecular Sciences, 20(24), 6223.

Straehla, J. P., Hajal, C., Safford, H. C., Offeddu, G. S., Boehnke, N., Dacoba, T. G., Wyckoff, J., Kamm, R. D., & Hammond, P. T. (2022). A predictive microfluidic model of human glioblastoma to assess trafficking of blood–brain barrier-penetrant nanoparticles. Proceedings of the National Academy of Sciences, 119(23), e2118697119.

Stringer, B. W., Day, B. W., D'Souza, R. C., Jamieson, P. R., Ensbey, K. S., Bruce, Z. C., Lim, Y. C., Goasdoué, K., Offenhäuser, C., & Akgül, S. (2019). A reference collection of

patient-derived cell line and xenograft models of proneural, classical and mesenchymal glioblastoma. Scientific reports, 9(1), 4902.

Stupp, R., Mason, W. P., Van Den Bent, M. J., Weller, M., Fisher, B., Taphoorn, M. J., Belanger, K., Brandes, A. A., Marosi, C., & Bogdahn, U. (2005). Radiotherapy plus concomitant and adjuvant temozolomide for glioblastoma. New England journal of medicine, 352(10), 987-996.

Sun, X.-Y., Ju, X.-C., Li, Y., Zeng, P.-M., Wu, J., Zhou, Y.-Y., Shen, L.-B., Dong, J., Chen, Y.-J., & Luo, Z.-G. (2022). Generation of vascularized brain organoids to study neurovascular interactions. Elife, 11, e76707.

Sundar, S. J., Shakya, S., Barnett, A., Wallace, L. C., Jeon, H., Sloan, A., Recinos, V., & Hubert, C. G. (2022). Three-dimensional organoid culture unveils resistance to clinical therapies in adult and pediatric glioblastoma. Translational oncology, 15(1), 101251.

Suri, V., Das, P., Jain, A., Sharma, M. C., Borkar, S. A., Suri, A., Gupta, D., & Sarkar, C. (2009). Pediatric glioblastomas: a histopathological and molecular genetic study. Neuro-Oncology, 11(3), 274-280.

Susaimanickam, P. J., Kiral, F. R., & Park, I.-H. (2022). Region specific brain organoids to study neurodevelopmental disorders. International Journal of Stem Cells, 15(1), 26-40.

Suzuki, I., Matsuda, N., Han, X., Noji, S., Shibata, M., Nagafuku, N., & Ishibashi, Y. (2023). Large-Area Field Potential Imaging Having Single Neuron Resolution Using 236 880 Electrodes CMOS-MEA Technology. Advanced Science, 10(20), 2207732.

Tatti, R., Haley, M. S., Swanson, O. K., Tselha, T., & Maffei, A. (2017). Neurophysiology and regulation of the balance between excitation and inhibition in neocortical circuits. Biological psychiatry, 81(10), 821-831.

Thomas, C. A., Tejwani, L., Trujillo, C. A., Negraes, P. D., Herai, R. H., Mesci, P., Macia, A., Crow, Y. J., & Muotri, A. R. (2017). Modeling of TREX1-dependent autoimmune disease using human stem cells highlights L1 accumulation as a source of neuroinflammation. Cell stem cell, 21(3), 319-331. e318.

Thompson, S. J., Leigh, L., Christensen, R., Xiong, X., Kun, L. E., Heideman, R. L., Reddick, W. E., Gajjar, A., Merchant, T., & Pui, C.-H. (2001). Immediate neurocognitive effects of methylphenidate on learning-impaired survivors of childhood cancer. Journal of Clinical Oncology, 19(6), 1802-1808.

Thorel, L., Perréard, M., Florent, R., Divoux, J., Coffy, S., Vincent, A., Gaggioli, C., Guasch, G., Gidrol, X., & Weiswald, L.-B. (2024). Patient-derived tumor organoids: a new avenue for preclinical research and precision medicine in oncology. Experimental & Molecular Medicine, 56(7), 1531-1551.

Tian, A., Muffat, J., & Li, Y. (2020). Studying human neurodevelopment and diseases using 3D brain organoids. Journal of Neuroscience, 40(6), 1186-1193.

Tinkle, C. L., Broniscer, A., Chiang, J., Campagne, O., Huang, J., Orr, B. A., Li, X., Patay, Z., Zhang, J., & Baker, S. J. (2021). Phase I study using crenolanib to target PDGFR kinase in children and young adults with newly diagnosed DIPG or recurrent high-grade glioma, including DIPG. Neuro-Oncology Advances, 3(1), vdab179.

Treanor, C. J., McMenamin, U. C., O'Neill, R. F., Cardwell, C. R., Clarke, M. J., Cantwell, M. M., & Donnelly, M. (2016). Non-pharmacological interventions for cognitive impairment due to systemic cancer treatment. Cochrane Database of Systematic Reviews(8).

Trujillo, C. A., Adams, J. W., Negraes, P. D., Carromeu, C., Tejwani, L., Acab, A., Tsuda, B., Thomas, C. A., Sodhi, N., & Fichter, K. M. (2021). Pharmacological reversal of synaptic and

network pathology in human MECP2-KO neurons and cortical organoids. EMBO molecular medicine, 13(1), e12523.

Trujillo, C. A., Gao, R., Negraes, P. D., Gu, J., Buchanan, J., Preissl, S., Wang, A., Wu, W., Haddad, G. G., & Chaim, I. A. (2019). Complex oscillatory waves emerging from cortical organoids model early human brain network development. Cell stem cell, 25(4), 558-569. e557.

Turtle, C. J., Hanafi, L.-A., Berger, C., Gooley, T. A., Cherian, S., Hudecek, M., Sommermeyer, D., Melville, K., Pender, B., & Budiarto, T. M. (2016). CD19 CAR–T cells of defined CD4+: CD8+ composition in adult B cell ALL patients. The Journal of clinical investigation, 126(6), 2123-2138.

Udaka, Y. T., Yeh-Nayre, L. A., Amene, C. S., VandenBerg, S. R., Levy, M. L., & Crawford, J. R. (2013). Recurrent pediatric central nervous system low-grade gliomas: the role of surveillance neuroimaging in asymptomatic children. Journal of Neurosurgery: Pediatrics, 11(2), 119-126.

Ueki, K., Ono, Y., Henson, J. W., Efird, J. T., Von Deimling, A., & Louis, D. N. (1996). CDKN2/p16 or RB alterations occur in the majority of glioblastomas and are inversely correlated. Cancer research, 56(1), 150-153.

Uppar, A. M., Sugur, H., Prabhuraj, A., Rao, M. B., Devi, B. I., Sampath, S., Arivazhagan, A., & Santosh, V. (2019). H3K27M, IDH1, and ATRX expression in pediatric GBM and their clinical and prognostic significance. Child's Nervous System, 35, 1537-1545.

Uzquiano, A., Kedaigle, A. J., Pigoni, M., Paulsen, B., Adiconis, X., Kim, K., Faits, T., Nagaraja, S., Antón-Bolaños, N., & Gerhardinger, C. (2022). Proper acquisition of cell class identity in organoids allows definition of fate specification programs of the human cerebral cortex. Cell, 185(20), 3770-3788. e3727.

Vadivelu, R. K., Kamble, H., Shiddiky, M. J., & Nguyen, N.-T. (2017). Microfluidic technology for the generation of cell spheroids and their applications. Micromachines, 8(4), 94.

Valvi, S., Manoharan, N., Mateos, M. K., Hassall, T. E., Ziegler, D. S., McCowage, G. B., Dun, M. D., Eisenstat, D. D., Gottardo, N. G., & Hansford, J. R. (2024). Management of patients with diffuse intrinsic pontine glioma in Australia and New Zealand: Australian and New Zealand Children's Haematology/Oncology Group position statement. Medical Journal of Australia.

Valyi-Nagy, K., Betsou, F., Susma, A., & Valyi-Nagy, T. (2021). Optimization of viable glioblastoma cryopreservation for establishment of primary tumor cell cultures. Biopreservation and Biobanking, 19(1), 60-66.

van der Plas, E., Spencer Noakes, T. L., Butcher, D. T., Weksberg, R., Galin-Corini, L., Wanstall, E. A., Te, P., Hopf, L., Guger, S., Spiegler, B. J., Hitzler, J., Schachar, R. J., Ito, S., & Nieman, B. J. (2020). Quantitative MRI outcomes in child and adolescent leukemia survivors: Evidence for global alterations in gray and white matter. NeuroImage: Clinical, 28, 102428. https://doi.org/https://doi.org/10.1016/j.nicl.2020.102428

Vasco, C., Canazza, A., Rizzo, A., Mossa, A., Corsini, E., Silvani, A., Fariselli, L., Salmaggi, A., & Ciusani, E. (2013). Circulating T regulatory cells migration and phenotype in glioblastoma patients: an in vitro study. Journal of neuro-oncology, 115, 353-363.

Velasco, S., Kedaigle, A. J., Simmons, S. K., Nash, A., Rocha, M., Quadrato, G., Paulsen, B., Nguyen, L., Adiconis, X., & Regev, A. (2019). Individual brain organoids reproducibly form cell diversity of the human cerebral cortex. Nature, 570(7762), 523-527.

Venkatesh, H. S., Morishita, W., Geraghty, A. C., Silverbush, D., Gillespie, S. M., Arzt, M., Tam, L. T., Espenel, C., Ponnuswami, A., & Ni, L. (2019). Electrical and synaptic integration of glioma into neural circuits. Nature, 573(7775), 539-545.

Verhaak, R. G., Hoadley, K. A., Purdom, E., Wang, V., Qi, Y., Wilkerson, M. D., Miller, C. R., Ding, L., Golub, T., & Mesirov, J. P. (2010). Integrated genomic analysis identifies clinically relevant subtypes of glioblastoma characterized by abnormalities in PDGFRA, IDH1, EGFR, and NF1. Cancer cell, 17(1), 98-110.

Vilgelm, A. E., Bergdorf, K., Wolf, M., Bharti, V., Shattuck-Brandt, R., Blevins, A., Jones, C., Phifer, C., Lee, M., & Lowe, C. (2020). Fine-needle aspiration-based patient-derived cancer organoids. Iscience, 23(8).

Vitanza, N. A., Johnson, A. J., Wilson, A. L., Brown, C., Yokoyama, J. K., Künkele, A., Chang, C. A., Rawlings-Rhea, S., Huang, W., & Seidel, K. (2021). Locoregional infusion of HER2-specific CAR T cells in children and young adults with recurrent or refractory CNS tumors: an interim analysis. Nature medicine, 27(9), 1544-1552.

Vitanza, N. A., Wilson, A. L., Huang, W., Seidel, K., Brown, C., Gustafson, J. A., Yokoyama, J. K., Johnson, A. J., Baxter, B. A., & Koning, R. W. (2023). Intraventricular B7-H3 CAR T cells for diffuse intrinsic pontine glioma: preliminary first-in-human bioactivity and safety. Cancer discovery, 13(1), 114-131.

Vivanco, I., Robins, H. I., Rohle, D., Campos, C., Grommes, C., Nghiemphu, P. L., Kubek, S., Oldrini, B., Chheda, M. G., & Yannuzzi, N. (2012). Differential sensitivity of glioma-versus lung cancer–specific EGFR mutations to EGFR kinase inhibitors. Cancer discovery, 2(5), 458-471.

Volik, S., Alcaide, M., Morin, R. D., & Collins, C. (2016). Cell-free DNA (cfDNA): clinical significance and utility in cancer shaped by emerging technologies. Molecular Cancer Research, 14(10), 898-908.

Walker, A. J., Majzner, R. G., Zhang, L., Wanhainen, K., Long, A. H., Nguyen, S. M., Lopomo, P., Vigny, M., Fry, T. J., & Orentas, R. J. (2017). Tumor antigen and receptor densities regulate efficacy of a chimeric antigen receptor targeting anaplastic lymphoma kinase. Molecular Therapy, 25(9), 2189-2201.

Walker-Daniels, J., Hess, A. R., Hendrix, M. J., & Kinch, M. S. (2003). Differential regulation of EphA2 in normal and malignant cells. The American journal of pathology, 162(4), 1037-1042.

Wang, L., Zhou, K., Fu, Z., Yu, D., Huang, H., Zang, X., & Mo, X. (2017). Brain development and Akt signaling: the crossroads of signaling pathway and neurodevelopmental diseases. Journal of Molecular Neuroscience, 61, 379-384.

Wang, Q., Cohen, J. D., Yukawa, T., Estrella, H., Leonard, C., Nunes, J., Choi, C., Mishra, N., Lewis, L., & Baker, K. S. (2022). Assessment of a 3D neural spheroid model to detect pharmaceutical-induced neurotoxicity. ALTEX-Alternatives to animal experimentation, 39(4), 560-582.

Wang, Q., Hu, B., Hu, X., Kim, H., Squatrito, M., Scarpace, L., DeCarvalho, A. C., Lyu, S., Li, P., & Li, Y. (2017). Tumor evolution of glioma-intrinsic gene expression subtypes associates with immunological changes in the microenvironment. Cancer cell, 32(1), 42-56. e46.

Wang, X., Chen, J.-x., Liu, Y.-h., You, C., & Mao, Q. (2013). Mutant TP53 enhances the resistance of glioblastoma cells to temozolomide by up-regulating O 6-methylguanine DNA-methyltransferase. Neurological Sciences, 34, 1421-1428.

Wang, Y., Wang, L., Zhu, Y., & Qin, J. (2018). Human brain organoid-on-a-chip to model prenatal nicotine exposure. Lab on a Chip, 18(6), 851-860.

Wang, Y., Wang, L., Guo, Y., Zhu, Y., & Qin, J. (2018). Engineering stem cell-derived 3D brain organoids in a perfusable organ-on-a-chip system. RSC advances, 8(3), 1677-1685.

Wang, Y., Tong, C., Lu, Y., Wu, Z., Guo, Y., Liu, Y., Wei, J., Wang, C., Yang, Q., & Han, W. (2023). Characteristics of premanufacture CD8+ T cells determine CAR-T efficacy in patients with diffuse large B-cell lymphoma. Signal Transduction and Targeted Therapy, 8(1), 409.

Warren, K. E., Gururangan, S., Geyer, J. R., McLendon, R. E., Poussaint, T. Y., Wallace, D., Balis, F. M., Berg, S. L., Packer, R. J., & Goldman, S. (2012). A phase II study of O6-benzylguanine and temozolomide in pediatric patients with recurrent or progressive high-grade gliomas and brainstem gliomas: a Pediatric Brain Tumor Consortium study. Journal of neuro-oncology, 106, 643-649.

Weber, J. D., Taylor, L. J., Roussel, M. F., Sherr, C. J., & Bar-Sagi, D. (1999). Nucleolar Arf sequesters Mdm2 and activates p53. Nature cell biology, 1(1), 20-26.

Weiswald, L.-B., Bellet, D., & Dangles-Marie, V. (2015). Spherical cancer models in tumor biology. Neoplasia, 17(1), 1-15.

Wen, P. Y., De Groot, J. F., Battiste, J. D., Goldlust, S. A., Garner, J. S., Simpson, J. A., Kijlstra, J., Olivero, A., & Cloughesy, T. F. (2020). Escalation portion of phase II study to evaluate the safety, pharmacokinetics, and clinical activity of the PI3K/mTOR inhibitor paxalisib (GDC-0084) in glioblastoma (GBM) with unmethylated O6-methylguanine-methyltransferase (MGMT) promotor status. In: American Society of Clinical Oncology.

Wetmore, C., Daryani, V. M., Billups, C. A., Boyett, J. M., Leary, S., Tanos, R., Goldsmith, K. C., Stewart, C. F., Blaney, S. M., & Gajjar, A. (2016). Phase II evaluation of sunitinib in the treatment of recurrent or refractory high-grade glioma or ependymoma in children: a children's Oncology Group Study ACNS1021. Cancer medicine, 5(7), 1416-1424.

Wevers, N. R., Kasi, D. G., Gray, T., Wilschut, K. J., Smith, B., van Vught, R., Shimizu, F., Sano, Y., Kanda, T., & Marsh, G. (2018). A perfused human blood–brain barrier on-a-chip for high-throughput assessment of barrier function and antibody transport. Fluids and Barriers of the CNS, 15, 1-12.

Wigmore, P. M., Mustafa, S., El-Beltagy, M., Lyons, L., Umka, J., & Bennett, G. (2010). Effects of 5-FU. In R. B. Raffa & R. J. Tallarida (Eds.), Chemo Fog: Cancer Chemotherapy-Related Cognitive Impairment (pp. 157-164). Springer New York. https://doi.org/10.1007/978-1-4419-6306-2_20

Williams, A. M., & Cole, P. D. (2021). Biomarkers of cognitive impairment in pediatric cancer survivors. Journal of Clinical Oncology, 39(16), 1766-1774.

Wilson, K., Shiuan, E., & Brantley-Sieders, D. M. (2021). Oncogenic functions and therapeutic targeting of EphA2 in cancer. Oncogene, 40(14), 2483-2495.

Wilson, T. A., Karajannis, M. A., & Harter, D. H. (2014). Glioblastoma multiforme: State of the art and future therapeutics. Surgical neurology international, 5.

Wisoff, J. H., Boyett, J. M., Berger, M. S., Brant, C., Li, H., Yates, A. J., McGuire-Cullen, P., Turski, P. A., Sutton, L. N., & Allen, J. C. (1998). Current neurosurgical management and the impact of the extent of resection in the treatment of malignant gliomas of childhood: a report of the Children's Cancer Group trial no. CCG-945. Journal of neurosurgery, 89(1), 52-59.

Wisoff, J. H., Sanford, R. A., Heier, L. A., Sposto, R., Burger, P. C., Yates, A. J., Holmes, E. J., & Kun, L. E. (2011). Primary neurosurgery for pediatric low-grade gliomas: a prospective multi-institutional study from the Children's Oncology Group. Neurosurgery, 68(6), 1548-1555.

Wong, C. H., Siah, K. W., & Lo, A. W. (2019). Estimation of clinical trial success rates and related parameters. Biostatistics, 20(2), 273-286.

Wu, S. Z., Roden, D. L., Al-Eryani, G., Bartonicek, N., Harvey, K., Cazet, A. S., Chan, C.-L., Junankar, S., Hui, M. N., & Millar, E. A. (2021). Cryopreservation of human cancers conserves tumour heterogeneity for single-cell multi-omics analysis. Genome medicine, 13(1), 81.

Wykosky, J., & Debinski, W. (2008). The EphA2 receptor and ephrinA1 ligand in solid tumors: function and therapeutic targeting. Molecular Cancer Research, 6(12), 1795-1806.

Wyss, J., Frank, N. A., Soleman, J., & Scheinemann, K. (2022). Novel pharmacological treatment options in pediatric glioblastoma—a systematic review. Cancers, 14(11), 2814.

Xiao, C., Shao, X. M., Olive, M. F., Griffin, W. C., Li, K.-Y., Krnjević, K., Zhou, C., & Ye, J.-H. (2009). Ethanol facilitates glutamatergic transmission to dopamine neurons in the ventral tegmental area. Neuropsychopharmacology, 34(2), 307-318.

Xiao, T., Xiao, Y., Wang, W., Tang, Y. Y., Xiao, Z., & Su, M. (2020). Targeting EphA2 in cancer. Journal of hematology & oncology, 13, 1-17.

Xie, R., Pal, V., Yu, Y., Lu, X., Gao, M., Liang, S., Huang, M., Peng, W., & Ozbolat, I. T. (2024). A comprehensive review on 3D tissue models: biofabrication technologies and preclinical applications. Biomaterials, 304, 122408.

Xie, W., Wittig Jr, J. H., Chapeton, J. I., El-Kalliny, M., Jackson, S. N., Inati, S. K., & Zaghloul, K. A. (2024). Neuronal sequences in population bursts encode information in human cortex. Nature, 1-8.

Yadav, N., Di Lisa, D., Giacomozzi, F., Cian, A., Giubertoni, D., Martinoia, S., & Lorenzelli, L. (2023). Development of multi-depth probing 3D microelectrode array to record electrophysiological activity within neural cultures. Journal of Micromechanics and Microengineering, 33(11), 115002.

Yan, H., Parsons, D. W., Jin, G., McLendon, R., Rasheed, B. A., Yuan, W., Kos, I., Batinic-Haberle, I., Jones, S., & Riggins, G. J. (2009). IDH1 and IDH2 mutations in gliomas. New England journal of medicine, 360(8), 765-773.

Yang, X., Forró, C., Li, T. L., Miura, Y., Zaluska, T. J., Tsai, C.-T., Kanton, S., McQueen, J. P., Chen, X., & Mollo, V. (2024). Kirigami electronics for long-term electrophysiological recording of human neural organoids and assembloids. Nature biotechnology, 1-8.

Yao, H., Hu, D., Wang, J., Wu, W., Zhao, H. H., Wang, L., Gleeson, J., & Haddad, G. G. (2023). Buprenorphine and methadone differentially alter early brain development in human cortical organoids. Neuropharmacology, 239, 109683.

Yao, H., Wu, W., Cerf, I., Zhao, H. W., Wang, J., Negraes, P. D., Muotri, A. R., & Haddad, G. G. (2020). Methadone interrupts neural growth and function in human cortical organoids. Stem Cell Research, 49, 102065.

Yi, Z., Prinzing, B. L., Cao, F., Gottschalk, S., & Krenciute, G. (2018). Optimizing EphA2-CAR T cells for the adoptive immunotherapy of glioma. Molecular Therapy Methods & Clinical Development, 9, 70-80.

Yin, F., Zhu, Y., Wang, Y., & Qin, J. (2018). Engineering brain organoids to probe impaired neurogenesis induced by cadmium. ACS biomaterials science & engineering, 4(5), 1908-1915.

Yoon, S.-J., Elahi, L. S., Pașca, A. M., Marton, R. M., Gordon, A., Revah, O., Miura, Y., Walczak, E. M., Holdgate, G. M., & Fan, H. C. (2019). Reliability of human cortical organoid generation. Nature methods, 16(1), 75-78.

Zeng, Y., Dong, J., Huang, M., Zhang, J.-e., Zhang, X., Xie, M., & Wefel, J. S. (2020). Nonpharmacological interventions for cancer-related cognitive impairment in adult cancer patients: a network meta-analysis. International journal of nursing studies, 104, 103514.

Zerrouqi, A., Pyrzynska, B., Febbraio, M., Brat, D. J., & Van Meir, E. G. (2012). P14ARF inhibits human glioblastoma–induced angiogenesis by upregulating the expression of TIMP3. The Journal of clinical investigation, 122(4), 1283-1295.

Zhang, P., Xia, Q., Liu, L., Li, S., & Dong, L. (2020). Current opinion on molecular characterization for GBM classification in guiding clinical diagnosis, prognosis, and therapy. Frontiers in Molecular Biosciences, 7, 562798.

Zhang, W., Jiang, J., Xu, Z., Yan, H., Tang, B., Liu, C., Chen, C., & Meng, Q. (2023). Microglia-containing human brain organoids for the study of brain development and pathology. Molecular psychiatry, 28(1), 96-107.

Zhang, Y., Dube, C., Gibert Jr, M., Cruickshanks, N., Wang, B., Coughlan, M., Yang, Y., Setiady, I., Deveau, C., & Saoud, K. (2018). The p53 pathway in glioblastoma. Cancers, 10(9), 297.

Zhang, Y., Gu, A., An, Z., Huang, S., Zhang, C., Zhong, X., & Hu, Y. (2024). B cells enhance EphA2 chimeric antigen receptor T cells cytotoxicity against glioblastoma via improving persistence. Human Immunology, 85(6), 111093.

Zhao, X., Yang, J., Zhang, X., Lu, X.-A., Xiong, M., Zhang, J., Zhou, X., Qi, F., He, T., & Ding, Y. (2020). Efficacy and safety of CD28-or 4-1BB-based CD19 CAR-T cells in B cell acute lymphoblastic leukemia. Molecular Therapy-Oncolytics, 18, 272-281.

Zhou, C., Zhuang, Y., Lin, X., Michelson, A. D., & Zhang, A. (2020). Changes in neurocognitive function and central nervous system structure in childhood acute lymphoblastic leukaemia survivors after treatment: a meta-analysis. British Journal of Haematology, 188(6), 945-961.

Zhu, H., Acquaviva, J., Ramachandran, P., Boskovitz, A., Woolfenden, S., Pfannl, R., Bronson, R. T., Chen, J. W., Weissleder, R., & Housman, D. E. (2009). Oncogenic EGFR signaling cooperates with loss of tumor suppressor gene functions in gliomagenesis. Proceedings of the National Academy of Sciences, 106(8), 2712-2716.

Zhu, S., Sridhar, A., Teng, J., Howard, R. J., Lindahl, E., & Hibbs, R. E. (2022). Structural and dynamic mechanisms of GABAA receptor modulators with opposing activities. Nature communications, 13(1), 4582.

Zhu, Y., Wang, L., Yin, F., Yu, Y., Wang, Y., Shepard, M. J., Zhuang, Z., & Qin, J. (2017). Probing impaired neurogenesis in human brain organoids exposed to alcohol. Integrative Biology, 9(12), 968-978.

Zourray, C., Kurian, M. A., Barral, S., & Lignani, G. (2022). Electrophysiological properties of human cortical organoids: current state of the art and future directions. Frontiers in Molecular Neuroscience, 15, 839366.

Zureick, A. H., McFadden, K. A., Mody, R., & Koschmann, C. (2019). Successful treatment of a TSC2-mutant glioblastoma with everolimus. BMJ Case Reports CP, 12(5), e227734.

Appendix

Supplementary data for Chapters 4 and 5.

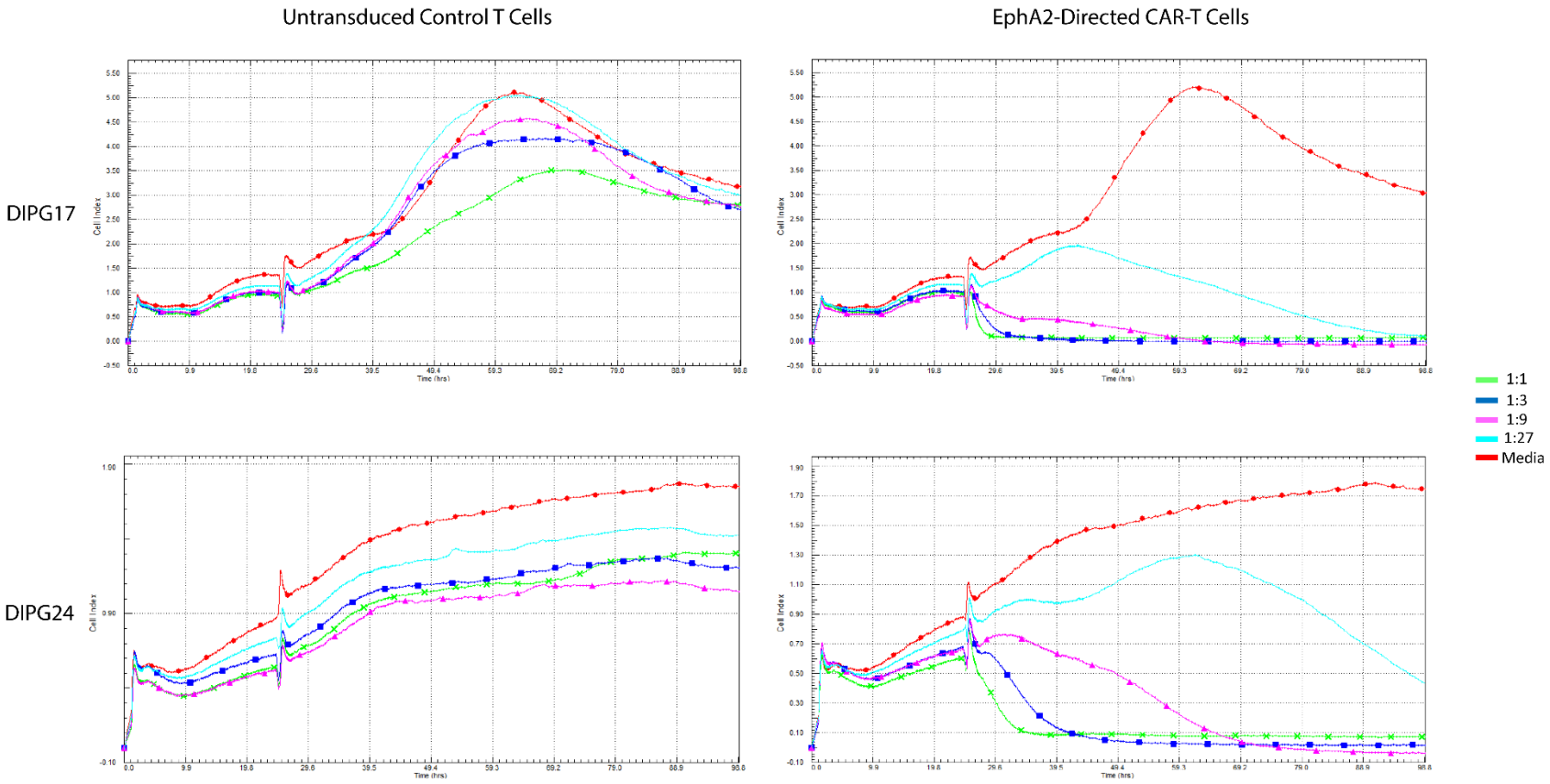

Supplementary Figure 4.1 – xCELLigence confirms EphA2-directed CAR-T cells target 2D DIPG cell lines.

DIPG17 and DIPG24 cells were seeded as 2D monolayers on xCELLigence E-plates and allowed to adhere and equilibrate for 24h. Electrical impedance was calculated by the unitless parameter Cell Index (y-axis). DIPG cells were then treated with untransduced control T cells or EphA2 CAR-T cells at a range of E:T ratios; 1:1 (green), 1:3 (dark blue), 1:9 (pink), and 1:27 (light blue). Untreated cells were used as a negative control (red). Cells were then monitored by the xCELLigence system for a further 3 days (98.8hr total). Data kindly supplied by Dr Jody MacLeod and Dr Yuyan Chen.

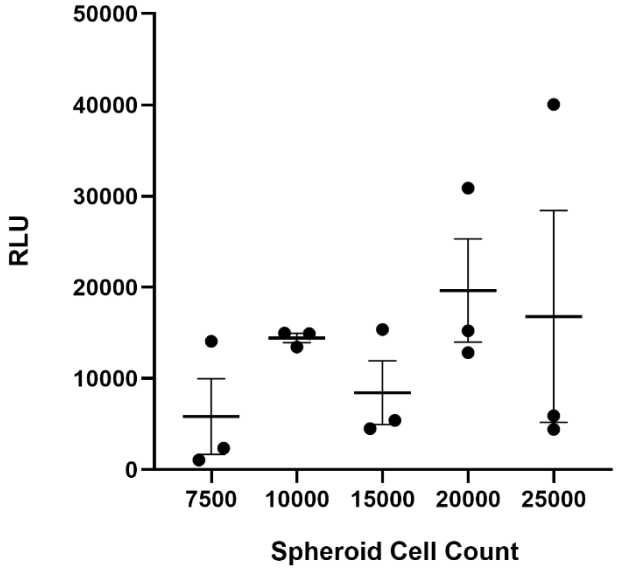

Supplementary Figure 4.2 - Bright-Glo readout from SpectraMax iD3 luminometer.

WK1-luc cells were seeded as spheroids at cell counts ranging from $7.5x10^3$ to $2.5x10^4$ ($n = 3$ spheroids per cell count). Following 96h aggregation, Bright-Glo luciferase assay was added to WK1-luc spheroids and luminescence recorded after 3 minutes using the SpectraMax iD3 luminometer. Luminescent signal was measured as relative light units (RLU). Error bars = mean ± SEM.

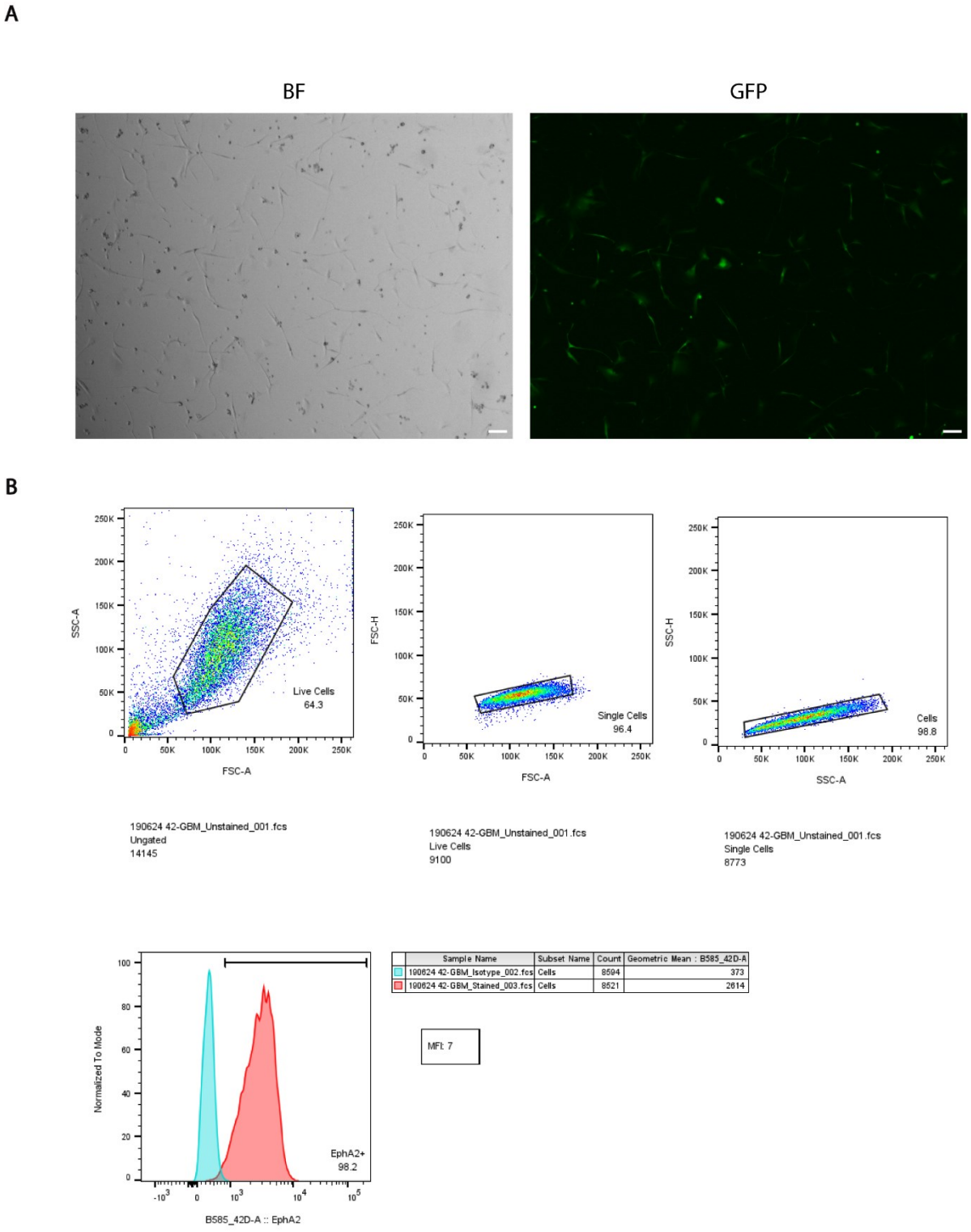

Supplementary Figure 4.3 - Transduction and characterisation of 2D pGBM-42 cells.

An adherent cell line was derived from CHW patient tumour sample pGBM-42. **A.** Cells were transduced with the eGFP-luciferase LVV, as shown by epifluorescence imaging (scale bars = 50µm). **B.** Flow cytometry data indicated % EphA2 expression and mean fluorescence intensity comparable to patient-derived DIPG cell lines.

Supplementary Table 5.1 - Consented patient tumour samples for culture

Sample ID	Tumour Type	3D PDO Establishment	Stable 2D Cell Line Establishment
3	Ewing sarcoma	No	No
4	Neuroblastoma	No	No
5	Neuroblastoma	No	No
6	Ewing sarcoma	No	No
7	Neuroblastoma	No	No
8	Paediatric glioblastoma	Yes	No
9	Neuroblastoma	No	Yes
10	Medulloblastoma; Non-Wnt, Non-SHH subtype	Yes	Yes
14	Pilocytic astrocytoma	No	No
15	Pilocytic astrocytoma	No	No
16	Pilocytic astrocytoma	No	No
17	Primitive neuroectodermal tumour (PNET)	Yes	No
19	Medulloblastoma; SHH subtype	No	No
21	Cystic nephroma	No	Yes
23	Medulloblastoma; Wnt subtype	Yes	Yes
24	Neuroblastoma	No	No
25	Embryonal rhabdomyosarcoma peritoneal metastasis	No	Yes
26	Osteosarcoma lung metastasis	No	No
31	Pineoblastoma	Yes	No
35	Neuroblastoma	No	No
40	Mixed germ cell brain tumour	Yes	No
42	Paediatric glioblastoma	Yes	Yes
43	Ewing sarcoma liver metastasis	Yes	No
44	Wilms tumour	No	No
47	Embryonal tumour with multilayered rosettes (ETMR)	No	No
55	Paediatric glioblastoma	Yes	No

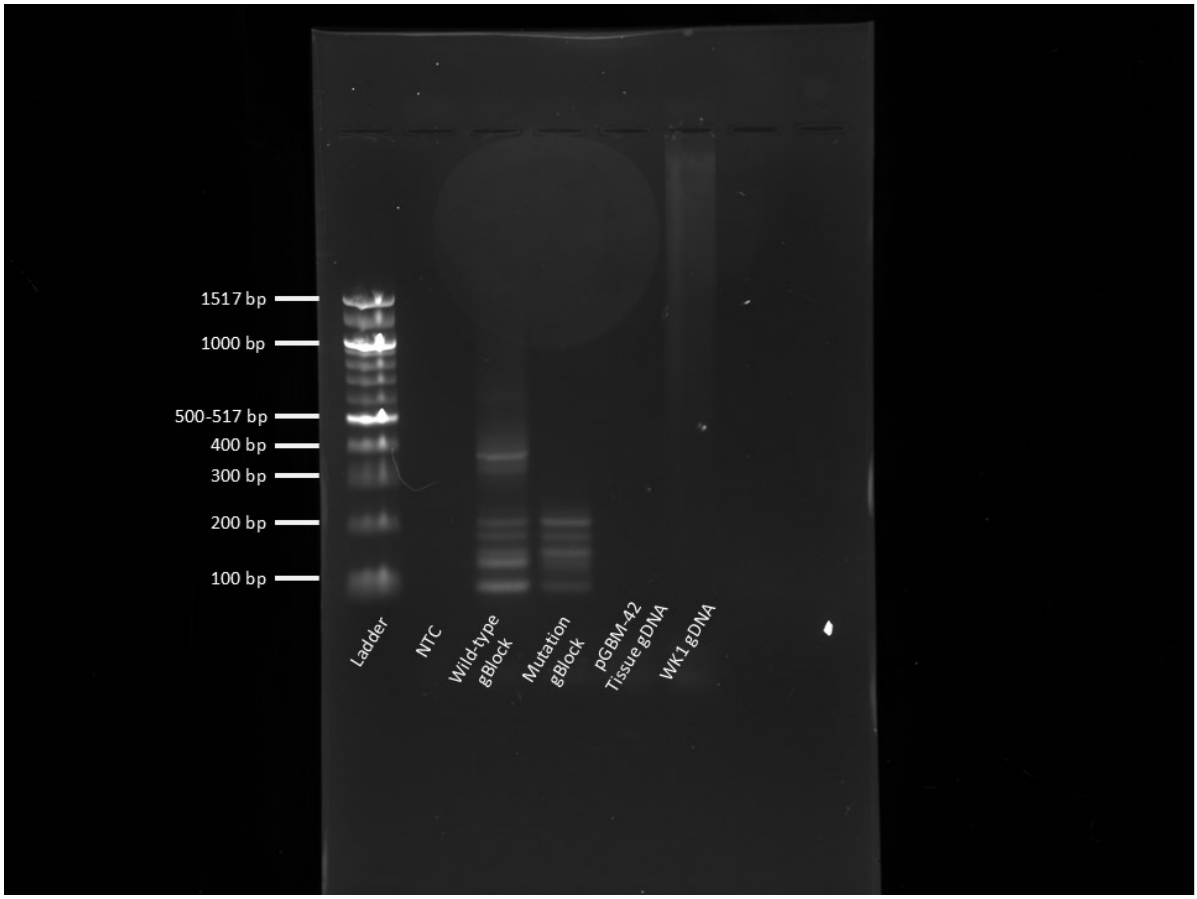

Supplementary Figure 5.1 - TERT sequences not detected in pGBM-42 by PCR.

Image shows a 2% (w/v) agarose gel with Quick-Load® 100 bp DNA ladder as reference. Samples were stained with 1:10000 GelRed fluorescent nucleic acid gel stain and gel electrophoresis performed at 120V for 40 minutes. The absence of bands in the pGBM-42 sample suggested lack of specificity of probes and primers for the *TERT* sequences.

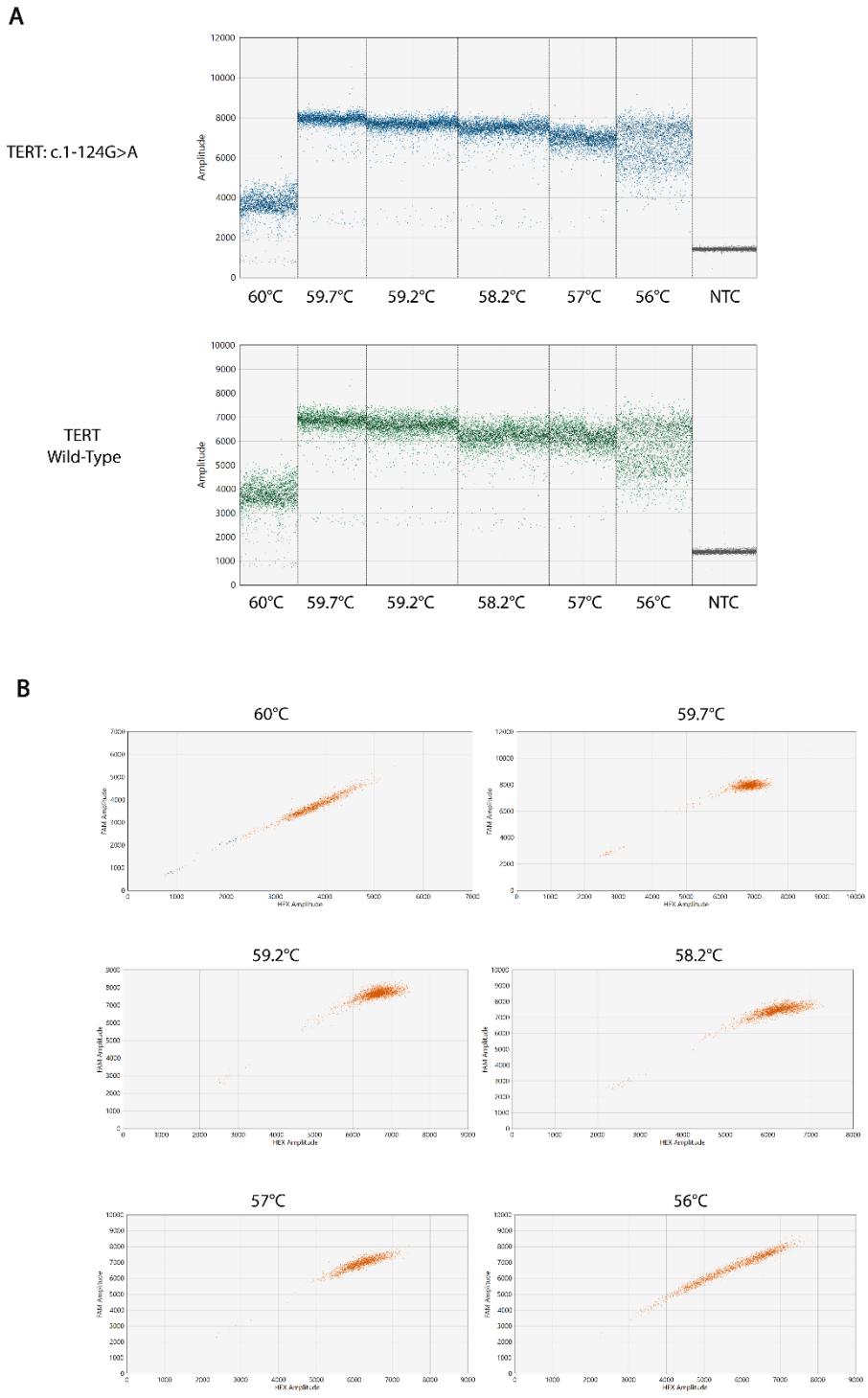

Supplementary Figure 5.2 - Annealing temperatures tested in TERT gBlocks.

Wild-type and mutant *TERT* sequence gBlocks were combined at 5ng/µl in TE buffer, then added to a master mix with probes and primers. Annealing was performed on a gradient of temperatures from 56-60°C for 40 cycles, then analysed by ddPCR. **A.** 1D amplitude plots show the recorded droplets containing the mutant sequence (blue) and wild-type sequence (green). **B.** 2D amplitude plots show predominantly 'double-positive' droplets containing both sequences (orange) and unable to delineate between individual gBlock populations.